



January 2019

Characteristics Of Convectively Induced Turbulence Determined From Tropical And Midlatitude Simulations

Katelyn Audrey Barber

Follow this and additional works at: <https://commons.und.edu/theses>

Recommended Citation

Barber, Katelyn Audrey, "Characteristics Of Convectively Induced Turbulence Determined From Tropical And Midlatitude Simulations" (2019). *Theses and Dissertations*. 2545.
<https://commons.und.edu/theses/2545>

This Dissertation is brought to you for free and open access by the Theses, Dissertations, and Senior Projects at UND Scholarly Commons. It has been accepted for inclusion in Theses and Dissertations by an authorized administrator of UND Scholarly Commons. For more information, please contact zeinebyousif@library.und.edu.

CHARACTERISTICS OF CONVECTIVELY INDUCED
TURBULENCE DETERMINED FROM TROPICAL AND
MIDLATITUDE SIMULATIONS

by

Katelyn A. Barber

Master of Science, University of North Dakota, 2015

Bachelor of Science, State University of New York at Oswego, 2013

A Dissertation

Submitted to the Graduate Faculty

of the

University of North Dakota

in partial fulfillment of the requirements

for the degree of

Doctor of Philosophy


Grand Forks, North Dakota

August

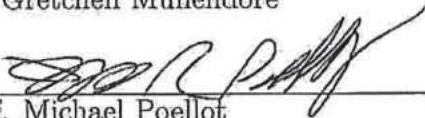
2019

Copyright 2019 Katelyn A. Barber

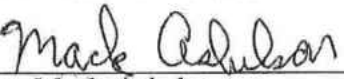
This thesis, submitted by Katelyn A. Barber in partial fulfillment of the requirements for the Degree of Doctor of Philosophy from the University of North Dakota, has been read by the Faculty Advisory Committee under whom the work has been done and is hereby approved.



Dr. Gretchen Mullendore



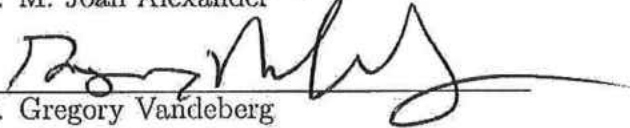
Prof. Michael Poellot



Dr. Mark Askelson



Dr. M. Joan Alexander



Dr. Gregory Vandenberg

This thesis is being submitted by the appointed advisory committee as having met all of the requirements of the School of Graduate Studies at the University of North Dakota and is hereby approved.



Chris Nelson
Dean of the School of Graduate Studies

7/30/19

DATE

PERMISSION

Title	Characteristics of convectively induced turbulence determined from tropical and midlatitude simulations
Department	Atmospheric Sciences
Degree	Doctor of Philosophy

In presenting this thesis in partial fulfillment of the requirements for a graduate degree from the University of North Dakota, I agree that the library of this University shall make it freely available for inspection. I further agree that permission for extensive copying for scholarly purposes may be granted by the professor who supervised my dissertation work or, in her absence, by the Chairperson of the department or the dean of the School of Graduate Studies. It is understood that any copying or publication or other use of this dissertation or part thereof for financial gain shall not be allowed without my written permission. It is also understood that due recognition shall be given to me and to the University of North Dakota in any scholarly use which may be made of any material in my dissertation.

Katelyn A. Barber
August 2, 2019

TABLE OF CONTENTS

LIST OF FIGURES	viii
LIST OF TABLES	xvii
ACKNOWLEDGMENTS	xix
ABSTRACT	xxi
CHAPTER	
1 INTRODUCTION	1
2 BACKGROUND	4
2.1 Convectively induced turbulence generation	5
2.2 Simulations of convectively induced turbulence	8
2.3 Convection and aviation	11
2.4 Turbulence indices and forecasting applications	16
2.5 Comparison of convective properties in the midlatitudes and tropics	19
3 OUT-OF-CLOUD CONVECTIVE TURBULENCE: ESTIMATION METHOD AND IMPACTS OF MODEL RESOLUTION	23
3.1 Motivation	23
3.2 Data and Methods	25
3.2.1 Pilot reports	25
3.2.2 Model setup	26
3.2.3 Turbulence metrics	30
3.2.4 Lateral avoidance	30
3.3 Results	33
3.3.1 Storms observed	33
3.3.2 S4 turbulence	39
3.3.3 Effects of varying resolution on turbulence	45
3.3.4 10–17 July S2 and S3 comparisons	52
3.4 Discussion and Conclusions	55

4	PREDICTING AVIATION HAZARDS: LOCATION OF OUT-OF-CLOUD TURBULENCE	58
4.1	Motivation	58
4.2	Data and Methods	62
4.2.1	Model setup	62
4.2.2	Eddy dissipation rate	63
4.2.3	Bulk analysis of turbulence location	63
4.2.4	Calculation of environmental variables	64
4.3	Results	65
4.3.1	Comparison of convective properties	65
4.3.2	Directional preference of turbulence (S4)	68
4.3.3	Influence of model resolution on the directional dis- tribution of turbulence	74
4.3.4	Influence of model resolution on environmental con- ditions	76
4.3.5	Correlation between environmental variables and turbulence intensity	89
4.4	Discussion and Conclusions	91
5	PROPERTIES OF CONVECTIVELY INDUCED TURBULENCE OVER DE- VELOPING OCEANIC CONVECTION	98
5.1	Motivation	98
5.2	Turbulence Incident in Southern Gulf of Mexico: 20 June 2017	100
5.3	Data and Methods	104
5.3.1	Model setup	104
5.3.2	Turbulence metrics	106
5.4	Results	107
5.4.1	Verification of simulated convection	107
5.4.2	WRF-derived turbulence predictors	111
5.4.3	Analysis of turbulence prediction in the vicinity of developing convection	117
5.5	Discussion and Conclusions	121
6	CHARACTERISTICS OF TROPICAL AND MIDLATITUDE OUT-OF-CLOUD CONVECTIVELY INDUCED TURBULENCE FROM HIGH RESOLUTION SIMULATIONS	125
6.1	Motivation	125
6.2	Data and Methods	127
6.3	Results	130
6.3.1	Case day and simulation overviews	130
6.3.2	Summary of turbulence diagnostics	149
6.3.3	Distributions of in-cloud and out-of-cloud turbulence	149

6.3.4	Characteristics of the simulated environment parameters near convection	151
6.4	Discussion and Conclusions	168
7	CONCLUSIONS	172
8	APPENDIX	178
8.1	Richardson number	178
8.2	Brown index	179
8.3	Dutton index	181
8.4	Ellrod index	181
8.5	Subgrid-scale eddy dissipation rate	182
8.6	Second-order structure functions	184
8.7	Colson-Panofsky turbulent kinetic energy	185
8.8	Marroquin DTF3	186
REFERENCES	188

LIST OF FIGURES

Figure	Page	
1	Model domain for model setup S1 (a), and model setups S2 and S3 (b). D02 represents the innermost nest of model setup S1 and D03 represents the innermost nest of model setups S2 and S3. The black circles represent the Mayville, ND and Bismarck, ND radars.	28
2	Model domain for model setup S4 on (a) 12 July 2015, (b) 13 July, and (c) 15 July.	29
3	Schematic depicting masking methodology for determining the turbulence distribution (color bar; $m^{2/3} s^{-1}$ within various distances from convective cores at various altitudes. Black grid cells represent echo top heights ≥ 8 km, blue color grid cells represent distances of (a) 10 mi (16.1 km) around ET cores, (b) 20 mi (32.2 km) around ET cores.	32
4	(a) Observed Mayville, ND radar reflectivity values (0.5° elevation angle) at 2155 UTC on 12 July and (b) simulated 1-km AGL radar reflectivity values at 0200 UTC on 13 July for S4 (forecast initialized at 0000 UTC on 12 July). Black box in (a) represents the model domain in (b). Black arrows are included to describe the northern complex discussed in above. See Fig. 2a for the complete model domain.	34
5	Maximum echo top heights (km) observed by Mayville and Bismarck, ND radar (a) and simulated by S4 (b).	35
6	Pilot reports of turbulence occurring on 12 July 2015 within S2-S3 model domain (innermost white box represents the 3km domain). Blue circles represent light turbulence reports and red represents moderate turbulence reports. Black dots within the circles indicate the report was made when the aircraft was greater than 8 km in altitude.	36

7	(a) Observed Mayville, ND radar reflectivity values (0.5° elevation angle) at 1925 UTC on 13 July and (b) simulated 1-km AGL radar reflectivity values at 1900 UTC on 13 July for S4 (forecast initialized at 0000 UTC on 13 July). Black box in (a) represents the model domain in (b). See Fig. 2b for the complete model domain.	37
8	(a) Observed Bismarck, ND radar reflectivity values (0.5° elevation angle) at 2325 UTC on 15 July and (b) simulated 1-km AGL radar reflectivity values at 0000 UTC on 16 July for S4 (forecast initialized at 0000 UTC on 15 July). Black box in (a) represents the model domain in (b). See Fig. 2c for the complete model domain.	38
9	(a) Observed Bismarck, ND radar reflectivity values (0.5° elevation angle) at 0225 UTC on 16 July and (b) simulated 1-km AGL radar reflectivity values at 0200 UTC on 16 July for S4 (forecast initialized at 0000 UTC on 15 July). Black box in (a) represents the model domain in (b). See Fig. 2c for the complete model domain.	38
10	(a) Eddy dissipation rate (magnitudes indicated using Lane et al. 2012) and (b) Ellrod index values at 8 km in altitude predicted from S4 at 0200 UTC 13 July 2015 (from 0000 UTC initialized forecast on 12 July). All colored regions in (b) are traditionally classified as "severe".	41
11	12 km normalized out-of-cloud eddy dissipation rate distribution $\geq 0.2 \text{ m}^{2/3} \text{ s}^{-1}$ (# of turbulent grid cells within bin divided by all grid cells with turbulence $\geq 0.2 \text{ m}^{2/3} \text{ s}^{-1}$) within (a) 10 mi (16.1 km), (b) 20 mi (32.2 km), and (c) 50 mi (80.5 km) of convective cores with echo top heights ≥ 8 km for S4. Dashed (cyan) and dotted (purple) vertical lines represent turbulence intensities based on Lane et al. (2012) and Sharman et al. (2014), respectively.	42
12	Normalized out-of-cloud eddy dissipation rate distribution $\geq 0.2 \text{ m}^{2/3} \text{ s}^{-1}$ (# of turbulent grid cells within bin divided by all grid cells with turbulence $\geq 0.2 \text{ m}^{2/3} \text{ s}^{-1}$) within 50 mi (80.5 km) of convective cores with echo top heights ≥ 8 km for S4. Dashed (cyan) and dotted (purple) vertical lines represent turbulence intensities based on Lane et al. (2012) and Sharman et al. (2014), respectively.	43
13	Maximum echo top heights (km) forecasted by S1-4 and estimated by radar on 12 July 2015 beginning at 0600 UTC.	46

14	Maximum echo top heights (km) forecasted by S1-4 and estimated by radar on 13 July 2015 beginning at 0600 UTC.	47
15	Maximum echo top heights (km) forecasted by S1-4 and estimated by radar on 15 July 2015 beginning at 0600 UTC.	48
16	Out-of-cloud eddy dissipation rate distribution values $\geq 0.2 \text{ m}^{2/3} \text{ s}^{-1}$ within 50 mi (80.5 km) of convective cores with echo top heights ≥ 8 km for S2-S4 on 12 July 2015. Dashed (cyan) and dotted (purple) vertical lines represent turbulence intensities based on Lane et al. (2012) and Sharman et al. (2014), respectively.	49
17	Out-of-cloud eddy dissipation rate distribution values $\geq 0.2 \text{ m}^{2/3} \text{ s}^{-1}$ within 50 mi (80.5 km) of convective cores with echo top heights ≥ 8 km for S2-S4 on 13 July 2015. Dashed (cyan) and dotted (purple) vertical lines represent turbulence intensities based on Lane et al. (2012) and Sharman et al. (2014), respectively.	51
18	Out-of-cloud eddy dissipation rate distribution values $\geq 0.2 \text{ m}^{2/3} \text{ s}^{-1}$ within 50 mi (80.5 km) of convective cores with echo top heights ≥ 8 km for S2-S4 on 15 July 2015. Dashed (cyan) and dotted (purple) vertical lines represent turbulence intensities based on Lane et al. (2012) and Sharman et al. (2014), respectively.	52
19	Distribution of eddy dissipation rate values $\geq 0.2 \text{ m}^{2/3} \text{ s}^{-1}$ within 50 mi (80.5 km) of convective cores with echo top heights ≥ 8 km for S2 and S3 across 8 simulation days, combining statistics at 8 km, 10 km, and 12 km in altitude. Dashed (cyan) and dotted (purple) vertical lines represent turbulence intensities based on Lane et al. (2012) and Sharman et al. (2014), respectively.	55
20	Compass degree definition of direction from convection.	64
21	Distributions of simulated echo tops (km) for S2 (red), S3 (blue), and S4 (green) on 12, 13, and 15 July.	66
22	Domain-wide distributions of simulated radar reflectivity (solid lines) and column-maximum simulated radar reflectivity (dashed lines) for S2 (red), S3 (blue), and S4 (green) on 12, 13, and 15 July.	66

23	Distribution of in-cloud (IC) and out-of-cloud (OC) vertical velocities (m s^{-1}) for S2 (red), S3 (blue), and S4 (green) on 12 (solid), 13 (dashed), and 15 (dotted) July between 8 km and 12 km.	67
24	Distribution of accumulated precipitation (mm) for S2 (red), S3 (blue), and S4 (green) on 12, 13, and 15 July.	68
25	Directional preference of out-of-cloud turbulence between 8 km and 12 km (all, light, and moderate or greater) in normalized percentage for S4 (top), S3 (middle), and S2 (bottom) on 12 July when convection is present (within 20 miles of convection).	70
26	Directional preference of out-of-cloud turbulence between 8 km and 12 km (all, light, and moderate or greater) in normalized percentage for S4 (top), S3 (middle), and S2 (bottom) on 13 July when convection is present (within 20 miles of convection).	72
27	Directional preference of out-of-cloud turbulence between 8 km and 12 km (all, light, and moderate or greater) in normalized percentage for S4 (top), S3 (middle), and S2 (bottom) on 15 July when convection is present (within 20 miles of convection).	73
28	Domain-wide distribution of static stability between 8 km and 12 km for S2 (red), S3 (blue), and S4 (green) on 12, 13, and 15 July.	77
29	Domain-wide distribution of vertical wind shear between 8 km and 12 km for S2 (red), S3 (blue), and S4 (green) on 12, 13, and 15 July.	77
30	Distribution of out-of-cloud static stability between 8 km and 12 km within 20 miles of convection on 12, 13, and 15 July subset by direction from convection for S2 (solid lines), S3 (dashed lines), and S4 (dotted lines). The vertical lines represents the mean static stability in the direction of greatest turbulence probability.	79
31	Distribution of out-of-cloud vertical wind shear between 8 km and 12 km within 20 miles of convection on 12, 13, and 15 July subset by direction from convection for S2 (solid lines), S3 (dashed lines), and S4 (dotted lines). The vertical lines represents the mean vertical wind shear in the direction of greatest turbulence probability.	82

32	Distribution of out-of-cloud Richardson number between 8 km and 12 km within 20 miles of convection on 12, 13, and 15 July subset by direction from convection for S2 (solid lines), S3 (dashed lines), and S4 (dotted lines). The vertical lines represents the mean Richardson number in the direction of greatest turbulence probability.	85
33	Distribution of out-of-cloud vertical velocities (absolute value) between 8 km and 12 km within 20 miles of convection on 12, 13, and 15 July subset by direction from convection for S2 (solid lines), S3 (dashed lines), and S4 (dotted lines). The vertical lines represents the mean vertical velocities in the direction of greatest turbulence probability.	88
34	Correlation of out-of-cloud static stability, vertical wind shear, vertical velocities, and turbulence intensity between 8 km and 12 km on 12 July, 20 miles within convection. Colored circles represent the direction turbulence probability is the greatest. Light, moderate, and severe turbulence thresholds are represented by the black, yellow, and pink vertical lines.	91
35	An example of the wind field (a and c) and turbulence intensity (b and d) at 10 km on 12 July for S2. Black contours represent echo top heights greater or equal to 10 km.	94
36	An example of the wind field (a and c) and turbulence intensity (b and d) at 10 km on 12 July for S3. Black contours represent echo top heights greater or equal to 10 km.	95
37	Baro-corrected altitude (km) and acceleration (g) recorded by the aircraft from 1552 UTC to 1800 UTC.	101
38	1500 UTC surface analysis issued by the Weather Prediction Center.	102
39	Observed brightness temperatures (K) from GOES-13 at a) 1545 UTC and b) 1645 UTC on 20 June, 2017. The Convective Diagnosis Oceanic Algorithm (CDO) hazards (c-d) at the same times as a-b (threshold descriptors in Table 11). Time (minute) of a detected lightning flash from 1530-1600 UTC (e), 1630-1700 UTC (f). White (a and b), blue (c and d) and black (e and f) stars represent the aircraft location at 1651 UTC.	103
40	Earth Networks lightning from 1645-1655 UTC (white crosses) and cloud top temperature (K) from GOES-13 at 1645 UTC. The black star represents the location of the aircraft at 1651 UTC.	105

41	Model domain for 20 June 2017 simulation. D02 represents the first nest within the domain with horizontal grid spacing of 9 km and D03 represents the innermost nest of the model set up with horizontal grid spacing of 3 km (red box). Area designated for convective development analysis is represented by the black box. The red star represents the location of the aircraft at 1651 UTC.	106
42	Simulated cloud top temperatures (K) at a) 1600 UTC and b) 1700 UTC on 20 June, 2017. White stars represent the approximate location of the aircraft at 1651 UTC.	108
43	2-km simulated radar reflectivity (a) and lightning flash densities per ten minutes determined from b) ice water path at 1650 UTC on 20 June, 2017. Black stars represent the approximate location of the aircraft at 1651 UTC.	109
44	Simulated echo tops (km) at 1650 UTC and maximum turbulence (minimum for Ri) at 1650 UTC diagnosed by b) Richardson number, c) EDR, and d) $\varepsilon^{1/3}$ (structure functions converted to EDR units) between the altitudes of 10 km and 12 km. Turbulence intensity is represented by light (green), moderate (yellow), and severe (red) thresholds. Black, blue, and magenta contours represent echo top heights greater than 10 km, 11 km and 12 km. Black (purple) stars represent the aircraft (shifted analysis) location at 1651 UTC.	113
45	Count of out-of-cloud (OC; red) and in-cloud (IC; blue) turbulent grid cells and probability density functions of OC and IC turbulent grid cells calculated from structure functions converted to EDR units from 1500-1800 UTC. Vertical dashed lines represent the turbulence intensity thresholds (light-green, yellow-moderate, and magenta-severe).	116
46	Distribution of structure functions converted to EDR units where only mature/dissipating (MDC) convective objects are within 30 km of a turbulent grid point (red) and where both mature/dissipating and developing convective objects are within 30 km of a turbulent grid point (blue). Vertical dashed lines represent the turbulence intensity thresholds (light-green, yellow-moderate, and red-severe).	119
47	Distribution of structure functions converted to EDR units closest to developing convection and mature and dissipating convection at 10 km, 11 km, and 12 km. Vertical dashed lines represent the turbulence intensity thresholds (light-green, yellow-moderate, and red-severe).	121

48	U-component of wind (a; m s^{-1}), b) v-component of wind (m s^{-1}), and c) vertical velocity (m s^{-1}) with locations of structure functions converted to EDR units greater or equal to $0.15 \text{ m}^{2/3} \text{ s}^{-1}$ (black contour) at 11 km in altitude.	123
49	Model domain of case studies. D01 and D02 have a horizontal grid spacing of 4.5 km and 1.5 km. Innermost nest (D03) has a horizontal grid spacing of 500 m. “X” represents the location of the turbulence encounter.	128
50	Echo top heights (a), minimum Richardson number (b), maximum eddy dissipation rate (c), and maximum second-order structure functions (d) for DCT (03 August 2009) at 1340 UTC between 8 km and 12 km. Echo tops greater than 8 km are shown in b-d as blue contours, and the black star represents the location of the aircraft at 0755 UTC.	134
51	Echo top heights (a), minimum Richardson number (b), maximum eddy dissipation rate (c), and maximum second-order structure functions (d) for DCM (10 July 1997) at 2210 UTC between 14 km and 16 km. Echo tops greater than 13 km are shown in b-d as blue contours, and the black star represents the location of the aircraft at 2141 UTC.	137
52	Echo top heights (a), minimum Richardson number (b), maximum eddy dissipation rate (c), and maximum second-order structure functions (d) for MCT (28 December 2014) at 0300 UTC between 8 km and 12 km. Echo tops greater than 8 (10 and 12) km are shown in b-d as blue (black and magenta) contours.	140
53	Echo top heights (a), minimum Richardson number (b), maximum eddy dissipation rate (c), and maximum second-order structure functions (d) for MCM (03 June 2018) at 2300 UTC between 8 km and 12 km. Echo tops greater than 8 (10 and 12) km are shown in b-d as blue (black and magenta) contours and the black (red) star represents the location of the aircraft at 0108 UTC on 04 June.	143
54	Echo top heights (a), minimum Richardson number (b), maximum eddy dissipation rate (c), and maximum second-order structure functions (d) for HCT (20 June 2017) at 1650 UTC between 8 km and 12 km. Echo tops greater than 8 (10 and 12) km are shown in b-d as blue (black and magenta) contours and the black (red) star represents the location of the aircraft at 1651 UTC.	146

55	Echo top heights (a), minimum Richardson number (b), maximum eddy dissipation rate (c), and maximum second-order structure functions (d) for HCM (29 June 2018) at 2250 UTC between 8 km and 12 km. Echo tops greater than 8 (10 and 12) km are shown in b-d as blue (black and magenta) contours and the black (red) star represents the location of the aircraft at 2257 UTC.	148
56	Distribution of in-cloud and out-of-cloud turbulence diagnosed using uncalibrated second-order structure functions and eddy dissipation rates between 8 km and 12 km when convection is present for the six cases. The green (yellow and magenta) vertical line represents the threshold for light (moderate and severe) turbulence.	152
57	Domain-wide distribution of echo top heights for the six simulations (10 minute output periods). Solid lines are the midlatitude cases and dashed lines are the tropical cases.	154
58	Percentage of convective objects identified as mature convection (MCO) and developing convection (DCO) for the six simulations. Bars with vertical lines represent developing convection.	155
59	Distribution of out-of-cloud turbulence diagnosed by second-order structure functions between 8 km and 12 km nearest to mature convection (MCO) and developing convection (DCO) for the six simulations. The green (yellow and magenta) vertical line represents the threshold for light (moderate and severe) turbulence.	156
60	Distribution of mean out-of-cloud static stability, mean vertical wind shear, and mean vertical velocity between 8 km and 12 km nearest to mature convection (MCO) and developing convection (DCO) for the six simulations (uncalibrated second-order structure functions).	158
61	Distribution of mean out-of-cloud static stability, mean vertical wind shear, and mean vertical velocity between 8 km and 12 km nearest to mature convection (MCO) and developing convection (DCO) for the six simulations subset by turbulence intensity (uncalibrated second-order structure functions).	162

62	Correlation of mean out-of-cloud static stability and turbulence intensity (uncalibrated second-order structure functions) between 8 km and 12 km nearest to mature convection (MCO) and developing convection (DCO) for the six simulations. The correlation coefficients for the data subset by convective object type (r_{mature} and r_{dev}).	165
63	Correlation of mean out-of-cloud vertical wind shear and turbulence intensity (uncalibrated second-order structure functions) between 8 km and 12 km nearest to mature convection (MCO) and developing convection (DCO) for the six simulations. The correlation coefficients for the data subset by convective object type (r_{mature} and r_{dev}).	166
64	Correlation of mean out-of-cloud vertical velocities and turbulence intensity (uncalibrated second-order structure functions) between 8 km and 12 km nearest to mature convection (MCO) and developing convection (DCO) for the six simulations. The correlation coefficients for the data subset by convective object type (r_{mature} and r_{dev}).	167
65	Structure functions (longitudinal direction- solid lines, transverse direction-dashed lines) as a function of separation distance, and the maximum of the Kolmogorov 2/3 inertial range (black line) for all heights from 1510-1800 UTC.	186

LIST OF TABLES

Table	Page	
1	Turbulence level descriptions, aircraft vertical acceleration magnitude (g ; $m\ s^{-2}$), and the cubed root of eddy dissipation rates $\varepsilon^{1/3}$ ($m^{2/3}\ s^{-1}$).	15
2	Model grid spacing and number of vertical levels. D02 represents the innermost nest of S1 (i.e., D02 = 1 parent and 1 nest), and D03 represents the innermost nest of S2–S4 (i.e., D03 = 1 parent and 2 nests).	27
3	Model parameterizations used in simulations. The cumulus parameterization is not applicable to model setup 4.	28
4	Turbulence intensity as determined from the cubed root of eddy dissipation rate (ε ; Lane et al. 2012; Sharman and Pearson 2017).	30
5	Number of grid cells with echo top heights ≥ 8 km.	53
6	Mean out-of-cloud static stability (s^{-2}) between 8 km and 12 km within 20 miles of convection. Bold represents the direction the highest percentage of turbulence is located.	80
7	Mean out-of-cloud vertical wind shear (s^{-2}) between 8 km and 12 km within 20 miles of convection. Bold represents the direction the highest percentage of turbulence is located.	83
8	Mean out-of-cloud Richardson number between 8 km and 12 km within 20 miles of convection. Bold represents the direction the highest percentage of turbulence is located.	86
9	Mean out-of-cloud vertical velocity ($m\ s^{-1}$) between 8 km and 12 km within 20 miles of convection. Bold represents the direction the highest percentage of turbulence is located.	89

10	Correlation coefficients for out-of-cloud static stability, vertical wind shear, vertical velocity, and eddy dissipation rate between 8 km and 12 within 20 miles of convection on 12 July. Bold represents the direction the highest percentage of turbulence is located.	92
11	Threshold descriptions of the Convective Diagnosis Oceanic Algorithm. . .	104
12	Model parameterizations used in 20 June 2017 simulation.	107
13	Initialization time, analysis period, and time period of increased temporal resolution.	129
14	Model parameterizations used in simulations.	130
15	Location and time of aviation encounter with turbulence.	131
16	Mean, median, mode, interquartile range (IQR), and standard deviation (STD) for out-of-cloud static stabilities between 8 and 12 km near mature and developing (<i>italicized</i>) convection.	157
17	Mean, median, mode, interquartile range (IQR), and standard deviation (STD) for out-of-cloud vertical wind shear between 8 and 12 km near mature and developing (<i>italicized</i>) convection.	159
18	Mean, median, mode, interquartile range (IQR), and standard deviation (STD) for out-of-cloud vertical velocities between 8 and 12 km near mature and developing (<i>italicized</i>) convection.	160
19	Correlation coefficients for out-of-cloud static stability, vertical wind shear, vertical velocity, and eddy dissipation rate between 8 km and 12 near mature and developing (<i>italicized</i>) convection.	171
20	Turbulence intensity as determined for the Brown 1 index (Brown 1973).	180
21	Turbulence intensity thresholds as determined from the cubed root of eddy dissipation rate (ε ; Lane et al. 2012, Sharman and Pearson 2017).	184
22	Turbulence intensity thresholds for CP (Sharman et al. 2006).	187
23	Turbulence intensity thresholds for DTF3 (Sharman et al. 2006).	187

ACKNOWLEDGMENTS

No numerical amount of thank yous can express my appreciation towards my advisor, Dr. Gretchen Mullendore. I would not be the scientist and person I am today without her advice, leadership, and friendship. I was extremely fortunate to have the opportunity to be a part of her research group, and I will miss working with her on a daily basis.

A big thank you to my entire dissertation committee, Prof. Michael Poellot, Dr. Mark Askelson, Dr. Joan Alexander, and Dr. Gregory Vandenberg for their feedback, direction, and assistance on this research. I truly appreciate their commitment on reading this (very long) document!

I would also like to thank Wiebke Deierling, Robert Sharman, Domingo Muñoz-Esparza, Cathy Kessinger, and Stanley Trier from NCAR (aka my NCAR family) for their constructive feedback on this work and collaboration. Their support of my research and personal growth over the past four years has helped me establish myself in aviation meteorology and reach a new audience. I would also like to acknowledge the EOL/RAL coffee break group for making each day at NCAR interesting, being incredibly inclusive, and getting me hooked on coffee.

I would also like to thank Tom Cortese at NCSA for his assistance with Blue Waters, as well as Scott Lathrop, and the entire Blue Waters fellowship team for their assistance and support.

Thank you to my past research group members for being catalysts towards efficient methodologies on various projects.

An additional thank you to the John D. Odegard School of Aerospace Sciences and the Advanced Study Program for their support of this research, and helping me attend numerous conferences to promote my research.

Thank you to the Earth Networks for providing the lightning data as an observational source.

Lastly, thank you to my family and friends for their endless encouragement and support over the past four years. Without you, I would not be confident to begin a new career in a new location.

This research was supported by the Northrop Grumman Corporation, the North Dakota Experimental Program to Stimulate Competitive Research (EPSCoR) through the National Science Foundation Grant OIA-1355466, and the Blue Waters sustained-petascale computing project, which is supported by the National Science Foundation (awards OCI-0725070 and ACI-1238993) and the state of Illinois. Blue Waters is a joint effort of the University of Illinois at Urbana-Champaign and its National Center for Supercomputing Applications. Portions of this work used the XSEDE Comet at the SDSC through allocation ATM110005; XSEDE is supported by National Science Foundation Grant ACI-1548562.

I would like to dedicate this dissertation to my Little Duck. We have been through so much the past four years and your unwavering friendship helped me through difficult times. Without you by my side I can confidently say I would not be where I am today. You have always helped me see the sun when everything around me was cloudy and uncertain. As Hemmingway said, “The clouds were building up now for the trade wind and he looked ahead and saw a flight of wild ducks etching themselves against the sky over the water, then blurring, then etching again and he knew no man was ever alone on the sea”. I am looking forward to the next stage of our lives and may the odds be ever in our favor.

ABSTRACT

Out-of-cloud convectively induced turbulence (CIT) poses both a serious threat to aviation operations and a challenge to forecasting applications. This challenge is particularly large in the tropics, as CIT prediction and avoidance are limited due to sparse observations and lack of tropical turbulence research. This study uses high resolution numerical simulations to investigate out-of-cloud CIT properties including intensity, areal coverage, and location using popular turbulence diagnostics in both the tropics and midlatitudes. Convective types are varied in both regions to determine the influence of convective strength and stage (developing versus mature) on CIT characteristics. The Ellrod index, Richardson number, subgrid-scale eddy dissipation rate (EDR), and second-order structure functions are evaluated across various model resolutions and compared with observations of turbulence. Static stability and vertical wind shear are examined to characterize the environment and turbulence potential around simulated convection in the tropics and midlatitudes. This study found that model resolutions similar to operational forecasting systems under-predicted the probability of turbulence, while high resolutions had a probability of turbulence at aviation cruising altitudes that better agreed with observations. The biases in the probability of turbulence for various model resolutions were affected by storm type and synoptic features, and had more agreement for cases with strong dynamical forcing. Model resolution also influenced the locations that CIT was predicted. An investigation of variations in static stability and vertical wind shear in different locations around convective cores showed that these parameters subtly varied with model resolution and often did not correlate with the preferred direction of

turbulence as would be expected from theory. A further study into convective stage found that developing convection poses the greatest threat to aviation as it is associated with the greatest turbulence intensity and probability of turbulence in both the tropics and midlatitudes. The environment near developing convection was altered more than near mature convection and likely increased turbulence production through shear-generation mechanisms and gravity wave propagation. This study motivates an increased effort to understand turbulence probability for convection globally in order to improve aviation thunderstorm avoidance guidelines.

CHAPTER 1

INTRODUCTION

Global air travel continues to be a growing endeavor and is projected to increase over 5% for the next two years (Statista 2018). While almost all regions are anticipated to add flights, Asia Pacific and Latin America alone are forecasted to increase by almost 6% (Statista 2018). Every day convection influences aviation operations by causing delays during take-off or landing, flight cancellations, and rerouting flight-paths. According to the Federal Aviation Administration (FAA), weather accounts for 68% of delays in U.S. airspace with the greatest amount of delays occurring May through August (FAA 2017; Weather Delays), the main cause being convection. Ball et al. (2010) found that aviation delays in the U.S. cost the industry over \$32 billion and over 25% of flights during the months of June through August experience a 15 minute delay. As the number of daily flights continue to increase, the amount of delays due to convection will also increase.

Convection not only poses the threat of causing delays in air traffic patterns, but it can also cause structural damage to the aircraft, injuries to passengers and crew, and instrumentation failure. Lightning, hail, and turbulence are the main hazards to aviation caused by convection. Sharman et al. (2006) found that 65% of all weather related aircraft incidents were caused by turbulence. According to the FAA, between 2002 and 2016 over 500 passengers and crew were injured due to turbulence in the U.S. (FAA 2017). These encounters with turbulence cost the airline

industries millions in insurance premiums, worker compensation, injury settlements, and mechanical repairs (Golding 2000).

Turbulence generated by convection is extremely difficult to predict for numerous reasons. First, turbulence generating processes are still poorly resolved or missed entirely in operational models. To mediate the resolution dependency, many turbulence prediction products rely on empirical indices that have been designed to diagnose large-scale fields that relate to turbulent sources from numerical simulations. Secondly, convective initiation and strength must be accurately simulated in order to correctly represent turbulent features, which are not always well predicted. Lastly, modeling studies are difficult to constrain with limited in situ observations of turbulence itself; therefore, the results are seldom implemented into turbulence avoidance policies. Unfortunately, as air traffic becomes more congested, the number of turbulence encounters will continue to rise unless turbulence prediction for all convective scenarios becomes more reliable.

Developing convection is of particular concern to aviation operations because of limited environmental observations and the small temporal scale in which it takes place. Pilots can be helpless during a developing convective scenario if the on-board radar is not oriented at an angle that can detect convection below. This situation can lead to injuries aboard the aircraft if turbulence is encountered while passengers are not securely fastened in their seats. Few research studies have solely focused on turbulence caused by developing convection, or the accuracy of commonly used turbulence indices during this particular stage. Airlines will continue to encounter turbulence caused by developing convection if the sensitivities of turbulence indices are not investigated. By understanding the magnitude and extent of turbulence during the developing stage of convection, thunderstorm avoidance guidelines may be altered and decrease passenger injuries.

The proposed research addresses the following scientific objectives: 1) Determines how model resolution influences the distribution of turbulence intensity calculated from popular turbulence metrics, 2) determines if a directional bias in turbulence location is found when model resolution is altered, 3) determines if common turbulence indices developed for midlatitude turbulence prediction can be accurately applied to tropical convective regimes for turbulence prediction, and 4) determines biases in turbulence prediction for various convective regimes in tropical oceanic and continental midlatitude regions. The Weather Research and Forecast (WRF) model was used to simulate convection in both midlatitude continental regions and tropical oceanic to accomplish these research objectives.

CHAPTER 2

BACKGROUND

Turbulence is defined by the American Meteorological Society Glossary as random and continuously changing air motions that are superposed on the mean motion of the air (AMS 2015). In comparison, the Federal Aviation Administration (FAA) simply defines turbulence as the bumpiness in flight that has effects on the aircraft and passengers (FAA 1977). This broad definition includes mechanically induced turbulence, thermally induced turbulence, and the formation and breakdown of gravity waves (Vinnichenko et al. 1980). Turbulence accounts for 65% of all weather related aviation accidents and costs the industry between \$150-500 million a year in structural repairs, insurance premiums, and injury settlements (Williams 2016; Kauffmann and Sousa-Poza 2001). Turbulence can be classified as clear air, mountain wave turbulence, or convectively induced, and can occur in cloud or out of cloud. Convectively induced turbulence in particular is of concern to aviation operations as forecasting systems are dependent on the accurate prediction of convection and the resolution of processes that induce turbulence and therefore will be the focus of this study. The following sections will discuss the theoretical understanding of convectively induced turbulence, the current understanding of convectively induced turbulence from modeling studies, aviation procedures utilized to decrease turbulence encounters, prediction systems and diagnostics in operation for turbulence prediction, and differences in convective properties in the midlatitudes and tropics that influence turbulence.

2.1 Convectively induced turbulence generation

Convectively induced turbulence (CIT) is a dynamical phenomenon that requires advanced prediction in order to reduce weather-related turbulence accidents. CIT often occurs in the immediate area surrounding convection due to moist instabilities and mixing (Lane et al. 2003), particularly near updrafts, downdrafts, and anvil cloud features. Strong vertical variations of velocities within the convective updraft cause in-cloud CIT of stronger intensity. In-cloud regions of turbulence are easily avoided by the detection of cloud boundaries both visually and with radar (Kim and Chun 2012), but the intensity of in-cloud CIT is not always correlated to the intensity of radar echoes. CIT is not limited to the immediate cloud area and can occur more than 100 km away from and 1-3 km above convective areas (Zovko-Rajak and Lane 2014; Lane and Sharman 2014; Lane et al. 2012; Lane et al. 2003; Pantley 1989; and USAF 1982). The three mechanisms known to generate out-of-cloud CIT are (1) enhancement of the background wind shear by convection penetrating into the upper troposphere, (2) cloud-induced deformation at the cloud boundary caused by buoyancy gradients, and (3) convectively generated gravity waves that propagate and break above convection (Lane et al. 2003).

Gravity waves generated by convection are especially hazardous to aviation and are responsible for much of the out-of-cloud CIT (Sharman and Trier 2018). Convectively induced gravity waves generally have horizontal wavelengths between 5 and 200 km, occur on temporal scales of 10 to 100 minutes, and are generated by mechanical and diabatic forcings, which in realistic convective clouds are coupled through nonlinear momentum and heat fluxes (Chun 2008; Lane and Sharman 2008; Alexander et al. 2006; Lane et al. 2003; Song et al. 2003; Beres et al. 2002; Lane et al. 2001). The nonlinear forcings refer to the mechanical oscillator effect (Clark

et al. 1986) and the obstacle effect (Pfister et al. 1993). The mechanical oscillator effect leads to the formation of vertically propagating gravity waves when updrafts and downdrafts intersect a stable layer, in turn causing vertical displacements of the isentropes at the base of the stable layer. The obstacle effect, also known as the moving mountain effect, causes gravity waves when a pressure field produced by the upward (and downward) convective region obstructs the environmental horizontal flow. The diabatic forcing (thermal forcing) which occurs when latent heat is released within the cloud during condensation (Lin and Smith 1986). While the formation of gravity waves during convective activity is common, turbulence may or may not be generated as the production of turbulence is influenced by the breakdown of gravity waves (Pantley 1989; Reiter and Lester 1968). The wavelength (λ) of vertically oscillating gravity waves can be mathematically expressed using

$$\lambda = \frac{2\pi\bar{u}}{N}, \quad (2.1)$$

where \bar{u} is the mean horizontal wind speed (m s^{-1}) and N is the Brunt frequency (s^{-1}), mathematically represented by

$$N = \left(\frac{g}{\theta}\right) \left(\frac{\partial\theta}{\partial z}\right)^{1/2}, \quad (2.2)$$

where g is the acceleration due to gravity (m s^{-2}) and θ is potential temperature (K). This equation assumes that the phase speed of the waves is zero, which is not the case for convectively induced gravity waves.

The breakdown of gravity waves in the environment is defined by Pantley (1989) as a transition from a coherent wave motion to turbulence. Prior to breakdown, as gravity waves vertically propagate and grow in a nonlinear manner, regions of strong overturning of isentropes surfaces are produced (Walterscheid and Schurbert

1990). The overturning of isentropes occurs when the amplitude of the wave grows large enough where the addition of the wave and the mean field of vertical temperature gradient becomes superadiabatic (Walterscheid and Schurbert 1990). Furthermore, Orlanski and Bryan (1969) found that the overturning of isentropes occurs in regions where upward propagating gravity waves are present when

$$u' + \bar{u} > c, \quad (2.3)$$

where c is the horizontal phase speed of the wave, u' is the wave horizontal velocity, and \bar{u} is the mean field horizontal velocity. The horizontal intrinsic phase speed of gravity waves, c_{px} can be represented by,

$$c_{px} = \frac{\pm N}{\sqrt{k^2 + m^2}} \quad (2.4)$$

where k and m are the wave number in the x and z direction (Lin 2007). This equation demonstrates that as propagating gravity waves enter a more stable region the phase speed of these waves will increase.

Many studies have examined the influence that atmospheric stability, environmental wind, and convective stage have on the propagation of gravity waves. Lane and Sharman (2008) used numerical simulations of convection to investigate the relationships between background flow conditions and gravity wave breaking above convection. The results from Lane and Sharman (2008) found that the instability in terms of areal coverage was maximized by optimal values of wind shear. In addition, it was found that the altitude of critical levels which induce breaking gravity waves are higher in low sheared environments, thereby influencing turbulence location. Lane and Sharman (2008) also found that areas where gravity waves break are in the down-shear regions above cloud as waves encompassing a spectrum of wavelengths reach

critical levels, which is consistent with other studies. Kuester et al. (2008) examined gravity waves generated around a hurricane, which lacks a strong background wind and has little shear. In this environment the gravity wave characteristics were influenced mainly by diabatic heating within the hurricane itself. Gravity waves were found to peak at vertical wavelengths 2 to 4 times the depth of the heating and propagated vertically across the tropopause at half of their original vertical wavelength due to refraction. Kuester et al. (2018) examined azimuthal shear and hypothesized the influence of the obstacle effect. Wimmers et al. (2018) used satellite information to examine gravity waves. Their study found for two cases of severe CIT, gravity waves did not propagate in the direction of the background flow but instead propagated orthogonally to the background flow, due to the highly sheared environment of the convective outflow. Beres et al. (2002) found that the phase speed spectrum of convectively induced gravity waves can be modified by the vertical structure of the horizontal wind and that the tropospheric winds can cause gravity waves above convection to refract. The results from Beres et al. (2002) demonstrated the asymmetric nature of gravity wave propagation due to tropospheric winds agreed with previous studies including (Lane et al. 2001; Piani et al. 2000; Alexander and Holton 1997; Alexander et al. 1995; Fovell et al. 1992).

2.2 Simulations of convectively induced turbulence

With the increase in computation resources available, the dynamics of CIT are being understood at remarkable rates. Model simulations are also being used to explain aviation turbulence encounters that were responsible for injuries or structural damage. Recently, Trier and Sharman (2016) investigated the mechanisms that caused a multiple day turbulence event where convection evolved throughout the period. The results of their study highlighted the complex interactions of shallow convec-

tion, the jet stream, gravity waves, and shear instabilities. In addition, their study found that to resolve much of the turbulent motions responsible for the numerous turbulence reports, model grid spacing needed to be less than 1 km, as 3 km could not resolve the turbulence mechanisms. This finding is extremely important because most operational forecasting models currently have model grid spacing equal to or greater than 3 km in the horizontal. Prior to this particular study, Trier et al. (2012) examined a cold-season turbulence outbreak event using high resolution simulations ($\Delta x = 667$ m). As was the case with Trier and Sharman (2016), Trier et al. (2012) found two main mechanisms that caused turbulence. The first mechanism was Kelvin-Helmholtz instabilities leading to convective instabilities above a convectively-enhanced jet stream. The second mechanism was vertically propagating gravity waves that were generated when shallow convection reached a layer of strong static stability. While both of these studies focused on the interactions of jet streams and convection during the cold-season, vertically propagating gravity waves have also been shown to cause turbulence during warm-season events (Lane and Sharman 2008; Lane et al. 2003).

Lane et al. (2003) investigated a turbulence encounter above a developing convective cell on 10 July, 1997 using high resolution idealized and full-physics simulations. Turbulence was found 1 km above the cloud top due to the convective updraft overshoot into the stratosphere and various distances away from the convective cell due to the propagation and break down of gravity waves. This study demonstrated the vast horizontal and vertical distances CIT can propagate away from developing convection and how aviation operations are at risk of encountering CIT. Kim and Chun (2012) examined a turbulence encounter with an extremely fine model grid spacing ($\Delta x = 120$ m). This study found as the dominant background wind advected convection near the encounter location, turbulence generated along the convective

cloud boundary was also advected, from the mature to dissipation stages. At the same time, vertically propagating gravity waves reached the critical level and began breaking. The numerical simulations showed that out-of-cloud CIT was located 2 km above the dissipating convection. The results of this study illustrate the potential for significant turbulence encounters during numerous convective stages, and not just the mature stage.

Zovko-Rajak and Lane (2014) utilized an idealized numerical framework with high resolution ($\Delta x = 500$ m) to investigate turbulence near supercells. The focus was out-of-cloud turbulence, several kilometers away from active convection. This study found turbulence more than 100 km downstream of active convection, generally associated with the upper-level outflow jet, near the tropopause. In the areas above and below the outflow jet, the Richardson number was less than 0.25 and overturning gravity waves were common.

Simulations of aviation encounters of CIT in the tropics are far less common than simulations of midlatitude turbulence incidents. Generally wave analyses of tropical simulations focus on large-scale waves that influence the quasi-biennial oscillation, El-Nino Southern Oscillation, and the Madden-Julian Oscillation, and less on turbulence at scales which influence aviation (Yang and Hoskins 2013; Haertel et al. 2008; Tanaka and Yoshizawa 1987). One of the few tropical studies of tropical CIT is Ahmad and Proctor (2011). They used large eddy simulations to model severe CIT experienced by commercial flights in tropical regions. Their study examined Continental Airlines Flight 128 (Boeing 767), which encountered turbulence north of Bavaro, Dominican Republic while flying at an altitude of 11 km over isolated cumulus congestus and cumulonimbus on 3 August, 2009. The simulation showed that light to moderate turbulence occurred in the top of the storm in regions of low radar

reflectivity values. In relationship to aviation, this finding is important because pilots generally rely upon on-board radar systems to avoid convective hazards.

Barber (2015) investigated the areal coverage and intensity distribution of CIT using the Weather Research and Forecasting (WRF) model for a tropical oceanic case on 5-6 August 2005. The Ellrod index was used as a diagnostic of turbulence (see the Appendix) and found that the extent of turbulence identified was far beyond what is observed in midlatitude regions and in the vicinity of tropical cyclones (Cecil et al. 2014; Lane et al. 2012). Although strong turbulence has been observed within the tropical transition layer and near the tropical tropopause using active sensing instrumentation (Alappattu and Kunhikrishnan 2010; Fujiwara et al. 2003; Yamamoto et al. 2003; Satheesan and Krishna Murthy 2002), the extent of turbulence in Barber (2015) highlighted the resolution sensitivity of the Ellrod index for the estimation of convectively induced turbulence. The comparison of turbulence estimated using the original model resolution simulation and a coarser resolution simulation indicated that the empirical values of the Ellrod index greatly depend upon model resolution. While individual model simulations are valuable as thorough details pertaining to turbulence are discovered, in order to provide legitimate guidance to aviation operations for a spectrum of convective situations in any region, limited case studies will not suffice. This is especially true for turbulent situations over tropical oceanic regions where forecasting systems are limited to nowcasting tools and previous results are concentrated over the midlatitudes.

2.3 Convection and aviation

According to the U.S. Department of Transportation Federal Aviation Administration Advisory Circular from 2017, all thunderstorms have potential conditions that are hazardous to aviation. These hazards include tornadoes, turbulence, icing, hail,

low ceiling and visibility, altimeter effects due to rapid pressure changes, lightning, and engine water ingestion. Turbulence is the number one cause of injuries to flight crew and passengers (Mecikalski et al. 2007). The majority of turbulence injuries occur when flight attendants are up and about the cabin serving passengers. Turbulence is a hazard to aircraft because additional stresses are placed on the aircraft while pilots attempt to hold a constant altitude (FAA 2017). Kaplan et al. (1999) found that 82% of reported turbulence incidents between 1990 and 1996 occurred near or within convective activity. Pantley (1989) summarized five main types of CIT hazardous to aviation: 1) updrafts and downdrafts within and near deep cumulus convection, 2) rapidly growing thunderstorms, 3) Kelvin-Helmholtz instability induced by outflows near the tropopause, 4) turbulent vortices that are formed due to breaking of convectively initiated waves above and downwind of thunderstorms, and 5) turbulent wakes caused by barrier type effects around and within the lee of thunderstorms.

A three year climatology of turbulence in the continental United States created by Wolff and Sharman (2008) indicated that 39% of turbulence encounters occurred above convective clouds, 53% of which were moderate or greater intensity. In addition, 9% of encounters occurred in convective cloud, 80% of which were moderate or greater. Clear-air turbulence (no clouds apparent) encounters occurred 44% of the time, 48% of which had moderate or greater intensity. An important finding from this study was that as cloud height increases to approximately 9-12 km, moderate or greater turbulence intensity encounters increase to 85% of encounters.

An in situ measurement used in aviation to determine the intensity of turbulence is the eddy dissipation rate (Emanuel et al. 2013). Eddy dissipation rate (EDR) is a universal measurement of the rate at which energy dissipates in the atmosphere. The value of EDR is in units of turbulent kinetic energy (TKE). According to Emanuel et al. (2013), there are three operational algorithms used to calculate EDR.

The first is an indirect method that uses the aircraft accelerometer, while the second uses vertical wind data directly measured from the aircraft, and the third estimates the longitudinal wind from the true airspeed. The following is a simplified example of an algorithm used to calculate EDR in flight using the aircraft accelerometer.

$$\varepsilon^{2/3} = \frac{\sigma_z^2}{I} \quad (2.5)$$

where σ_z is the variance of the vertical acceleration spectrum, and I is the integral of the aircraft response bandpass filtered function H (Cornman et al. 2004). A response bandpass filter is used to remove aircraft maneuver-induced accelerations. Eddy dissipation rates in thunderstorms can also be estimated using ground-based Doppler radar (Meischner et al. 2001), although this method has serious limitations such as poor resolution at large distances (Williams 2004).

With so many potential hazards associated with convection, there have been several aviation avoidance policies put in place to limit the number of convection related accidents (US DOT FAA 2013, 2017). The current policy states that pilots should avoid any severe thunderstorm (i.e., thunderstorm with an intense radar echo) by at least 20 miles (32.2 km). Next, pilots should circumnavigate an entire area if the respective region has six tenths thunderstorm coverage. Furthermore, the use of extreme caution when flying near any thunderstorm with echo tops greater than 35,000 feet is advised. Finally, pilots should also avoid flying beneath the anvil region and through thunderstorms even if the path through to the other side is visible. It is important to note that prior to 2013, thunderstorms identified as severe required a vertical clearance of 1,000 ft for every 10 kt wind speed at cloud top (FAA 2012).

The FAA categorizes turbulence into four verbal descriptors (Table 1) that are easy to communicate between pilots and traffic control, and corresponds to in

situ numerical eddy dissipation rates ε ($\text{m}^{2/3} \text{s}^{-1}$) and vertical acceleration (m s^{-2}) (FAA 2014; Lane et al. 2012; Pololovich et al. 2011; Bowles and Buck 2009). Light turbulence is described by the FAA as turbulence that momentarily causes slight, erratic changes in altitude and or pitch, roll, and yaw, and passengers may feel a slight strain against their seat belts. Moderate turbulence is described as being similar to Light turbulence but with a greater intensity. During Moderate turbulence, changes in altitude and attitude occur but the aircraft remains in positive control at all times, and variations in indicated airspeed are experienced. Furthermore, passengers feel a definite strain against their seat belts and walking around the cabin is difficult. Turbulence that causes large, abrupt changes in altitude, attitude (orientation of the aircraft to Earth's horizon), and indicated airspeed is described as Severe. In addition, the aircraft may be temporally out of control. Severe turbulence also causes passengers to be violently forced against their seats. Lastly, Extreme turbulence is described as a situation when the aircraft is violently tossed about, is practically impossible to control, and can suffer structural damage. This magnitude of turbulence is described as truly frightening for those aboard.

Table 1: Turbulence level descriptions, aircraft vertical acceleration magnitude (g; m s⁻²), and the cubed root of eddy dissipation rates $\varepsilon^{1/3}$ (m^{2/3} s⁻¹).

Turbulence	Aircraft reaction	Aircraft vertical acceleration magnitude (g; m ⁻²)	$\varepsilon^{1/3}$ (m ^{2/3} s ⁻¹)
Light	Turbulence that momentarily causes slight, erratic changes in altitude and/or attitude (pitch, roll, and yaw).	0.2-0.5	0.1-0.3
Moderate	Turbulence that is similar to Light turbulence but of greater intensity. Changes in altitude and/or attitude occur but the aircraft remains in positive control at all times. It usually causes variation in indicated speed.	0.5-1.0	0.3-0.5
Severe	Turbulence that causes large, abrupt changes in altitude and/or attitude. It usually causes large variations in indicated airspeed. Aircraft may be momentarily out of control.	1.0-2.0	0.5-0.7
Extreme	Turbulence in which the aircraft is violently tossed about and is practically impossible to control. It may cause structural damage.	>2.0	>0.7

2.4 Turbulence indices and forecasting applications

Other derived meteorological parameters have been scientifically accepted as appropriate for turbulence prediction when applied to aviation operations. These parameters include and are not limited to: vertical and horizontal wind shear, stretching and shearing deformation, absolute vorticity, convergence, divergence, horizontal temperature gradient, frontogenesis, resolved and diagnostic turbulent kinetic energy, structure functions, and eddy dissipation rate (Ahmad and Proctor 2012; Ellrod and Knox 2010; Frehlich and Sharman 2004a,b; Marroquin 1998; Ellrod and Knapp 1992; Dutton 1980; Buldovskii et al. 1976; Brown 1973; Colson and Panofsky 1965; equations provided in the Appendix). The use of indices (calculated from derived parameters) for turbulence prediction is fairly popular for aviation, especially because turbulence that impacts aviation occurs on a very small scale (10 m to 1000 m; Lester 1994) that current operational models cannot resolve. Many of these indices are included within the Graphical Turbulence Guidance product (discussed below; Sharman et al. 2006) and other turbulence prediction systems for aviation operations.

As the model grid spacing in the operational setting continues to increase, several of these indices are no longer realistically representing turbulent regions and turbulence intensity due to a resolution sensitivity. For example, when the Ellrod index (Ellrod and Knapp 1992; equation provided in the Appendix) was designed, it utilized derived wind shear and deformation fields from a model resolution greater than 50 km and was then calibrated to pilot reports. When the Ellrod index is calculated on grid-scales less than 10 km, severe turbulence is abundant in the majority of the domain (Barber et al. 2018). The Brown index (Brown 1973; equation provided in the Appendix) which calculates absolute vorticity, stretching deformation, and shearing deformation is also susceptible to a resolution sensitivity, where each of

the individual terms alone produce severe turbulence. Another limitation with the majority of the current spectrum of turbulence indices used is the removal of suspected CIT observations in the original calibration. By ignoring CIT incidents in the calibration procedure, these indices cannot be accurately relied upon to diagnose CIT. Lastly, the majority of these indices were calibrated against pilot reports recorded in the United States which is not representative of global atmospheric conditions. The following section will discuss turbulence prediction systems currently being used for aviation operations.

The Graphical Turbulence Guidance product (also known as GTG-2; Sharman and Pearson 2017; Pearson and Sharman 2017; Sharman et al. 2006) is the culmination of over 40 turbulence indices that are weighted and rescaled using a lognormal distribution to represent eddy dissipation to the one-third power (complete index list provided in Sharman and Pearson 2017). The cause of turbulence is considered in the overall turbulence intensity estimation, being either clear-air turbulence (shear induced without convection), mountain wave, or CIT. The numerical value of each of the diagnostic is calibrated to eddy dissipation rate (EDR) assuming a log-normal distribution of EDR observations in the upper troposphere. Observations of EDR are gathered from pilot reports and in situ measurements from aircraft. The ten best diagnostics are then incorporated into a weighted ensemble and disseminated to various platforms every 15 minutes. GTG-2 is undergoing an update as the base model that the diagnostics are computed from has changed from the Rapid Refresh model (RAP; grid spacing of 12 km) to the High Resolution Rapid Refresh (HRRR; grid spacing of 3 km). With this alteration in base models, all indices are being recalibrated. In addition, GTG-2 will be distinguishing between in-cloud and out-of-cloud turbulence.

The Convective Diagnosis Oceanic (CDO) Algorithm was developed to improve safety and efficiency along trans-oceanic flights (Herzogh 2002). The algorithm

currently has four inputs (observational and numerical) that are used to detect convective hazards and better resolve convective structure (Kessinger 2017; Kessinger et al. 2008). These inputs include cloud top height (CTH) from infrared brightness temperature, the Global Convective Diagnosis- the difference between the brightness temperature of the infrared channel and the brightness temperature of the water vapor channel, GOES-R Overshooting Tops algorithm, and combined lightning interest. The CDO algorithm estimates convective intensity on a scale of 1 to 6 every 15 minutes and is calculated on global scale using six geostationary satellites. While CDO does not explicitly warn pilots of turbulence intensity or location, it can still be used as a forecasting aid for CIT.

The NCAR (National Center for Atmospheric Research) Turbulence Detection Algorithm (NTDA) produces 5 minute three-dimensional in situ observations of in-cloud turbulence for the contiguous U. S. at 15 height levels (Williams et al. 2011). The use of NTDA for turbulence verification has increased recently (Pearson and Sharman 2017) and has been shown to perform well for in-cloud turbulence prediction. Correlations between lightning and in-cloud turbulence estimated by NTDA are also being examined for use in future adaptations of GTG-2 (Deireling 2018). However, the skill of NTDA for out-of-cloud turbulence intensity has not been well-tested. In addition, out-of-cloud turbulence intensity can only be determined using NTDA in-cloud turbulence observations.

Pilot reports (PIREPS) are in situ observations of turbulence that are recorded and disseminated. These reports include the estimated turbulence intensity, time and location of the turbulence encounter, and whether the aircraft was in-cloud or out-of-cloud at the time. While PIREPS are extremely helpful for nowcasting turbulence and aiding in turbulence avoidance there are numerous limitations associated with the use of PIREPS in scientific research. PIREPS give a limited validity of turbulence

location and intensity for scientific research and are dependent on pilot perception of turbulence, especially when in situ measurements of EDR are unavailable. In addition, turbulence at various scales impacts aircraft of various sizes differently. For example, moderate turbulence encountered by a small general public aircraft may not be moderate turbulence to a larger commercial aircraft. Another critical limitation of PIREPS is that most aviation routes are going to avoid convection based on company determined lateral and vertical distances. This avoidance drastically decreases the amount of CIT observations and restricts direct comparisons to model output. Lastly, PIREPS without in situ EDR measurements are subject to human error and can be reported incorrectly (Sharman et al. 2014; Wolff and Sharman 2008).

2.5 Comparison of convective properties in the midlatitudes and tropics

It is commonly understood that there are vast dynamical and physical differences between the various types of convection that occur in the continental midlatitudes and maritime tropics (Vant-Hull et al. 2016; Liu and Zipser 2005; Yuter et al. 2005; Chin et al. 1995). The key differences include: the maximum height of convection and the probability of convection overshooting into the stratosphere, maximum vertical velocities of updrafts, diurnal variation of convection, and hazard potential. The height of convection in the midlatitudes and tropics is influenced substantially by the height of the tropopause which is higher in the tropics (Hoinka 1999). Observational studies using ground-based radar systems found that over 1% of convection occurring in maritime tropical regions exceeded 14 km in altitude (Barber 2015; Cetrone and Houze 2006; Liu and Zipser 2005), while satellite-based observations had a slightly lower frequency (Barber 2015; Houze et al. 2015; Nesbitt et al. 2006; Alcala and Dessler 2002). In the midlatitudes, the vertical extent of the majority of deep convection remains below 12 km. Severe storms such as supercells can have vertical

extents greater than 12 km but supercells are the most uncommon type of convection (Markowski and Richardson 2010). Vant-Hull et al. (2016) found that the majority of tropical convection over land and ocean had cloud top temperatures (CTTs) near 210 K while convection in the midlatitudes had CTTs near 225 K, indicative of lower convective heights in the midlatitudes.

Overshooting convection into the stratosphere is a phenomenon that is commonly used as a convective intensity proxy (Romps and Kuang 2009; Liu and Zipser 2005; Zipser 2003; Alcala and Dessler 2002; Heymsfield et al. 1991; Adler and Mack 1986). Over tropical oceanic regions, overshoots occur less than one percent of the time (Hong et al. 2008; Liu and Zipser 2005; Alcala and Dessler 2002). Liu and Liu (2016) found that convection in the midlatitudes overshoot into the stratosphere as often as tropical convection but the height of the overshoot is more frequently limited to 13 km. Another distinction between overshooting convection in the midlatitudes and tropics during the summer months is the greater overshooting area of midlatitude convection.

Mean vertical velocities of maritime tropical convection is known to be less than continental midlatitude convection. Several field campaigns and numerical studies have measured the vertical velocities using a multitude of platforms and have found that the majority of tropical updrafts have velocities less than 3-5 m s^{-1} (Xu and Randall 2001; Lucas et al. 1994a,b; LeMone and Zipser 1980; Zipser and LeMone 1980). In comparison, vertical velocities of midlatitude continental convection are approximately 1.5 m s^{-1} greater than tropical convection velocities (Xu and Randall 2001). The greatest difference in vertical velocities is between the most severe convection in the two regions. The vertical velocities of supercells has been documented to exceed 50 m s^{-1} (Bunkers et al. 2006; Lehmiller et al. 2001; Bluestein et al. 1988;

Musil et al. 1986) while tropical cyclones rarely exceed 20 m s^{-1} (Eastin et al. 2005; Black et al. 1996; Jorgensen et al. 1989).

The diurnal cycle of convection in the midlatitudes and tropical oceans also differs. Maximum convective activity over the tropical ocean generally occurs during the nocturnal-early morning period following an afternoon initiation (Liu and Moncrieff 1998; Gray and Jacobson 1977). Convection is sustained following initiation due to the diurnal heating of the ocean and boundary layer (Futyan and Del Genio 2007). Further, the diurnal cycle over tropical oceanic regions is dependent on the areal coverage of the cloud shield which can lead to a bi-diurnal cycle (Chen and Houze 1997). In contrast, convection occurring in the midlatitudes follows the solar diurnal cycle initiating in the afternoon-early afternoon and ceasing soon after night-fall (Zhang and Klein 2010; Nesbitt and Zipser 2003; Yang and Slingo 2001; Dai 2001; Soden 2000; Dai et al. 1999; Gray and Jacobson 1977).

The fundamental differences of convection in the midlatitudes and tropics influence the probability of turbulence encounters in the following aspects. Commercial aviation operates between approximately 8-13 km (Trier and Sharman 2016; Smit et al. 2008; Güsten et al. 2003) where overshooting midlatitude convection occurs. Aviation operations in the midlatitudes are more likely to encounter turbulence caused by vertically propagating gravity waves as the aircraft attempts to fly over convection. In comparison, tropical aviation routes cannot fly above overshooting convection and reroute laterally, therefore decreasing the probability of encountering vertical propagating gravity waves. The weaker vertical velocities of tropical oceanic convection also reduces the propagation of turbulence caused by moist-instabilities within the updraft. Lastly, as air traffic is more congested over midlatitude continental regions, aircraft are more likely to encounter turbulence generated by gravity waves in the horizontal and along cloud boundaries due to limited airspace. Flights over tropical

oceanic routes are fewer in number and have more options in adjusting height and flight-path.

The remaining sections will discuss current turbulence diagnostics, the influence of model resolution on turbulence distributions and directional preference, properties of CIT caused by developing convection, and the characteristics of tropical and midlatitude CIT.

CHAPTER 3

OUT-OF-CLOUD CONVECTIVE TURBULENCE: ESTIMATION METHOD AND IMPACTS OF MODEL RESOLUTION

3.1 Motivation

Convectively induced turbulence (CIT) is an aviation hazard that can cause moderate to severe damage to aircraft and costs the aviation industry millions of dollars (Golding 2000). Traditionally, forecast models have had limited success with turbulence prediction because the utilized model resolution is too coarse to resolve individual turbulent eddies. To mitigate this problem, several metrics have been developed to diagnose turbulence on larger synoptic scales. These indices include the Brown index, the Dutton index, the Ellrod index, and the Ellrod–Knox index (Brown 1973; Dutton 1980; Ellrod and Knapp 1992; Ellrod and Knox 2010). A major limitation with all of these indices for CIT prediction is that the turbulence intensity is an empirical value determined from correlating large-scale meteorological variables to pilot reports that did not include CIT. In addition, the turbulence thresholds were determined based on model simulations with much coarser model resolutions than are in operation today. Behne (2008) reported an overestimation of turbulence potential when implementing the Ellrod index. This overestimation by the Ellrod index was also noted in a recent study of tropical cases (Barber 2015). Although a conservative estimation of turbulence may seem to be a safeguard of approaching air travel, in reality the estimate influences flight routes, traffic patterns, takeoffs, and landings, and is overall eco-

nominally inefficient. Therefore, more accurate turbulence prediction that maintains safety and is economically efficient is needed.

More recently, high-resolution numerical models are being used to gain a better understanding of the generation, propagation, and dissipation of out-of-cloud turbulence (e.g., Trier and Sharman 2016; Lane and Sharman 2014; Kim et al. 2014; Lane et al. 2012; Trier et al. 2010; Sharman et al. 2012; Lane et al. 2009). However, simulating CIT using high-resolution models is challenging because the scale of motion that influences aircraft (10–1000m; Lester 1994) is similar to or smaller than the scale of mesoscale processes (Bryan et al. 2003) that generate CIT. Accurately resolving both the mesoscale source and turbulent response simultaneously is critical for turbulence prediction (Lane and Sharman 2014; Zovko-Rajak and Lane 2014). Lane and Sharman (2014), using large-eddy simulations, found that the most intense turbulence locations were outside of the convective cloud, well beyond the FAA guidelines, and not within cloud. An additional challenge specific to forecasting CIT is correctly forecasting the location, strength, and type of convection (Wakimoto and Murphey 2009; Weisman et al. 2008; Bernardet et al. 2000; McNulty 1995). Last, the computational and temporal expenses limit the use of high-resolution models in an operational forecast environment for turbulence prediction.

CIT prediction depends on model resolution and the accuracy of convective forecasts. The goal of this research is to identify statistical biases in popular turbulence metrics estimated from both common operational model setups and high-resolution simulations. Biases in convection will also be investigated amongst various model setups and convective morphologies. Turbulence is estimated from Weather Research and Forecasting (WRF) Model simulations over a 1-week period over the North Dakota region in July 2015. The results are compared with observed pilot reports collected from various airlines. Out-of-cloud turbulence estimations are in-

cluded in the analysis of model accuracy. The biases found will be useful for ongoing development of resolution-dependent turbulence intensities for independent indices.

3.2 Data and Methods

3.2.1 Pilot reports

Pilot reports (PIREPs) gathered from the Aviation Weather Center (A. Terborg 2016, personal communication) and the Iowa Environmental Mesonet (<https://mesonet.agron.iastate.edu/request/gis/pireps.php>) are used as observations of turbulence from various aircraft in the northern Great Plains region during 10–17 July 2015. These reports include the estimated turbulence intensity, time, and location of the turbulence encounter, and whether the aircraft was in cloud or out of cloud at the time. PIREPs that are reported on a 0–8 scale can be converted to eddy dissipation rate (EDR) values following the methodology outlined in Sharman and Pearson (2017) and Sharman et al. (2014). A caveat with this conversion is that the constants may be height dependent. While PIREPs are extremely helpful for nowcasting turbulence and aiding in turbulence avoidance, there are numerous limitations associated with the use of PIREPs in scientific research. PIREPs give a limited validity of turbulence location and intensity for scientific research and are dependent on pilot perception of turbulence, especially when in situ measurements of EDR are unavailable. In addition, turbulence at various scales impacts aircraft of various sizes differently. Specifically, moderate turbulence encountered by a small general public aircraft may not be moderate turbulence to a larger commercial aircraft. Another critical limitation of PIREPs is that most aviation routes are going to avoid convection based on company-determined lateral and vertical distances. This avoidance drastically decreases the number of CIT observations and restricts direct

comparisons with model output. Last, PIREPs without in situ EDR measurements are subject to human error and can be reported incorrectly (Sharman et al. 2014; Wolff and Sharman 2008). Because of these limitations, direct comparisons of the location and timing of PIREPs will not be made with simulated EDR in this study.

The National Center for Atmospheric Research (NCAR) Turbulence Detection Algorithm (NTDA) produces 5-min 3D in situ observations of in-cloud turbulence for the contiguous United States at 15 height levels (Williams et al. 2011). The use of NTDA for turbulence verification has increased recently (Pearson and Sharman 2017) and has shown to perform well for in-cloud turbulence prediction. However, the skill of NTDA for out-of-cloud turbulence intensity has not been well tested. In addition, out-of-cloud turbulence intensity can only be determined using NTDA in-cloud turbulence observations. NTDA observations will not be used in this study because the focus is out-of-cloud turbulence, and therefore only PIREPs will be considered as turbulence observations.

3.2.2 Model setup

In this study, 30-h forecasts of convection in the northern Great Plains from 10 to 17 July 2015 are made using the Advanced Research WRF Model, version 3.7 (Skamarock and Klemp 2008). All simulations are initialized at 0000 UTC with ERA-Interim (<http://www.ecmwf.int/en/research/climate-reanalysis/era-interim>) global reanalysis data and run using Extreme Science and Engineering Discovery Environment (XSEDE) resources (Towns et al. 2014). Forecasts are then analyzed from 0600 to 0600 UTC (forecast hours 7–30). Four sets of horizontal and vertical grid spacings are used for these simulations and range from 12 km to 500 m in the horizontal (Table 2) with one-way nesting implemented. Model setup 1 (S1) is designed to be similar in resolution to the North American Model (NAM),

Table 2: Model grid spacing and number of vertical levels. D02 represents the innermost nest of S1 (i.e., D02 = 1 parent and 1 nest), and D03 represents the innermost nest of S2–S4 (i.e., D03 = 1 parent and 2 nests).

Model	Horizontal grid spacing	No. of vertical levels	Mean vertical grid spacing (7-11 km in height)
S1	12 km (D02)	65	550 m
S2	3 km (D03)	65	550 m
S3	3km (D03)	100	325 m
S4	500 m (D03)	100	325 m

setup 2 (S2) is similar to the operational High Resolution Rapid Refresh (HRRR) model, setup 3 (S3) is comparable to the HRRR but with a finer vertical resolution, and setup 4 (S4) will be used as the high resolution simulations and considered to be “truth.” This spectrum of grid spacings encompasses operational and research applicable model setups. Parameterizations for all of the simulations are provided in Table 3. The model top in all simulations is set to 10 hPa (approximately 30 km), and a 10-km-deep damping layer is used at the model top. The model domains for S1–S3 remain unaltered and encompass the same geographical area for all eight simulation periods. For S4, the model domain varies with simulation period based on the known location of convection from observations in order to limit the computational costs (i.e., the model domain for each simulation period does not cover the same geographical area). The model domain for each simulation is provided in Figs. 1 and 2. The results will highlight findings from three simulation days on which the convective types included linear features, weak and intense isolated convection, and decaying mesoscale convective systems.

Table 3: Model parameterizations used in simulations. The cumulus parameterization is not applicable to model setup 4.

Parameterizations	Model setup
Microphysics	WDM6
PBL	MYJ
Surface layer	MM5 similarity
Land surface	Noah
Shortwave radiation	Dudhia
Longwave radiation	RRTM
Cumulus	Kain-Fritsch (D01 and D02, N/A for S4)

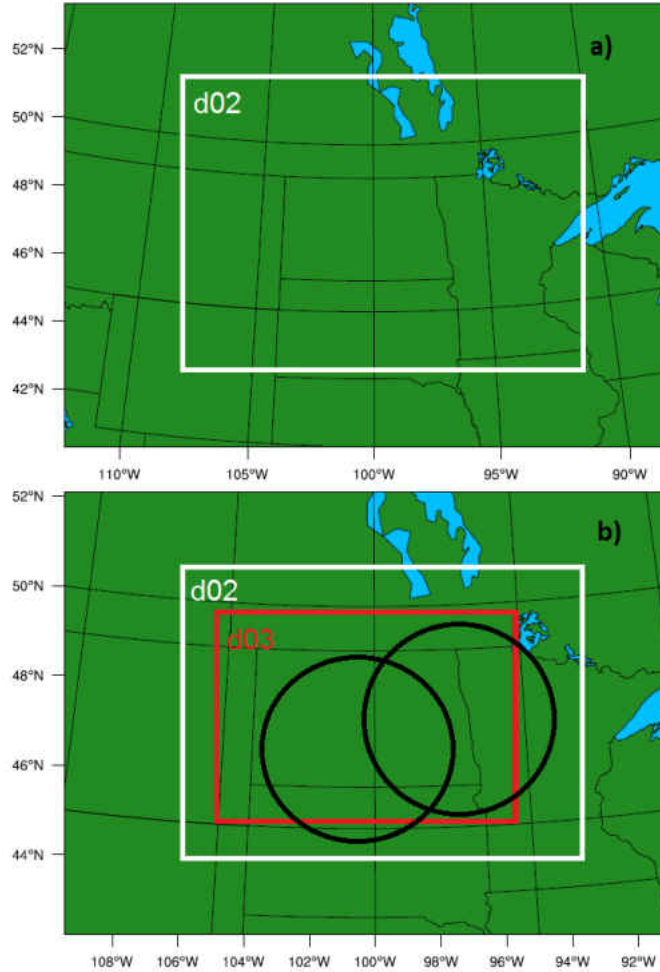


Figure 1: Model domain for model setup S1 (a), and model setups S2 and S3 (b). D02 represents the innermost nest of model setup S1 and D03 represents the innermost nest of model setups S2 and S3. The black circles represent the Mayville, ND and Bismarck, ND radars.

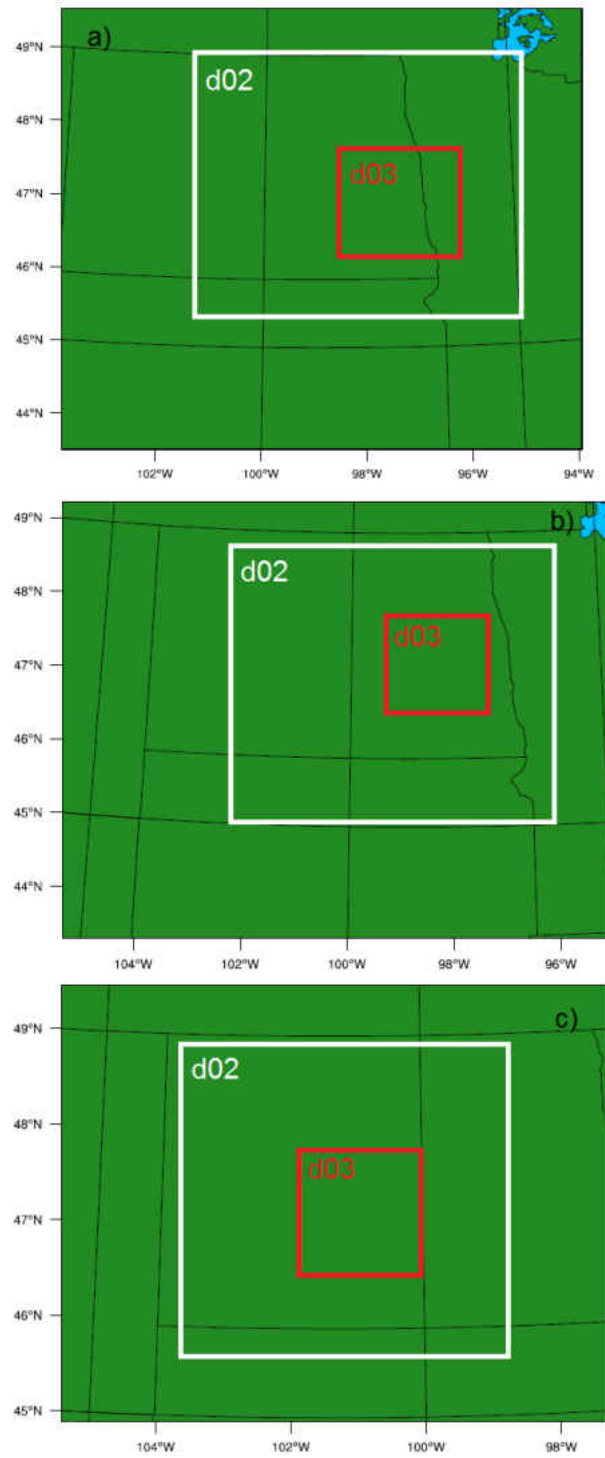


Figure 2: Model domain for model setup S4 on (a) 12 July 2015, (b) 13 July, and (c) 15 July.

Table 4: Turbulence intensity as determined from the cubed root of eddy dissipation rate (ε ; Lane et al. 2012; Sharman and Pearson 2017).

Turbulence intensity	$\varepsilon^{1/3}$ ($\text{m}^{2/3} \text{s}^{-1}$)	
	Lane et al. (2012)	Sharman and Pearson (2017) median
Light	0.1-0.3	0.01
Moderate	0.3-0.5	0.22
Severe	0.5-0.7	0.47

3.2.3 Turbulence metrics

Turbulence intensity (TI) is estimated by computing EDR from turbulent kinetic energy (TKE) of each simulation as discussed in the Appendix. Atmospheric turbulence is commonly defined as light, moderate, and severe based on the cubed root of EDR ($\text{m}^{2/3} \text{s}^{-1}$; Tables 4 and 21; Lane et al. 2012). This study will use thresholds corresponding to Lane et al. (2012) provided in Table 4. Recently, new EDR values have been proposed (Sharman et al. 2014; Sharman and Pearson 2017; Pearson and Sharman 2017) based on climatological PIREPs and various sources including the Global Turbulence Guidance (GTG-2) product. This study will mainly discuss the former thresholds but provide both thresholds in figures to demonstrate the various intensities based on which thresholds are used. In addition to EDR, the Ellrod index (T2) will be used as a turbulence metric (see the Appendix for calculation).

3.2.4 Lateral avoidance

Current FAA thunderstorm guidelines are implemented to reduce the frequency of thunderstorm hazard encounters by aircraft. These guidelines include a lateral avoidance of 20 mi from a thunderstorm. In this study, lateral avoidance will be examined by creating range circles around simulated convection. The following discussion will describe this methodology. Echo top height is used as a proxy for convection and

considered in cloud. An 18-dBZ threshold for simulated radar reflectivity is used to determine the echo top height. Individual grid cells with echo top heights (ET) greater than 8 km in altitude are masked out within the domain. Radius ranges of 10 mi, 20 mi, and 50 mi (16.1 km, 32.2 km, and 80.5 km) are calculated for each grid cell that has ETs ≥ 8 km (Fig. 3). Turbulence grid cells within these radius ranges are out-of-cloud if there is no ET greater than 8 km in the same location. Out-of-cloud turbulence will be analyzed within 10 mi, 20 mi, and 50 mi of convection. Out-of-cloud turbulent grid cells within the lateral distances of convection are examined at 8 km, 10 km, and 12 km in altitude (common cruising altitudes of commercial aircraft).

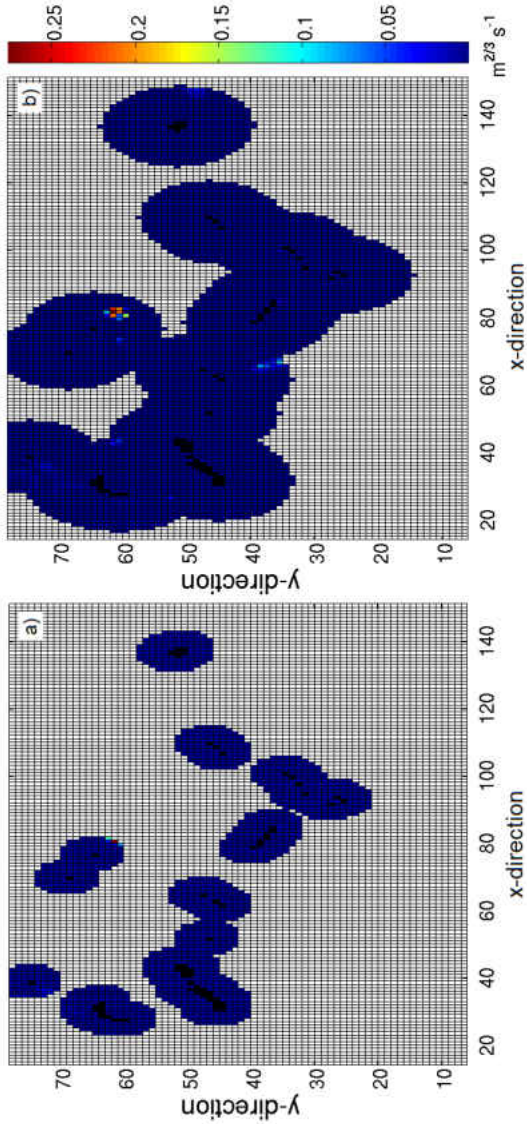


Figure 3: Schematic depicting masking methodology for determining the turbulence distribution (color bar; $\text{m}^{2/3} \text{s}^{-1}$ within various distances from convective cores at various altitudes. Black grid cells represent echo top heights ≥ 8 km, blue color grid cells represent distances of (a) 10 mi (16.1 km) around ET cores, (b) 20 mi (32.2 km) around ET cores.

3.3 Results

This section highlights findings from three simulation days (12, 13, and 15 July 2015) from 0600 to 0600 UTC of the forecast period. These days were selected for analysis because convection was severe with numerous storm reports and pilot reports recorded in the North Dakota region. The convective types observed during these analysis times included linear features, weak and intense isolated convection, and decaying mesoscale convective systems. A detailed overview of the S4 simulation and a comparison with observed storm characteristics is first presented, as S4 will be considered to be truth in the model comparisons. The other model configurations are then compared with S4 to assess the impacts of resolution on simulated turbulence.

3.3.1 Storms observed

3.3.1.1 12 July 2015 (0600 UTC 12 July–0600 UTC 13 July)

Convection on 12 July was severe and produced large hail, severe winds, and several tornadoes (EF0–EF2 on the enhanced Fujita scale) in the eastern portion of North Dakota (ND) and western Minnesota (MN). Storms began as intense individual cells in the northeast and southeast portion of ND around 2000 UTC. Near 2200 UTC the convection merged into two large convective regions with radar reflectivity values at 1-km AGL exceeding 55 dBZ along the ND–MN border (Fig. 4a). The northern complex began to weaken around 0100 UTC 13 July while the southern complex continued to strengthen until 0200 UTC. Maximum echo top (ET; ≥ 18 dBZ) heights are used in this study as a proxy for convective strength. ETs are determined from level-III radar data. Observed ETs for this convective period exceeded 15 km in both the northern and southern convective segments (Fig. 5a). There were 27 PIREPs from 0600UTC 12 July to 0600 UTC 13 July, with 5 reports classified as light and

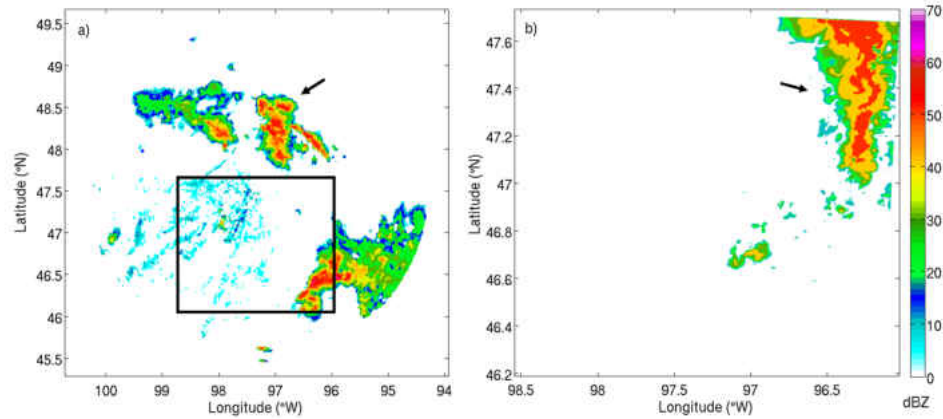


Figure 4: (a) Observed Mayville, ND radar reflectivity values (0.5° elevation angle) at 2155 UTC on 12 July and (b) simulated 1-km AGL radar reflectivity values at 0200 UTC on 13 July for S4 (forecast initialized at 0000 UTC on 12 July). Black box in (a) represents the model domain in (b). Black arrows are included to describe the northern complex discussed in above. See Fig. 2a for the complete model domain.

22 as moderate. Of the 27 PIREPs, 24 PIREPs were above 8 km at the time of the report. The majority of the encounters were located near the ND–MN border in the afternoon (Fig. 6) and were out of cloud. The EDR values of these reports when converted using Sharman et al. (2014) methodology varied between 0.18 and $0.27 \text{ m}^{2/3} \text{ s}^{-1}$ (i.e., moderate intensity).

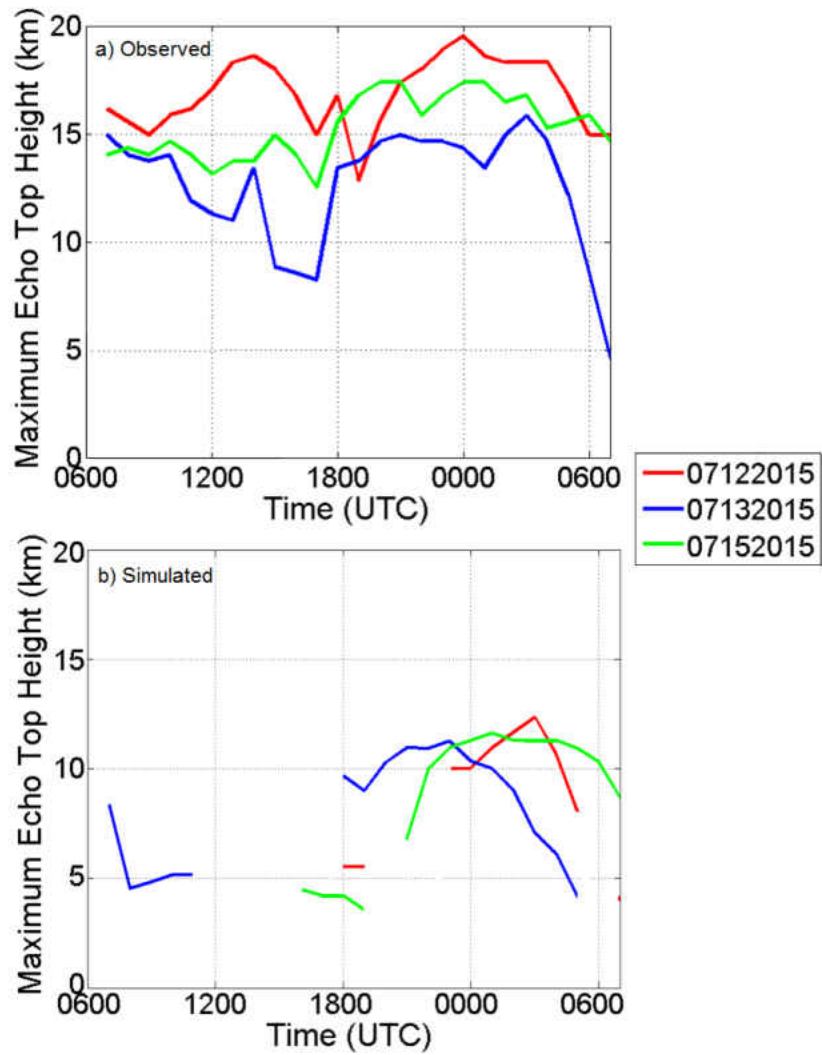


Figure 5: Maximum echo top heights (km) observed by Mayville and Bismarck, ND radar (a) and simulated by S4 (b).

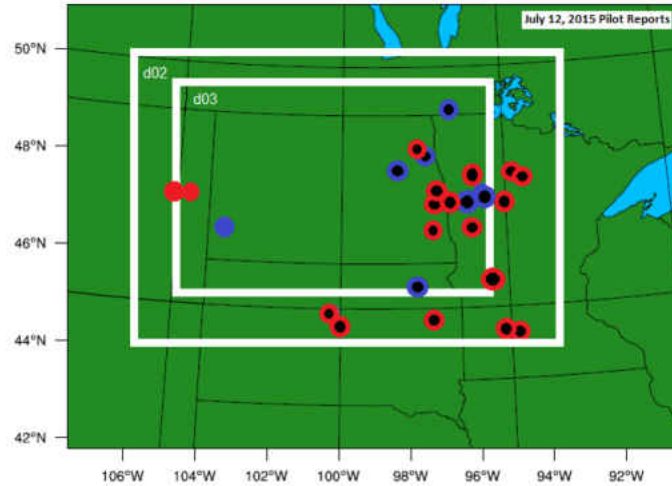


Figure 6: Pilot reports of turbulence occurring on 12 July 2015 within S2-S3 model domain (innermost white box represents the 3km domain). Blue circles represent light turbulence reports and red represents moderate turbulence reports. Black dots within the circles indicate the report was made when the aircraft was greater than 8 km in altitude.

3.3.1.2 13 July 2015 (0600 UTC 13 July–0600 UTC 14 July)

Convection on 13 July was nonsevere and mainly isolated cells that formed from weak frontal boundaries in the northern region of ND. These cells began to develop around 1800 UTC and dissipated near 0100 UTC (Fig. 7a); 1-km AGL reflectivity values of these convective cells exceeded 50 dBZ. Observed ETs extended past 14 km in altitude in multiple isolated cells west of the ND–MN border around 2000 UTC but began decreasing in altitude shortly after 2200 UTC (Fig. 5a). From 0600 UTC 13 July to 0600 UTC 14 July, pilots reported nine turbulence encounters in the ND–MN–South Dakota (SD) region, all of which were moderate intensity. Eight of the nine were above 8 km and out of cloud.

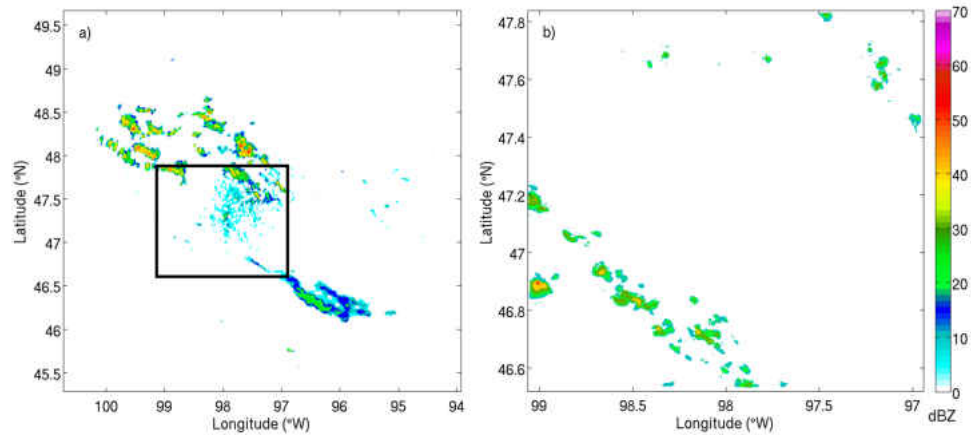


Figure 7: (a) Observed Mayville, ND radar reflectivity values (0.5° elevation angle) at 1925 UTC on 13 July and (b) simulated 1-km AGL radar reflectivity values at 1900 UTC on 13 July for S4 (forecast initialized at 0000 UTC on 13 July). Black box in (a) represents the model domain in (b). See Fig. 2b for the complete model domain.

3.3.1.3 15 July 2015 (0600 UTC 15 July–0600 UTC 16 July)

Convection that occurred on 15 July produced hail greater than 1 in. in diameter and three severe wind reports. Convection began overnight (0600 UTC, 0100 local time) in western ND as large isolated cells that propagated into central ND and organized into a weak convective complex by 1300 UTC. Radar reflectivity values were less than 55dBZ at 1-km AGL. The complex formed a bowing segment near 1800 UTC in the southeast region of ND with radar reflectivity values exceeding 55 dBZ. This bowing feature dissipated by 2300 UTC in western MN, while more intense isolated convection developed in the western portion of ND (Fig. 8a). At 0200 UTC a strong linear feature with radar reflectivity values exceeding 60 dBZ was present in northwest ND (Fig. 9a) and 2 h later weakened into a stratiform-dominant feature. Observed ETs exceeded 16 km in altitude in western ND near 1800 UTC (Fig. 5a). On 15 July there were 10 reports of turbulence, 8 of which were moderate intensity. All of the reports of moderate turbulence were above 8 km in altitude and out of cloud.

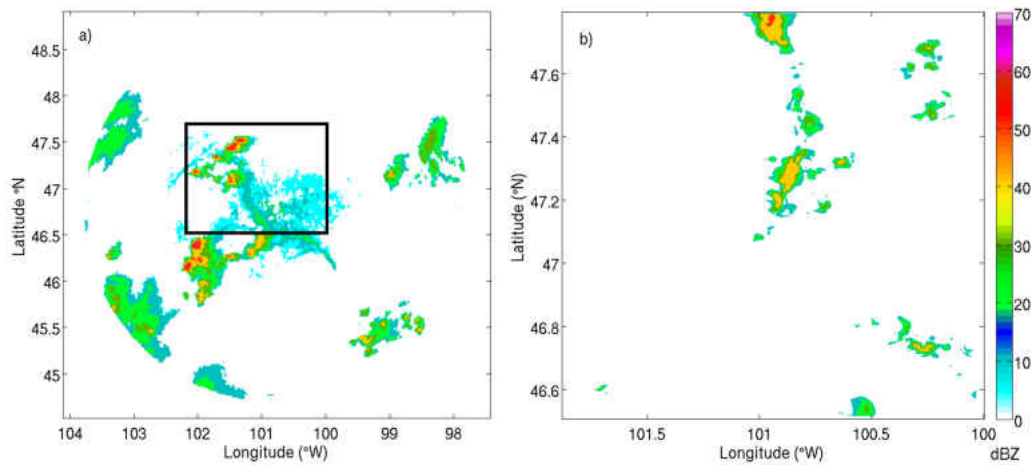


Figure 8: (a) Observed Bismarck, ND radar reflectivity values (0.5° elevation angle) at 2325 UTC on 15 July and (b) simulated 1-km AGL radar reflectivity values at 0000 UTC on 16 July for S4 (forecast initialized at 0000 UTC on 15 July). Black box in (a) represents the model domain in (b). See Fig. 2c for the complete model domain.

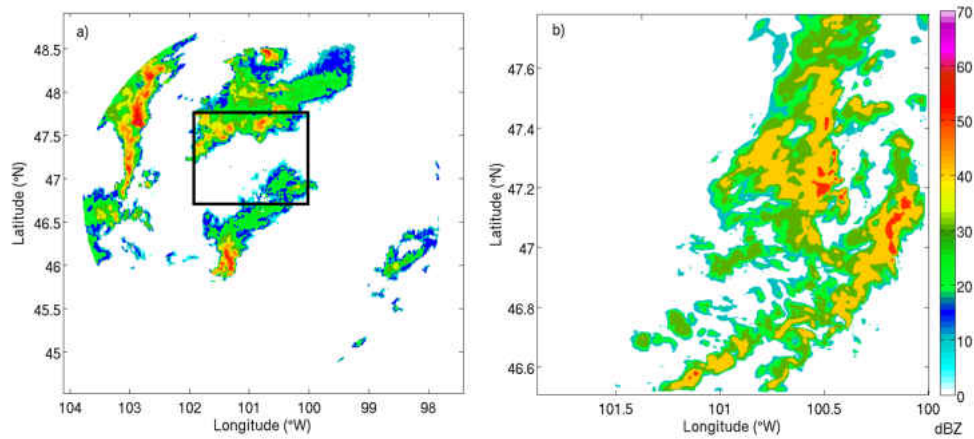


Figure 9: (a) Observed Bismarck, ND radar reflectivity values (0.5° elevation angle) at 0225 UTC on 16 July and (b) simulated 1-km AGL radar reflectivity values at 0200 UTC on 16 July for S4 (forecast initialized at 0000 UTC on 15 July). Black box in (a) represents the model domain in (b). See Fig. 2c for the complete model domain.

3.3.2 S4 turbulence

Convection simulated by S4 for the three simulation days was generally accurate in morphology but often inaccurate in intensity and timing. For example, the morphology of a simulated isolated convective segment in the northern region of the S4 domain was very similar to observations on 12 July (Fig. 4b), but was lagging in time by approximately 4 h and was located farther south in latitude. In addition, S4 simulated ETs above 11 km after 2200 UTC with a maximum of approximately 12 km after 0200 UTC (Fig. 5b), but observed ETs were greater than 15 km. For 13 July, S4 simulated the correct type of convection (isolated), developed and dissipated simulated convection in the same time period as observed convection, but had weaker reflectivity intensity at 1-km AGL (Fig. 7b). Simulated vertical depth of convection on 13 July was also lower than observed (Figs. 5a and b). These results were also consistent for simulated convection on 15 July (correct morphology and timing but shallower depth; Figs. 8b, 9b, and 5b). Previous studies have shown that the microphysical scheme implemented can influence simulated ET height. Stephan and Alexander (2014) compared ETs and cloud tops for the WRF double-moment 6-class microphysics scheme (WDM6) with other microphysical schemes. Relative to the Morrison or Thompson scheme, WDM6 had fewer high ETs but similar cloud-top heights. The lower ETs were likely related to lower column-integrated ice amounts. Although the vertical depth of simulated convection was substantially less than observations indicated, turbulence magnitude will be evaluated and compared with PIREPs.

The Ellrod index is examined in the S4 domain at 8 km, 10 km, and 12 km altitudes. During the simulation period, the minimum nonzero values of the Ellrod index exceed the severe threshold of 12 by an order of magnitude and cover large portions of the domain. A direct comparison of the Ellrod index and EDR predicted by S4 at 8 km in altitude at 0200 UTC is provided in Fig. 10. This comparison demonstrates

a large areal coverage of severe turbulence estimated by the Ellrod index (blue color contour = severe) and a smaller areal coverage of moderate turbulence estimated by EDR (purple color contour = moderate). This overestimation of turbulence magnitude and occurrence by the Ellrod index was consistent through the entire simulation period, for all heights and all lateral distances away from convection. This analysis highlights the resolution sensitivity of the Ellrod index at higher model resolutions. Upon further investigation, the vertical wind shear term in the calculation of the Ellrod index was found to have the largest impact on the magnitude of turbulence. At this time the Ellrod index is not a useful measure across different model resolutions unless a resolution-scale-dependent threshold were developed. The empirical values originally derived for the Ellrod index are not applicable to model setups with finer grid spacing without calibration or reverification of new values to PIREPs. The Ellrod index similarly overestimated turbulence at the 3 km resolution (not shown; see also Barber 2015). Because of the extreme resolution sensitivity of the Ellrod index, the remainder of this study will not discuss the Ellrod index.

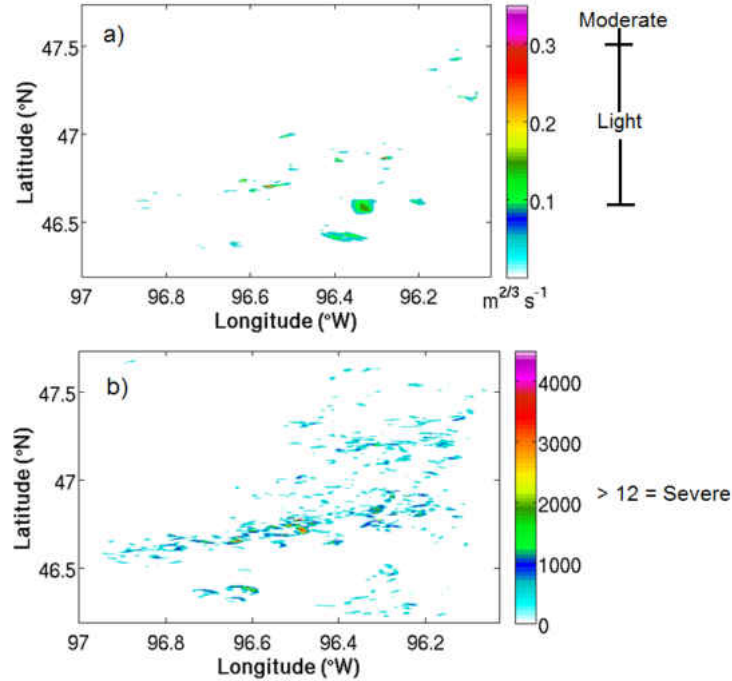


Figure 10: (a) Eddy dissipation rate (magnitudes indicated using Lane et al. 2012) and (b) Ellrod index values at 8 km in altitude predicted from S4 at 0200 UTC 13 July 2015 (from 0000 UTC initialized forecast on 12 July). All colored regions in (b) are traditionally classified as "severe".

Out-of-cloud EDR values are examined within 10, 20, and 50 mi from convection at 8, 10, and 12 km in altitude (12 km analysis provided in Fig. 11) on 12 July. At 12 km in altitude, more of the turbulent grid cells were light in magnitude within 50 mi of convection and more of the turbulent grid cells were moderate in magnitude within 10 mi of convection. Similar relationships in turbulence intensity and distance are seen at both 8 and 10 km in height. Although there was a higher percentage of turbulent grid cells with moderate intensity within 10 mi away from convection, turbulence within 50 mi of convection is important to forecast because it is farther than the 20 mi lateral distance avoidance guideline set by the FAA. Because of this finding, turbulence within 50 mi of convective cores will be discussed hereinafter.

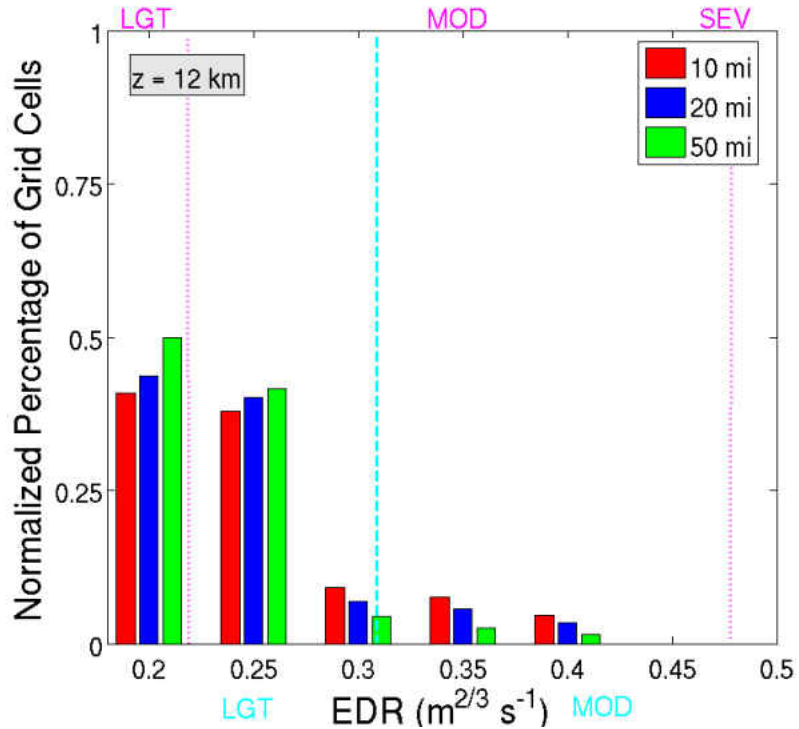


Figure 11: 12 km normalized out-of-cloud eddy dissipation rate distribution $\geq 0.2 \text{ m}^{2/3} \text{ s}^{-1}$ (# of turbulent grid cells within bin divided by all grid cells with turbulence $\geq 0.2 \text{ m}^{2/3} \text{ s}^{-1}$) within (a) 10 mi (16.1 km), (b) 20 mi (32.2 km), and (c) 50 mi (80.5 km) of convective cores with echo top heights ≥ 8 km for S4. Dashed (cyan) and dotted (purple) vertical lines represent turbulence intensities based on Lane et al. (2012) and Sharman et al. (2014), respectively.

3.3.2.1 12 July 2015 (0600 UTC 12 July–0600 UTC 13 July)

Figure 12a provides the EDR values within 50 mi of convective cores with ETs greater than 8 km in altitude. The lowest EDR values had the greatest areal coverage, indicating that there is a significant amount of area experiencing light turbulence. The highest EDR values were predicted at 8 and 12 km in altitude for S4, below and above the maximum ET. Although the areal coverage of the highest EDR values was small, the prediction of these values is crucial. In relationship to the PIREPs on 12 July, turbulence estimated by EDR was the same magnitude as the PIREPs: light and moderate intensity above 8 km.

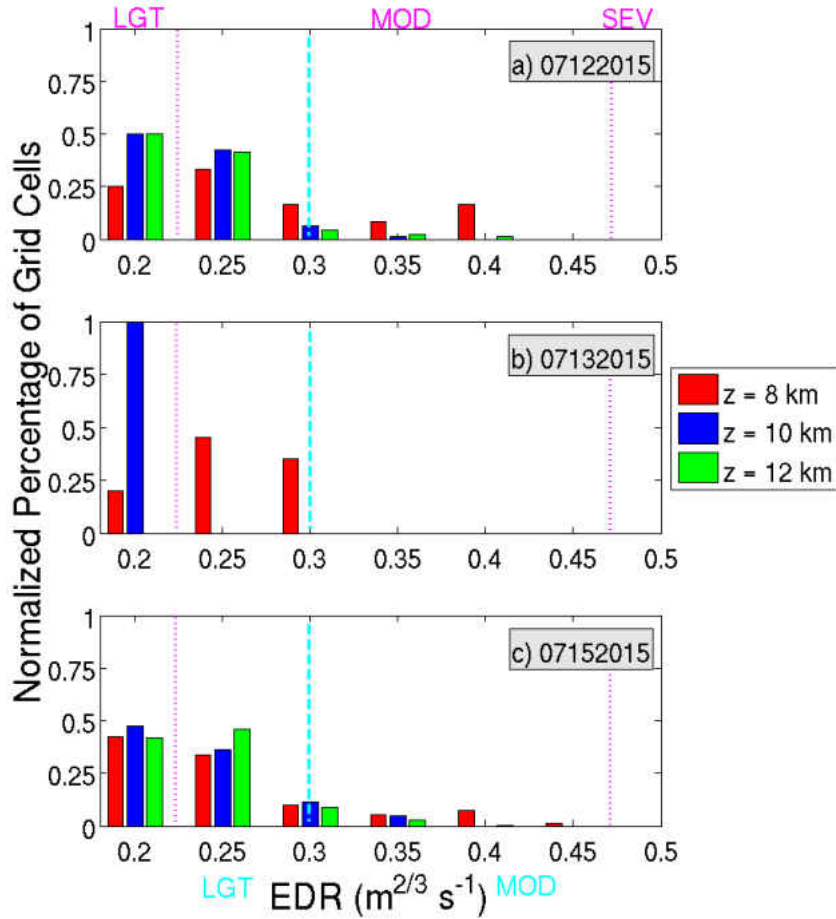


Figure 12: Normalized out-of-cloud eddy dissipation rate distribution $\geq 0.2 \text{ m}^{2/3} \text{ s}^{-1}$ (# of turbulent grid cells within bin divided by all grid cells with turbulence $\geq 0.2 \text{ m}^{2/3} \text{ s}^{-1}$) within 50 mi (80.5 km) of convective cores with echo top heights $\geq 8 \text{ km}$ for S4. Dashed (cyan) and dotted (purple) vertical lines represent turbulence intensities based on Lane et al. (2012) and Sharman et al. (2014), respectively.

Although simulated convection was lagging in time and predicted ETs significantly lower than observations, estimated turbulence magnitude was similar to observations. In a real-time operational setting (assuming the S4 simulation could be performed in a timely manner), moderate turbulence caused by deep convection would have been forecast in the ND area at altitudes near where commercial aviation

had reported. S4 could have been utilized in an operational setting for the prediction of turbulence.

3.3.2.2 13 July 2015 (0600 UTC 13 July–0600 UTC 14 July)

The distribution of out-of-cloud EDR values within 50 mi of convection on 13 July is significantly narrower than on 12 July (Fig. 12b) and the majority of EDR values are less than $0.1 \text{ m}^{2/3} \text{ s}^{-1}$. The maximum EDR value predicted by S4 was $0.3 \text{ m}^{2/3} \text{ s}^{-1}$ and occurred at 8 km in altitude. At both 10 and 12 km, S4 did not predict any EDR values greater than $0.25 \text{ m}^{2/3} \text{ s}^{-1}$. Again, the likelihood of encountering light turbulence is far greater than experiencing moderate turbulence, especially below 10 km in altitude. S4 did predict moderate turbulence, although it was at a lower altitude than the majority of PIREPs indicated.

For this case day, convective morphology (isolated) and timing was well predicted by S4. However, the storm intensity was too weak, as evidenced by both reflectivity and echo top heights. This is the likely reason that S4 in general under-predicted the turbulence intensity. While at times turbulence intensity was correct, the predicted altitude was too low. This suggests the S4 simulations of turbulence have difficulty with convection that is isolated, is less intense, and has a shorter lifespan.

3.3.2.3 15 July 2015 (0600 UTC 15 July–0600 UTC 16 July)

The distribution of out-of-cloud EDR values forecast by S4 on 15 July again shows mostly light turbulence at 10 and 12 km (Fig. 12c). This suggests a higher likelihood of aircraft encountering lower-intensity turbulence near convection because of wide areal coverage. The maximum EDR values predicted by S4 are at both 12 and 8 km in altitude. Moderate turbulence was predicted by S4 at 8, 10, and 12 km, which

agrees with observed pilot reports of turbulence. The usage of S4 in a real-time operational setting would have been beneficial, as simulated radar reflectivity at 1 km in altitude was comparable to observed radar reflectivity and the morphology of convection was similar to observations. Once again, the convective depth was lower than observations. However, the prediction of turbulence intensity and location did not seem to be directly affected by lower simulated ETs.

3.3.3 Effects of varying resolution on turbulence

To examine the effects of horizontal resolution on predicted turbulence, S4 will be compared with S1, S2, and S3, treating S4 as truth. Figures 13–15 provide the maximum ETs for each model setup for 12, 13, and 15 July. Important features from this analysis are the relatively low ETs for S1, which never exceeded 7 km on both 12 and 13 July. Weak convection that does not extend far in the vertical is less of a hazard for aviation operations flying above 8 km in altitude. The weak convection and low ETs simulated from S1 highlight that coarse horizontal model resolution, such as the 12 km grid spacing used here, is not appropriate for the calculation of eddy dissipation rates because of the significant under prediction of convection and convective depth. Therefore, S1 will not be discussed hereinafter. However, the use of indices that are calibrated for large-scale conditions could still be applied at coarser resolutions, similar to indices utilized in the Graphical Turbulence Guidance product (Sharman et al. 2006) from the Rapid Refresh products. The setups with higher vertical resolution achieved ETs >12 km on 12 July, suggesting that higher vertical resolution is important for accurately predicting the convective depth of linear convective features and in turn turbulence. However, on 13 and 15 July, the relationship between maximum ETs and vertical model resolution is less apparent, especially on 15 July. It is possible that model resolution in the vertical has greater

influence on the strength of simulated isolated convection and is less important for convection that has stronger dynamical forcing, such as organized mesoscale systems that are severe in strength, extensive in areal coverage, and long lasting, or convection that is forced by synoptic frontal boundaries.

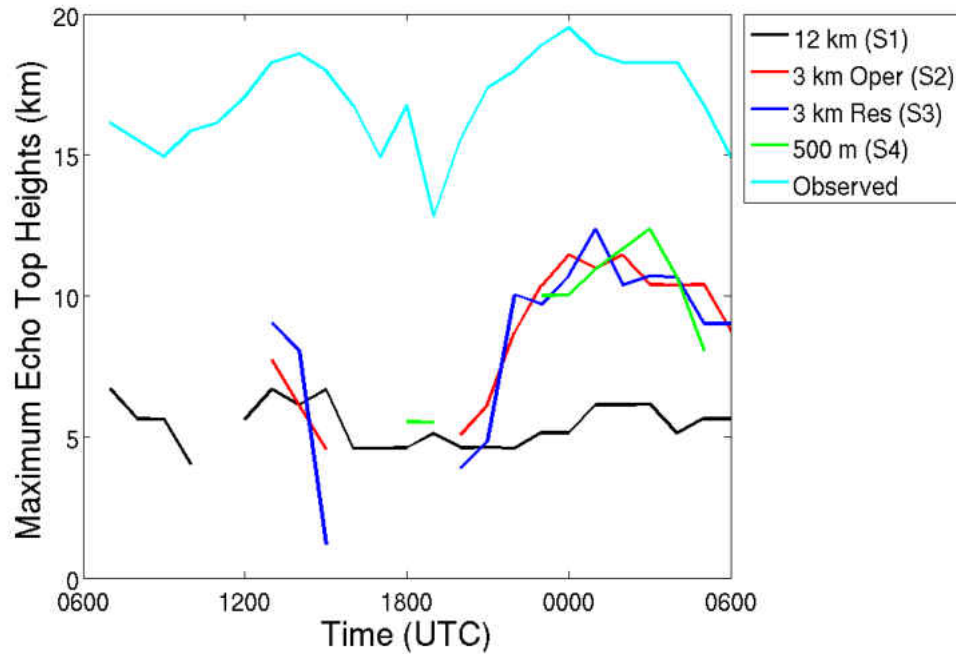


Figure 13: Maximum echo top heights (km) forecasted by S1-4 and estimated by radar on 12 July 2015 beginning at 0600 UTC.

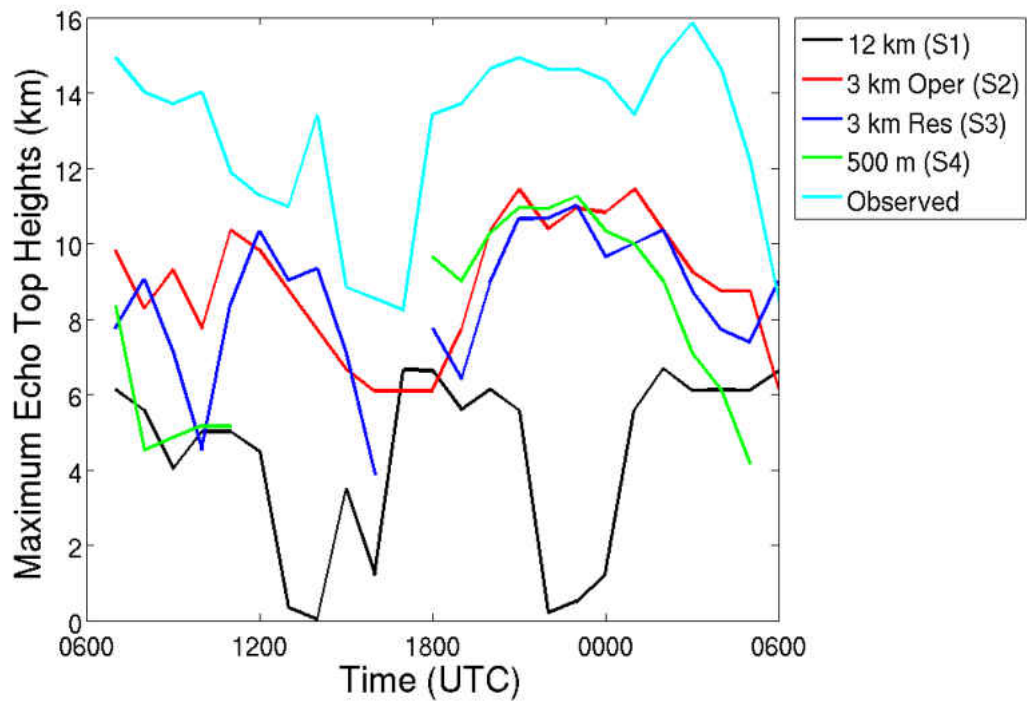


Figure 14: Maximum echo top heights (km) forecasted by S1-4 and estimated by radar on 13 July 2015 beginning at 0600 UTC.

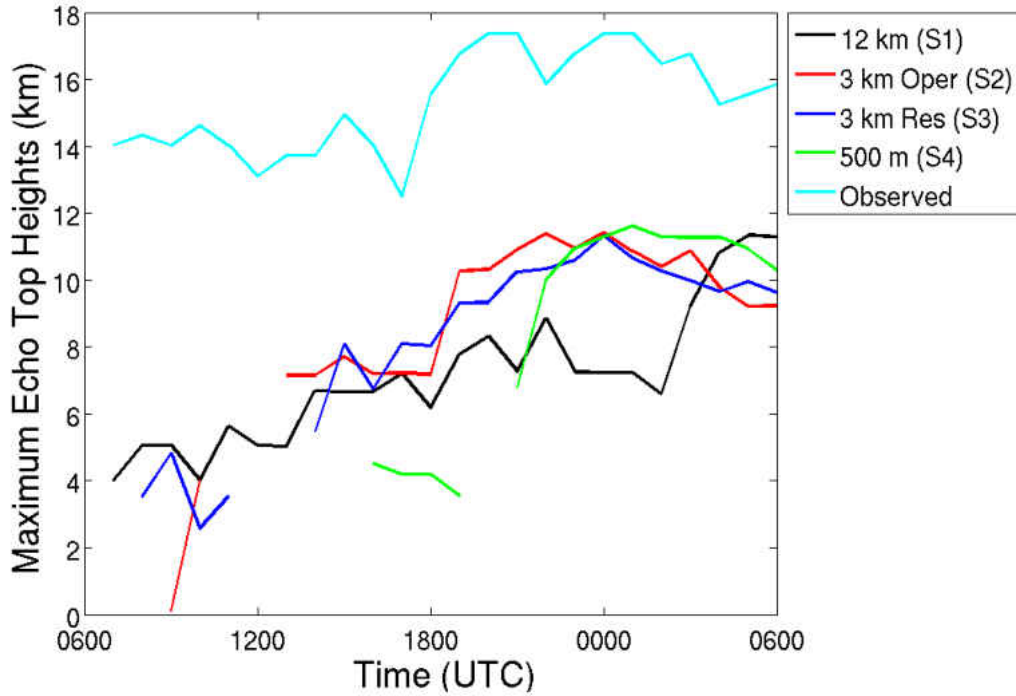


Figure 15: Maximum echo top heights (km) forecasted by S1-4 and estimated by radar on 15 July 2015 beginning at 0600 UTC.

The examination of out-of-cloud EDR values from 12 July within 50 mi from convection at 8, 10, and 12 km in altitude for S2 and S3 demonstrates that lower EDR values have the greatest areal coverage (for both normalized and raw area values; all further results discuss normalized area values, but results hold for raw area values as well), indicating that there is a significant amount of area experiencing light turbulence (Fig. 16). This result is consistent with S4, where S4 predicted large areas of light turbulence at 8 km, 10 km, and 12 km in altitude. Interestingly, all of the model setups predict the most light turbulence at 10 km in altitude with the greatest areal coverage by S3. The highest EDR values were predicted at 12 km in altitude for S2–S3, and 8 km in altitude for S4. The maximum EDR value was predicted by S4, suggesting that higher resolution in the vertical and horizontal is needed in order to simulate turbulence intensities similar to observations. On 12 July, all three

simulations predicted moderate turbulence at 8 km or higher, comparable to PIREPs. However, S2 and S4 predicted moderate turbulence at all three height levels, while S3 predicted moderate turbulence only at 8 km and 12 km.

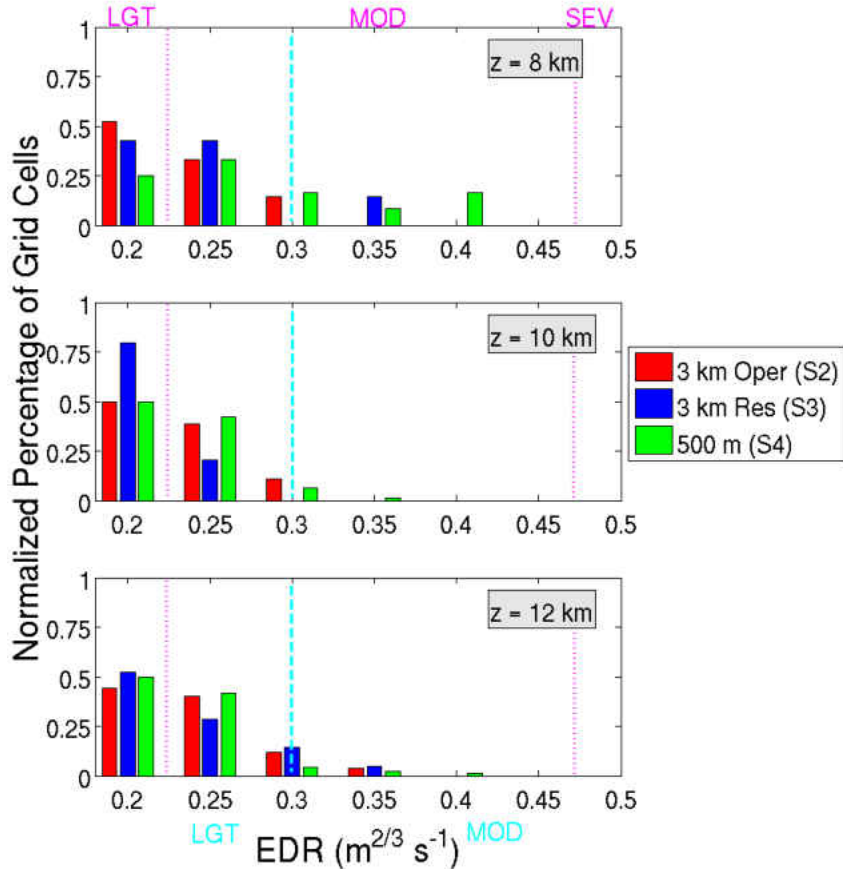


Figure 16: Out-of-cloud eddy dissipation rate distribution values $\geq 0.2 \text{ m}^{2/3} \text{ s}^{-1}$ within 50 mi (80.5 km) of convective cores with echo top heights $\geq 8 \text{ km}$ for S2-S4 on 12 July 2015. Dashed (cyan) and dotted (purple) vertical lines represent turbulence intensities based on Lane et al. (2012) and Sharman et al. (2014), respectively.

On 13 July, when convection is isolated and weaker in strength, neither S2 nor S3 predict moderate turbulence (Fig. 17). On this particular day, the highest vertical and horizontal resolution is necessary to predict turbulence magnitudes similar to observations. Last, some moderate values of EDR are evident above 8 km in all simulations of 15 July (Fig. 18). However, only S4 predicts moderate turbulence at all

height levels, where S2 predicts moderate turbulence only at 10 and 12 km in altitude, and S3 only predicts moderate turbulence at 12 km in altitude. For convection that is dynamically forced (i.e., synoptic-scale lifting mechanism such as a frontal boundary), as is the case on 15 July, all simulations do produce turbulence with the same magnitude as observations, but the occurrence is highly height dependent. The major differences between turbulence intensity and areal coverage between the various model setups are the higher areal coverages of lower-intensity values for S2 and S3 and the higher intensity EDR values predicted by S4. It is clear that higher horizontal and vertical resolution is necessary to accurately predict turbulence intensity.

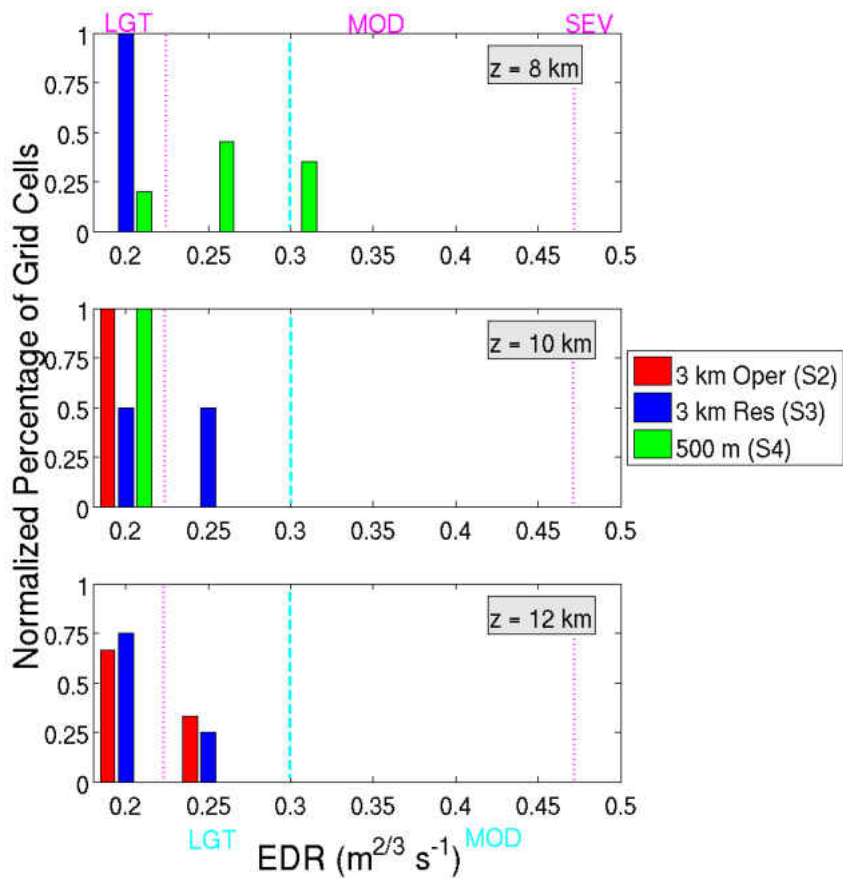


Figure 17: Out-of-cloud eddy dissipation rate distribution values $\geq 0.2 \text{ m}^{2/3} \text{ s}^{-1}$ within 50 mi (80.5 km) of convective cores with echo top heights $\geq 8 \text{ km}$ for S2-S4 on 13 July 2015. Dashed (cyan) and dotted (purple) vertical lines represent turbulence intensities based on Lane et al. (2012) and Sharman et al. (2014), respectively.

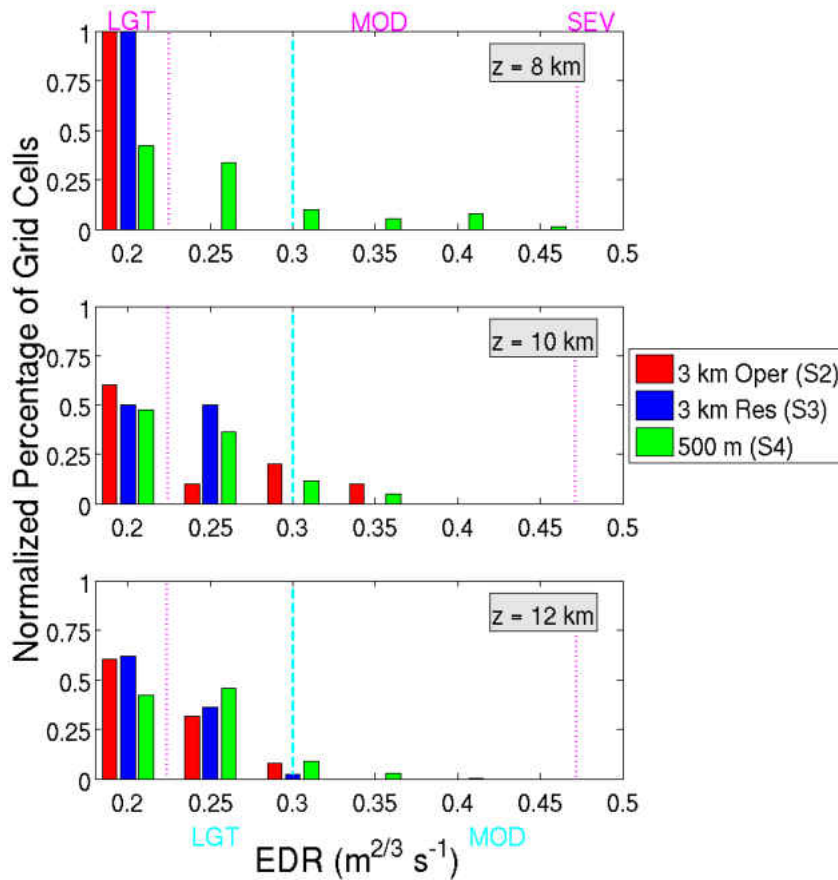


Figure 18: Out-of-cloud eddy dissipation rate distribution values $\geq 0.2 \text{ m}^{2/3} \text{ s}^{-1}$ within 50 mi (80.5 km) of convective cores with echo top heights ≥ 8 km for S2-S4 on 15 July 2015. Dashed (cyan) and dotted (purple) vertical lines represent turbulence intensities based on Lane et al. (2012) and Sharman et al. (2014), respectively.

3.3.4 10–17 July S2 and S3 comparisons

A further investigation examines the influence of vertical resolution alone on turbulence intensity using model setups 2 and 3 (64 and 100 vertical levels). These vertical grid spacings represent those used in common operational forecasting frameworks and more research oriented frameworks. Results will be analyzed at 8, 10, and 12 km in altitude (in cloud and out of cloud) for eight simulation days. Turbulent grid cells within convection (in cloud) are now included in the analysis. Seven of the eight

Table 5: Number of grid cells with echo top heights ≥ 8 km.

Simulation day	S2	S3
10 Jul 2015	392	260
11 Jul 2015	1199	785
12 Jul 2015	1343	1139
13 Jul 2015	399	367
14 Jul 2015	380	383
15 Jul 2015	1353	970
16 Jul 2015	1554	1215
17 Jul 2015	764	657

simulation days had convection for several hours in the model domain. The purpose of this analysis is to determine if there is a statistical bias in EDR values greater than $0.2 \text{ m}^{2/3} \text{ s}^{-1}$ when using two different vertical resolutions.

The number of grid cells for both S2 and S3 that have ETs ≥ 8 km are determined for each of the eight simulation days (Table 5). Interestingly, S2 predicts more grid cells with ETs ≥ 8 km in altitude than S3 for seven of the eight days. This finding is substantial because if ETs were used as the only turbulence proxy, then increased vertical resolution would not positively benefit the prediction of storm depth and intuitively turbulence. Furthermore, as was shown in Figs. 13–15, the maximum hourly ETs predicted by the two 3 km runs were comparable, but still far less than observations. However, a frequency analysis does show that S2 is predicting greater ETs slightly more often than S3, which intuitively influences the turbulence production and strength (Table 5). It would be hypothesized that the model setup with the highest storm heights would produce more turbulence at higher altitudes. Yet, as was discussed in the previous sections (Figs. 16–18), S2 never had the greatest EDR values at 8, 10, or 12 km.

The normalized distribution of EDR values from 10 to 17 July (0600–0600 UTC) for S2 and S3 at 8, 10, and 12 km are provided in Fig. 19 (comparisons of

raw area distributions show similar results, not shown). As was noted in the three individual simulation days, S3 has a greater percentage of grid cells (59%) with EDR values between 0.17 and 0.22 $\text{m}^{2/3} \text{ s}^{-1}$ than S2 for the 8-day period. S3 also has a larger percentage of grid cells with EDR values between 0.32 and 0.47 $\text{m}^{2/3} \text{ s}^{-1}$ (4%). However, S2 has a larger percentage of grid cells with EDR values between 0.22 and 0.32 $\text{m}^{2/3} \text{ s}^{-1}$ (35%). This again demonstrates that higher vertical resolution produces the extremes of the EDR distribution; more widespread light turbulence and more extreme values. However, statistical testing shows that these results are not statistically significant. The coarser vertical resolution (S2) distributes the majority of EDR values within the middle of the spectrum and hardly any in the maximum. If the prediction of turbulence is solely based on exceeding one EDR threshold value such as 0.2 $\text{m}^{2/3} \text{ s}^{-1}$, S2 would predict grid cells above this threshold more often than S3, but once again this difference is not statistically significant. However, from this evaluation, it was found that S3 does exceed the EDR threshold of 0.2 $\text{m}^{2/3} \text{ s}^{-1}$ more than S2 when convection was long lasting, extensive in areal coverage, and severe in strength. This finding indicates that convective type does influence turbulence prediction for various model setups.

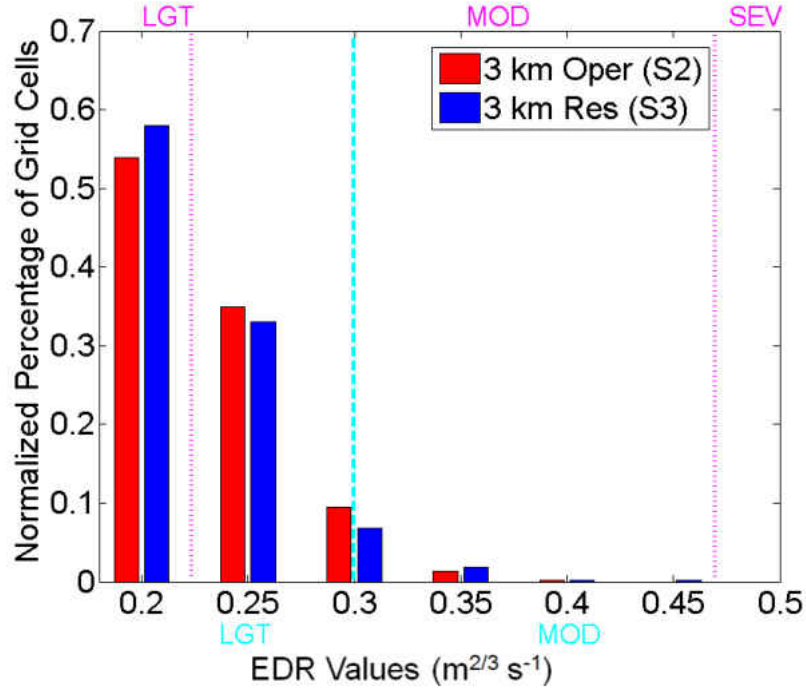


Figure 19: Distribution of eddy dissipation rate values $\geq 0.2 \text{ m}^{2/3} \text{ s}^{-1}$ within 50 mi (80.5 km) of convective cores with echo top heights ≥ 8 km for S2 and S3 across 8 simulation days, combining statistics at 8 km, 10 km, and 12 km in altitude. Dashed (cyan) and dotted (purple) vertical lines represent turbulence intensities based on Lane et al. (2012) and Sharman et al. (2014), respectively.

3.4 Discussion and Conclusions

CIT is currently treated as a nowcasting problem because turbulence encounters occur on scales much finer than model resolutions used for forecasting applications. Forecasts that predict the intensity of turbulence are generated in 15-min intervals by utilizing several convective and turbulence indices (Pearson and Sharman 2017); however, in-depth details about precise locations of turbulence on 10–1000-m scales are not available. Furthermore, forecasting operations continue to trend toward higher-resolution configurations in both the vertical and horizontal, but performance of these turbulence indices at these higher resolutions has not been examined. This study

evaluated turbulence prediction from commonly implemented model configurations (i.e., NAM, HRRR, and research) for numerous convectively active days in the North Dakota region. This study found that simulations with horizontal grid spacing of 12 km (S1) cannot be used for CIT prediction because this model setup frequently under predicts convective depth and intensity, unless convection is driven by large-scale forcing. Among the remaining model setups, the simulated convection was not significantly different. In general, convective type and intensity were forecast well. However, all model setups underpredicted maximum storm depth when compared with observations and S2–S3 more often underpredicted storm depth when compared with S4. These consistent errors in storm depth are likely important for forecasting turbulence.

Overall, turbulence forecasts were mixed. The finest model resolution (horizontal and vertical; S4) predicted the most intense turbulence values over small areas. The 3 km simulations (S2 and S3) with varying vertical resolution altered the distribution of lower EDR values that encompass larger areas. The height of maximum turbulence values and areal coverage were also influenced by model resolution. This suggests that the mechanisms that drive turbulence production and propagation are altered by model resolution. This study has demonstrated how turbulence intensity and areal coverage are very sensitive to model resolution, which means scale-aware thresholds are vitally needed.

The Ellrod index, a popular operational diagnostic for turbulence thresholds, was investigated, and while it is an adequate tool for large-scale turbulence prediction (e.g., jet stream turbulence, frontal passage turbulence), it cannot be used as a CIT diagnostic at operational and research model resolutions without coarsening the model input to resolutions used in the original formulation (i.e., 10–100 km). Application of TI2 to the latest operational model resolutions (i.e., 3 km) will produce unrealistic

results. The Ellrod index is very sensitive to model resolution and over predicts the intensity and areal coverage of turbulence. The Ellrod index used in conjunction with additional products may be effective, but should not be used as an individual diagnostic on resolution scales less than 10 km.

Results from this study show that moderate CIT can surpass the current FAA avoidance guideline of 20 mi (32.2 km) and can be present out to 50 mi (80.5 km) from active convection. These results are in agreement with recent studies by Lane et al. (2012), Lane and Sharman (2014), and Zovko-Rajak and Lane (2014). This finding emphasizes how additional research of CIT identification for various types of convection is needed. It also brings into question how efficient and useful strict lateral avoidance thresholds are for avoiding CIT when CIT is variable from storm to storm and spatially limited. For example, on 12 July 2015, above 8 km in altitude, moderate-to-severe turbulence within 20 and 50 mi of convection covered less than 1% of those areas. Is there a better approach to CIT avoidance when moderate-severe turbulence is extremely spatially limited? Although the areal coverage of the most intense EDR values was spatially limited, the greatest EDR values were found at 8 km for the highest-resolution simulations and 12 km for the coarser simulations, which are common altitudes used by commercial aviation. To improve turbulence forecasting tools and redesign avoidance procedures, more observations and research are needed.

CHAPTER 4

PREDICTING AVIATION HAZARDS: LOCATION OF OUT-OF-CLOUD TURBULENCE

4.1 Motivation

Convectively induced turbulence (CIT) is an atmospheric process that occurs at remarkable frequencies over the continental U.S. Sharman and Trier (2018) found that CIT occurs more than 40% of the time in the Great Plains and more than 60% of the time in Texas, Florida, the Gulf of Mexico, and the Atlantic during the summer months. The high frequency of CIT in the U.S. directly influences aviation operations because flights have an increased likelihood of encountering CIT, flights are rerouted around convection to avoid turbulence hazards, and delays at airports occur. More specifically, CIT decreases aviation efficiency and costs the industry 150–500 million a year in structural repairs, insurance premiums, and injury settlements (Kauffmann and Sousa-Poza 2001; Williams 2016).

To reduce the effects of convective hazards on the aviation industry the Federal Aviation Administration provides avoidance guidelines for all U.S. aviation operations in national and international airspace. These guidelines recommend that pilots remain 20 mi (32.2 km) from severe convection (Federal Aviation Administration 2017; FAA). However, this guideline is limited as CIT has been shown to occur more than 100 km (62 miles) away from convective sources (Barber et al. 2018; Lane and Sharman 2014; Zovko-Rajak and Lane 2014; Lane et al. 2012; Lane et al. 2003; Pantley and Lester 1990; USAF 1982). Another caveat with this recommendation is the dynamic nature

of CIT. CIT does not behave as an isotropic feature that extends uniformly from convection in all directions. The background environmental wind (i.e. wind shear) and stability of the atmosphere will influence the propagation direction of gravity waves generated from convection, the location of breaking gravity waves, the cascade of energy to turbulent scales (10-1000 m for aviation; Lester 1994), and regions of shear which lead to shear-induced turbulence (Lane and Sharman 2008; Lane et al. 2003). As breaking gravity waves are responsible for much of the out-of-cloud CIT (Sharman and Trier 2018) these waves are considered especially hazardous to aviation operations. Convectively induced gravity waves often have horizontal wavelengths on the order of 10 km to 10^2 km, occur on temporal scales of 10 to 10^2 minutes, and are generated by mechanical and diabatic forcings, which in realistic convective clouds are coupled through nonlinear momentum and heat fluxes (Chun 2008; Lane and Sharman 2008; Alexander et al. 2006; Lane et al. 2003; Song et al. 2003; Beres et al. 2002; Lane et al. 2001). While the formation of gravity waves during convective activity is common, the breakdown of gravity waves is most important for turbulence production (Pantley and Lester 1990; Reiter and Lester 1968).

Many studies have examined the influence of atmospheric stability, environmental wind shear, and convective stage on turbulence produced through breaking gravity waves. Lane and Sharman (2008) used numerical simulations of convection to investigate the relationships between background flow conditions and gravity wave breaking above convection. Lane and Sharman (2008) found that the instability in terms of areal coverage was maximized by optimal values of wind shear. In addition, it was found that the altitude of critical levels which induce breaking gravity waves are higher in low sheared environments, thereby influencing turbulence location, and making it more prevalent in the downshear region above cloud. Wimmers et al. (2018) used satellite observations to examine gravity waves in relation to turbulence.

Their study found for two cases of severe CIT, gravity waves did not propagate in the direction of the background flow but, instead propagated orthogonally to the background flow, due to the highly sheared environment of the convective outflow. Beres et al. (2002) and Alexander et al. (2006) showed how the phase speed spectrum of convectively induced gravity waves can be modified by the vertical structure of the horizontal wind above convection and can cause gravity waves to refract. The results from Beres et al. (2002) demonstrated the asymmetric nature of gravity waves propagation due to tropospheric winds and agreed with previous studies including Fovell et al. (1992), Alexander et al. (1995), Alexander and Holton (1997), Piani et al. (2000), and Lane et al. (2001).

Numerous methodologies are in operation to assist pilots in turbulence avoidance. These methods include: nowcasting applications that identify convection and convective hazards along flight paths (Kessinger 2017; Kessinger et al. 2008; Herzegh 2002); in situ turbulence measurements, subjective pilot reports; and forecast models that diagnose turbulence from meteorological fields such as frontogenesis, vorticity, shearing and stretching deformation, perturbations in velocity fields (Ahmad and Proctor 2012; Ellrod and Knox 2010; Frehlich and Sharman 2004a,b; Marroquin 1998; Ellrod and Knapp 1992; Dutton 1980; Buldovskii et al. 1976; Brown 1973; Colson and Panofsky 1965). These methods are beneficial to the aviation community, but no method currently resolves the turbulent scales of motions themselves, as all methods are approximations for turbulence. To implement better forecasting tools for turbulence prediction many studies have been using numerical models to further understand the physical attributes of CIT and the role of gravity waves. But, the nonlinear characteristics of gravity waves, the complex interaction of atmospheric stability and wind shear, and the accuracy of convective forecasting itself (location, timing, morphology, and strength) continues to hinder the forecasting capabilities

of convectively induced gravity waves and turbulence. Improved computer resources have become more accessible to the forecasting community, leading to more efficient modeling systems that are capable of resolving physical processes on small temporal and spatial scales. As the trend in increased horizontal and vertical resolution continues, resolving and therefore forecasting CIT will be possible. However, resolution has been found to impact the total power of gravity waves and the vertical propagation of gravity waves (Lane and Knievel 2005), gravity wave characteristics (Doyle et al. 2011), and the location of most intense turbulence (Lane and Sharman 2014). Barber et al. (2018) found that resolution influenced the simulated storm height, as well as the accuracy of popular turbulence diagnostics including the Ellrod index and eddy dissipation rate. The examination of turbulence distribution found enhanced vertical resolution is crucial to accurately predict the magnitude of turbulence intensity.

The goals of this study are to investigate the impact of model resolution on convective parameters such as depth and intensity, environmental variables such as static stability and vertical wind shear in the vicinity of convection, and ultimately how out-of-cloud turbulence location varies due to these differences. This study will determine if the frequency of high sheared and unstable out-of-cloud environments occur with different frequency in higher resolution models, and determine the influence of these variables on turbulence production. Richardson number and vertical velocities are used as proxies for gravity wave production and propagation/breaking when the characteristics of convectively induced gravity waves cannot be resolved due to coarse model and temporal resolution.

4.2 Data and Methods

4.2.1 Model setup

In this study, 30-hour convective forecasts in the northern Great Plains are made using the Advanced Research WRF Model, version 3.7 (Skamarock and Klemp 2008) to examine convectively induced turbulence. All simulations were initialized at 0000 UTC with ERA-Interim (<http://www.ecmwf.int/en/research/climate-reanalysis/era-interim>) global reanalysis data and run using Extreme Science and Engineering Discovery Environment (XSEDE) resources (Towns et al. 2014). Analysis times used in this study are the 7th-30th forecast hours from each simulation day (12, 13, and 15 July 2015). Barber et al. (2018) investigated the influence of grid spacing with four modeling setups and found that 12 km horizontal grid spacing (similar to the NAM and RAP models) was inadequate to replicate convective activity and turbulence in this region. Therefore, this study will examine the results from the three higher resolution modeling setups (S2, S3 and S4) used in Barber et al. (2018; Table 2 in chapter 3). Setup 2 (S2) is similar to the operational High-Resolution Rapid Refresh (HRRR) model and has 3 km horizontal grid spacing and 65 vertical levels. Setup 3 (S3) also has 3 km horizontal grid spacing and is comparable to the HRRR, but a finer vertical grid spacing (100 vertical levels) is implemented. Lastly, setup 4 (S4) is considered high-resolution with 500 m horizontal grid spacing and 100 vertical levels. Parameterizations for all of the simulations are provided in Table 3 in chapter 3. The model top for all simulations is set to 10 hPa (approximately 30 km) with a 10 km deep damping layer at the model top. The model domains for S2–S3 remain unaltered and encompass the same geographical area for the entire 90-h of simulations (see Fig. 1). Due to limits of computational costs, the simulation period of S4 only includes 12 July, 13 July, and 15 July 2015 and does not cover the same geographical area as

S2 and S3 (see Fig. 2). Additional 10-minute output from 1800 UTC to 0600 UTC is used for comparison on 12 July.

4.2.2 Eddy dissipation rate

Turbulence intensity (TI) is estimated by computing EDR from turbulent kinetic energy (TKE) of each simulation as discussed in the Appendix. Atmospheric turbulence is commonly defined as light, moderate, and severe based on the cubed root of EDR ($\text{m}^{2/3} \text{s}^{-1}$; Tables 4 and 21; Lane et al. 2012). This study will use thresholds corresponding to Sharman and Pearson 2017 based on climatological PIREPs and various sources including the Global Turbulence Guidance (GTG-2) product (Table 21). Echo tops are used to determine if a turbulent grid cell is out of cloud or in cloud. Echo top height is calculated from the simulated radar reflectivity using a threshold of 18-dBZ. A turbulent grid cell is considered out of cloud if the echo top height at the same grid point location is less than the analysis height. A turbulent grid cell is considered to be in cloud if the echo top height at the same grid point location is greater or equal to analysis height.

4.2.3 Bulk analysis of turbulence location

To determine the location of turbulence relative to convection, convective objects (CO) are defined as consecutive regions where echo tops (18-dBZ threshold) are greater or equal to 8 km. A threshold of 8 km is adequate because deep convection generally exceeds 8 km in altitude during the summer months in the midlatitudes. The centroid location of each CO is determined and distance from the grid point location of turbulence to the CO centroid location is calculated. After each turbulent grid cell is associated with the CO closest to its location, the direction turbulence occurs relative to the CO centroid location is determined by subtracting the vector

location of turbulence from the vector location of the CO. Directions are divided into compass definitions of north, east, south, and west (Fig. 20). The environment around convection is analyzed within 20 miles (~ 32.2 km) of the convective object's boundaries. It is important to note that this method does not address the source of CIT, but only the relationship between out-of-cloud turbulent grid points and the location of convection. When convection is near the boundaries of the simulation domain, if a radius of 20 miles cannot be computed in all four directions, the time period is not utilized to ensure that a direction is not preferred simply because it has more areal coverage.

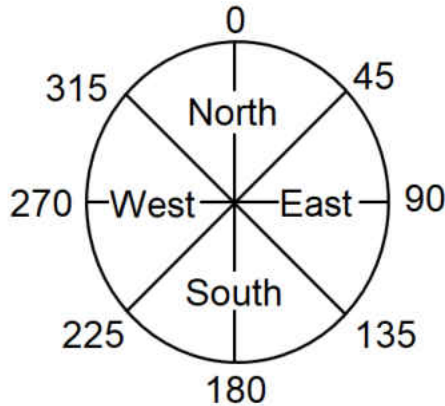


Figure 20: Compass degree definition of direction from convection.

4.2.4 Calculation of environmental variables

The environmental variables vertical wind shear (S_v^2), static stability (N^2), Richardson number (Ri), and simulated vertical velocity (w) are calculated for regions 20 miles (32.2 km) around convective boundaries. Vertical wind shear produces turbulence through Kelvin Helmholtz instabilities and a variation in static stability produces turbulence through convective instabilities. Richardson number is the ratio between static stability and the vertical shear. The gradient Richardson number is

expressed as,

$$Ri = \frac{N^2}{S_v^2}, \quad (4.1)$$

where S_v^2 is the vertical wind shear defined as,

$$S_v^2 = \left(\left| \frac{\partial u}{\partial z} \right|^2 + \left| \frac{\partial v}{\partial z} \right|^2 \right), \quad (4.2)$$

and N^2 is defined in the section 2.1, equation 2.1.

In Eq. 4.2, u and v are the horizontal components of velocity (m s^{-1}), and z is height (m). Ri values less than 0.25 are indicative of gravity wave breakdown and turbulence. Ri values have been found to be low near outflow regions and regions where deep convection penetrates the tropopause.

4.3 Results

4.3.1 Comparison of convective properties

The distributions (normalized by total count for the entirety of the model simulation) of simulated convective properties such as echo top height, 2-km radar reflectivity values, and column-maximum radar reflectivity values are provided in Figures 21-22. For the case days where convection was forced through large-scale synoptic dynamics (12 and 15 July), the percentage of simulated echo tops exceeding 8 km is higher for S4 than either S2 or S3. The distributions of echo tops for S2 and S3 are nearly equal and not influenced by the variation in vertical resolution. The variability in the amount of echo tops exceeding 8 km likely influences the turbulence production through the generation of gravity waves if those waves begin to break. The tropopause heights for the three days were 9.5 km, 11.1 km, and 12.3 km. S4 had more than 10% of echo tops surpassing the tropopause. The distributions of simulated 2-km

radar reflectivity values are very similar between S2, S3, and S4 (Fig. 5). The subtle differences (less than 0.5%) are in the weaker reflectivity bins (20-30 dBZ), where S4 has a slightly higher percentage. S4 again has a larger percentage of greater reflectivity values, implying stronger convection on two of the three case days. These findings are consistent in the column-maximum simulated reflectivity field.

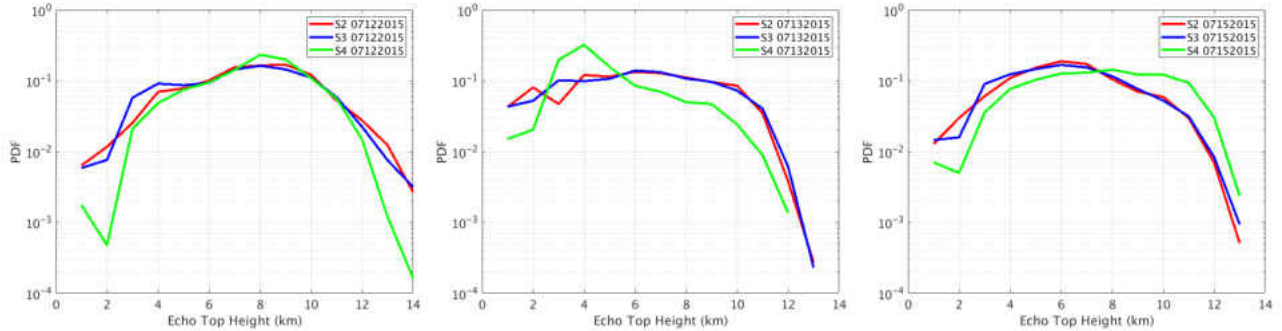


Figure 21: Distributions of simulated echo tops (km) for S2 (red), S3 (blue), and S4 (green) on 12, 13, and 15 July.

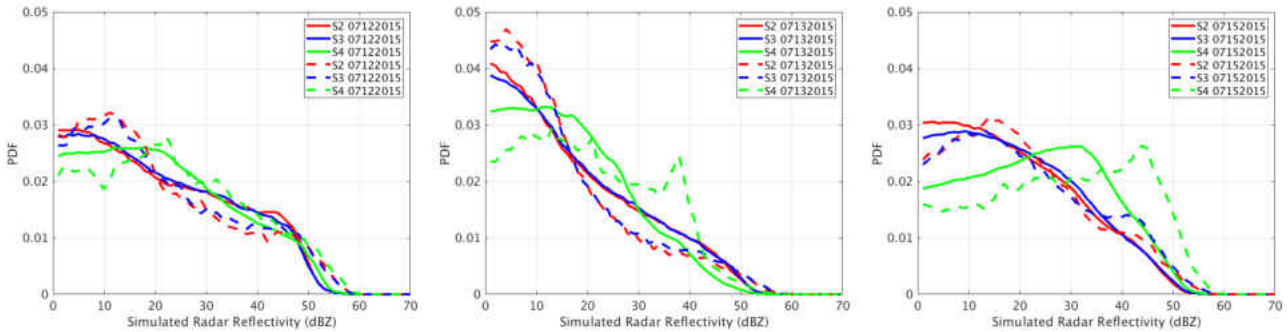


Figure 22: Domain-wide distributions of simulated radar reflectivity (solid lines) and column-maximum simulated radar reflectivity (dashed lines) for S2 (red), S3 (blue), and S4 (green) on 12, 13, and 15 July.

Distributions of in-cloud and out-of-cloud vertical velocity between 8 km and 12 km (Fig. 23) and domain-wide accumulated precipitation (Fig. 24) are examined. Vertical velocity is a good proxy for convective strength and accumulated precipitation can be used as a proxy for latent heating and therefore gravity wave amplitude

(Stephan and Alexander 2015; Stephan and Alexander 2014). The distribution of out-of-cloud vertical velocities for the three model setups is the greatest between -3 m s^{-1} and 2 m s^{-1} (greater than 45%). At the extremes of the distributions (greater than 10 m s^{-1}) the model setups are within 0.005% of one another, but S4 is slightly greater than S2 and S3. There is larger variability in the distribution of in-cloud vertical velocities between the model setups. The largest differences between S2, S3, and S4 vertical velocities are on the stronger convective days (12 and 15 July). These variations are also apparent in the accumulated precipitation distributions, suggesting that gravity wave amplitude is greater for S4.

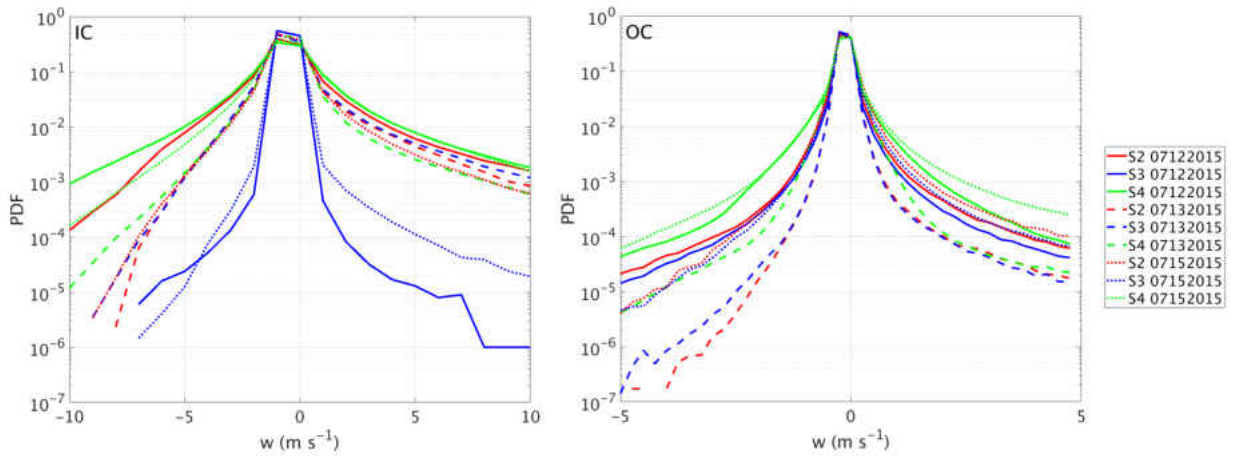


Figure 23: Distribution of in-cloud (IC) and out-of-cloud (OC) vertical velocities (m s^{-1}) for S2 (red), S3 (blue), and S4 (green) on 12 (solid), 13 (dashed), and 15 (dotted) July between 8 km and 12 km.

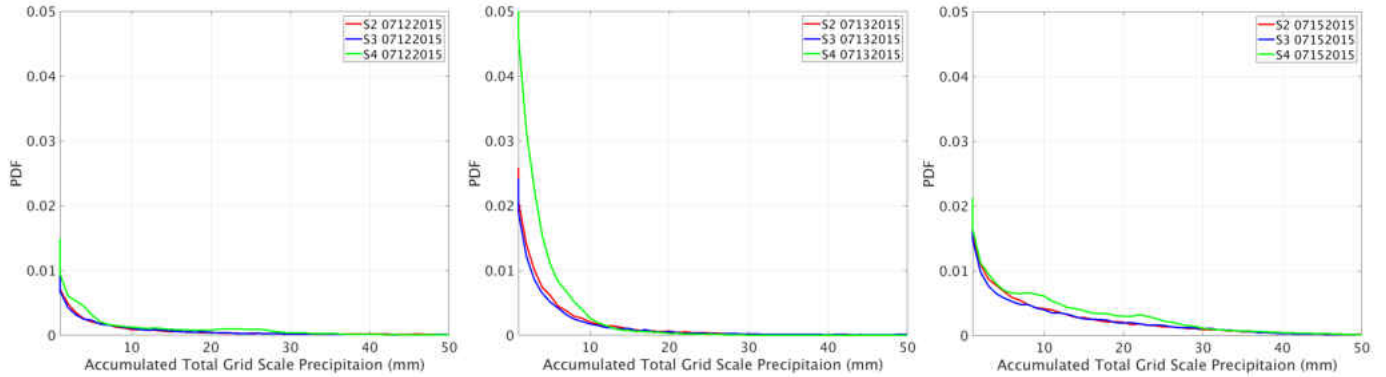


Figure 24: Distribution of accumulated precipitation (mm) for S2 (red), S3 (blue), and S4 (green) on 12, 13, and 15 July.

The variation in the convective properties will influence convectively induced turbulence production in this study mainly through the production of gravity waves as storm tops surpass the tropopause and break, and energy cascades to turbulent scales. Storms simulated by S4 to exceed the tropopause 5-10% more often than S2 and S3. Other attributes of simulated convection, specifically, outflows (regions of enhanced vertical wind shear) are hypothesized to be dynamically similar between the model setups.

4.3.2 Directional preference of turbulence (S4)

Out-of-cloud convectively induced turbulence between 8 km and 12 km in altitude is analyzed on 13 July (0000-0600 UTC from the forecast initialized at 0000 UTC on 12 July and referred to as 12 July in text), 13 July (1700-0100 UTC), and 15 July 2015 (2100-0600 UTC) for S4 and is categorized as light (LGT) or moderate or greater (MOG). The altitude range of 8 km to 12 km is applicable for cruising altitudes of commercial aviation. A complete summary of the convection observed and simulated on these dates can be found in Barber et al. (2018).

Briefly, severe convection occurred in the eastern portion of North Dakota and western Minnesota on 12 July producing hail, severe winds, and tornadoes. Individual cells initiated near 2000 UTC and intensified into two large convective complexes with echo tops exceeding 15 km in height and radar reflectivity values exceeding 55 dBZ. S4 simulated both the observed convective morphology and also the observed timing and location. However, the intensity and depth of the simulated convection was underpredicted when radar reflectivity values and echo top heights are compared to observations. S4 generated 337 convective objects between 0000 UTC and 0400 UTC. There were 26529 out-of-cloud turbulent grid points within 20 miles of convection between 8 km and 12 km from 0000 UTC to 0400 UTC. Of the turbulent grid points, 78% were categorized as LGT and 22% MOG. Figure 25 provides the directional distribution of out-of-cloud CIT between cruising altitudes. The majority of turbulence is located north of convection (33% of turbulent cells) for all intensity thresholds. The remaining 67% of turbulent grid points are distributed between the south (20%), east (24%), and west (23%) directions. These results suggest that aviation operations navigating around this convective system at cruising altitude would have had the highest probability of experiencing turbulence when flying to the north of the convective complex. While MOG turbulence only accounted for 22% of the total turbulent grid points, the greatest likelihood of experiencing MOG turbulence occurred to the west of convection (32%). Applying these results to aviation operations, the lowest probability of experiencing MOG turbulence is to the south and east of convection.

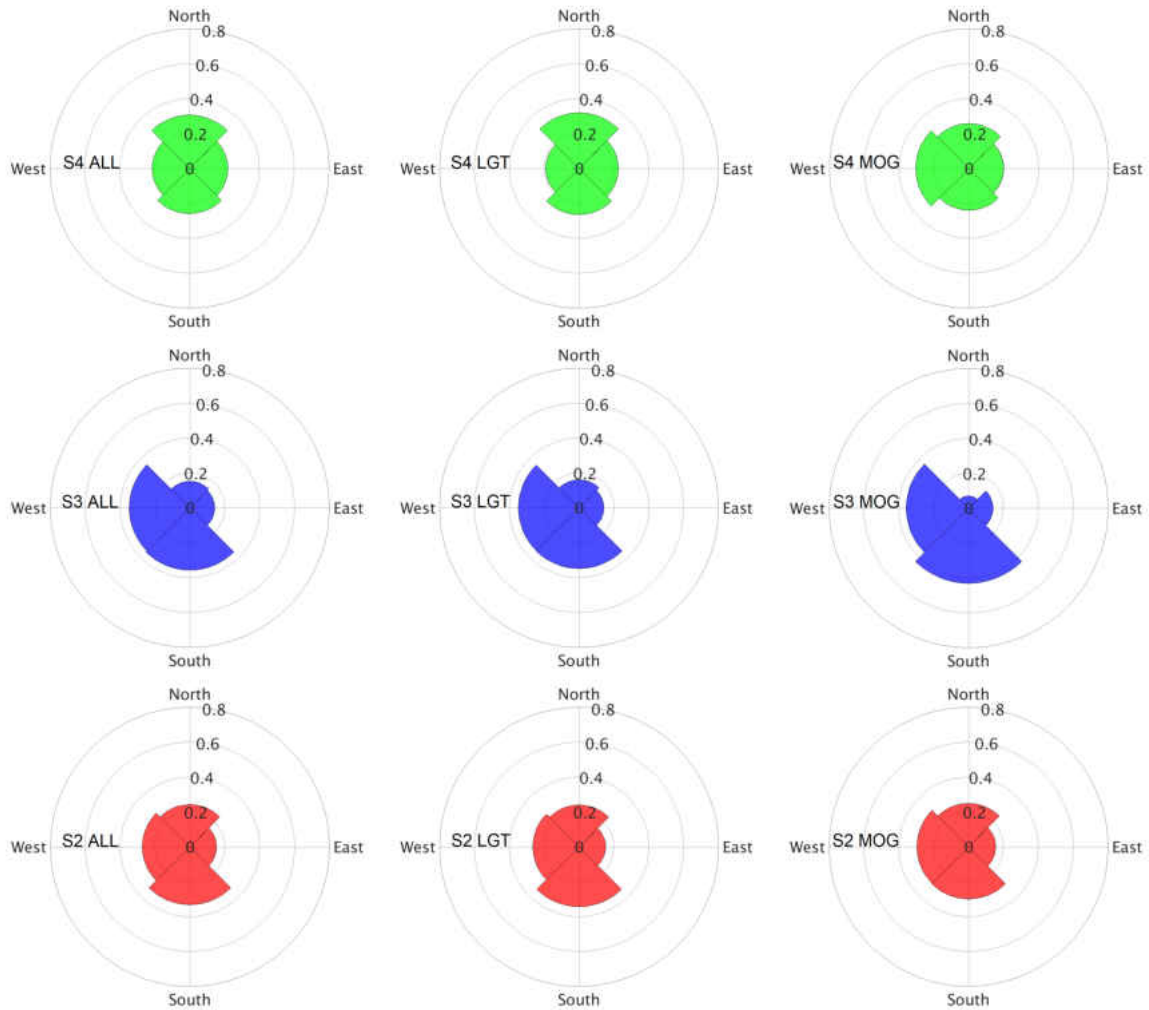


Figure 25: Directional preference of out-of-cloud turbulence between 8 km and 12 km (all, light, and moderate or greater) in normalized percentage for S4 (top), S3 (middle), and S2 (bottom) on 12 July when convection is present (within 20 miles of convection).

Convection on 13 July initiated around 1800 UTC from weak frontal boundaries occurring in the northern ND. This convection was non-severe, isolated in nature, and dissipated near 0100 UTC. Radar reflectivity values exceeded 50 dBZ and echo tops reached 14 km in altitude. S4 generated 253 convective objects between 1900 UTC and 0100 UTC. One hundred and sixty two turbulent grid points within 20 miles of convection between 8 km and 12 km were produced, of which 68% were LGT and

32% were MOG. The significant decrease of turbulent grid points present on 13 July is due to the weakly forced, isolated nature of the particular convection. The directional distribution is provided in Figure 26 and shows that the highest probability of LGT and MOG turbulence is to the east of convection (48% and 45%). There is larger variability in the directional distribution of turbulence identified as LGT than on 12 July. The overall likelihood of experiencing turbulence on 13 July was significantly lower than 12 July and these results suggest that west of convection has the lowest likelihood of experiencing turbulence of any intensity.

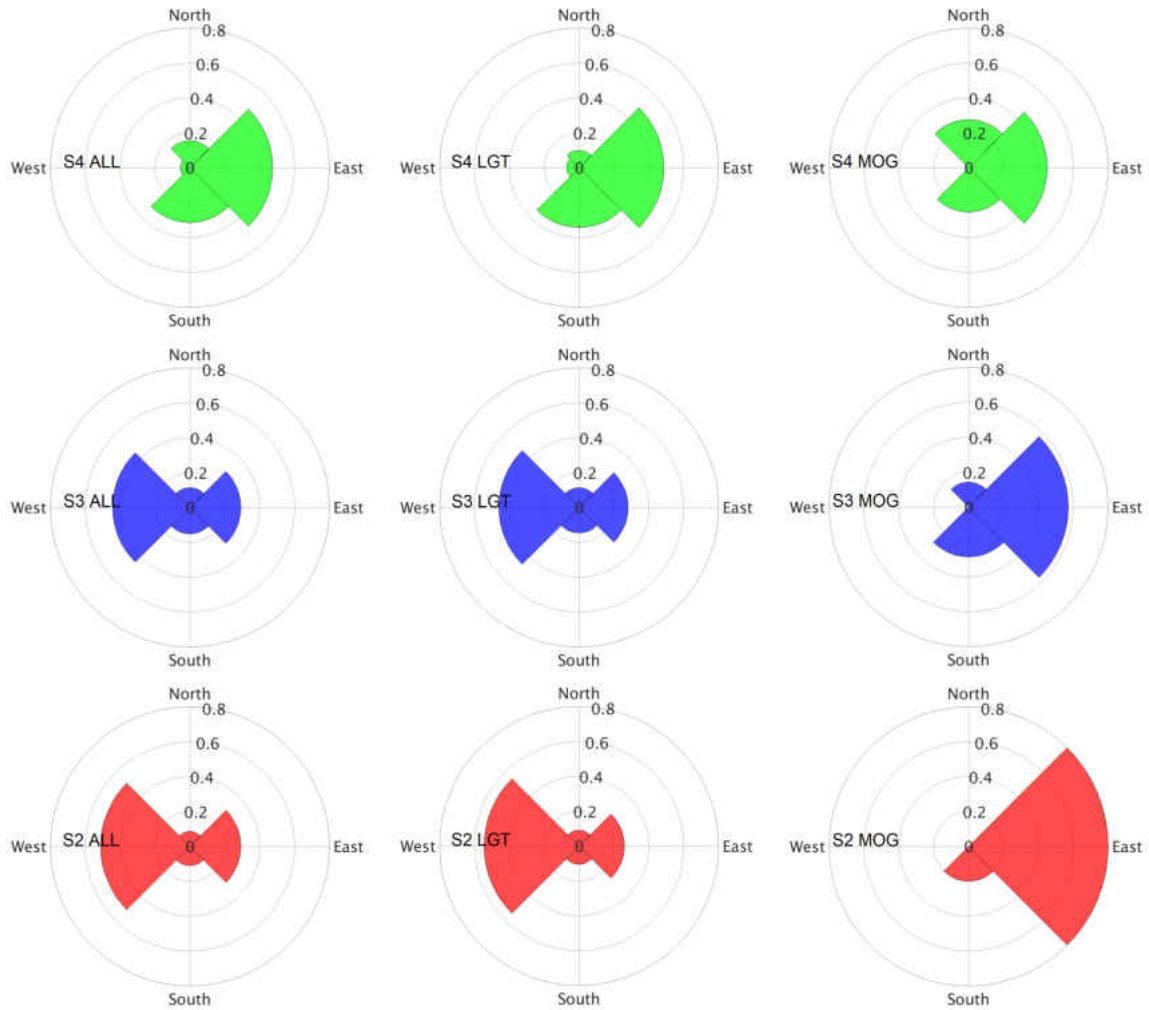


Figure 26: Directional preference of out-of-cloud turbulence between 8 km and 12 km (all, light, and moderate or greater) in normalized percentage for S4 (top), S3 (middle), and S2 (bottom) on 13 July when convection is present (within 20 miles of convection).

Convection on 15 July was severe, producing hail and severe wind reports. Convection initiated in western ND before 1600 UTC and organized into a convective complex with a bowing feature in central ND that persisted through 0200 UTC. S4 generated 224 convective objects between 2100 UTC and 0600 UTC. S4 produced 3879 turbulent grid points. Of the turbulent grid points, 81% were LGT and 19% were MOG. For this case day, within 20 miles of convection the highest probability of

encountering turbulence is to the north (Fig. 27). The lowest likelihood of encountering turbulence is to the south of convection (17%). When turbulence is subset by intensity, the north has a higher likelihood of MOG turbulence.

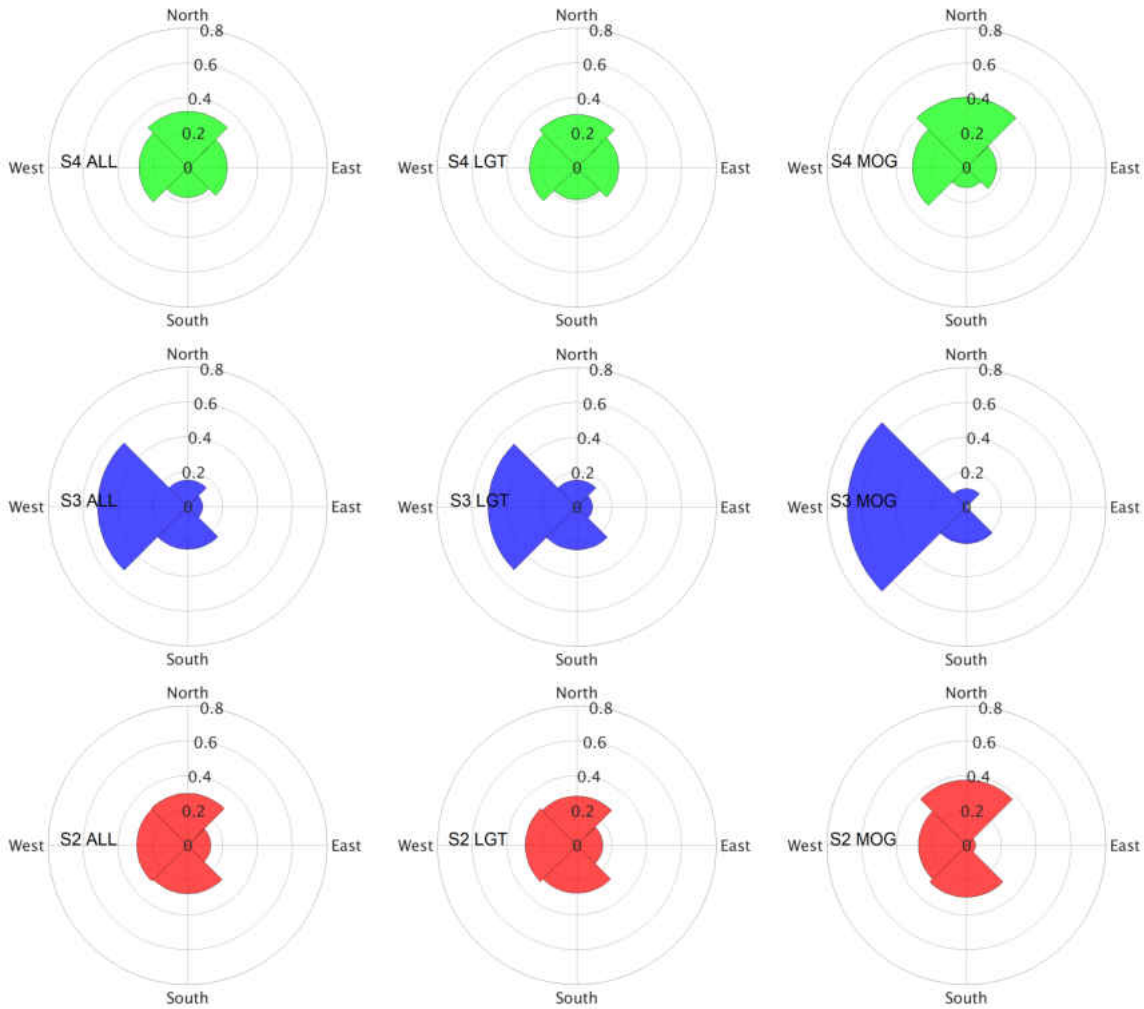


Figure 27: Directional preference of out-of-cloud turbulence between 8 km and 12 km (all, light, and moderate or greater) in normalized percentage for S4 (top), S3 (middle), and S2 (bottom) on 15 July when convection is present (within 20 miles of convection).

Variability in the location of turbulence for the three case days is apparent. On 12 July, two organized intense convective complexes produced a significant number of turbulent grid points, the majority located to the north of convection. The isolated,

weakly forced convection on 13 July produced few turbulent grid cells, most of which had an eastern preference. Lastly, the convection on 15 July, a strong squall-line with a bowing echo, produced a significant amount of turbulence, which was primarily to the north of convection. It is hypothesized that varying convective morphology and intensity for the three case days influences the amount and intensity of turbulence found in the simulation domain. The location of out-of-cloud turbulence is likely influenced by the environmental conditions present around convection (i.e. the vertical wind shear and static stability) and will be discussed below in section 4.3.4.

4.3.3 Influence of model resolution on the directional distribution of turbulence

In this section the directional preference of turbulence of model setups S2 and S3 will be compared against S4. The domain size differences between the model setups influence the duration that convection is present in the domain. However, the type, intensity, and timing of convection present in all three setup domains is similar for all three setups on each case day. Recall that S2 and S3 have the same horizontal resolution (3-km), and S3 has a higher vertical resolution than S2 (S3 vertical resolution matches S4, 100 vertical levels).

The raw count of turbulent grid points for the three days within 20 miles of convection is 5985 for S2 and 15770 for S3. The significant increase in count for S3 is due to the increase in vertical layers. The total number of grid points for the three days for S2 and S3 is far lower than for S4 (30570 total for the three days), but when normalized against the size of each grid cell, the areal coverage is similar. Figures 25-27 demonstrate the directional variation of turbulence for the three model setups for the case days. The direction distributions of turbulence in S2 and S3 on 12 July are in disagreement with S4 (southern preference versus northern preference). Interestingly,

the distribution of turbulence is heavily skewed in two directions (south and west) for S3, while turbulence is more evenly distributed in all directions for S2 and S4. The percentage of MOG grid points varies significantly between S2 (26%), S3 (10%), and S4 (22%). The location of the largest percentage of MOG turbulence is to the south for S2 and S3 in contrast to the west for S4. These results suggest that turbulence prediction on 12 July would have varied significantly based on model resolution. The coarser resolution model setups (S2 and S3) indicate turbulence likelihood is less to the east of convection, while the finer resolution model setup indicates less likelihood of turbulence to the south of convection.

The turbulence distribution on 13 July again varies between the three model setups, however the coarser model setups (S2 and S3) are in agreement with one another (western preference), while the greatest turbulence likelihood was to the east of convection for S4 (Fig. 26). Although the direction of all turbulence is in contrast between the model setups, the majority of MOG turbulence was located to the east of convection for all simulations. Weak convection, as simulated on 13 July, reduced the influence of model resolution, especially on the location of MOG turbulence.

On 15 July, S4 and S2 distribute turbulence nearly evenly in three directions while in S3 the majority of turbulence is in one direction (Fig. 27). Turbulence is preferred to the west of convection for S3 in comparison to the north for S2 and S4. S2 and S4 also agree in the preferred direction of MOG turbulence. S3 again distributes MOG turbulence to one preferred direction (west) and S2 and S4 distribute turbulence to three directions and the largest percentage is to the north of convection. Model resolution is influencing the direction of turbulence for all cases of convection. The coarser model setups are not in agreement with one another with the direction of greatest turbulence probability. There is disagreement in the location of greatest turbulence likelihood between the finest and coarser model setups, but interestingly,

S4 distributes turbulence in a manner more in comparison to S2 for the stronger convective cases.

4.3.4 Influence of model resolution on environmental conditions

Out-of-cloud static stability (N^2), vertical wind shear (S_v^2), and Richardson number (Ri) are used as indicators of turbulence potential, while vertical velocity (w) is used as a proxy for gravity wave potential. Richardson number is an indicator of breaking gravity waves and values less than 0.25 suggest turbulence at the location. These parameters are examined in direction subsets of north, east, south, and west within 20 miles (32 km) of convective objects between 8 km and 12 km for all three model setups and related to the turbulence frequency. An examination of static stability between 8 km and 12 km (in-cloud and out-of-cloud) for the three case days within the entire model domain (Fig. 28) has little variability between the model setups for the stronger convective days (12 and 15 July). The similarities in the distributions of static stability indicates that model resolution is not impacting static stability, and therefore turbulence production by instability processes should be occurring at similar frequencies between the model setups. In comparison, the distribution of vertical wind shear between 8 km and 12 km varies significantly between the model setups for the three case days (Fig. 29). Interestingly, S4 has the lowest probability of large vertical wind shear and is more than an order of magnitude smaller than S3 for all case days. The implications of the lower vertical wind shear values between 8 km and 12 km for S4 likely influences turbulence production through Kelvin-Helmholtz instability processes. The following section will compare the environmental variables subset by direction from convection for the three modeling setups. A brief review of the convective setup and directional preference of turbulence will be provided.

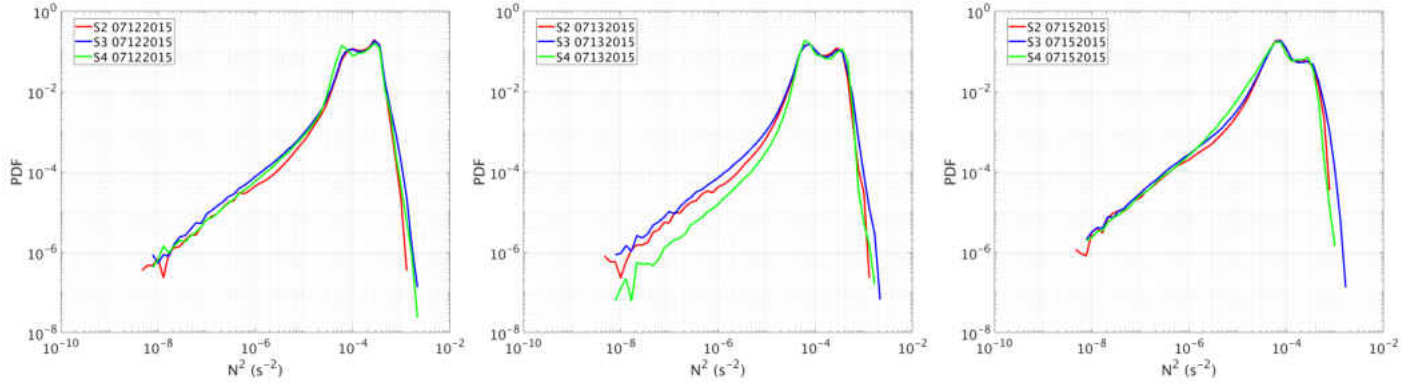


Figure 28: Domain-wide distribution of static stability between 8 km and 12 km for S2 (red), S3 (blue), and S4 (green) on 12, 13, and 15 July.

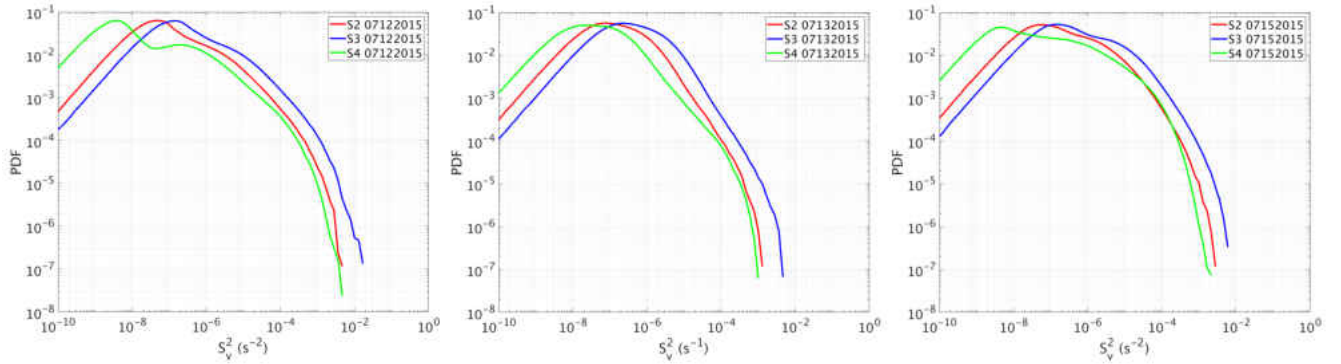


Figure 29: Domain-wide distribution of vertical wind shear between 8 km and 12 km for S2 (red), S3 (blue), and S4 (green) on 12, 13, and 15 July.

Static stability

Convection on 12 July was two large convective complexes that persisted for more than four hours in all three model domains. The greatest probability of turbulence was to the north of convection for S4 and to the south of convection for S2 and S3. Out-of-cloud static stability distributions and statistics on 12 July are provided in Fig. 30 and Table 6. The lowest mean static stabilities between 8 km and 12 km are associated with S4. The lowest mean static stabilities for S4 are to the north and east of convection. These directions are associated with the greatest probability of turbulence in this height range for S4. The mean static stabilities of S2 and S3

are very similar to one another but the lowest mean static stability is to the west of convection, not the preferred direction of turbulence for both setups. The variation in static stability between the direction subsets for S2 and S3 is smaller than the variation of S4, indicating that vertical resolution does not influence the static stability.

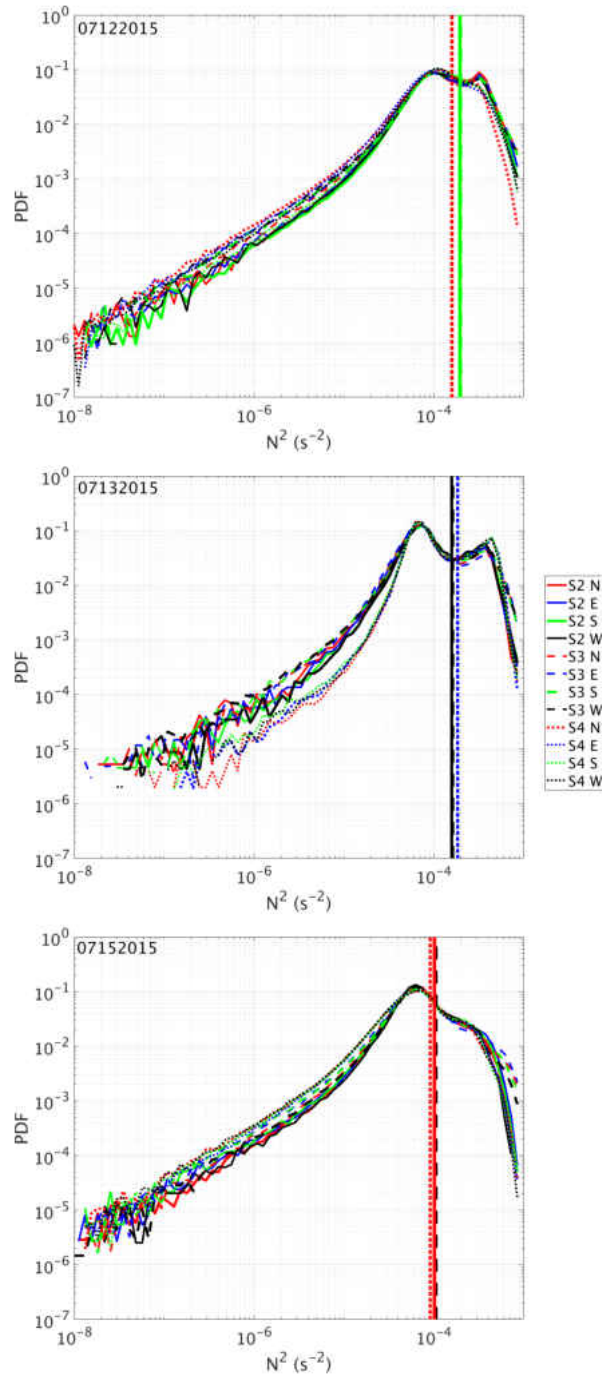


Figure 30: Distribution of out-of-cloud static stability between 8 km and 12 km within 20 miles of convection on 12, 13, and 15 July subset by direction from convection for S2 (solid lines), S3 (dashed lines), and S4 (dotted lines). The vertical lines represents the mean static stability in the direction of greatest turbulence probability.

Table 6: Mean out-of-cloud static stability (s^{-2}) between 8 km and 12 km within 20 miles of convection. Bold represents the direction the highest percentage of turbulence is located.

Case day	Model setup	North	East	South	West
12 July	S2	1.98×10^{-4}	1.92×10^{-4}	1.95×10^{-4}	1.87×10^{-4}
	S3	2.00×10^{-4}	1.98×10^{-4}	1.99×10^{-4}	1.89×10^{-4}
	S4	1.59×10^{-4}	1.59×10^{-4}	1.75×10^{-4}	1.65×10^{-4}
13 July	S2	1.47×10^{-4}	1.46×10^{-4}	1.57×10^{-4}	1.58×10^{-4}
	S3	1.53×10^{-4}	1.50×10^{-4}	1.61×10^{-4}	1.62×10^{-4}
	S4	1.84×10^{-4}	1.84×10^{-4}	1.83×10^{-4}	1.83×10^{-4}
15 July	S2	1.01×10^{-4}	1.05×10^{-4}	1.03×10^{-4}	1.01×10^{-4}
	S3	1.09×10^{-4}	1.11×10^{-4}	1.09×10^{-4}	1.06×10^{-4}
	S4	9.11×10^{-5}	9.34×10^{-5}	9.36×10^{-5}	9.15×10^{-5}

Convection on 13 July was isolated and weak, with very little turbulence diagnosed. The greatest probability of turbulence was found to the east of convection for S4 and to the west of convection for S2 and S3. The mean static stability for S2 and S3 is lower on 13 July than 12 July and greater on 13 July for S4 (Fig. 30 and Table 6). The variability of static stability between the directions is also much less for S4 than on 12 July even though variability in turbulence direction was found, suggesting that static stability variations were not responsible for the preferred turbulence direction. While S2 and S3 had larger directional variations of static stability, the lowest stabilities were not related to the preferred turbulence direction.

Convection on 15 July was intense and persisted for more than eight hours. The greatest probability of turbulence was found to the north of convection for S4 and S2 and to the west of convection for S3. The lowest static stabilities were found north of convection for S4 and S2 and west of convection for S3, the same directions of greatest turbulence probability (Figs. 30 and Table 6). The mean static stabilities for all three modeling setups were lower than the previous two case days, likely influencing the convective type. The variability in stability between the model setups is the least

when compared to the previous convective days, suggesting that model resolution did not influence the stability near convection on 15 July.

Vertical wind shear

Out-of-cloud vertical wind shear distributions on 12 July significantly vary between the model setups (Fig. 31 and Table 7). As was found with the domain-wide distribution of vertical wind shear, S4 has a lower probability of greater wind shear in all directions when compared to S2 and S3. For this environmental variable, the direction with the greatest probability of increased shear values is associated with the preferred direction of turbulence (east). However, this relationship between probability of larger shear values and direction is not consistent for S2 and S3. The greater variation in vertical wind shear between direction and model setup indicates that horizontal and vertical resolution are influencing vertical wind shear near convection, likely as the production of convective outflows.

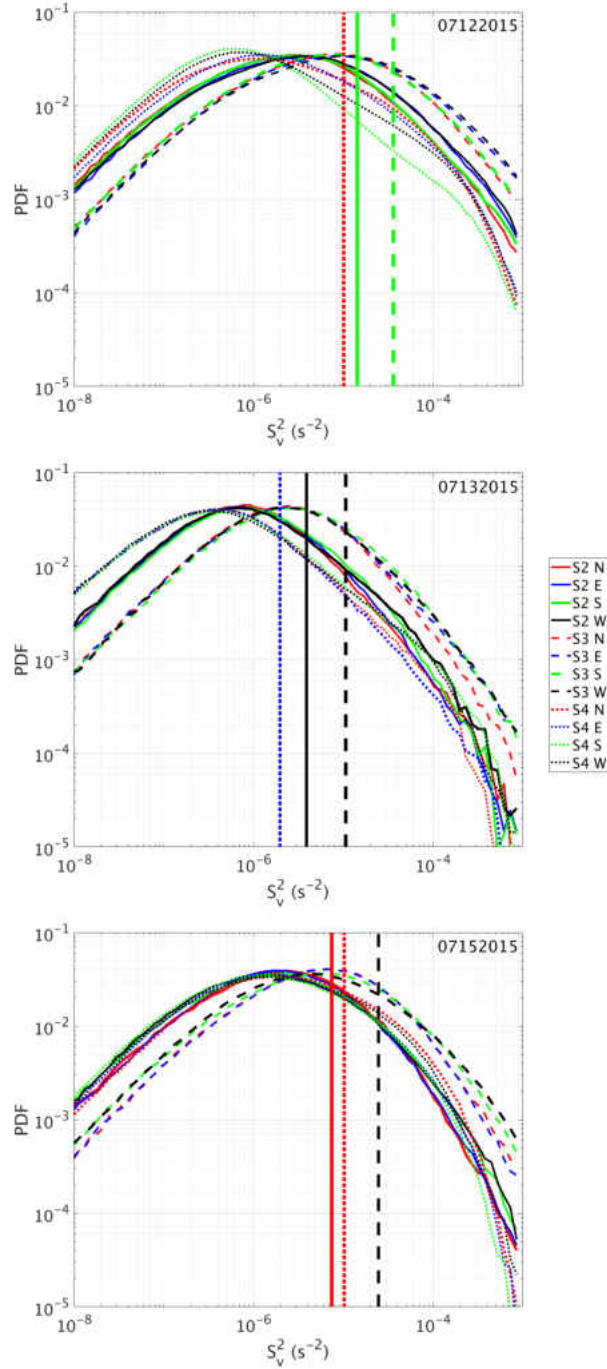


Figure 31: Distribution of out-of-cloud vertical wind shear between 8 km and 12 km within 20 miles of convection on 12, 13, and 15 July subset by direction from convection for S2 (solid lines), S3 (dashed lines), and S4 (dotted lines). The vertical lines represents the mean vertical wind shear in the direction of greatest turbulence probability.

Table 7: Mean out-of-cloud vertical wind shear (s^{-2}) between 8 km and 12 km within 20 miles of convection. Bold represents the direction the highest percentage of turbulence is located.

Case day	Model setup	North	East	South	West
12 July	S2	1.33×10^{-5}	1.77×10^{-5}	1.43×10^{-5}	1.86×10^{-5}
	S3	3.37×10^{-5}	4.70×10^{-5}	3.58×10^{-5}	4.99×10^{-5}
	S4	1.01×10^{-5}	1.00×10^{-5}	5.22×10^{-6}	8.34×10^{-6}
13 July	S2	2.99×10^{-6}	3.09×10^{-6}	3.56×10^{-6}	3.89×10^{-6}
	S3	7.92×10^{-6}	1.00×10^{-5}	1.08×10^{-5}	1.06×10^{-5}
	S4	2.16×10^{-6}	1.97×10^{-6}	3.08×10^{-6}	2.84×10^{-6}
15 July	S2	7.43×10^{-6}	7.34×10^{-6}	8.35×10^{-6}	8.20×10^{-6}
	S3	2.00×10^{-5}	1.89×10^{-5}	2.28×10^{-5}	2.46×10^{-5}
	S4	1.02×10^{-5}	7.63×10^{-6}	7.05×10^{-6}	8.92×10^{-6}

Vertical wind shear on average for 13 July is less than the vertical wind shear on 12 July but still has directional variation (Fig. 31). S3 again has the largest mean vertical wind shear by an order of magnitude when compared to S2 and S4. Increased vertical wind shear in the direction of increased turbulence likelihood is not found for S3 and S4, but is found for S2. For weak convection, directional subsets of vertical wind shear distributions are not effective as indicators of turbulence potential across varying model resolutions. The same findings hold for vertical wind shear on 15 July, with the exception that the greatest mean vertical wind shear is found in the same direction of greatest turbulence probability for S3 and S4.

Richardson number

Richardson number diagnosed out of cloud on 12 July had very subtle directional variation between the model setups (Fig. 32 and Table 8). On average, S4 has the lowest Richardson number east of convection. For all directions with Richardson number less than one, more than 20% of grid points are less than 0.25 (criteria for breaking gravity waves). In comparison, north and west of convection has the lowest Richardson number for S2 and S3. The direction of minimum Richardson number

subtly varied amongst S2 and S3 and a similar percentage of grid points (20%) had Richardson numbers less than 0.25. The likelihood of breaking gravity waves between the model setups is similar and does not indicate a directional preference due to model resolution. As was discussed previously, the height of convection did vary between the setups and was hypothesized to influence gravity wave production and breaking as storms exceeded the tropopause, however using Richardson number as a proxy for gravity wave breaking, the under prediction of storm height for the coarser simulations did not influence gravity wave breaking.

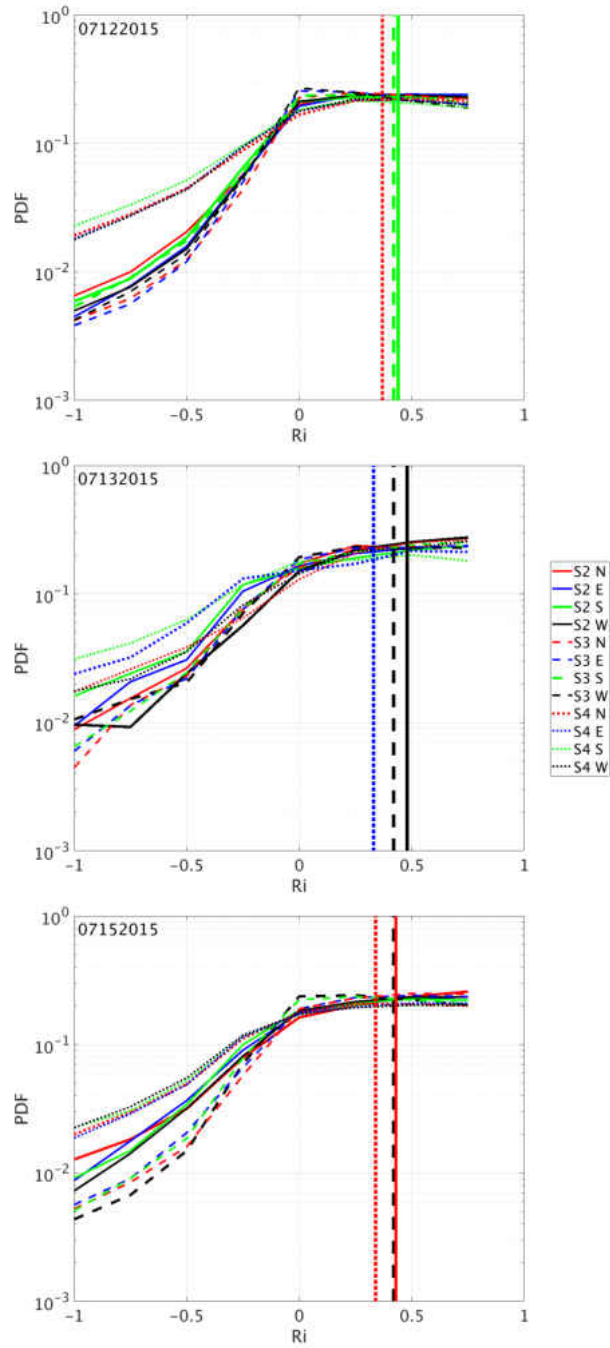


Figure 32: Distribution of out-of-cloud Richardson number between 8 km and 12 km within 20 miles of convection on 12, 13, and 15 July subset by direction from convection for S2 (solid lines), S3 (dashed lines), and S4 (dotted lines). The vertical lines represents the mean Richardson number in the direction of greatest turbulence probability.

Table 8: Mean out-of-cloud Richardson number between 8 km and 12 km within 20 miles of convection. Bold represents the direction the highest percentage of turbulence is located.

Case day	Model setup	North	East	South	West
12 July	S2	0.44	0.46	0.44	0.45
	S3	0.45	0.42	0.42	0.41
	S4	0.37	0.36	0.33	0.36
13 July	S2	0.43	0.41	0.39	0.48
	S3	0.45	0.44	0.45	0.42
	S4	0.43	0.33	0.29	0.41
15 July	S2	0.43	0.41	0.40	0.42
	S3	0.46	0.45	0.41	0.42
	S4	0.34	0.35	0.34	0.33

The percentage of Richardson number values less than 0.25 is again near 20% on 13 July, and the directional variability is nearly the same for S2 and S3, indicating that breaking gravity waves do not have a directional preference (Fig. 32) in this convective scenario. S4 again had the lowest mean Richardson number but when subset by direction was not associated with the direction of greatest turbulence probability. The same findings hold for 15 July.

Vertical velocity

Out-of-cloud vertical velocities also had a large variation in the mean between the coarser model setups and the finest model setup (Fig. 33 and Table 9). The mean vertical velocity of S4 was nearly twice that (or more) of S2 and S3 especially on 15 July. The maximum mean vertical velocity of S4 was north of convection, the same direction of the greatest probability of turbulence on 12 July. The greatest mean vertical velocities for S2 and S3 were west of convection, not the preferred direction of turbulence on 12 July. There was little consistency between greatest mean vertical velocity and direction of greatest turbulence probability. However, if vertical velocity is used as a proxy for gravity wave production, it would be hypothesized that S4 would

have a higher frequency of gravity waves. The frequency at which the generated waves begin to break is similar between the model simulations, and therefore would produce turbulence at similar rates. Additional simulations with increased temporal output is needed to verify this hypothesis.

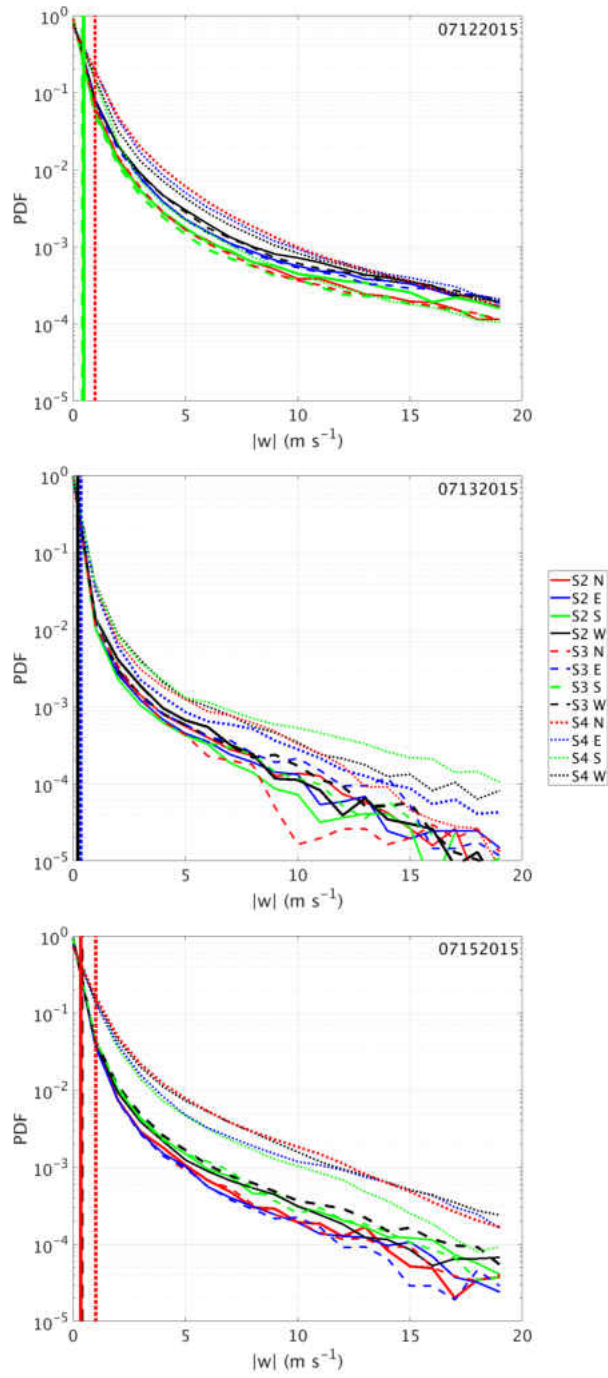


Figure 33: Distribution of out-of-cloud vertical velocities (absolute value) between 8 km and 12 km within 20 miles of convection on 12, 13, and 15 July subset by direction from convection for S2 (solid lines), S3 (dashed lines), and S4 (dotted lines). The vertical lines represents the mean vertical velocities in the direction of greatest turbulence probability.

Table 9: Mean out-of-cloud vertical velocity (m s^{-1} between 8 km and 12 km within 20 miles of convection. Bold represents the direction the highest percentage of turbulence is located.

Case day	Model setup	North	East	South	West
12 July	S2	0.47	0.57	0.48	0.61
	S3	0.47	0.56	0.44	0.59
	S4	0.98	0.95	0.70	0.83
13 July	S2	0.20	0.19	0.18	0.21
	S3	0.20	0.22	0.21	0.21
	S4	0.38	0.36	0.41	0.40
15 July	S2	0.35	0.34	0.38	0.37
	S3	0.35	0.35	0.39	0.40
	S4	1.02	0.85	0.79	0.97

In summary, the environmental variables out of cloud were related to the directional preference of turbulence inconsistently, especially for S2 and S3. For S4 on 12 and 15 July north of convection, the static stability on average was lower than the other directions, and the vertical wind shear and vertical velocity were greater than the other directions. For weaker convection on 13 July, static stability, vertical wind shear, and vertical velocity subset by direction away from convection was not related to the direction of greatest turbulence probability.

4.3.5 Correlation between environmental variables and turbulence intensity

It is hypothesized that the preferred direction of turbulence would be associated with the lowest static stabilities, greatest vertical wind shear, and greatest vertical velocities, with correlations between these variables and the intensity of turbulence. Figure 34 and Table 10 shows the correlations between static stability, vertical wind shear, vertical velocity, and turbulence intensity on 12 July. For the three model setups there is a weak negative correlation between out-of-cloud static stabilities and turbu-

lence intensity. When subset by direction, all three setups have the greatest negative correlation in the direction of greatest turbulence probability (S2-south, S3-south, and S4-north). While this result is only for one particular case, it could motivate additional examination to determine the feasibility of correlations being implemented as forecasting metrics for direction specific avoidance. A weak positive correlation between vertical wind shear and turbulence intensity and vertical velocity and turbulence intensity is also present for the three model setups. The strongest correlations are no longer associated with the direction of greatest turbulence probability, suggesting that vertical wind shear and vertical velocity alone cannot be utilized to avoid turbulence in specific directions.

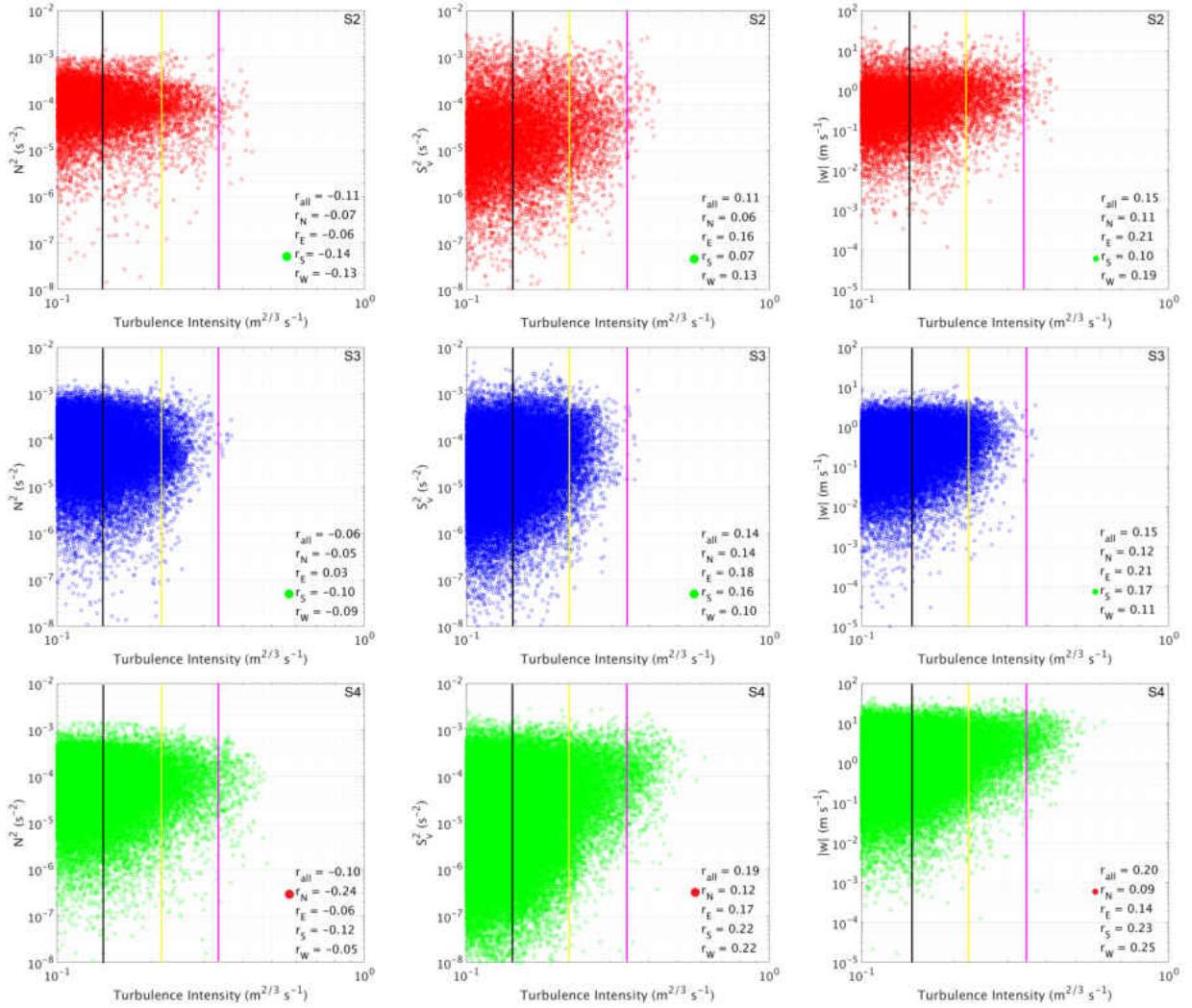


Figure 34: Correlation of out-of-cloud static stability, vertical wind shear, vertical velocities, and turbulence intensity between 8 km and 12 km on 12 July, 20 miles within convection. Colored circles represent the direction turbulence probability is the greatest. Light, moderate, and severe turbulence thresholds are represented by the black, yellow, and pink vertical lines.

4.4 Discussion and Conclusions

This study examined the influence model resolution has on the directional preference of turbulence for three convective days in North Dakota. Three model setups rep-

Table 10: Correlation coefficients for out-of-cloud static stability, vertical wind shear, vertical velocity, and eddy dissipation rate between 8 km and 12 within 20 miles of convection on 12 July. Bold represents the direction the highest percentage of turbulence is located.

Variable	Model setup	All	North	East	South	West
N^2	S2	-0.11	-0.07	-0.06	-0.14	-0.13
	S3	-0.06	-0.05	0.03	-0.10	-0.09
	S4	-0.10	-0.24	-0.06	-0.12	-0.05
S_v^2	S2	0.11	0.06	0.16	0.07	0.13
	S3	0.14	0.14	0.18	0.16	0.10
	S4	0.19	0.12	0.17	0.22	0.22
$ w $	S2	0.15	0.11	0.21	0.10	0.19
	S3	0.15	0.12	0.21	0.17	0.11
	S4	0.20	0.09	0.14	0.23	0.25

resenting operational and research forecasting systems were utilized. Convection for the three case days included an intense mesoscale convective complex, weak, isolated convection, and an intense squall line. Turbulence location was found to vary between the model setups. The highest frequency of turbulence was found to the north of convection (mesoscale convective complex) for the high resolution simulation (S4) on 12 July. The majority of turbulence on 12 July was found to the south of convection for the coarser model setups (S2 and S3). Turbulence was less likely on 13 July (weak, isolated convection), and the preferred direction was east for S4 and west for S2 and S3. On 15 July (squall line), the majority of turbulence was found to the north of convection for S4 and west for S2 and S3. The convective type (i.e. isolated, weak convection versus dynamically forced convection) influences the agreement in the turbulence direction. Convective properties such as echo top heights, reflectivity, and vertical velocity were compared between the model setups. S4 had higher frequencies of lower echo tops (and radar reflectivity values) for two of the three case days, and much higher frequencies on 15 July. The distribution of vertical velocities

found that S4 has higher frequencies of higher vertical velocities, but is statistically insignificant. Turbulence production was likely influenced by the variation in convective strength as convective cells approached or surpassed the tropopause, but the frequency of breaking gravity waves was similar between the setups.

Another popular methodology to subset turbulence location is identifying regions upshear and downshear of convection. Anecdotally (and based on scientific research of gravity wave propagation), pilots avoid flying downshear of mesoscale convective systems. One caveat with this methodology is defining upshear and downshear on a consistent basis from limited observations at various altitudes. Simply, defining upshear and downshear for an operational use is more difficult than compass directions. Nonetheless, it is a valuable methodology to characterize turbulence potential and relate turbulence to the environmental conditions. Figures 35 and 36 show wind vectors and turbulence intensity at 10 km near similar convective features for S2 and S3 on 12 July. Turbulence for S2 is generally downshear of convection while turbulence for S3 is upshear in this example. Analysis such as this could be completed on a larger dataset to determine the influence of resolution by defining upshear and downshear. However, for aviation operations it could be potentially difficult to translate upshear and downshear turbulence potential for numerous convective regimes in real time to the pilots and air traffic control.

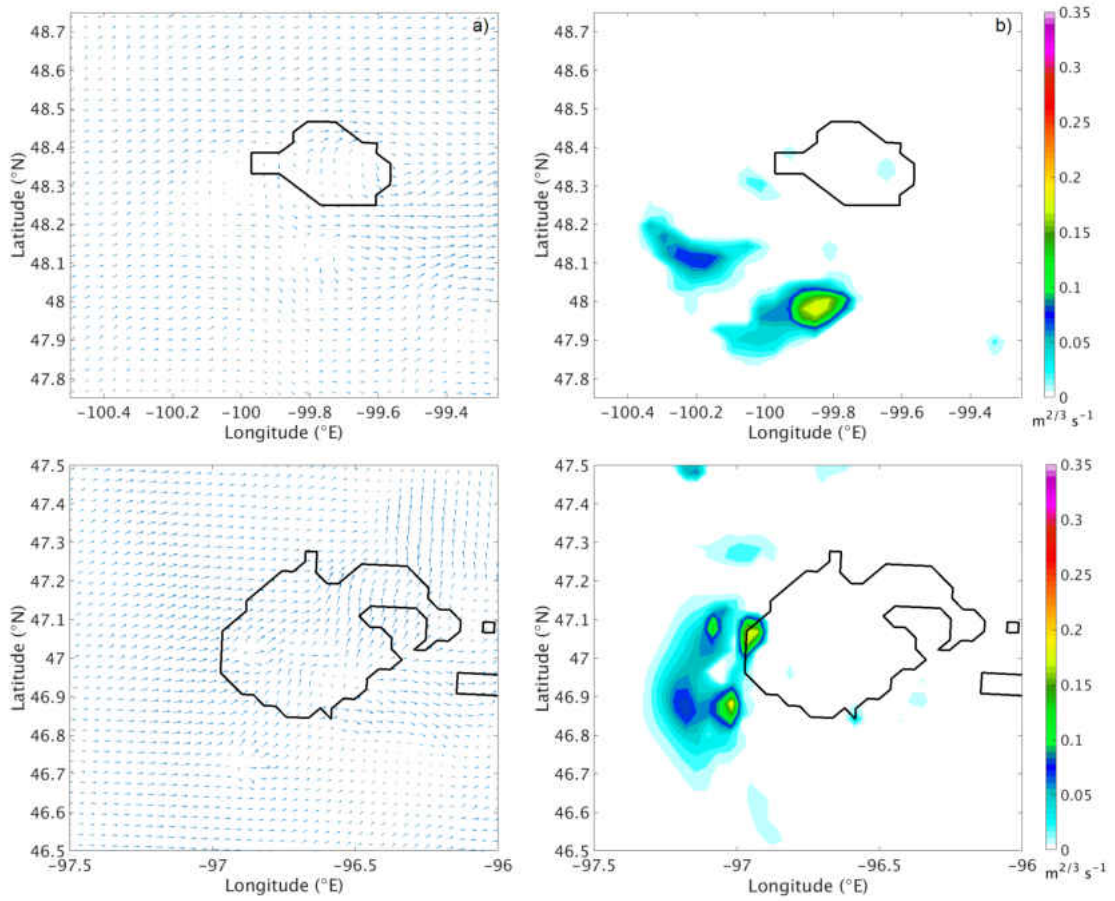


Figure 35: An example of the wind field (a and c) and turbulence intensity (b and d) at 10 km on 12 July for S2. Black contours represent echo top heights greater or equal to 10 km.

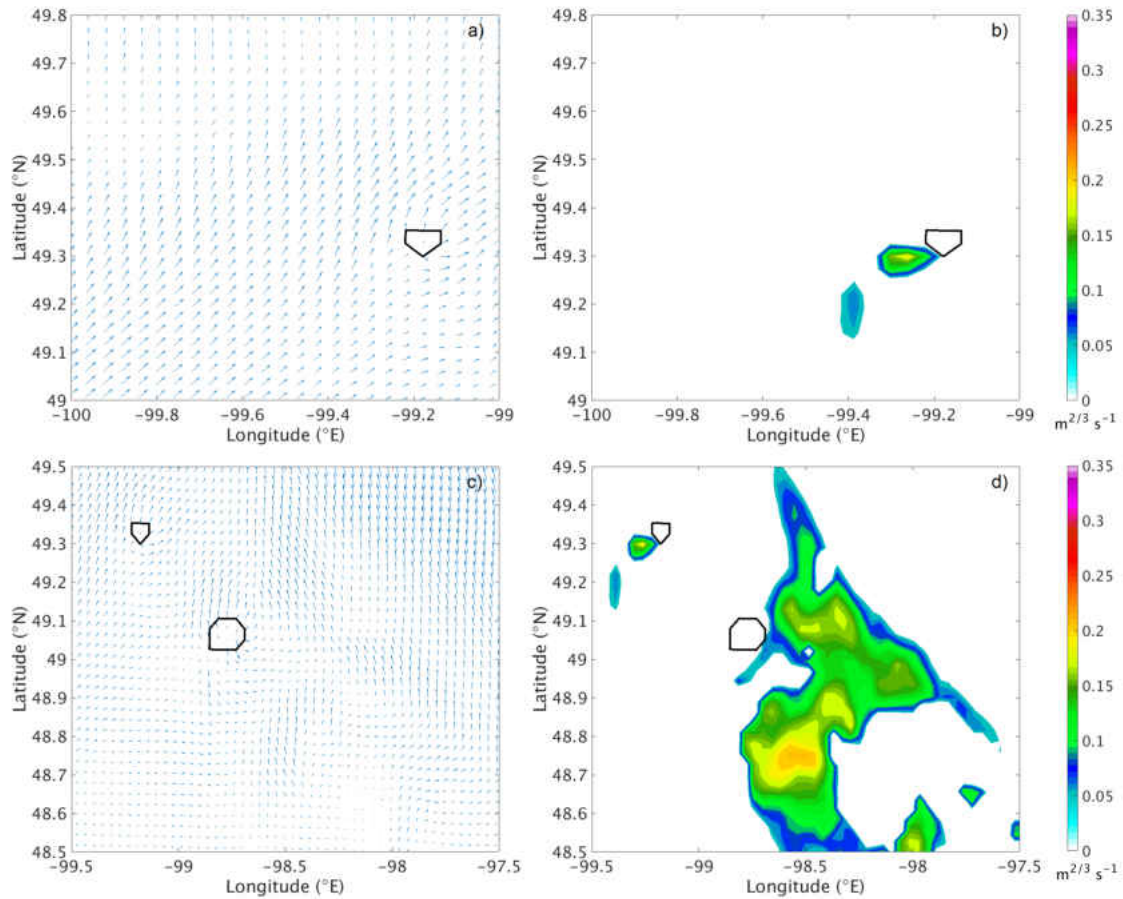


Figure 36: An example of the wind field (a and c) and turbulence intensity (b and d) at 10 km on 12 July for S3. Black contours represent echo top heights greater or equal to 10 km.

Environmental parameters that influence turbulence were analyzed and compared for the various model setups. Static stability produces turbulence through convective instabilities. Model resolution alters the distribution of stability within 20 miles (32 km), but was not found to be significantly different based on direction away from convection. Above 8 km in altitude, outside of convective cloud and convective outflows, the static stability profile should not vary significantly in relationship to direction away from convection (Lane and Sharman 2014). S4 had the lowest mean stability, while S2 and S3 had the greatest mean stability on 12 and 15 June. Vertical

shear produces turbulence through Kelvin-Helmholtz instabilities. The mean environmental shear was found to be the least for S4 and greatest for S3. A directional preference in vertical wind shear is apparent in the results especially for stronger convective days. Richardson number is a diagnostic used to identify regions where breaking gravity waves and subsequent turbulence are likely. The frequency of the Richardson number being less than 0.25 was nearly the same for all three model setups and did not have a significant directional preference for stronger convective days. This result suggests that breaking convectively induced gravity waves are equally as likely in model simulations with various resolutions. Lane and Knievel (2005) found that the gravity wave spectrum and momentum fluxes varied with model resolution. Unfortunately in this study the model resolution and temporal output was too coarse to compute specific gravity wave characteristics, such as wavelengths, phase speeds, and momentum fluxes. However, if vertical velocities and accumulated precipitation are utilized as proxies for gravity waves, there is a significant variation in frequency and location between model resolutions.

In regards to aviation applications, this study found that resolution influences the direction turbulence is located away from convection. Current Federal Aviation Administration thunderstorm avoidance guidelines recommend that pilots use a lateral avoidance range of 20 miles from severe convection. While turbulence is not isotropic in nature, resolution alters the direction distribution of turbulence, more specifically, particular directions have less turbulence and could be safer to fly through than others. Convective types alters the directional preference of turbulence. More research, both with observational and modeling platforms is vitally needed to verify the directional preference of turbulence around various types of convection if aviation is to be more efficient during convective seasons. Idealized modeling and further

investigation of planetary boundary layer schemes (calculation of TKE) is necessary for turbulence prediction improvement.

CHAPTER 5

PROPERTIES OF CONVECTIVELY INDUCED TURBULENCE OVER DEVELOPING OCEANIC CONVECTION

5.1 Motivation

Convectively induced turbulence (CIT) continues to be a prediction challenge for global aviation operations. Some studies have examined CIT encounters through dedicated numerical simulations in more detail. These studies have led to some advancement in our understanding of CIT but more research needs to be done to fully understand all physical processes that lead to convection related turbulence. Furthermore, the majority of these studies have been limited to mature convection in the midlatitudes (Barber et al. 2018; Trier and Sharman 2016; Lane and Sharman 2014; Zovko-Rajak and Lane 2014; Lane and Sharman 2012; Trier et al. 2012; Lane et al. 2009; Trier and Sharman 2009; Lane and Sharman 2008; Koch et al. 2005; Lane et al. 2003). Because the scientific research on turbulence associated with tropical convection (developing and mature) is sparse, aviation operations in tropical regions abide by thunderstorm avoidance policies designed from research of mature midlatitude convection. The Federal Aviation Administration (FAA) in the U.S. set policies that include a lateral avoidance of 20 mi (32.2 km) from severe convection (U.S. DOT-FAA 2017).

While consistency in operations between the midlatitudes and tropics may reduce the number of guidelines needed to avoid convective hazards, it could also be inefficient for flight routing and planning when tropical convection is significantly dif-

ferent than midlatitude convection. It is commonly understood that there are some significant dynamical and physical differences between the convection populations that occur in the continental midlatitudes and maritime tropics (Vant-Hull et al. 2016; Liu and Zipser 2005; Yuter et al. 2005; Chin et al. 1995). These differences are discussed further in section 2.5. There is also a difference in the stability and shear profiles of the tropical and midlatitude environments. Generally, vertical wind shear is lower in the tropical environment (Wissmeier and Goler 2009) and moist static stability is less (Saha and Singh 1972; Garstang and Fitzjarrald 1999; Frierson 2006; Frierson and Davis 2011). Tropical developing convection poses a challenge to aviation because nowcasting products used for the identification of developing convection are limited temporally and spatially. Current operational forecasting systems also have difficulties accurately predicting the location and timing of developing convection. Due to these numerous challenges associated with developing convection, hazards to aviation operations are not completely understood and no specific FAA or ICAO (International Civil Aviation Organization) avoidance guidelines exist. Pilots do have on-board radar systems that can detect developing convection. However, the operation and tilt management of the radar at cruising altitude is at the discretion of the pilot, which can lead to unexpected CIT encounters when on-board radar is improperly used (M. Poellot 2018, personal communication; Marconnet et al. 2016; AIRBUS 2007).

In this study, a numerical simulation of a severe turbulence encounter is compared against observations and in situ measurements of turbulence. Indices commonly used for turbulence prediction are used as turbulence diagnostics and examined during time periods near the turbulence encounter. Indices that perform well for the convective environment are used to analyze turbulence during the developing and

mature stages of the convective cycle to understand the influences of convective stage on turbulence.

5.2 Turbulence Incident in Southern Gulf of Mexico: 20 June 2017

On 20 June 2017, a commercial aircraft (Boeing 737) traveling from Panama City, Panama to Houston, Texas at approximately 11 km cruising altitude encountered severe turbulence 90 miles east of Cancun, Mexico. The encounter occurred at 1651 UTC near 21.84 °N, -86.16 °E. During the encounter the aircraft experienced normal load factors of -0.73 to 1.6 g for approximately 20 seconds and decreased in altitude by 120 m (Fig. 37). Nine passengers and one crew member sustained injuries and received medical attention. Synoptically, the jet stream was located north of 37 °N and was in a zonal flow pattern with a jet streak located west of Washington state over the Pacific ocean (CIMSS, NOAA, WPC, College of Dupage, not shown here). Winds aloft over the Gulf of Mexico were weak and had a northerly component along the flight trajectory. There were enhanced regions of vertical wind shear over the Gulf of Mexico between the 350 mb and 200 mb (9.7 km and 11 km) and speed shear of 30-40 kts between the upper (less than 300 mb) and lower atmosphere (greater than 700 mb). The horizontal gradient of vertical wind shear was oriented almost exactly along the flight trajectory. In addition to wind shear along the flight trajectory, there was deformation and enhanced upper level divergence. High values of absolute vorticity were limited in areal coverage over the Gulf of Mexico but had a local maximum northeast of the Yucatán Peninsula.

A broad region of low pressure was located over the Gulf of Mexico (Fig. 38). The low pressure center became more organized over the Gulf of Mexico on 20 June and developed into Tropical Storm Cindy by 1800 UTC. An extensive cloud field with embedded deep convection extended east of the low pressure center in the

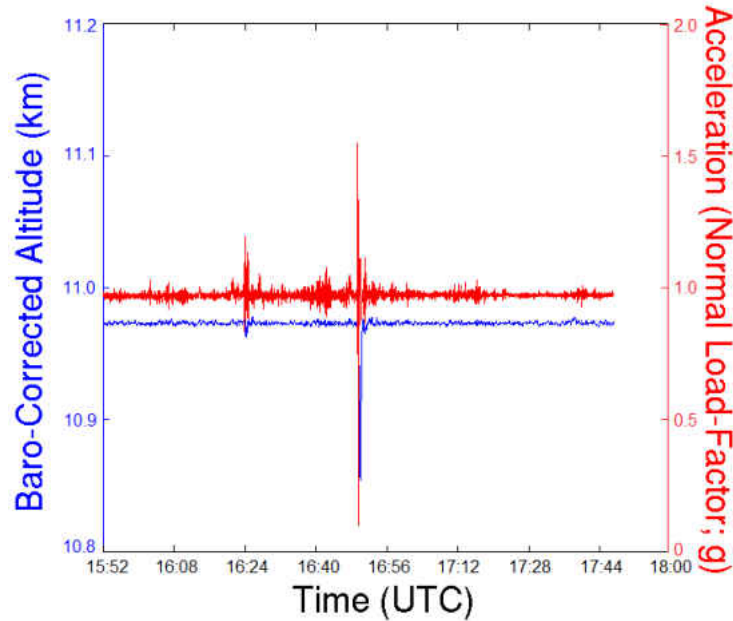


Figure 37: Baro-corrected altitude (km) and acceleration (g) recorded by the aircraft from 1552 UTC to 1800 UTC.

Gulf of Mexico. In relation to the flight path, convection was abundant but satellite imagery and pilot records indicate the aircraft was out of cloud at the time of the incident in a clear region above lower cloud tops. Brightness temperatures calculated from GOES-13 radiances reached minimum temperatures of 190 K in isolated areas to the west and north of the aircraft around the time of the encounter and near 220 K in the vicinity of the aircraft (Fig. 39a-b; note that here and in subsequent figures the location of the aircraft at the time of the severe turbulence encounter is indicated with a star symbol).

The Convective Diagnosis Oceanic Algorithm (CDO) is a nowcasting tool developed to improve safety and efficiency along trans-oceanic flights (Herzogh 2002). The algorithm has four inputs (observational and numerical) that are used to detect convective hazards and better identify convective structure (Kessinger et al. 2008; Kessinger 2017). These inputs are cloud top height (CTH) from infrared brightness

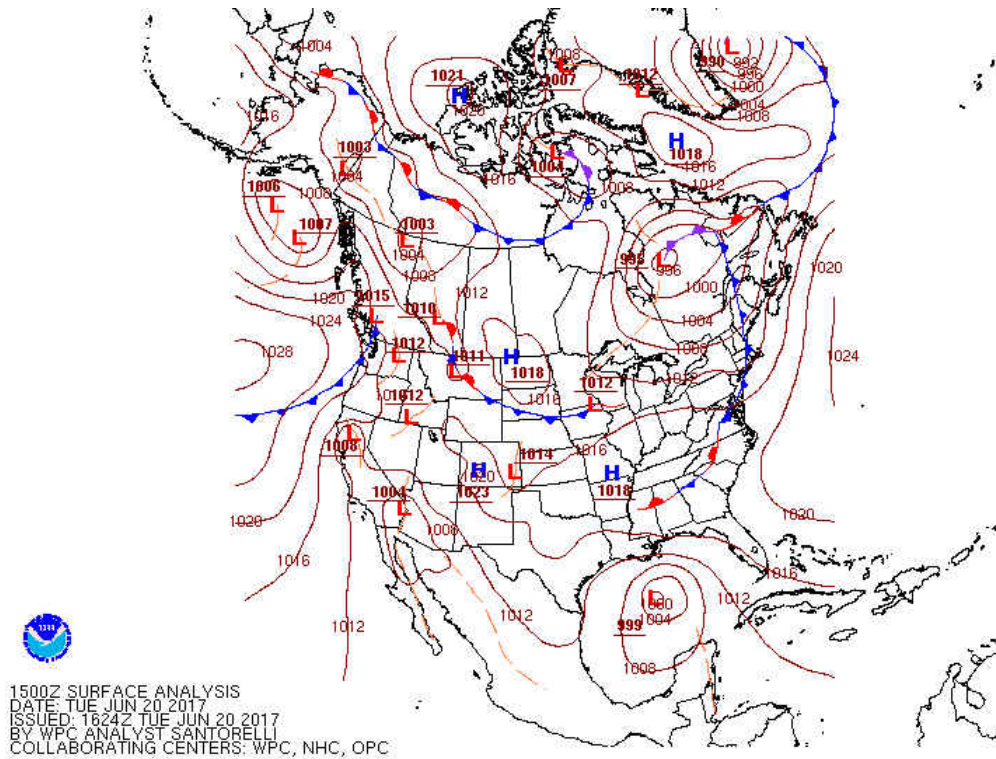


Figure 38: 1500 UTC surface analysis issued by the Weather Prediction Center.

temperature, the global convective diagnosis- the difference between the brightness temperature of the infrared channel and the brightness temperature of the water vapor channel, GOES-R Overshooting Tops algorithm, and a 15 minute lightning density field. The CDO algorithm estimates convective intensity on a scale of 1 to 6 every 15 minutes and is calculated on a global scale using 6 geostationary satellites.

CDO identified the Gulf of Mexico as an area with convective hazards. Regions of lightning and overshooting tops near the aircraft at the time of the turbulence incident occurred based on the GOES-R Overshooting Tops algorithm and Earth Networks lightning data (Figs. 39c-f and 40). Numerous lightning strikes were recorded within 5 minutes of the turbulence incident. Echo top heights determined by CDO were estimated to be 10.7 km near the location of the turbulence encounter at 1700 UTC and greater than 13 km in isolated cells to the west, south, and north of the



Figure 39: Observed brightness temperatures (K) from GOES-13 at a) 1545 UTC and b) 1645 UTC on 20 June, 2017. The Convective Diagnosis Oceanic Algorithm (CDO) hazards (c-d) at the same times as a-b (threshold descriptors in Table 11). Time (minute) of a detected lightning flash from 1530-1600 UTC (e), 1630-1700 UTC (f). White (a and b), blue (c and d) and black (e and f) stars represent the aircraft location at 1651 UTC.

Table 11: Threshold descriptions of the Convective Diagnosis Oceanic Algorithm.

Threshold	Description
2	Satellite data only contributed to diagnosis
3	Lightning but not through the entire analysis period and no overshooting top
5	Lightning present at the 15 th , 30 th , and 60 th minute but no overshooting top
6	Same as 5, but an overshooting top is present

aircraft. While CDO performed well for this particular case, it cannot provide forecasting information of convection needed for flight planning operations. The synoptic and mesoscale atmospheric conditions suggest that turbulence was likely convectively induced and enhanced in regions of wind shear. To adequately predict turbulence for this case day, turbulence diagnostics must capture both large scale features such as vorticity, mesoscale features such as stability, deformation, and wind shear, and subgrid-scale motions such as turbulent kinetic energy.

5.3 Data and Methods

5.3.1 Model setup

In this study, a 24 hour hindcast of tropical convection from 20 June 2017 is made using the Advanced Research WRF (ARW) model version 3.9 (Skamarock and Klemp 2008). This simulation is initialized at 0000 UTC with quarter degree GFS analysis data (<http://rda.ucar.edu/datasets/ds084.1>). One parent and two nested domains are used in this simulation with a horizontal grid spacing of 3 km in the innermost domain and 100 vertical levels (Fig. 41). The vertical grid spacing between 8 km and 12 km is approximately 325 m. The horizontal resolution of this simulation is comparable

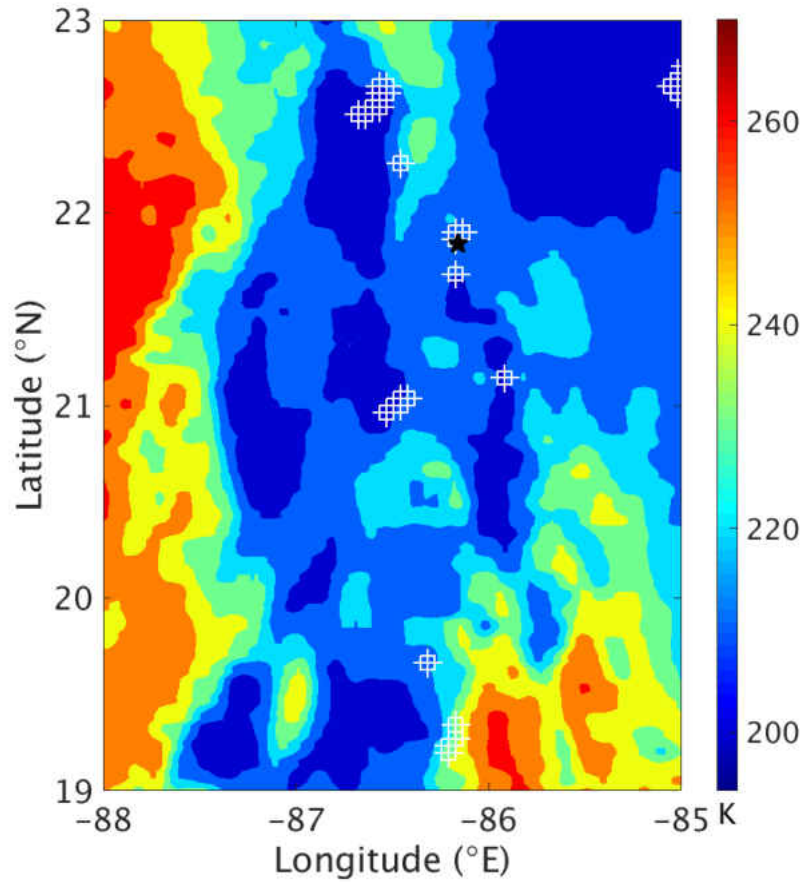


Figure 40: Earth Networks lightning from 1645-1655 UTC (white crosses) and cloud top temperature (K) from GOES-13 at 1645 UTC. The black star represents the location of the aircraft at 1651 UTC.

to operational modeling systems currently used and the increased vertical resolution has been shown to be adequate for turbulence prediction (Barber et al. 2018). A 10-km damping layer is used at the model top which is set to approximately 30 km (10 hPa). This study uses the Thompson microphysical parameterization, the Tiedke cumulus scheme, and the Mellor-Yamada-Janjić (MYJ) planetary boundary layer scheme (additional parameterization information is provided in Table 12). Simulation output is saved every 10 minutes to examine convective development, maturity, and



Figure 41: Model domain for 20 June 2017 simulation. D02 represents the first nest within the domain with horizontal grid spacing of 9 km and D03 represents the innermost nest of the model set up with horizontal grid spacing of 3 km (red box). Area designated for convective development analysis is represented by the black box. The red star represents the location of the aircraft at 1651 UTC.

dissipation of individual convective cells. The output variables include simulated radar reflectivity which is calculated from the WRF radar routine.

5.3.2 Turbulence metrics

Turbulence diagnostics that are used in this study include the Richardson number, eddy dissipation rate, and second-order structure functions with a separation distance of $10\Delta x$ (see the Appendix for more details). These indices are chosen based on the environmental conditions of the case day and previous usage in turbulence studies and NCAR’s Graphical Turbulence Guidance system (GTG-2; Sharman and Pearson 2017). Additional indices that are commonly used for diagnosing turbulence including the Brown index (Brown 1973), Colson-Panofsky turbulent kinetic energy metric (Colson and Panofsky 1965), the Dutton index (Dutton 1980), the Ellrod index (T2; Ellrod and Knapp 1992), and the DTF3 index (Marroquin 1998) were also computed for this case day, but will not be discussed due to poor performance. More specifically,

Table 12: Model parameterizations used in 20 June 2017 simulation.

Model physics	Model setup
Microphysics	Thompson
PBL	MYJ
Surface layer	MM5
Land surface	Noah
Shortwave radiation	RRTMG SW
Longwave radiation	RRTMG LW
Cumulus	Tiedke (D01 and D02)

the Brown and Ellrod index suffered resolution sensitivity as was found in Barber et al. (2018). The calculations and additional information about these diagnostics can be found in the Appendix.

5.4 Results

5.4.1 Verification of simulated convection

The simulated synoptic features of 20 June 2017 include a low pressure center north of the Yucatán Peninsula that deepens with time throughout the simulation. The simulated wind shear along the plane trajectory is both directional and speed shear. In the domain, simulated cloud features include a convective line similar to observations (as shown in Fig. 39a). Simulated cloud top temperatures (CTTs) calculated using the mixing ratios of the microphysical species from 1500-1800 UTC show the vertical convective structure and the intense development and decay of the convective line (Fig. 42). Within the convective line (squall line), embedded cells had CTTs less than 210 K and a larger area of colder cloud tops to the north of the aircraft. Simulated CTTs were warmer than observed and biased in the western direction (compare Fig. 42 with Fig. 39a-b). This direction bias is important because observed CTTs imply

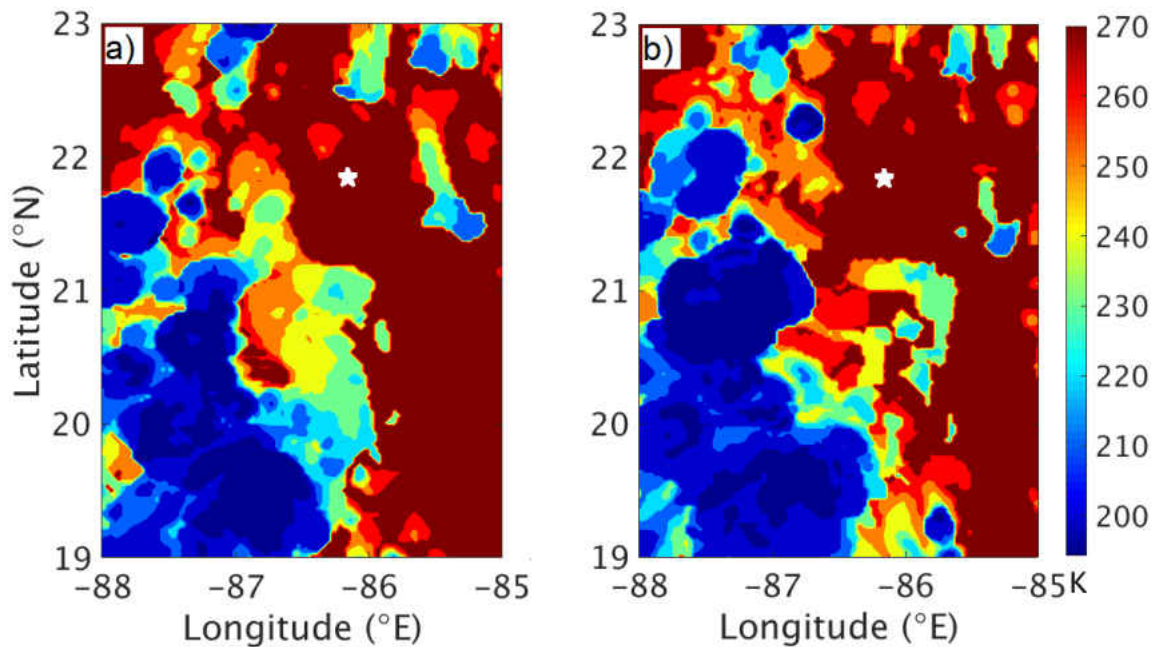


Figure 42: Simulated cloud top temperatures (K) at a) 1600 UTC and b) 1700 UTC on 20 June, 2017. White stars represent the approximate location of the aircraft at 1651 UTC.

that there were clouds directly below the aircraft while simulated CTTs indicate the aircraft would have been out of cloud with no cloud field underneath near the time of the turbulence encounter. The bias in cloud location and convection also influences the location of simulated turbulence.

The same squall line discussed above is shown using simulated radar reflectivity values (Fig. 43a). The convective line structure has a north-south orientation with a larger complex to the north. 2-km simulated radar reflectivity values exceed 55 dBZ in the embedded cells. With regard to the location of the turbulence encounter (21.84°N, -86.16°E), 2-km simulated radar reflectivity values are zero while directly to the west maximum values exceed 50 dBZ. There is also an area of convection directly to the north of the aircraft's location that was decaying throughout the analysis period.

Echo top heights (not shown; calculated from simulated radar reflectivity values with a threshold of 18-dBZ) that correspond with the regions of maximum 2-km radar reflectivity values exceed 14 km. At the location of the aircraft no echo tops are simulated but directly to the west a cell developed to heights greater than 14 km and growth was more than 10 km during an hour. The analysis of the change of echo top height with time shows the greatest convective development was between 1500-1700 UTC. Closest to the aircraft convection was mainly decaying, but numerous cells within 100 km of the aircraft were rapidly growing.

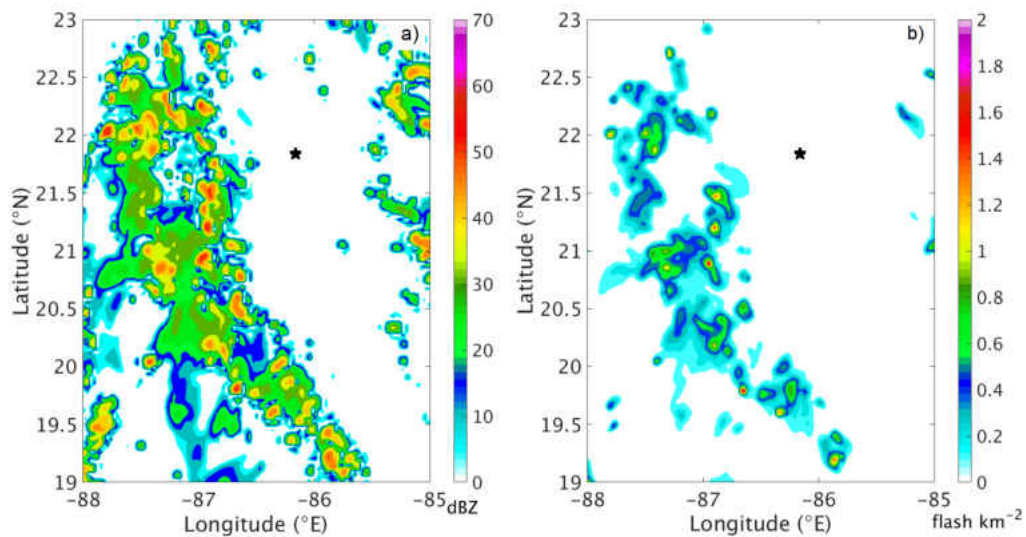


Figure 43: 2-km simulated radar reflectivity (a) and lightning flash densities per ten minutes determined from b) ice water path at 1650 UTC on 20 June, 2017. Black stars represent the approximate location of the aircraft at 1651 UTC.

Lightning was prevalent in the region near the time of the turbulence encounter, specifically around convective cores. Within the region of interest, more than 2000 lightning flashes were recorded by Earth Networks lightning detection network between 1500-1800 UTC with the highest frequency between 1600-1700 UTC. Near the time of the turbulence encounter lightning was recorded near the trajec-

tory of the aircraft (Fig. 39f). Lightning from the model simulation was determined based on various empirical relationships that relate model variables of maximum updraft velocity, ice water path (column integrated ice, snow, and graupel mass for temperatures below $-5\text{ }^{\circ}\text{C}$), graupel mass and ice mass fluxes to lightning flash rate (see Barthe et al. 2010 for these relationships). These relationships were adapted to predict lightning densities per km^2 for this model simulation by comparing observed lightning densities with the above model parameters (e.g. Allen et al. 2016). These parameters differ between observational and modeling data and also depend on model simulation setups such as grid spacing and a chosen microphysics scheme. At the time of the turbulence encounter, simulated lightning was frequent within simulated convective cores and anvil cloud regions based various predicted lightning density-model parameter relationships. Figure 43b shows an example of predicted lightning density based on ice water path.

In summary, the model simulation was able to capture the morphology of the convective line extending north to south in the Gulf of Mexico and the depth of convection as compared to observations. The simulated convection was intense in nature with echo tops exceeding the typical cruising altitudes of commercial aviation and frequent lightning. While the type of convection, depth, and hazards such as lightning were similar to observations, the location of the convective line was approximately 100 km too far west as compared to the location of the turbulence encounter. Due to the location bias of convection, the analysis of turbulence will be focused at a hypothetical aircraft location also approximately 100 km to the west. However, turbulence is still analyzed across the entire domain and the shift in aircraft location only influences the hypothetical flight path. Within figures, this location is designated with a second star.

5.4.2 WRF-derived turbulence predictors

Richardson number (Ri), second-order structure functions (SF), and eddy dissipation rate (EDR) are used to diagnose turbulence from the model simulation. The objective of the diagnostic comparison is to examine the performance of each diagnostic in a convective environment where the diagnostics have not been evaluated in previous studies (i.e. the tropics and developing convection). The success of the turbulence diagnostic in the simulated convective environment will motivate the examination of the diagnostic for specific life stages of convection (section 5.4.3). Horizontal cross sections of the various indices will focus on the prediction of turbulence between the altitudes of 10 km, 11 km (altitude of the aircraft), and 12 km, as these altitudes are common cruising altitudes. Echo top heights are used as a proxy for cloud and an indicator of in-cloud or out-of-cloud. More specifically, if an echo top intersects the analysis height, the grid cell at the analysis height is considered in cloud. If an echo top is less than the analysis height, the grid cell at the analysis height is considered out of cloud (following the methodology implemented in Barber et al. 2018).

Ri is used in this study to indicate regions that are likely turbulent, but cannot be used to differentiate between various intensities of turbulence. Ri indicates areas of turbulence outside of convective regions and the likelihood of turbulence increases with height. In areas where Ri is less than 0, analysis of isentropes suggest convectively generated gravity waves began to break. Prior to, during, and after the turbulence encounter, turbulence diagnosed by Ri subtly varies in areal coverage and magnitude. Between 10 km to 12 km in altitude, Ri less than 0.25 is within 20-50 km of convective features (Fig. 44b). If Ri was the only diagnostic used as a forecast tool for turbulence avoidance, the altitudes between 10 km to 12 km would be forecasted as a high likelihood of experiencing turbulence within 50 km of convection and extremely unlikely to the east of the convective line (west of -86.5°E). The

probability of experiencing turbulence increases significantly with height and flying over convection would be hazardous (Lane et al. 2012). Importantly, the turbulence that is diagnosed has a higher likelihood of being out-of-cloud than in-cloud, and is therefore an additional concern to aviation.

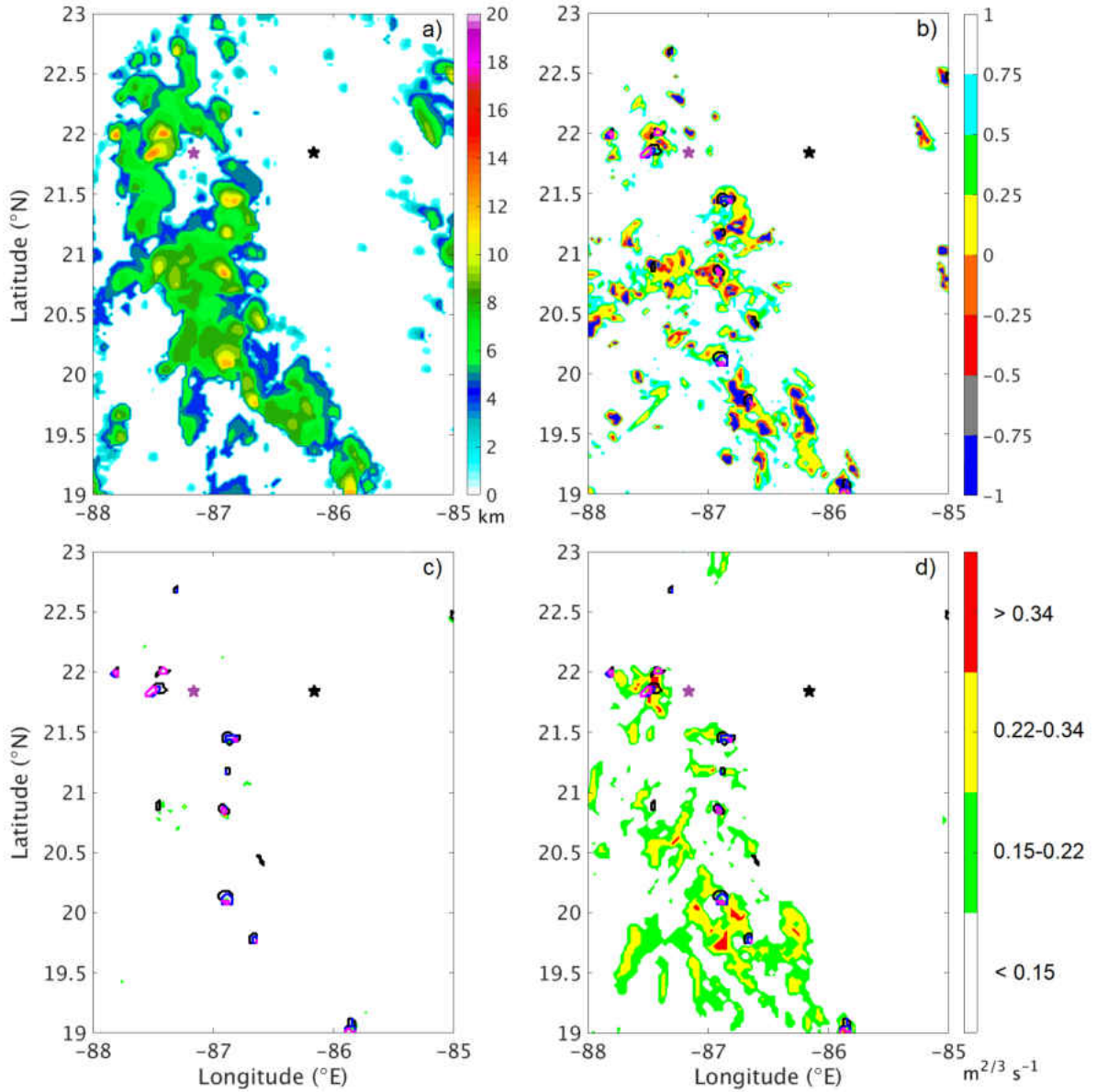


Figure 44: Simulated echo tops (km) at 1650 UTC and maximum turbulence (minimum for Ri) at 1650 UTC diagnosed by b) Richardson number, c) EDR, and d) $\varepsilon^{1/3}$ (structure functions converted to EDR units) between the altitudes of 10 km and 12 km. Turbulence intensity is represented by light (green), moderate (yellow), and severe (red) thresholds. Black, blue, and magenta contours represent echo top heights greater than 10 km, 11 km and 12 km. Black (purple) stars represent the aircraft (shifted analysis) location at 1651 UTC.

Barber et al. (2018) simulated a week of convective cases in North Dakota, in which EDR was shown to reasonably match PIREPS. However, in this case EDR under-predicted intensity of turbulence when compared to the turbulence intensity observed by aircraft (Fig. 44c). EDR rarely exceeded a value of $0.15 \text{ m}^{2/3} \text{ s}^{-1}$ or the intensity of light. Similar to Ri, the areal coverage of turbulence increases with height. At the time of the turbulence encounter, there were areas with EDR values between $0.2\text{-}0.3 \text{ m}^{2/3} \text{ s}^{-1}$ (moderate) between the altitudes of 10 km and 12 km, approximately 100 km to the southwest of the turbulence encounter location. However, between 10 km and 12 km ten minutes prior to the turbulence encounter and twenty minutes afterwards, EDR was less than $0.2 \text{ m}^{2/3} \text{ s}^{-1}$ and limited to fewer than 100 grid pixels. If EDR was the sole turbulence diagnostic for this case day, EDR would not have been successful in forecasting turbulence around convection and in clear air regions. Due to this under prediction of turbulence by the EDR diagnostic, it will not be used to analyze turbulence around developing convection (section 5.4.3).

Converting SF to EDR units (see the Appendix) turbulence intensity can be discussed as EDR metrics (Fig. 44d). Relating the converted SF in EDR units to turbulence intensity thresholds provided in Table 21, moderate to severe turbulence is diagnosed between the altitudes of 10 km and 12 km. At these altitudes there is moderate turbulence diagnosed near the aircraft location. The most severe turbulence is located to the west and south of the aircraft, with the largest areal coverage of severe turbulence near 19.7°N , -87°E . Very localized regions of moderate-severe turbulence are present substantial distances (more than 50 km away in the horizontal direction) from cloud boundaries at all heights. The use of SF converted to EDR units aids in assessing the intensity of turbulence that aviation may experience and in this case would have predicted out-of-cloud turbulence of moderate intensity near the aircraft.

Turbulence distributions are important indicators of how turbulence diagnostics perform. It is also important to understand in-cloud and out-of-cloud turbulence distributions for aviation applications. SF converted to EDR units (see the Appendix) between the altitudes of 10 km and 12 km from 1500-1800 UTC is provided in (Fig. 45) and illustrates the greater areal coverage (nearly an order of magnitude) of out-of-cloud turbulence when compared to in-cloud turbulence. The distribution of out-of-cloud turbulence using SF finds nearly 1% of SF values are light and less than 0.1% are moderate or severe. The maximum EDR value of in-cloud turbulence is nearly the same as out-of-cloud, but the relative likelihood of experiencing the most severe turbulence while in cloud is greater than while out of cloud. The greatest hazard remains with out of cloud turbulence as pilots generally avoid flying through convective cloud. The distribution of turbulence at various heights (not shown) for a forecast period of 1500 UTC to 1800 UTC highlights that 10 km in altitude would have the greatest likelihood of experiencing both in-cloud and out-of-cloud turbulence

In summary, Ri and SF performed adequately at diagnosing turbulence near active convection at common cruising altitudes. The majority of turbulence diagnosed is out-of-cloud and occurs near the time of the observed turbulence encounter and location. However, the location of turbulence relative to convection does differ between the diagnostics which highlights how the type of turbulence each diagnostic is designed for influences the prediction. SF will be used to diagnose turbulence during the developing stage of convection because of the better performance for the convective environment and because it can be converted to an intensity threshold without requiring any calibration (section 5.4.3).

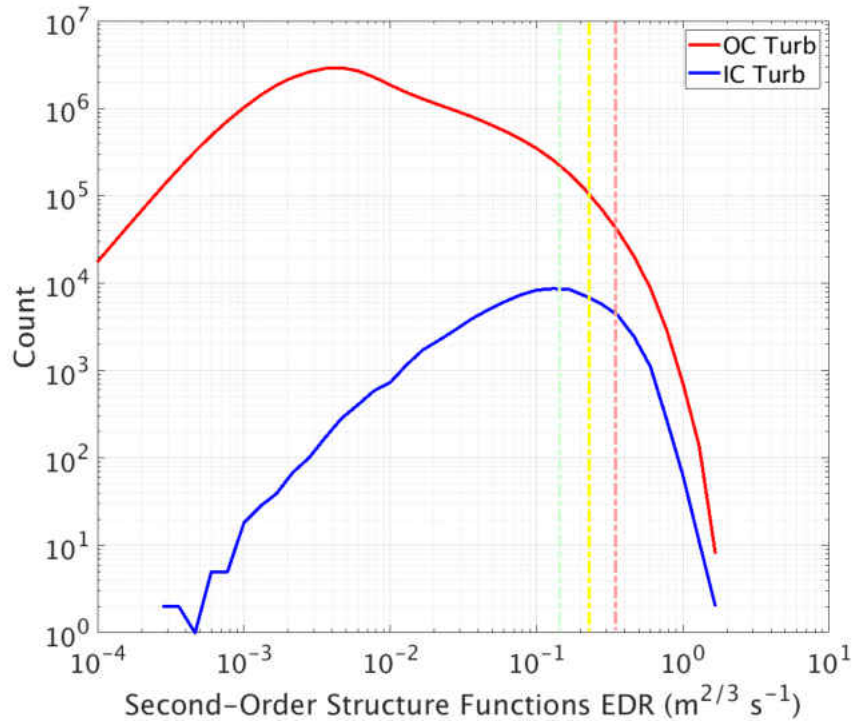


Figure 45: Count of out-of-cloud (OC; red) and in-cloud (IC; blue) turbulent grid cells and probability density functions of OC and IC turbulent grid cells calculated from structure functions converted to EDR units from 1500-1800 UTC. Vertical dashed lines represent the turbulence intensity thresholds (light-green, yellow-moderate, and magenta-severe).

5.4.3 Analysis of turbulence prediction in the vicinity of developing convection

Numerous meteorological parameters can be used to distinguish between developing, mature, and dissipating convection. Developing convection in past studies has been defined by echo tops that increase in height with time, the presence of an updraft only, vertical growth only, vertical velocities near 10 m s^{-1} , insignificant convective rain totals, and the absence of cold rain processes (Lin 2010; Markowski and Richardson 2010; Futyan and Del Genio 2007; Byers and Braham 1949). Mature convection in past studies has been defined as echo tops that reach a maximum in altitude, the presence of an updraft, downdraft, and anvil, the maximum frequency of lightning, significant convective rain totals, vertical velocities that exceed various percentiles, sustained updraft strength, and maximum areal coverage (Mullendore et al. 2013; Markowski and Richardson 2010; Carey and Rutledge 2000; Tapia et al. 1998; Byers and Braham 1949). In this study, individual convective objects (CO) are defined as contiguous regions with echo tops greater than 8 km in height. The COs are followed through time using the object's centroid location. A new object is defined if the centroid location of a previous convective object has changed by more than 10 km in a 10 minute period. Developing convection is defined as a convective object in which the simulated maximum vertical velocity for that object is less than the 90th percentile of all maximum vertical velocities of that object's lifespan and less than the maximum vertical velocity of the following time period. To determine if turbulence is associated with developing convection or mature convection, distance is calculated between the turbulent grid cell and the boundaries of the convective object.

Developing convection is examined by creating a subset within the study domain between the longitudinal range of -89°E to -86°E and the latitudinal range of 20°N to 23°N (black box in Fig. 41). This particular region had numerous convective

cells evolving with time and large variations in echo top height. To isolate developing convection from mature and dissipating convection, maximum vertical velocities within convective objects are used as thresholds (as discussed above). From 1510-1800 UTC, 77 convective objects were identified as developing and maximum vertical velocities of the objects varied from 3 m s^{-1} to 14 m s^{-1} . Convection intensified in three distinct periods from 1510-1600 UTC, 1600-1710 UTC, and 1710-1800 UTC, in which 46 developing convective objects were present in the first active period, 26 in the second active period, and 4 in the third active period. For the convective objects that are identified as mature, the vertical velocity magnitudes in the mature convection (i.e., the 90th percentile of vertical velocity) exceeded 5 m s^{-1} for 24 objects and 10 m s^{-1} for 4 objects, while the mean vertical velocity was 3.86 m s^{-1} . The timespan for the majority of convective objects identified as developing to transition to mature occurred in 10 minutes and the maximum time for development was 40 minutes.

Out-of-cloud turbulence is analyzed in relationship to the number of CO that are within 30 km of the turbulence location. By examining turbulence at 10 km (the height with the greatest likelihood of experiencing turbulence) in this manner, the influence of convective stage can be further understood in terms of aviation safety. Figure 46 shows the distribution of turbulence values for turbulent grid points that are within 30 km of CO. The areal coverage of turbulence within 30 km of only mature/dissipating CO is greater than the areal coverage of turbulence within 30 km of both mature/dissipating and developing CO. However, turbulence intensities are found to be the greatest when developing convection is present in the region. While the exact convective source of turbulence cannot be determined, these results suggests that a flight path near developing convection is likely to experience the most severe turbulence.

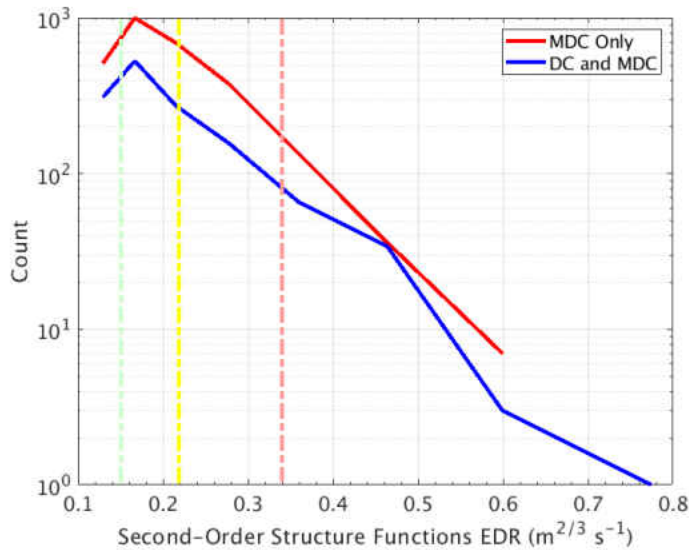


Figure 46: Distribution of structure functions converted to EDR units where only mature/dissipating (MDC) convective objects are within 30 km of a turbulent grid point (red) and where both mature/dissipating and developing convective objects are within 30 km of a turbulent grid point (blue). Vertical dashed lines represent the turbulence intensity thresholds (light-green, yellow-moderate, and red-severe).

Turbulence is then analyzed in relationship to the distance from CO. The distribution of turbulence closest to developing convection demonstrates that the majority of values were less than $0.22 \text{ m}^{2/3} \text{ s}^{-1}$ (moderate) at all three analysis heights (Fig. 47) while the most extreme turbulence values were located at 10 km in altitude. At 11 km and 12 km in altitude, turbulence closest to developing convection does exceed $0.22 \text{ m}^{2/3} \text{ s}^{-1}$ (moderate) but occurs at a lower frequency when compared to 10 km in altitude. Turbulence nearest to mature and dissipating convection is mostly less than $0.22 \text{ m}^{2/3} \text{ s}^{-1}$ (moderate) but at a higher frequency than developing convection turbulence (Fig. 47). The majority of severe turbulence is closest to mature convection and is more frequent than severe turbulence closest to developing convection at all three analysis heights (results hold true for various methodologies of defining developing and mature convective objects). However, the grid cells with highest turbulence intensities were co-located with developing convection at 10 km in

altitude (not shown in previous discussion due to analysis procedure). The particular developing CO that was co-located with the highest turbulence value had maximum vertical velocities increase more than 9 m s^{-1} in ten minutes. In addition, echo top heights of the CO increased more than 3 km in altitude during the same development period.

It can be hypothesized that the rapid development of convection likely formed gravity waves as convection extended in stable regions (Lane et al. 2003); however additional high resolution simulations (spatially and temporally) are needed to adequately examine gravity wave characteristics and determine the exact dynamical cause of the most severe turbulence. While the areal coverage of the most severe turbulent cells co-located with developing convection is very limited, these regions are more dangerous to aviation operations because of lack of avoidance guidelines during developing convective scenarios. One important caveat with this analysis is that turbulence co-located with developing convection may actually be caused by dynamics associated with nearby mature convection. Turbulence can occur more than 100 km away from mature convection (Lane and Sharman 2014; Zovko-Rajak and Lane 2014; Lane et al. 2012; Lane et al. 2003; Pantley and Lester 1990; USAF 1982), and the particular complexity of this simulation does not allow for the analysis of the primary source of turbulence. More specifically, turbulence co-located with developing convection may not have been caused solely by the developing convection. But we hypothesize that even when mature convection contributes to the turbulence signal, the developing convection is playing an important role in modifying (often increasing) the turbulence magnitude, especially in the limited timespan of development in this study. These results highlight that the most severe values of turbulence can be located near developing convection and pilots should use extreme caution around developing convection. These results also stress the necessity of additional research to address

the likelihood of turbulence generated by developing convection through the use of high resolution simulations.

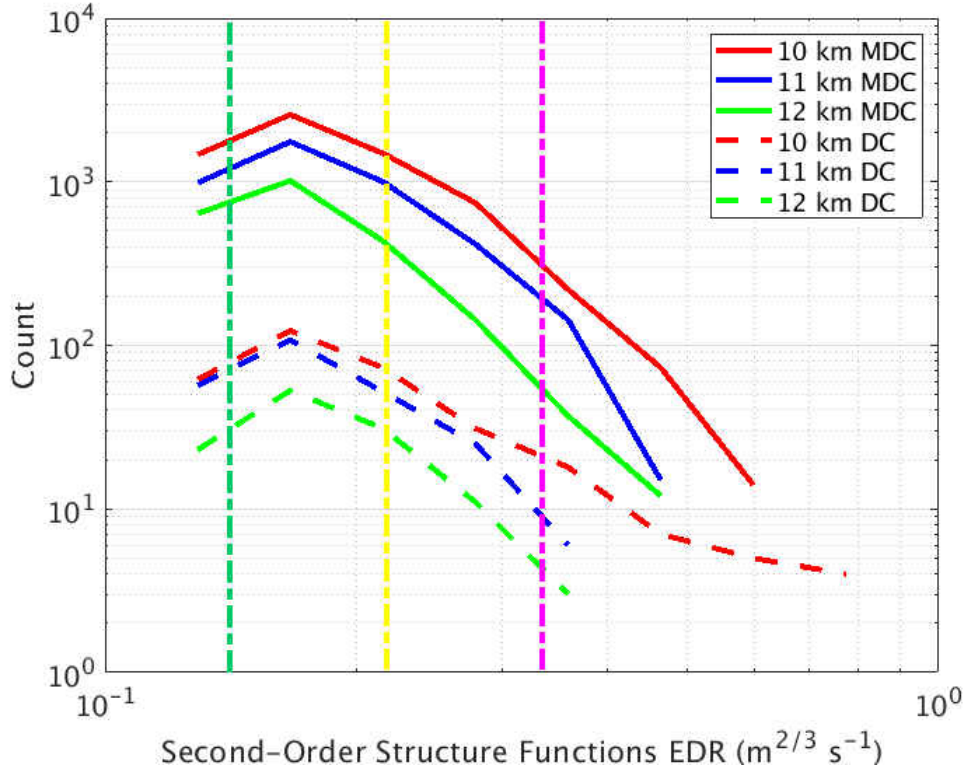


Figure 47: Distribution of structure functions converted to EDR units closest to developing convection and mature and dissipating convection at 10 km, 11 km, and 12 km. Vertical dashed lines represent the turbulence intensity thresholds (light-green, yellow-moderate, and red-severe).

5.5 Discussion and Conclusions

Convectively induced turbulence (CIT) prediction is a challenging problem globally and more so in data-sparse regions such as tropical oceans. This study examined turbulence prediction from a WRF simulation for an aviation case that experienced severe turbulence near areas of active convection. Various indices including Richardson number (Ri), subgrid-scale eddy dissipation rate (EDR), and second-order struc-

ture functions (SF) were used to diagnose turbulence. These particular indices were chosen as turbulence predictors based on the synoptic and mesoscale conditions of the convective environment. While Ri deduces environments that are favorable for turbulence production, such as sheared environments and gravity wave breaking (Lane et al. 2012), the precise intensity of turbulence that may occur in these regions cannot be determined, limiting the usefulness for aviation operations. However, in stably stratified environments it can be used as a scaling factor for other indices (Muñoz-Esparza and Sharman 2018; Sharman and Pearson 2017).

EDR is a common turbulence diagnostic that is physically based and in past studies has predicted turbulence in the midlatitudes accurately (Barber et al. 2018; Ahmad and Proctor 2012). However, in this oceanic study EDR under-predicted turbulence. A limitation with the calculation of EDR is the designation of the length scale. Various methods in past studies have been used including constants, resolution dependent length scales, and direct model output of length scale. Unfortunately, there is no consensus on which approach is the most appropriate for the calculation of EDR. Here, EDR was calculated from the TKE output by the Mellor-Yamada-Janjić PBL scheme; further investigation using PBL schemes more commonly used for WRF simulations for tropical convection is recommended.

SF was adequate at diagnosing turbulence near active convection at common cruising altitudes. One problem that may occur through the methodology of calculating structure functions is contamination by the updraft. Figure 48 shows the locations of updraft regions within convective cells, the u and v-components of wind, and locations of turbulence at 11 km. Turbulence is located near regions of updrafts (where vertical motions are large), as these regions have perturbations and gradients in both the u and v field. However, turbulence is also found where vertical motions

are negligible and only strong gradients in the horizontal component of winds are present.

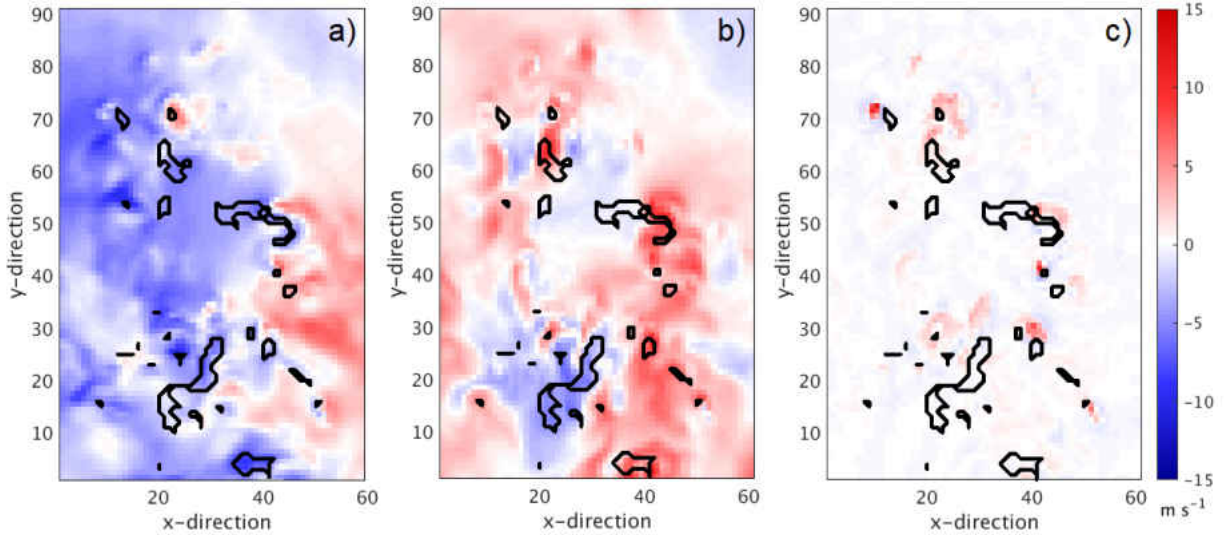


Figure 48: U-component of wind (a; m s^{-1}), b) v-component of wind (m s^{-1}), and c) vertical velocity (m s^{-1}) with locations of structure functions converted to EDR units greater or equal to $0.15 \text{ m}^{2/3} \text{ s}^{-1}$ (black contour) at 11 km in altitude.

This study finds that the turbulence indices (both used for CAT and CIT) are limited in accuracy for tropical CIT prediction for this particular case. These results highlight the need for more investigation of tropical turbulence prediction and turbulence diagnostics. When radar observations and other in situ observations can be utilized, nowcasting products provide the best guidance for turbulence prediction. However, without radar coverage such as in this tropical oceanic case, SF and Ri provides guidance to aviation operations in avoiding turbulence, but many more studies of tropical turbulence are needed to statistically verify these indices. More specifically, indices designed for midlatitude continental CIT may not perform as well for tropical oceanic CIT motivating additional studies of diagnostic performance. While this study did not investigate the influence of model resolution on the performance of

the turbulence diagnostics, resolution sensitivity is a known limitation of large scale diagnostics such as the Brown and Ellrod index. Additional research on resolution sensitivity and calibration procedures of turbulence diagnostics is needed as model resolution increases in operational forecasting.

Convection poses a hazard to aviation during multiple stages of the convective life cycle. Forecasting developing convection is difficult due to the limited accuracy of simulated convective initiation, including timing and location. These challenges associated with forecasting developing convection further impact the prediction of turbulence caused by developing convection. Although convective and turbulence ensembles mitigate some of the challenges of forecasting convection in general (Carlberg et al. 2018; Storer et al. 2018; Iyer et al. 2016; Evans et al. 2014), nowcasting is more heavily relied upon for developing convection in aviation applications. In this study, a location bias in the convective feature of approximately 100 km was present, motivating the need for convective ensembles for aviation operations such as flight planning.

This study examined turbulence during an active period of convective growth. Turbulence associated with developing convection was found to represent a small portion of all turbulence during an active convective period. However, turbulence near developing convection was more severe in magnitude than turbulence near mature convection. While most turbulence was found to be associated with mature convection, the severity of turbulence associated with developing convection is likely to influence aviation more as pilots avoid regions with mature convection. In order to reduce the number of aviation turbulence encounters globally, more research is needed to understand the variation of CIT and the limitations of current prediction systems.

CHAPTER 6

CHARACTERISTICS OF TROPICAL AND MIDLATITUDE OUT-OF-CLOUD CONVECTIVELY INDUCED TURBULENCE FROM HIGH RESOLUTION SIMULATIONS

6.1 Motivation

Convectively induced turbulence (CIT) is an operational challenge to aviation as global flight routes increase and air space becomes more congested (Statista 2018). While numerous forecast guidance systems including real time avoidance algorithms and preflight forecast systems like the Graphical Turbulence Product (GTG-2; Sharman and Pearson 2017; Pearson and Sharman 2017; Sharman et al. 2006) are in use and are frequently updated to provide pilots with more information, the complexity of CIT is not always depicted by these systems. To address the limitations of prediction systems and reduce the number of aviation encounters with convective hazards, the FAA has thunderstorm avoidance guidelines in place. The most impactful guideline that influences flight routes and Air Traffic Control is the lateral avoidance of 20 miles from severe convection. While the guidelines are based on scientific research of CIT in the midlatitudes, because the understanding of tropical CIT is limited, the same guidelines are also followed by U.S. airlines along tropical flight routes. However, convective and environmental properties are known to vary between the midlatitudes and tropics, from the strength, depth, and duration of convection, to the environmental shear and stability profiles, all of which influence the hazards aviation could encounter.

The hazards to aviation caused by convection are also dependent on the type and stage of convection. Variations in turbulence probability from specific convective events are not currently addressed by the FAA guidelines, but only convection identified as severe is avoided. More specifically, developing convection is a hazard not addressed by the FAA guidelines if not severe in intensity. Developing convection is a concern to aviation as it is generally poorly forecasted in terms of timing and location, and therefore cannot be accounted for in flight planning with confidence (Barber et al. 2019) without nowcasting products. In addition, without real time observations of convection from satellite and ground-based radar systems, the pilot has to rely on visual cues of developing convection and proper usage of on-board radar.

High resolution modeling is commonly used to examine small-scale processes that operational forecasting systems cannot resolve. CIT occurs across multiple scales from 10 m to 1000 m (Lester 1994), and is generally parameterized in operational forecasts. High resolution simulations allow for more in depth analysis of convective processes that in turn produce turbulence, which aids in the development of new prediction systems. These small-scale and temporally limited processes include the generation of convective gravity waves, enhancement deformation zones along cloud boundaries, and enhancement of shear as convection penetrates the tropopause. High resolution simulations of convection allow for further examination of the characteristics of turbulence and the relationship of convective intensity.

This study will examine the influence of environmental conditions on the distribution of out-of-cloud CIT for tropical and midlatitude convective simulations to determine if the probability of experiencing CIT varies between regions using high resolution simulations. More specifically, this study will investigate if the environmental conditions are similar for convective type in the midlatitudes and tropics and if the likelihood of turbulence is similar. Six encounters of moderate to severe CIT in various

convective regimes are used as simulation case days and compared to observations. Suggestions of improved turbulence prediction in the tropics and midlatitudes will be a result of this research. These simulations are analyzed to identify improvements to global turbulence prediction.

6.2 Data and Methods

In this study, 24 to 30 hour simulations of midlatitude and tropical convection are made using the Advanced Research WRF (ARW) model version 3.7 (Skamarock and Klemp 2008). All simulations are initialized with ERA-Interim global reanalysis data at various times (Table 13). One parent and two nested domains are used in these simulations with a horizontal grid spacing of 4.5 km, 1.5 km, and 500 m from the outer to innermost domain (Fig. 49). All domains have 100 vertical levels. The vertical grid spacing between 8 km and 12 km is approximately 325 m. The number of vertical levels is decreased to 65 (~ 550 m grid spacing between 8 km and 12 km) for 04 June 2018, due to a numerical instability issue in the simulation, likely due to the terrain. A 10-km damping layer is used at the model top which is set to approximately 30 km (10 hPa). This study uses the WDM6 microphysical parameterization and the Mellor-Yamada-Janjić (MYJ) planetary boundary layer scheme (additional parameterization information is provided in Table 14) for all simulations except 10 July 1997 and 03 August 2009. These particular cases use the Morrison microphysical scheme as it produces convection that is in better agreement with observations. Simulation output is saved every 10 minutes during periods of convective activity to examine convective development, maturity, and dissipation of individual convective cells (Table 13).

Turbulence is identified in this study using a suite of commonly used diagnostics including the Brown Index, Colson-Panofsky turbulent kinetic energy, Richardson number, DTF3, eddy dissipation rate, and second-order structure functions (see Ap-

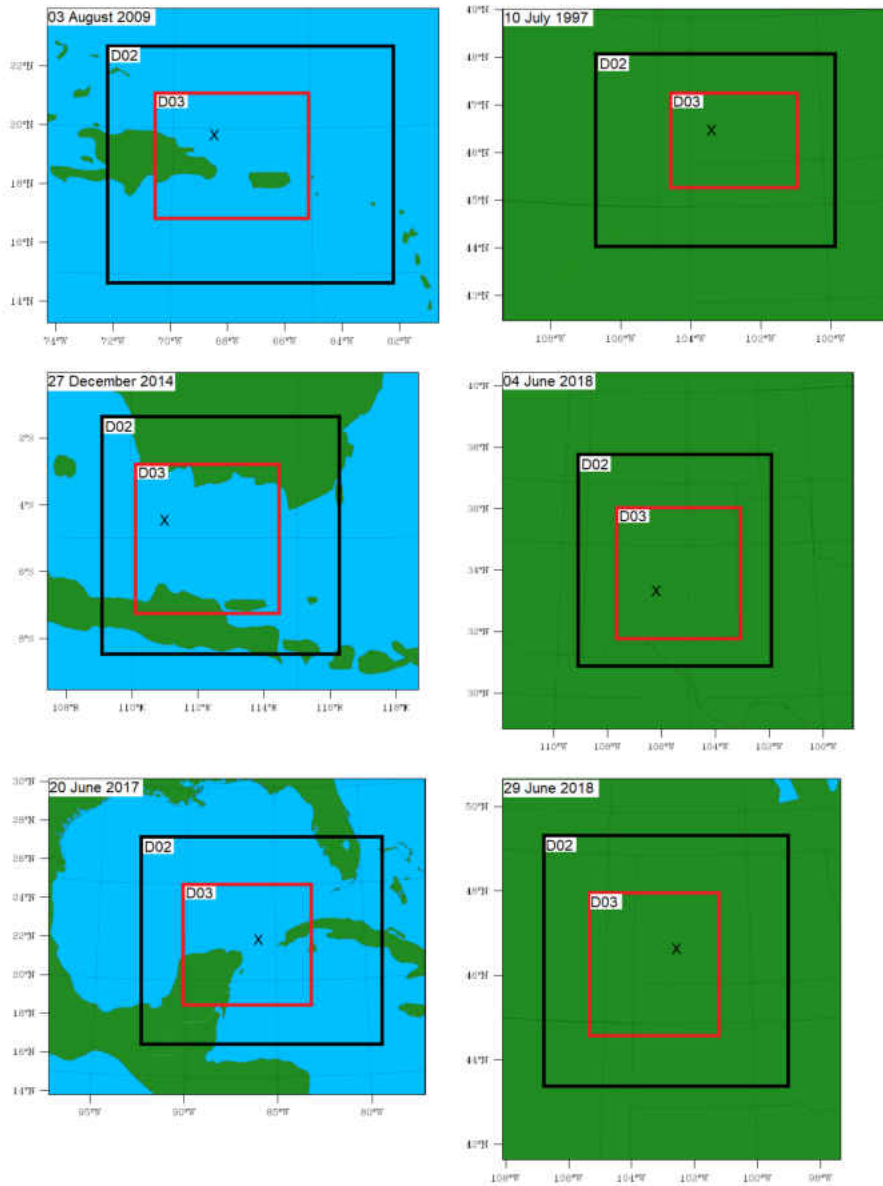


Figure 49: Model domain of case studies. D01 and D02 have a horizontal grid spacing of 4.5 km and 1.5 km. Innermost nest (D03) has a horizontal grid spacing of 500 m. “X” represents the location of the turbulence encounter.

Table 13: Initialization time, analysis period, and time period of increased temporal resolution.

Case day	Initialization time	Analysis period	Period of increased temporal resolution
03 Aug 2009 (DCT)	1200 UTC 02 Aug	1800-1800 UTC	1200-1400 UTC
10 July 1997 (DCM)	0000 UTC 10 Jul	0600-0600 UTC	1800-2300 UTC
27 Dec 2014 (MCT)	0000 UTC 27 Dec	0600-0600 UTC	0000-0400 UTC
04 Jun 2018 (MCM)	1200 UTC 03 Jun	1800-0600 UTC	1900-2300 UTC
20 Jun 2017 (HCT)	0000 UTC 20 Jun	0600-0600 UTC	1200-1800 UTC
29 Jun 2018 (HCM)	1200 UTC 29 Jun	1800-1800 UTC	1800-0000 UTC

pendix for calculations). Structure functions and eddy dissipation rate in particular are chosen based on their performance from previous studies in the midlatitudes and tropics (Barber et al. 2018; 2019). A separation distance of $7\Delta x$ is used for the calculation of structure functions in this study. The alteration in separation distance from Barber et al. (2019) and chapter 5 ($10\Delta x$) is based on previous investigation of separation distance when 500 m resolution is implemented. In-cloud and out-of-cloud turbulence are differentiated from one another using the mixing ratios of cloud ice and cloud water. A threshold of greater than or equal to 0.1 g kg^{-1} (Lane et al. 2003) defines in cloud and less than 0.1 g kg^{-1} defines out of cloud. An 18-dBZ threshold for simulated radar reflectivity is used to determine the echo top height which is used as a proxy for storm height. The distinction between developing convection and mature will follow the methodology of Barber et al. (2019) and chapter 5, with the distinction that the 90th percentile calculation is performed on all vertical velocities of the object instead of only the maximum velocity of the column. The calculations

Table 14: Model parameterizations used in simulations.

Model physics	Model setup
Microphysics	WDM6 (Morrison for DCT and DCM)
PBL	MYJ
Surface layer	MM5
Land surface	Noah
Shortwave radiation	RRTMG SW
Longwave radiation	RRTMG LW

of static stability (N^2 ; square of Brunt Vaisala frequency) and vertical wind shear (S_v^2) follow the calculations of chapter 4. Static stability, vertical wind shear, and vertical velocity are used to characterize the environment around convection as many of them relate to turbulence generation.

6.3 Results

6.3.1 Case day and simulation overviews

In this section, details regarding six aviation encounters of convectively-induced turbulence are summarized. Each case is identified in text through acronyms describing the type of convection that was the likely cause of turbulence (i.e., developing convection- DC, mature convection- MC, or hybrid- HC) and the region the case occurred in (i.e., tropical- T or midlatitude- M). Each tropical turbulence case is paired with a midlatitude turbulence case in which the convective type and apparent cause of turbulence was similar. Table 15 provides a summary of the time and location of the turbulence encounters. Richardson number (Ri), eddy dissipation rate (EDR), and second order structure functions (SF) for each case day are provided in Figures 50-55 as depictions of areal coverage and turbulence intensity in the region of interest. The height of interest of each case varies in order to be related to the flight altitude at

Table 15: Location and time of aviation encounter with turbulence.

Case day	Time of encounter	Location of encounter
DCT	0755 UTC	19.73 °N, -68.55 °E
DCM	2141 UTC	46.4 °N, -103.6 °E
MCT	2317 UTC	3.62 °S, 109.70 °E
MCM	0108 UTC	33.4 °N, -106.4 °E
HCT	1651 UTC	21.84 °N, -86.16 °E
HCM	2257 UTC	46.51 °N, -102.46 °E

the time of the turbulence encounter. The results discussed below are the diagnostics without calibration.

03 August 2009 (DCT)

On 03 August 2009, a Boeing 767 encountered severe turbulence while flying to the northeast of the Dominican Republic (19.73 °N, -68.55 °E) at 0755 UTC. Convection in the area was rapidly developing and the aircraft flew through the top of a convective updraft (Monette and Sieglaff 2014; Ahmad and Proctor 2011; NTSB 2011; Vasquez 2009) causing 33 minor injuries. Vertical accelerations experienced by the aircraft ranged from -1 g to 2 g between 11 km and 11.5 km for no more than 8 seconds. While convection was forecasted for this region, turbulence was not predicted along the aircraft’s flight path by the deformation-vertical shear index (NTSB 2011). Although turbulence was not predicted, the captain was aware of convection in the area and had begun safety procedures to limit hazards associated with convection. A meteorological overview of this case day was compiled by Vasquez (2009). Briefly, the area in which the flight experienced turbulence was influenced by the Bermuda high with weak winds aloft, but instability was present in sounding observations between 8 km and 12 km. Convection was very isolated, extending past 11 km in very few cells, and likely was enhanced by a tropical easterly wave propagating through the region. Satellite observations were used to confirm the aircraft had penetrated a developing

convective cell. This case highlights the limitations of turbulence prediction systems (forecasts and nowcasts), communication procedures between the pilot and passengers, as well as the hazards associated with developing convection in data sparse regions. The following paragraph will discuss the simulated convective properties for DCT.

Isolated cells with simulated radar reflectivity values greater than 35 dBZ at 2-km initiate over the land features of the Dominican Republic and Haiti, due to diurnal heating three hours into the simulation on 02 August 2009. Oceanic convection initiates nine hours later at 0000 UTC on 03 August as weak isolated cells (radar reflectivity values less than 50 dBZ) in the northeast region of the domain. Oceanic convection persists north of the Dominican Republic for the next 18 hours of simulation and reaches maximum intensity near 1340 UTC as convection propagates westward. Echo top heights over the ocean are less than 8 km through the simulation period, until after 1200 UTC when the depth of three convective cells northeast of the Dominican Republic exceed 10 km. The morphology and depth of convection resembles the observed convection (weak isolated cells). Convective available potential energy (CAPE) in the domain was greater than 2000 J kg^{-1} and the tropopause was near 13.5 km. Compared to radar observations from San Juan, the simulated convection over the ocean initiates approximately four hours later than observations, but the location of the convective cell that likely influenced the aircraft is within 50 km of observations. The time period of 1200 UTC to 1400 UTC on 03 August will be used to analyze the influence of convective stage on turbulence as it compares well against observations, where cells are increasing in depth.

Simulated echo top heights, minimum Richardson number (Ri), maximum eddy dissipation rate (EDR), and maximum second-order structure functions (SF) at 1340 UTC are shown in Fig. 50 between 8 km and 12 km, as the turbulence

encounter was near 10 km, and observed convection was extending past the altitude of the aircraft. A large region of turbulence diagnosed by Ri is present to the south of active convection between 8 km and 12 km from 1330 UTC to 1400 UTC. The majority of the turbulence is out of cloud and increases in areal coverage with time. Near the convective cell most representative of the cell the aircraft penetrated, turbulence is not diagnosed by Ri. The use of Ri as a diagnostic for turbulence on this case day would have indicated the presence of out of cloud turbulence south of convection, but not turbulence directly near or within the convective cells themselves. EDR highlights a similar area of possible turbulence as Richardson number. Again, the hazardous region is to the south of convection and is out of cloud. However, when EDR is converted to turbulence intensity and uncalibrated, the intensity is light and null. The use of EDR with current thresholds and without calibration would not have predicted turbulence greater than light along the flight path and would have predicted an extremely small likelihood of experiencing turbulence in cloud. Maximum SF values occur in the same region as Ri and EDR indicated, as well as to the north of the turbulence encounter location. Without calibration, the conversion of SF to turbulence intensity is light or null out of cloud. However, SF does indicate moderate or greater turbulence between 8 and 12 km in the simulated convective cell most similar to the observed cell. In terms of prediction, SF would have been a beneficial diagnostic to aviation flying near developing convective cells.

10 July 1997 (DCM)

On 10 July 1997, a Boeing 757 encountered severe turbulence while out of cloud flying southwest of Dickinson, ND (46.4 °N, -103.6 °E) at 2141 UTC. The aircraft was navigating between numerous convective cells that were extending higher than the altitude of the aircraft (11.2 km) near the time of the incident (NTSB 1997). The aircraft passed over a developing convective cell that was located between two mature

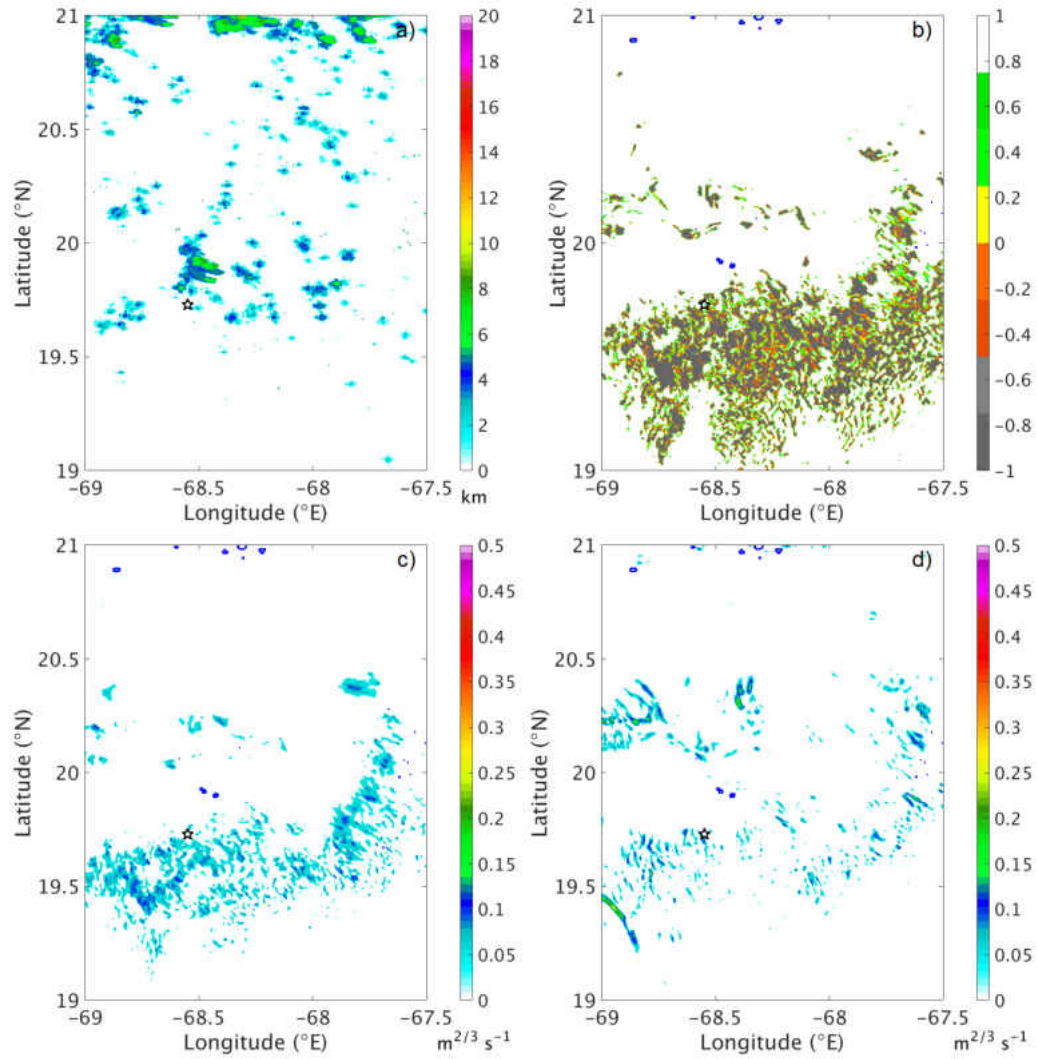


Figure 50: Echo top heights (a), minimum Richardson number (b), maximum eddy dissipation rate (c), and maximum second-order structure functions (d) for DCT (03 August 2009) at 1340 UTC between 8 km and 12 km. Echo tops greater than 8 km are shown in b-d as blue contours, and the black star represents the location of the aircraft at 0755 UTC.

convective cells, causing 22 injuries. Vertical accelerations ranged between 1.77 g and -0.65 g for less than 2 seconds. As was the case for DCT, convection was forecasted in the region, but turbulence was not predicted along the flight path. The pilot had warned the passengers of possible turbulence when convection was in the region, but the “FASTEN SEATBELT” sign was not illuminated. This particular case has been examined with numerical simulations in Lane et al. (2003) in which a limited meteorological overview is provided. Convection was initiated by a frontal system that was associated with a prefrontal trough. The region was favorable for convective activity as convective available potential energy (CAPE) was greater than 3500 J kg^{-1} and the tropopause was near 11 km. This case again highlights the limitations of turbulence prediction systems (forecasts and nowcasts), communication procedures between the pilot and passengers, and the hazards associated with developing convection. DCM is paired with DCT as the turbulence incidents were caused by rapidly developing convective cells as aircraft passed through and over. The following paragraph will discuss the convective properties simulated for DCM.

Simulated convection on 10 July initiates in the domain at 2000 UTC and develops into two intense convective complexes with 2-km simulated radar reflectivity values exceeding 55 dBZ over the next four hours of simulation time. Compared to observations near the time of the aircraft encounter with the developing convective cell, three individual simulated convective features (two more intense and one weaker) are present in the domain at 2200 UTC. By 2300 UTC the all three cells have increased in strength and echo top heights exceed 12 km. The convective cell that likely is associated with the turbulence encounter rapidly increases in vertical extent and areal coverage from 2200 UTC to 2300 UTC. CAPE in the domain is greater than 3000 J kg^{-1} and the tropopause is near 12 km. The morphology of simulated convection compares well to previous scientific investigation of this case, however the intensity

is too strong as a result of the microphysics used in this simulation. Maximum vertical velocities exceed 60 m s^{-1} which is likely unrealistic and a byproduct of the microphysics. However, the Morrison microphysical parameterization was used in order to be consistent with DCT. The time period of 1800 UTC to 2300 UTC on 10 July will be used to analyze the influence of convective stage on turbulence as it compares well against observations, where the suspect cell is rapidly increasing in vertical depth.

Simulated echo top heights, minimum Ri, maximum EDR, and maximum SF at 1340 UTC are shown in Fig. 51. Due to the differences in convective height, the turbulence diagnostics are evaluated between 14 km and 16 km to be representative of an aircraft flying above a convective cell that is rapidly developing. The height range of 2 km is also applicable to the vertical envelop of turbulence above convection (1-3 km; Lane et al. 2003). As the convective cell increases in depth and areal coverage, Ri out of cloud above the cell decreases, and is indicative of turbulence. The areal coverage of EDR again agrees with the areal coverage of Ri and indicates localized regions of moderate to severe turbulence above cloud. Both Ri and EDR adequately predict turbulence above a rapidly growing convective cell. SF also diagnoses moderate to severe turbulence above the convective cell, but the areal coverage is much greater than both EDR and Ri predict. Through time, SF diagnoses severe turbulence before the convective cell reaches a height of 13 km. While, SF does predict turbulence of appropriate intensity above the convective cell, and the lateral distance from convection is within 50 km of convection, the areal coverage varies drastically from the other diagnostics. The individual values of SF also far exceed the threshold of severe turbulence by more than one order of magnitude. SF for this particular case likely needs to undergo calibration.

27 December 2014 (MCT)

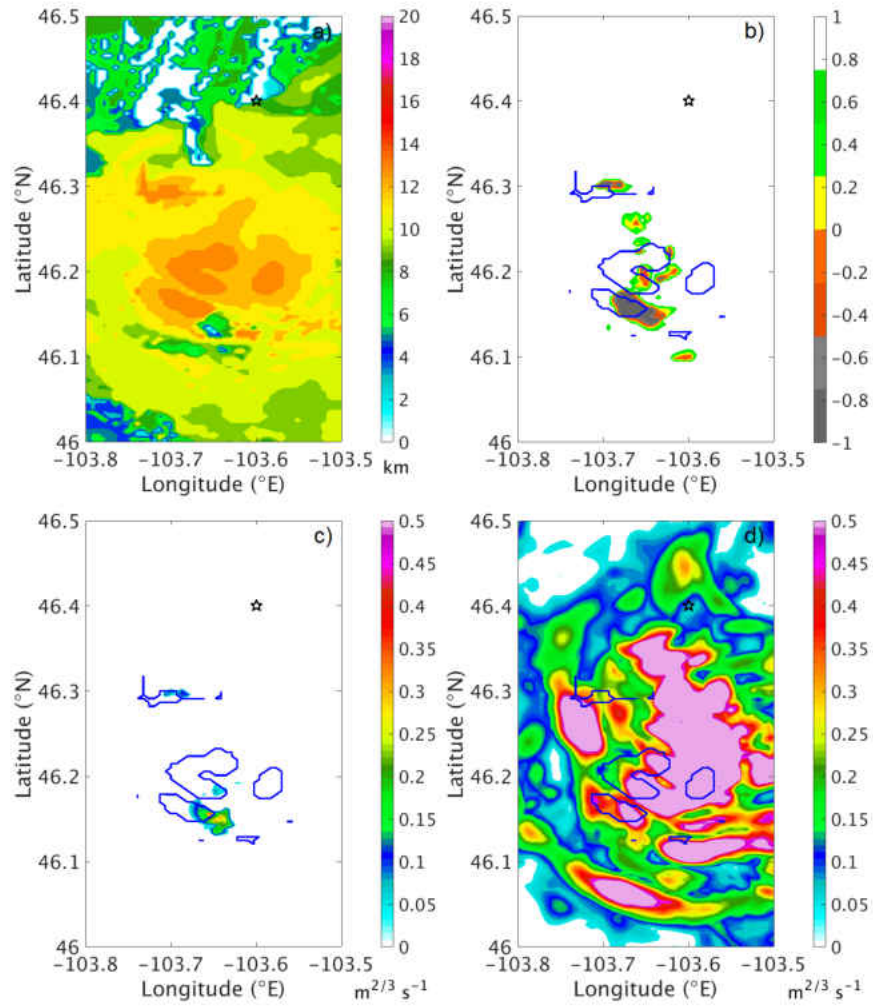


Figure 51: Echo top heights (a), minimum Richardson number (b), maximum eddy dissipation rate (c), and maximum second-order structure functions (d) for DCM (10 July 1997) at 2210 UTC between 14 km and 16 km. Echo tops greater than 13 km are shown in b-d as blue contours, and the black star represents the location of the aircraft at 2141 UTC.

On 27 December 2014, at approximately 2317 UTC, an Airbus A320 flying at 9.75 km went into an unrecoverable aerodynamic stall over the Java Sea (3.62 °S, 109.70 °E). Convection was present along the flight route and pilots had requested numerous altitude changes in order to avoid the convection. While the Aircraft Accident Investigation Report (KNKT 2015) concluded that the accident was not directly caused by weather, but was unfortunately caused by pilot error, this case is a favorable candidate for assessing turbulence prediction in tropical regions. The flight path was through a region with active convection and the predetermined flight altitudes were turbulent, suggesting prediction systems were underestimating turbulence intensity and convective hazards. A squall line was present in the region, propagating westward, and echo top heights varied between 7.3 km and 13.4 km with the proposed flight path intercepting two mature convective cells with echo top heights greater than 10 km. The convection was likely caused by the migration of the Intertropical Convergence Zone. The tropopause was located above 16 km in altitude. This case illustrates the limitations of turbulence prediction systems (forecasts and nowcasts) and the challenges pilots face while navigating around convection. The following paragraph will discuss the simulated convective properties for MCT.

Simulated convection on 27 December 2014 initiates from a boundary near the land feature of Singapore with intense convective cores that weaken and dissipate by 1200 UTC. After 1200 UTC, a secondary boundary oriented along 5 °S latitude propagates northward and initiates a convective line more than 100 km long over the Java Sea. Convection along the boundary has echo top heights greater than 15 km and 2-km radar reflectivity values greater than 50 dBZ, but dissipates by 2200 UTC. The particular convective feature that likely influenced the aircraft along its flight path occurred near 0300 UTC on 28 December, approximately four hours after observations. This convection was linear, extending again along 5 °S latitude and 4.5

°S latitude with echo top heights 14 km in three regions. Maximum simulated vertical velocities within the convective cores were greater than 25 m s^{-1} . The simulated tropopause height on 27 December 2014 is 15.5 km and the environment is favorable for convection with CAPE greater than 2200 J kg^{-1} . The time period of 0000 UTC to 0400 UTC on 28 December will be used to analyze the influence of convective stage on turbulence as the simulated convection is oriented along the flight path with the vertical depths and areal coverage similar to observations.

Simulated echo top heights, minimum Ri, maximum EDR, and maximum SF are evaluated between 8 km and 12 km (Fig. 52). Of interest is the areal coverage of out-of-cloud turbulence around the convection, as the aircraft was navigating around the observed convection. Ri predicts localized regions of turbulence along boundary features near and away from convection. The areal coverage of the lowest Ri are found in the western portion of the domain, near the same longitude that the aircraft was requesting altitude changes. Out-of-cloud turbulence is diagnosed by Ri along the flight path and between the altitudes the aircraft was operating in. Interestingly, EDR for this case does not diagnose turbulence out of cloud around active convection and the probability of in-cloud turbulence with intensity greater than light is very low. SF has a similar area coverage as Ri and diagnoses out-of-cloud turbulence within 30 km of active convection with the most intense turbulence to the southeast and northwest of the western convective cell. The localized turbulence regions identified by SF is representative of observations as the aircraft navigated around the convection with and without encountering turbulence.

04 June 2018 (MCM)

On 04 June 2018, an Airbus A319 flying in New Mexico at approximately 10 km intercepted a convective hailcore at 0108 UTC. The aircraft experienced substantial structural damage with all windshield panels shattered and the nose of the aircraft

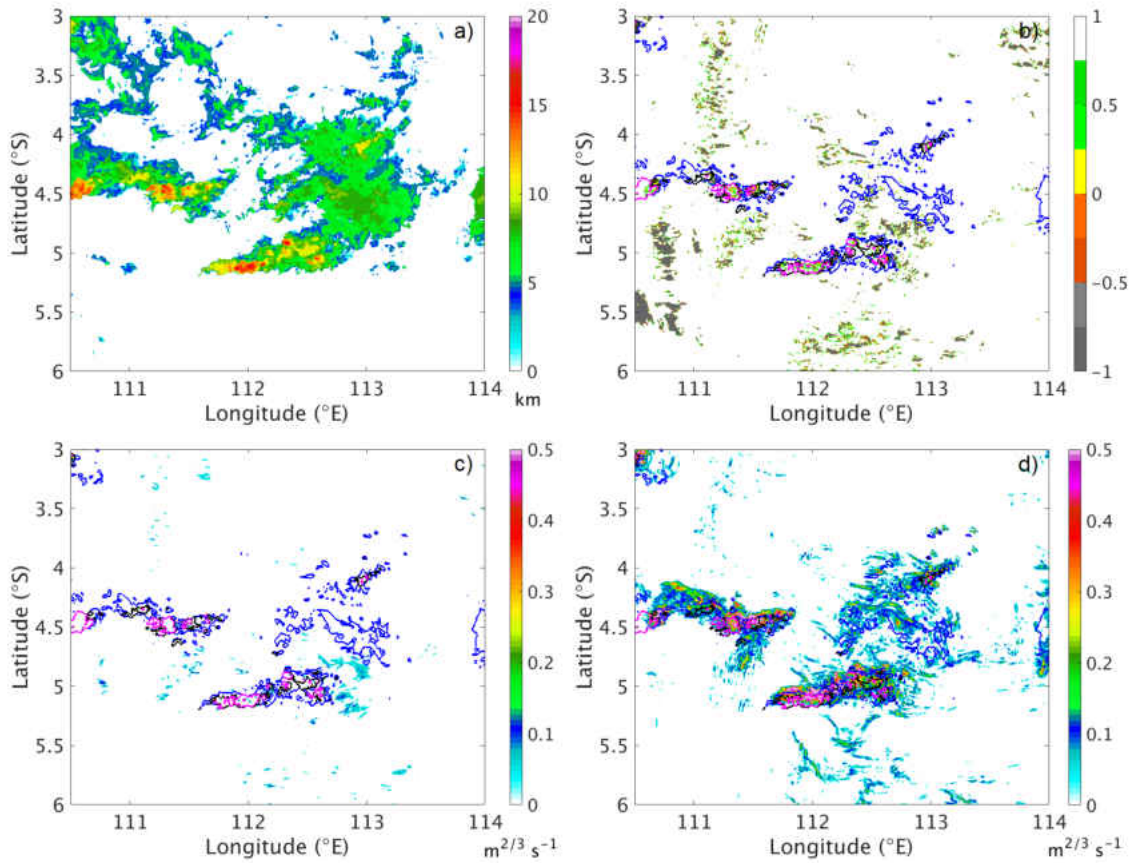


Figure 52: Echo top heights (a), minimum Richardson number (b), maximum eddy dissipation rate (c), and maximum second-order structure functions (d) for MCT (28 December 2014) at 0300 UTC between 8 km and 12 km. Echo tops greater than 8 (10 and 12) km are shown in b-d as blue (black and magenta) contours.

destroyed, forcing an emergency landing in El Paso, TX. Fortunately, no passenger or flight crew injuries occurred because the safety protocols were followed by those aboard the flight. It is hypothesized that the A319 was attempting to navigate between convective cells that were growing past typical cruising altitudes. A second aircraft in the vicinity of the A319 reported severe turbulence at 33.4 °N, -106.4 °E while flying at 11 km. Convection was forced by an upper level front extending from Colorado to New Mexico and was forecasted to be severe in intensity due to high CAPE (greater than 3000 J kg⁻¹) and bulk shear. Numerous reports of tornadoes and hail occurred in New Mexico and Texas. Echo top heights ranged from 10 km to over 16 km in the most intense cells and the tropopause on this day was above 12 km. The complexity of navigating through regions with active convection and maintaining a safe and efficient flight is illustrated by this turbulence encounter. This case day is paired with MCT because convection was severe in strength, was similar in convective morphology, and turbulence production is hypothesized to be through similar mechanisms. The following paragraph will discuss the simulated convective properties for MCM.

Simulated convection on 03 June 2018 initiates in an environment with CAPE greater than 1900 J kg⁻¹ at 1500 UTC on the east side of the San Andres mountain range. As the diurnal heating intensifies, a second, stronger line of convection with simulated radar reflectivity values greater than 55 dBZ forms along the mountain range and propagates to the east. The convective line begins to form a bowing segment near 0100 UTC as it moves out of the domain. Echo top heights exceed 12 km after 2200 UTC in four regions along a 200 km convective line. Convection propagates across the region of interest approximately two hours too early when compared to observations with slightly lower echo tops than observed. Simulated vertical velocities exceed 40 m s⁻¹ within the convective cores and is favorable for

hail production. The simulated cells most representative of the observed convection both aircraft were navigating through occurs near 2300 UTC at 33.5 °N, -106.6 °E. The time period of 1900 UTC to 2300 UTC on 03 June will be used to analyze the influence of convective stage on turbulence as the simulated convection resembles observed convection in location, strength, and morphology. Echo top heights increase in depth along the north and south portions of the convective line from 2230 UTC to 2300 UTC.

Simulated echo top heights, minimum Ri, maximum EDR, and maximum SF are evaluated between 8 km and 12 km (Fig. 53). For this case, two aircraft encountered convective hazards while in cloud, navigating between severe convective cells. The convective properties simulated in this study agree well with observations in the strength and location, however, out-of-cloud turbulence identified with Ri and EDR is null between the heights of interest. This result is likely influenced by the alteration of vertical resolution in this particular simulation. As was found in Barber et al. (2018), a coarser vertical resolution distributed out-of-cloud turbulence towards lighter intensity bins. However, in-cloud turbulence (MOG for EDR) is identified by both diagnostics in similar convective locations (e.g. 33.6 °N, -106.6 °E and 32.6 °N, -107.3 °E) in the strongest portions of the convective line, but is again localized. SF identifies much of the convective region as MOG in-cloud turbulence, and regional maximums of MOG out of cloud. The variation in areal coverage of turbulence is quite pronounced in this simulation, suggesting that vertical resolution is an important factor of turbulence prediction. In terms of a turbulence forecast for aviation, all three diagnostics identify in-cloud turbulence with MOG intensity.

20 June 2017 (HCT)

On 20 June 2017, a Boeing 737 encountered severe turbulence at 11 km in altitude while flying over the Gulf of Mexico (21.84 °N, -86.16 °E) near 1651 UTC.

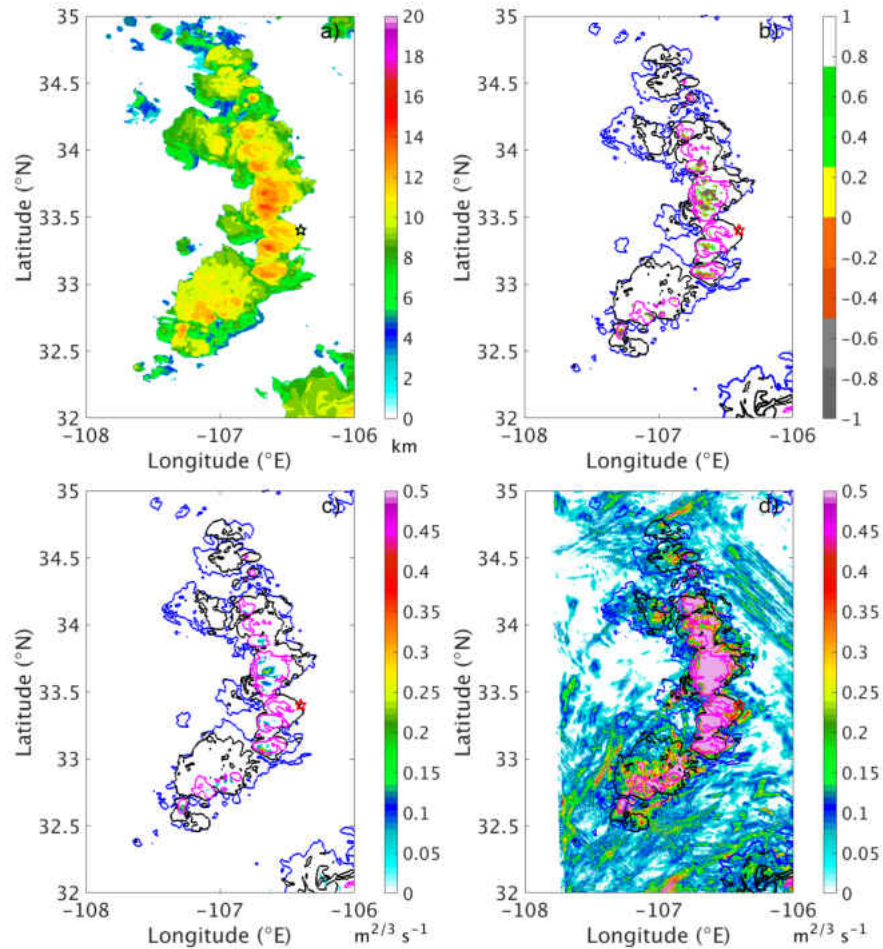


Figure 53: Echo top heights (a), minimum Richardson number (b), maximum eddy dissipation rate (c), and maximum second-order structure functions (d) for MCM (03 June 2018) at 2300 UTC between 8 km and 12 km. Echo tops greater than 8 (10 and 12) km are shown in b-d as blue (black and magenta) contours and the black (red) star represents the location of the aircraft at 0108 UTC on 04 June.

Convection was present along the flight route as the aircraft traveled from Panama City to Houston, TX. The aircraft decreased in altitude by 120 m and experienced normal load factors of -0.73 to 1.6 g for approximately 20 seconds (see Fig. 2 in Barber et al. 2019 or Fig. 37 in chapter 5). Nine passengers and one crew member sustained injuries and received medical attention. Additional information regarding the synoptic conditions for this particular case can be found in Chapter 5 or Barber et al. (2019). Convection was abundant in the flight region with storm depths exceeding 14 km in altitude. The tropopause on this day was above 14.3 km and CAPE was greater than 1500 J kg^{-1} . Observations and flight records indicate the plane was out of cloud at the time of the turbulence encounter, navigating between two regions of developing convection. This case highlights the complexity of navigating through regions with active convection and communication limitations between the pilot and passengers. The following paragraph will discuss the simulated convective properties for HCT.

Simulated convection initiates north of the Yucatán Peninsula at 1000 UTC as a narrow convective line with 2-km radar reflectivity values greater than 45 dBZ. As a sea breeze boundary forms to the east of the Yucatán Peninsula at 1200 UTC, convection initiates along the same longitude as the original simulated convection in chapter 5 (Barber et al. 2019). The convective line continues to intensify and persists between -87°E and -86°E through 1800 UTC. The simulated environment was very favorable for intense convection with CAPE values greater than 2500 J kg^{-1} for the majority of the simulation period. Echo top heights exceeded 13 km after 1240 UTC along the convective line and reached 17 km in numerous cells. Simulated convective depth was slightly higher than observations. Interestingly, the location of the convective line compares better to observations than the previous simulations with 3 km horizontal resolution (chapter 5). The time period of 1200 UTC to 1800 UTC

on 20 June will be used to analyze the influence of convective stage on turbulence probability.

Simulated echo top heights, minimum Ri, maximum EDR, and maximum SF at 1650 UTC are shown in Fig. 54. Ri indicates localized regions of favorable turbulence likelihood within the convective cores along the convective line. Out-of-cloud turbulence is not predicted by Ri along or near the cloud boundaries but approximately 50 km away from the convective boundaries (east and west). It is hypothesized that Ri is diagnosing a large-scale convectively generated gravity wave that is breaking in favorable regions away from convection. The vertical velocity field between 10 km and 12 km indicates in the area of increased out-of-cloud turbulence, vertical velocities oscillate between -2 m s^{-1} and 2 m s^{-1} (not shown). EDR indicates regions of turbulence in cloud but with less areal coverage than Richardson number. Interestingly, out of cloud approximately 50 km away from the cloud boundaries, EDR predicts light turbulence in the same areas indicated by Richardson number. The intensity of this turbulence is less than observations. SF indicates MOG turbulence in cloud along the convective line and LGT to MOG turbulence along the cloud boundaries. As was the case for Ri and EDR, approximately 50 km to the east and west of the convective line, a broad area of increased turbulence severity is present. In regards to aviation operations for this case day, the diagnostics are in contrast with one another especially in convective cloud. EDR under-predicts out-of-cloud and in-cloud turbulence (no in-cloud turbulence with lighter or greater severity and localized region of out-of-cloud light turbulence), while SF predicts much greater turbulence probability in cloud and out of cloud. SF would have been most beneficial diagnostic for turbulence avoidance because it captures various turbulence types.

29 June 2018 (HCM)

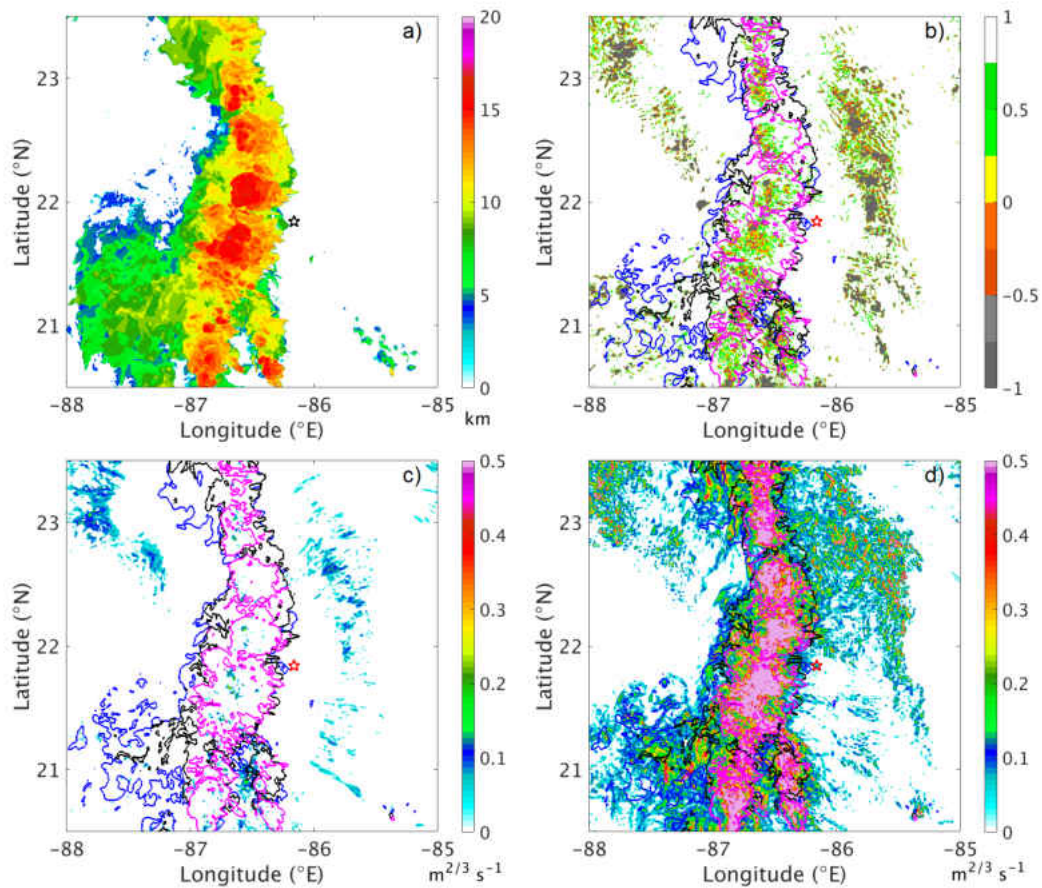


Figure 54: Echo top heights (a), minimum Richardson number (b), maximum eddy dissipation rate (c), and maximum second-order structure functions (d) for HCT (20 June 2017) at 1650 UTC between 8 km and 12 km. Echo tops greater than 8 (10 and 12) km are shown in b-d as blue (black and magenta) contours and the black (red) star represents the location of the aircraft at 1651 UTC.

On 29 June 2018, at 2257 UTC an Airbus 320 enroute to Newark, NJ experienced severe turbulence while flying at an altitude of 11 km near Dickinson, ND (46.51 °N, -102.46 °E). The aircraft decreased more than 600 m and decreased in speed by 50 kts at the time of the encounter. Convection was present along the flight path, with composite radar reflectivity values exceeding 45 dBZ in isolated cells west of Bismarck, ND and more intense cells exceeding radar reflectivity values of 55 dBZ in northwest SD. It is important to note that the flight path was along a region of Montana, North Dakota, and South Dakota where there is a void in radar coverage. Convection was severe in western SD where numerous storm reports were recorded including tornadoes, large hail, and severe winds within the hour of the turbulence encounter. CAPE exceeded 3000 J kg^{-1} and echo top heights were greater than 14.7 km. While no injuries occurred due to the encounter with severe turbulence, this case illustrates the challenges associated with flight planning and navigating near active convection. This case day is paired with HCT because the convective field was complex with storms of various intensity and stages, and limited ground observations were available for nowcasting products. The time period of 1800 UTC to 0000 UTC on 29-30 June will be used to analyze the influence of convective stage on turbulence probability in south west ND (Fig. 49). The following paragraph will discuss the simulated convective properties for HCM.

Simulated convection initiates at 1900 UTC near the western South Dakota, North Dakota border. Isolated cells intensify in two distinct regions with simulated 2-km radar reflectivity values greater than 50 dBZ. The cells propagate eastward and weaken by 0000 UTC on 30 June. Echo top heights exceed 10 km throughout the period of interest with the deepest storms to the south.

Simulated echo top heights, minimum Ri, maximum EDR, and maximum SF at 2250 UTC are shown in Fig. 55. Ri indicates a broad region of turbulence out of

cloud between the convective cells. In cloud, Ri also identifies a greater likelihood of turbulence in the deepest cells in the southeast of the domain. Interestingly, EDR highlights similar areas out of cloud near convection as turbulent. In these areas, turbulence is MOG. While out-of-cloud turbulence diagnosed by EDR agrees with Ri, in-cloud turbulence is much less than identified by Ri. SF diagnoses a large region of MOG both in cloud and out of cloud near convection. The regions of MOG turbulence do agree with both Ri and EDR. In regards to aviation operations, all three diagnostics identify regions of turbulence in and out of cloud and would have been beneficial for turbulence avoidance.

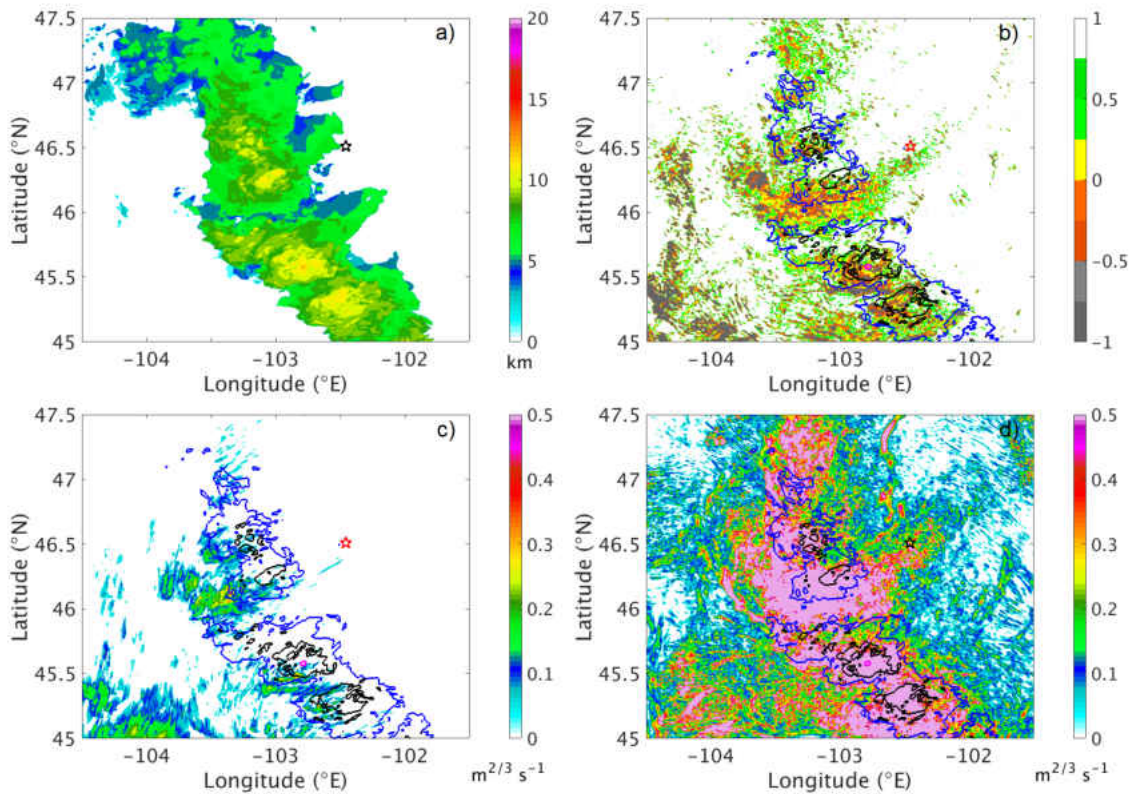


Figure 55: Echo top heights (a), minimum Richardson number (b), maximum eddy dissipation rate (c), and maximum second-order structure functions (d) for HCM (29 June 2018) at 2250 UTC between 8 km and 12 km. Echo tops greater than 8 (10 and 12) km are shown in b-d as blue (black and magenta) contours and the black (red) star represents the location of the aircraft at 2257 UTC.

6.3.2 Summary of turbulence diagnostics

Overall for the six cases, convective type, timing, and morphology were well simulated. The success of the diagnostics was mixed and was dependent on storm type and region. Ri predicted in-cloud and out-of-cloud turbulence well for five of the six cases, but underpredicted the out-of-cloud turbulence for MCM. EDR underpredicted in-cloud and out-of-cloud turbulence for three of the six cases (two of which were in the tropics). It is likely that the turbulent kinetic energy from the boundary layer scheme which only includes the vertical component of velocity is inaccurate. SF predicts in-cloud and out-of-cloud turbulence for all six cases, and captures turbulence generated by numerous sources, but needs to be calibrated for strong convection in the midlatitudes.

6.3.3 Distributions of in-cloud and out-of-cloud turbulence

The previous discussion has illustrated the intensity and areal coverage variations in turbulence diagnostics both in cloud and out of cloud during periods where simulated convection resembled observations of aircraft encounters with turbulence. There is also value in comparing the probability distributions of the turbulence diagnostics throughout all simulated convective periods in order to relate the differences to turbulence prediction through statistical methods. The optimal result for turbulence diagnostics is that the probability of encountering turbulence with specific intensity is accurately represented by the distribution of turbulence. Past studies have found that clear air turbulence distributions created from observations and model simulations are log-normal (Sharman and Pearson 2017; Frehlich and Sharman 2004a, Frehlich and Sharman 2004b; Cho et al. 2003; Nastrom and Gage 1985). The probability of light clear air turbulence from numerous diagnostics ranges from 10^{-1} to 10^{-2} and the probability of moderate or greater clear air turbulence is less than 10^{-3} . The probability of encountering MOG turbulence is greater in cloud than out of cloud

(Pearson et al. 2019). Furthermore, Cho et al. (2003), found that the distributions of environmental variables including shear, stability, and Richardson number from aircraft data were also log normal. Few studies have investigated the distributions of in-cloud and out-of-cloud CIT diagnosed by various methods in both the midlatitudes and tropics, for a variety of convective types, from individual model simulations. Distributions are also helpful indicators of which diagnostics are in need of calibration to theoretical values. It is hypothesized that the probability of experiencing turbulence in a convective environment is greater than in an environment without convection and the absence of a jet feature.

Figure 56 provides the in-cloud and out-of-cloud turbulence distributions diagnosed from EDR and SF for the six simulated cases between 8 km and 12 km. The distributions of turbulence for DCT (03 August 2009) are in stark contrast to DCM (10 July 1997) in probability for both diagnostics and location (in-cloud versus out-of-cloud). The probability of out-of-cloud and in-cloud turbulence for DCT is much less than for DCM for both diagnostics. However, the probability of in-cloud turbulence is in close agreement between SF and EDR for DCT. The decrease in probability for DCT is likely because the convection was weaker and did not reach the tropopause. The probability of encountering turbulence diagnosed by SF for DCM is an order of magnitude greater than EDR, and does not decrease at a rate shown in previous studies (Sharman and Pearson 2017). As was previously discussed, the individual values of SF are well beyond the intensity thresholds normally observed in the atmosphere and used in prediction systems, and the discrepancies between EDR and SF suggest that SF needs to be recalibrated for this particular case. EDR, out of cloud is one order of magnitude lower than previous work has found even with adjustments to past intensity thresholds (i.e., Lane et al. 2012). These findings suggests that the variation in probability for specific diagnostics is related to the strength of convec-

tion (i.e., weak convection, lower turbulence probability, stronger convection, higher turbulence probability). This hypothesis is further supported by the distributions of SF for MCT (Fig. 56-27 December 2014), MCM (Fig. 56-04 June 2018), HCT (Fig. 56-20 June 2017), HCM (Fig. 56-29 June 2018) which shows very similar probabilities of turbulence from convection with similar properties (height, morphology, likely generated gravity waves).

In terms of aviation turbulence prediction, the probability of out-of-cloud turbulence predicted by EDR is lower than SF in these convective regimes. The probability of encountering in-cloud turbulence is in closer agreement between SF and EDR, where moist instabilities are diagnosed by both methods. It is hypothesized that out-of-cloud turbulence probabilities from EDR are lower for the three weaker convective regimes because EDR is derived from the vertical velocity component within the boundary layer scheme, where SF is analyzing the horizontal components of the velocity field. In Barber et al. (2018), EDR distributions varied dramatically for each convective case. It is unlikely that a calibration of EDR would increase the accuracy of out-of-cloud turbulence prediction. Instead, EDR calculated from all components of the velocity field would likely improve the skill of EDR. Additional simulations are needed to test this hypothesis. In summary, SF needs to be calibrated for strong, rapidly developing convection in the midlatitudes and EDR under predicts out-of-cloud turbulence for both midlatitude and tropical convection.

6.3.4 Characteristics of the simulated environment parameters near convection

In this section comparisons of the simulated environment around simulated mature and developing convection for the six cases will be made and related to the likelihood of turbulence. Mean out-of-cloud static stability, vertical wind shear, and vertical

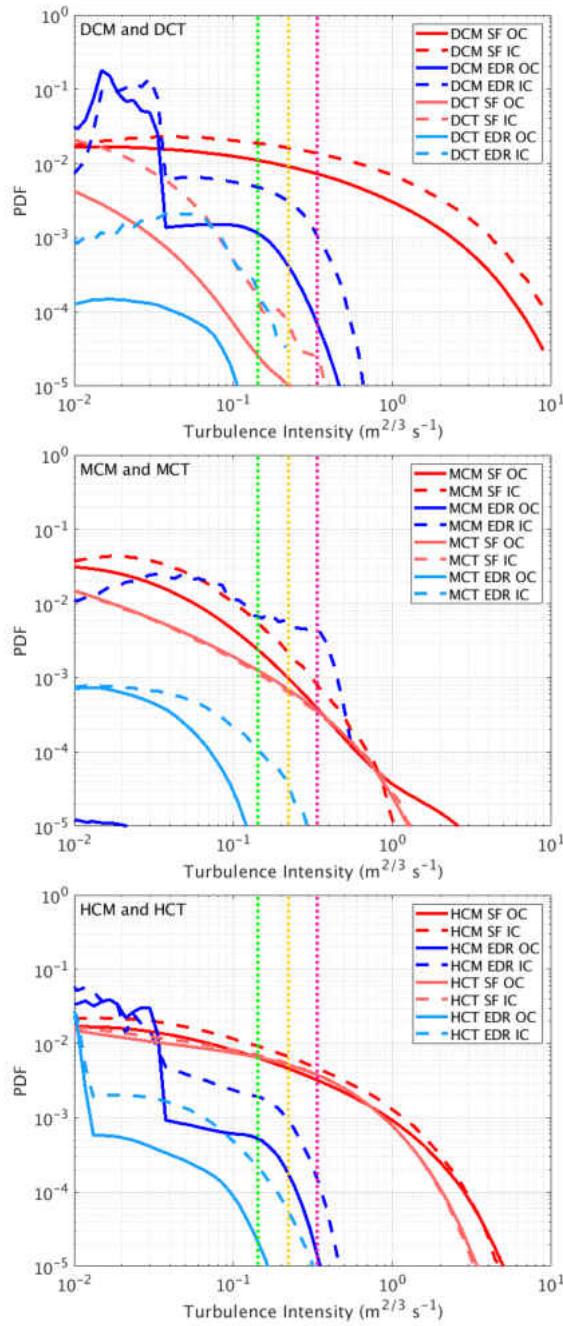


Figure 56: Distribution of in-cloud and out-of-cloud turbulence diagnosed using uncalibrated second-order structure functions and eddy dissipation rates between 8 km and 12 km when convection is present for the six cases. The green (yellow and magenta) vertical line represents the threshold for light (moderate and severe) turbulence.

velocity are examined between 8 km and 12 km for all grid points closest to mature convective objects and all grid points closest to developing convective objects, at a frequency of 10 minutes during the time periods shown in Table 13. The objective of this analysis is to determine if the simulated environmental conditions near similar convective types in the midlatitudes and tropics are similar and if turbulence diagnostics are influenced by the variation in environmental conditions. More specifically, are the stability and shear distributions the same during similar tropical and midlatitude convective periods and is the turbulence response the same? Additionally, does the stage of convection influence the environmental parameters and is there a variation in out-of-cloud turbulence areal coverage and strength. This analysis will use SF instead of EDR because EDR underpredicted the turbulence intensity out-of-cloud for more than half of the simulations when compared to the observed turbulence intensity and expected in-cloud areal coverage. In addition, SF were able to capture turbulence generated by the many convectively induced mechanisms including gravity waves for many of the simulations. It is noted that out-of-cloud vertical velocities are used as a diagnostic of turbulence potential through gravity wave processes, and not a characteristic of the environment.

Simulated echo top height distributions are created to analyze the frequency of convection surpassing the tropopause for the simulations, which is related to turbulence production. Convective type and region influences the distribution of echo top heights (Fig. 57). While, the stronger tropical cases (MCT and HCT) have a higher percentage of echo top heights that exceed 15 km, because the tropopause height is higher in the tropics, the percentage of simulated convective cells surpassing the tropopause is similar for their paired cases (MCM and HCM). Although convective type varied between the simulations, it is of interest to examine the frequency at which convection was identified as developing for the simulations versus mature,

especially as further discussion will compare the environment near the two stages of convection. In general, developing convection accounts for nearly 30% of the convection for the six simulations (Fig. 58). DCT had much weaker convection than DCM, but the percentage of developing cells are nearly the same, suggesting that the environment is being modified by similar frequencies of convection. MCM and HCM have slightly higher percentages of developing convection likely as a result of backbuilding over elevated terrain.

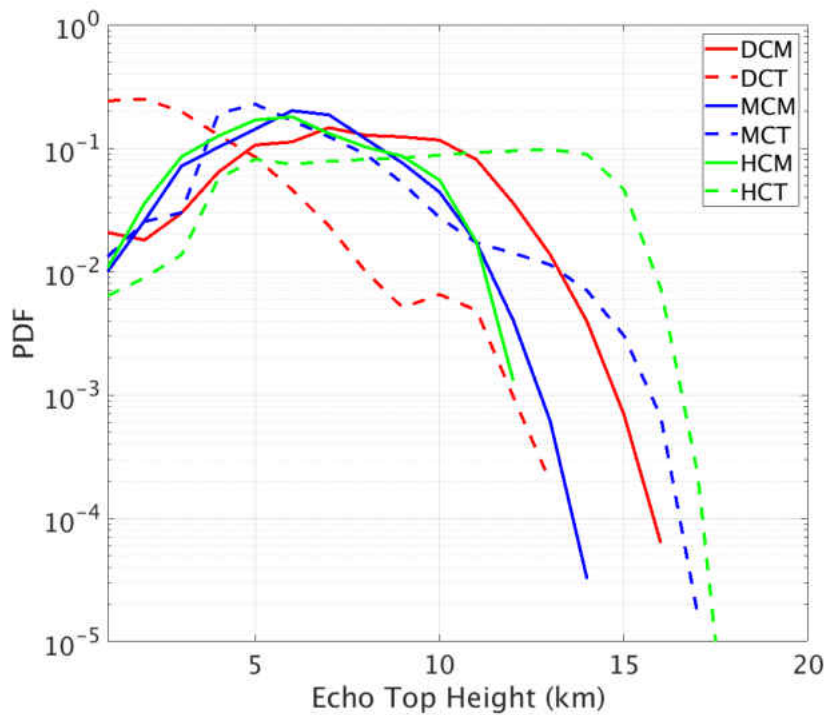


Figure 57: Domain-wide distribution of echo top heights for the six simulations (10 minute output periods). Solid lines are the midlatitude cases and dashed lines are the tropical cases.

Figure 59 provides the distribution of out-of-cloud turbulence (from SF) for each case day for grid points closest to mature convective objects and closest to developing convective objects between 8 km and 12 km. First, the turbulence probability for the region around mature convection varies significantly for the paired cases and

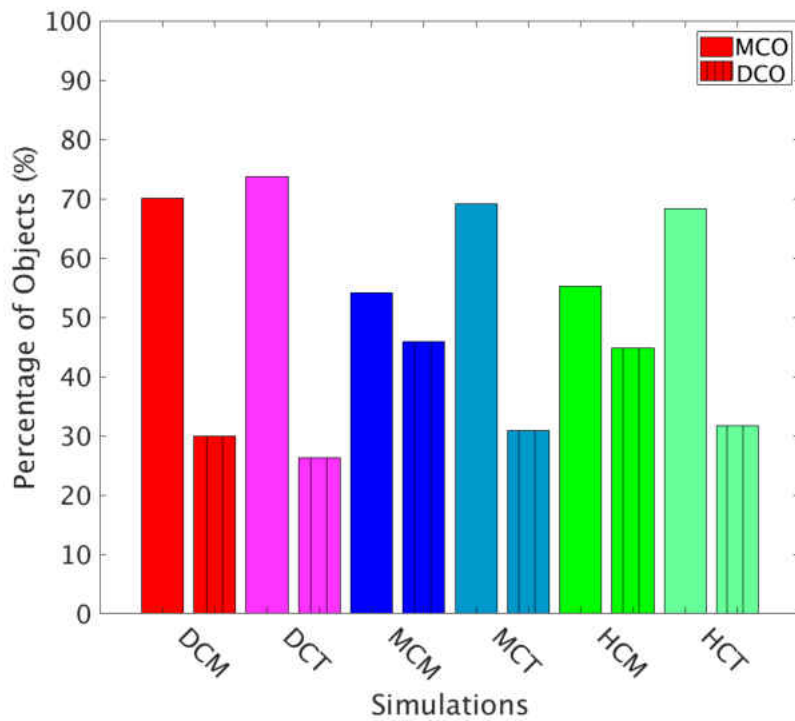


Figure 58: Percentage of convective objects identified as mature convection (MCO) and developing convection (DCO) for the six simulations. Bars with vertical lines represent developing convection.

for midlatitudes versus the tropics. Near mature convection, the midlatitudes have a higher probability of turbulence. Interestingly, HCM and HCT have similar turbulence distributions likely because the probability of storms surpassing the tropopause were similar. The probability of turbulence is greater for all the cases near developing convective objects (an order of magnitude larger than for mature for all cases except DCM). This finding highlights the hazards associated with developing convection in regards to aviation operations. The greatest increase in turbulence probability from the mature subset to the developing subset occurs for the tropical cases, illustrating the hazards associated with developing convection in regions with limited real time data (ground-based radar coverage and satellite observations).

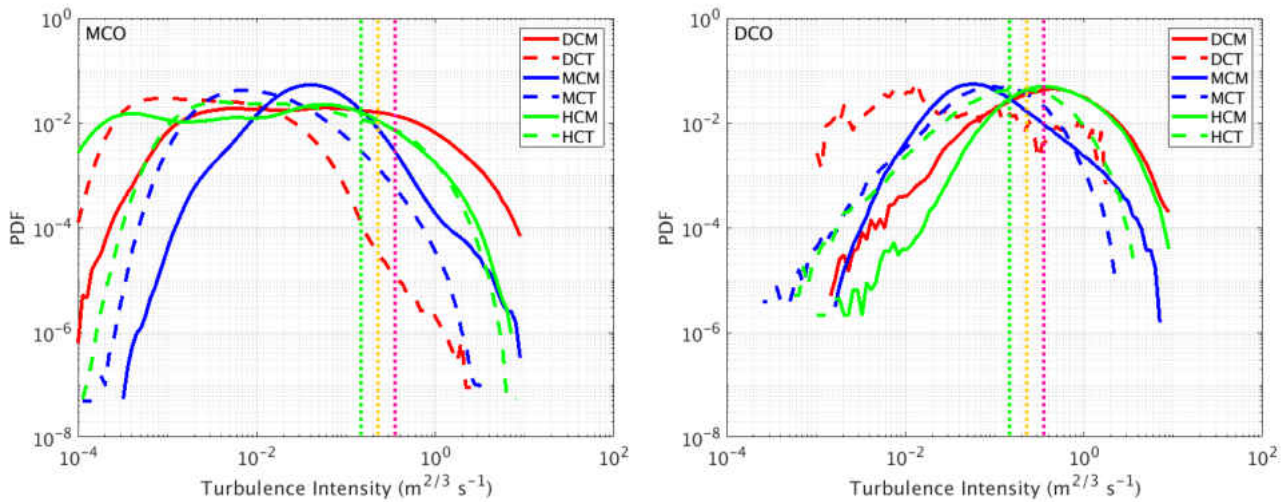


Figure 59: Distribution of out-of-cloud turbulence diagnosed by second-order structure functions between 8 km and 12 km nearest to mature convection (MCO) and developing convection (DCO) for the six simulations. The green (yellow and magenta) vertical line represents the threshold for light (moderate and severe) turbulence.

The distributions of mean static stability for the six cases are shown in Fig. 60. It is important to note that the distribution of N^2 for MCM is influenced significantly by the decreased number of vertical levels, therefore limiting the comparison to the other cases. Near mature convective objects, the mean static stability is lower for

Table 16: Mean, median, mode, interquartile range (IQR), and standard deviation (STD) for out-of-cloud static stabilities between 8 and 12 km near mature and developing (italicized) convection.

Case day	Mean	Median	Mode	IQR	STD
DCT	7.98×10^{-5}	7.87×10^{-5}	7.52×10^{-5}	9.18×10^{-6}	6.20×10^{-6}
	<i>7.69×10^{-5}</i>	<i>7.63×10^{-5}</i>	<i>7.42×10^{-5}</i>	<i>4.70×10^{-6}</i>	<i>5.35×10^{-6}</i>
DCM	1.54×10^{-4}	1.58×10^{-4}	1.64×10^{-4}	1.84×10^{-5}	2.08×10^{-5}
	<i>1.30×10^{-4}</i>	<i>1.35×10^{-4}</i>	<i>9.00×10^{-5}</i>	<i>4.75×10^{-5}</i>	<i>3.37×10^{-5}</i>
MCT	7.41×10^{-5}	7.43×10^{-5}	7.54×10^{-5}	6.59×10^{-6}	5.07×10^{-6}
	<i>7.00×10^{-5}</i>	<i>6.96×10^{-5}</i>	<i>6.62×10^{-5}</i>	<i>7.02×10^{-6}</i>	<i>5.58×10^{-6}</i>
MCM	4.71×10^{-4}	4.70×10^{-4}	4.71×10^{-4}	1.99×10^{-5}	1.59×10^{-5}
	<i>4.75×10^{-4}</i>	<i>4.74×10^{-4}</i>	<i>4.74×10^{-4}</i>	<i>2.23×10^{-5}</i>	<i>1.67×10^{-5}</i>
HCT	7.32×10^{-5}	7.26×10^{-5}	7.20×10^{-5}	9.87×10^{-6}	7.73×10^{-6}
	<i>7.17×10^{-5}</i>	<i>7.11×10^{-5}</i>	<i>6.44×10^{-5}</i>	<i>1.03×10^{-5}</i>	<i>8.25×10^{-6}</i>
HCM	1.84×10^{-4}	1.86×10^{-4}	1.79×10^{-4}	4.70×10^{-5}	3.66×10^{-5}
	<i>1.30×10^{-4}</i>	<i>1.24×10^{-4}</i>	<i>1.08×10^{-4}</i>	<i>7.50×10^{-5}</i>	<i>5.14×10^{-5}</i>

the tropical cases than the midlatitude cases, which is expected. The variation in static stability for the tropical cases is limited and is not influenced by convective type. The breadth of the static stability distributions is greater for the midlatitude cases and the stronger convection influences the probability of lower stabilities. Near developing convection, again the tropical cases have a lower mean static stability than the midlatitude cases, and little variation between the cases themselves. Interestingly, the midlatitude distributions are more alike near developing convection than mature convection, suggesting that storm type does not influence the static stability during the developing stage. Importantly, for all six cases the mean static stability is lower near developing convection compared to mature convection (Table 16). These results indicate that turbulence probability through stability processes is greater for both the midlatitudes and tropics near developing convection.

The out-of-cloud vertical shear distributions between 8 km and 12 km (Fig. 60 and Table 17) near mature convection have a large variability between the six cases,

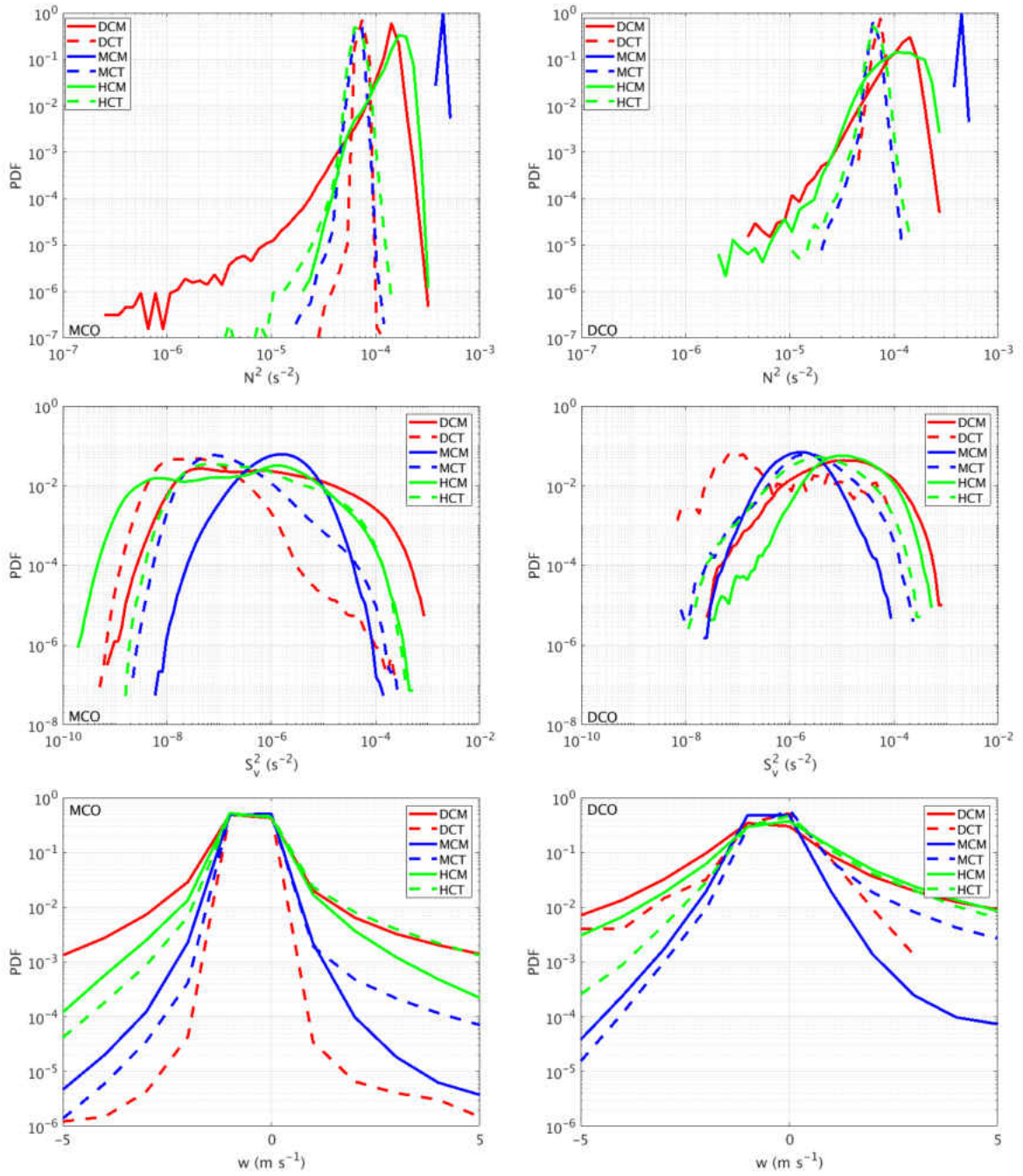


Figure 60: Distribution of mean out-of-cloud static stability, mean vertical wind shear, and mean vertical velocity between 8 km and 12 km nearest to mature convection (MCO) and developing convection (DCO) for the six simulations (uncalibrated second-order structure functions).

Table 17: Mean, median, mode, interquartile range (IQR), and standard deviation (STD) for out-of-cloud vertical wind shear between 8 and 12 km near mature and developing (italicized) convection.

Case day	Mean	Median	Mode	IQR	STD
DCT	9.05×10^{-8}	3.48×10^{-8}	1.58×10^{-8}	7.20×10^{-8}	4.59×10^{-7}
	<i>4.97×10^{-6}</i>	<i>1.59×10^{-7}</i>	<i>7.39×10^{-9}</i>	<i>1.90×10^{-6}</i>	<i>1.45×10^{-5}</i>
DCM	6.11×10^{-6}	4.17×10^{-7}	2.34×10^{-8}	2.45×10^{-6}	2.35×10^{-5}
	<i>2.66×10^{-5}</i>	<i>1.15×10^{-5}</i>	<i>9.48×10^{-6}</i>	<i>2.61×10^{-5}</i>	<i>4.31×10^{-5}</i>
MCT	3.87×10^{-7}	1.15×10^{-7}	6.39×10^{-8}	2.18×10^{-7}	1.74×10^{-6}
	<i>5.29×10^{-6}</i>	<i>2.63×10^{-6}</i>	<i>1.06×10^{-6}</i>	<i>4.21×10^{-6}</i>	<i>8.71×10^{-6}</i>
MCM	2.41×10^{-6}	1.53×10^{-6}	1.08×10^{-6}	2.30×10^{-6}	2.81×10^{-6}
	<i>2.42×10^{-6}</i>	<i>1.64×10^{-5}</i>	<i>1.42×10^{-6}</i>	<i>2.14×10^{-5}</i>	<i>2.76×10^{-6}</i>
HCT	1.98×10^{-6}	2.12×10^{-6}	4.80×10^{-6}	8.26×10^{-6}	7.10×10^{-6}
	<i>8.85×10^{-6}</i>	<i>4.05×10^{-6}</i>	<i>1.19×10^{-6}</i>	<i>7.98×10^{-6}</i>	<i>1.41×10^{-6}</i>
HCM	2.26×10^{-6}	4.50×10^{-7}	1.29×10^{-8}	1.89×10^{-7}	6.64×10^{-6}
	<i>2.35×10^{-6}</i>	<i>1.27×10^{-6}</i>	<i>3.65×10^{-6}</i>	<i>2.21×10^{-6}</i>	<i>3.05×10^{-5}</i>

likely as a result of the variation in convective type. The greatest mean vertical wind shear is associated with the midlatitude cases which is expected. The breadth of vertical wind shear is also the greatest for the midlatitudes. Near developing convection, the vertical wind shear distributions shift towards higher shear values by more than an order of magnitude. Interestingly, in the tropics and midlatitudes the probability of increased vertical wind shear is similar between the cases and is no longer influenced by storm type, but is still influenced by region. The larger vertical shear present near developing convection is hypothesized to be caused by deformation at the cloud boundary and increases the probability of turbulence through shear producing mechanisms.

Mean out-of-cloud vertical velocity is used as a proxy for the presence of gravity waves between 8 km and 12 km. Near mature convection, the six cases have a similar probability of vertical velocities near 0 m s^{-1} (highest probability less than 0 m s^{-1} due to binning procedure). The extremes of the distributions of vertical velocity vary

Table 18: Mean, median, mode, interquartile range (IQR), and standard deviation (STD) for out-of-cloud vertical velocities between 8 and 12 km near mature and developing (italicized) convection.

Case day	Mean	Median	Mode	IQR	STD
DCT	4.31×10^{-4}	5.84×10^{-4}	6.26×10^{-2}	1.08×10^{-1}	9.86×10^{-2}
	<i>4.68×10^{-2}</i>	<i>4.86×10^{-2}</i>	<i>-5.52</i>	<i>3.53×10^{-1}</i>	<i>7.90×10^{-1}</i>
DCM	3.25×10^{-5}	-9.33×10^{-5}	-2.10×10^{-5}	2.21×10^{-6}	1.28
	<i>3.78×10^{-5}</i>	<i>3.86×10^{-3}</i>	<i>-5.36</i>	<i>1.31</i>	<i>2.77</i>
MCT	4.33×10^{-3}	3.65×10^{-3}	-1.75×10^{-1}	1.85×10^{-1}	2.18×10^{-1}
	<i>3.60×10^{-1}</i>	<i>1.99×10^{-1}</i>	<i>1.38×10^{-1}</i>	<i>5.53×10^{-1}</i>	<i>8.78×10^{-1}</i>
MCM	4.18×10^{-3}	4.75×10^{-3}	-2.51×10^{-1}	2.17×10^{-1}	2.41×10^{-1}
	<i>-1.89×10^{-3}</i>	<i>-8.96×10^{-4}</i>	<i>-6.00×10^{-1}</i>	<i>4.78×10^{-1}</i>	<i>4.70×10^{-1}</i>
HCT	9.77×10^{-2}	4.00×10^{-3}	-2.02×10^{-1}	3.25×10^{-1}	6.74×10^{-1}
	<i>5.24×10^{-1}</i>	<i>2.34×10^{-1}</i>	<i>-3.34×10^{-1}</i>	<i>9.15×10^{-1}</i>	<i>1.35</i>
HCM	1.40×10^{-2}	-1.08×10^{-2}	-3.24×10^{-1}	2.16×10^{-1}	4.73×10^{-1}
	<i>5.12×10^{-1}</i>	<i>2.39×10^{-1}</i>	<i>-5.39×10^{-1}</i>	<i>1.27</i>	<i>1.79</i>

significantly by storm type (Fig. 60 and Table 18). More specifically, the paired cases with similar convective types and intensity have similar distributions of vertical velocity. Interestingly, the distributions are not equal when examined as greater or less than 0 m s^{-1} (i.e., positive or negative vertical velocity). There is greater spread amongst the paired cases (and cases subset by region) when vertical velocities greater than 0 m s^{-1} are examined. The mean vertical velocities for all cases increase near developing convection, with the greatest increase for the tropical cases. These results suggest that the likelihood of turbulence produced through gravity waves increases near developing convection, especially in the tropics.

The distributions of static stability, vertical wind shear, and vertical velocity are subset by turbulence intensity to discern if turbulence intensity is influenced by the environment (Fig. 61). More specifically, does the environment alter for all cases where there is only light and moderate or greater turbulence? When stability is examined as a subset of turbulence intensity, stability in the midlatitudes decreases

for MOG turbulence. The static stability of the tropical cases is not influenced by turbulence intensity. These results are consistent for developing convection, but the variation for the midlatitudes is less than was found for mature convection. In relationship to aviation operations, the environmental stability in the midlatitudes is significantly different for MOG turbulence versus LGT turbulence near convective objects and the broadening of the stability distributions could be an indicator of increased turbulence potential. However, the distributions vary slightly in the tropical environment, meaning that stability distributions would not provide enough information to discern between the likelihood of null turbulence or LGT or MOG turbulence.

The distributions of vertical wind shear between 8 km and 12 km subset by turbulence intensity for the six cases are shifted towards higher shear values, indicating that turbulence with greater intensity is occurring more frequently in regions of increased shear (Fig. 61). In comparison to the subset stability distributions, both tropical and midlatitude cases have a significant alteration in their respective distributions. The most likely vertical wind shear for all cases has increased by an order of magnitude. The greatest shift in the vertical wind shear distributions for all cases is for the environments closest to mature convective objects. In relationship to aviation operations, the environmental vertical wind shear in the midlatitudes is significantly different for turbulent regions than null regions near convection. The significant shift towards higher values of vertical wind shear could be an indicator of increased turbulence potential. The same application of vertical wind shear could be used in the tropics near convection. The distinction in distributions between the mature convective environment and the developing convective environment would be limited, meaning the same shift in distribution could be used for turbulence prediction near mature and developing convection. Storm type in the midlatitudes influences the

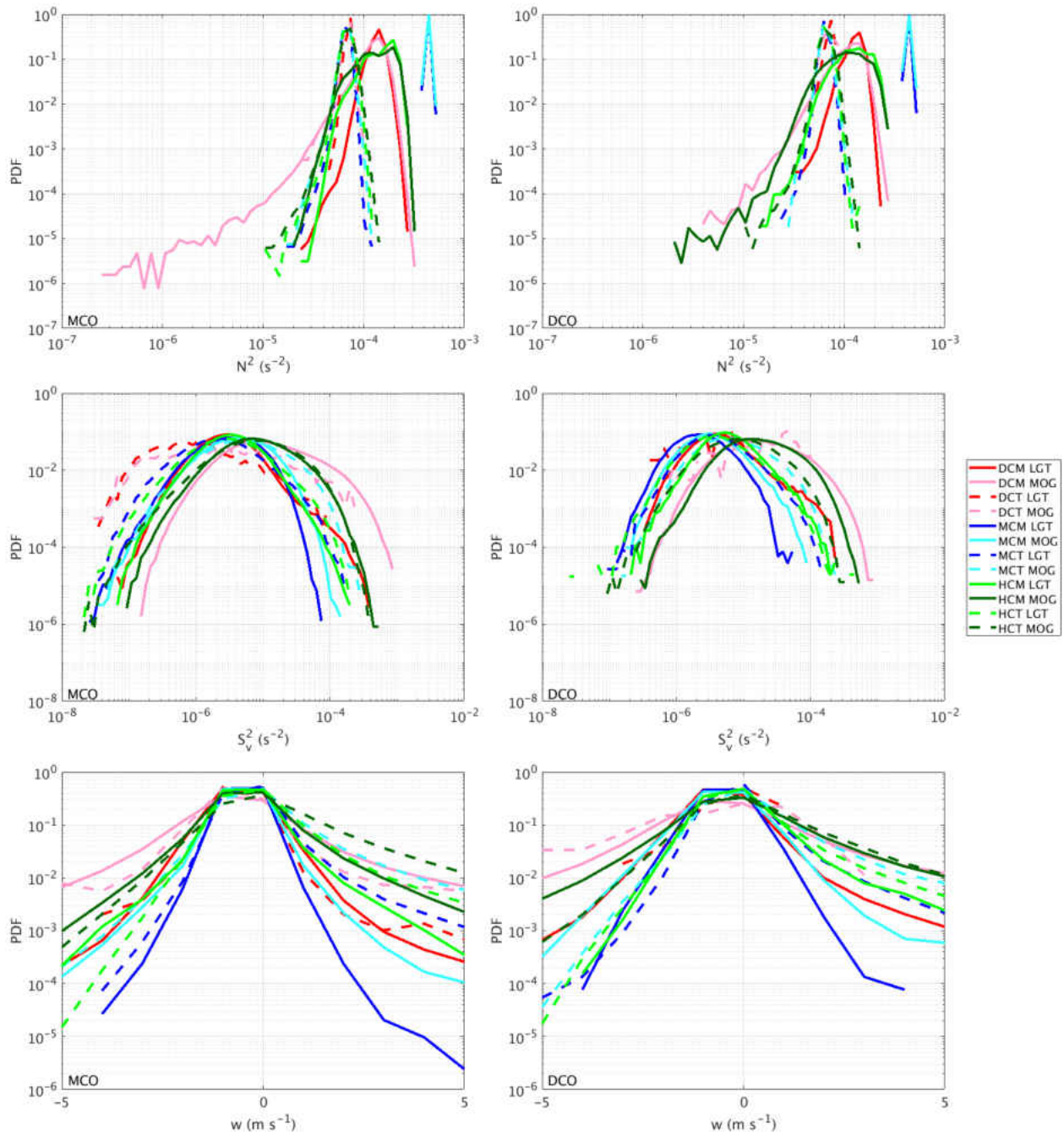


Figure 61: Distribution of mean out-of-cloud static stability, mean vertical wind shear, and mean vertical velocity between 8 km and 12 km nearest to mature convection (MCO) and developing convection (DCO) for the six simulations subset by turbulence intensity (uncalibrated second-order structure functions).

distributions more so than in the tropics and more cases would need to be examined in order to design prediction diagnostics.

The most discernible variation in parameters subset by turbulence intensity is the vertical velocities between 8 km and 12 km (Fig. 61). The probability of larger positive and negative velocities increases for all cases when only turbulence is examined. The greatest change in probabilities of larger velocities are associated with MOG turbulence and have increased by more than one order of magnitude for the tropical cases, especially near mature convection. The shift in probabilities for vertical velocities is region and storm type dependent. However, the broadening of the distribution could be used as an indicator of increased turbulence prediction.

Correlations between static stability, vertical wind shear, vertical velocities, and turbulence intensity are computed to determine if turbulence intensity can be estimated by the parameters near convection (Figs. 62-64 and Table 19). More specifically, does turbulence relate to increased vertical wind shear and lower stabilities in both the tropics and midlatitudes. Figure 62 shows the correlation of static stability and turbulence for all cases subset by mature and developing convection. For the tropical cases there is no correlation between static stability and turbulence intensity for the environment near mature or developing convection. For the midlatitude cases, there is a slightly stronger negative correlation for developing convection than for mature convection. This suggests that static stability could be used to diagnose turbulence potential in the midlatitudes and is not storm type dependent. Figure 63 shows the correlation of vertical wind shear and turbulence for all cases subset by mature and developing convection. For all six cases there is a positive correlation between vertical wind shear and turbulence intensity. The correlations are generally greater for mature convection and the midlatitude cases. The same results are found for the correlations between vertical velocity and turbulence intensity (Fig. 64). For

the correlation of vertical velocity and turbulence intensity, the paired cases have correlations more similar to one another than the other variables.

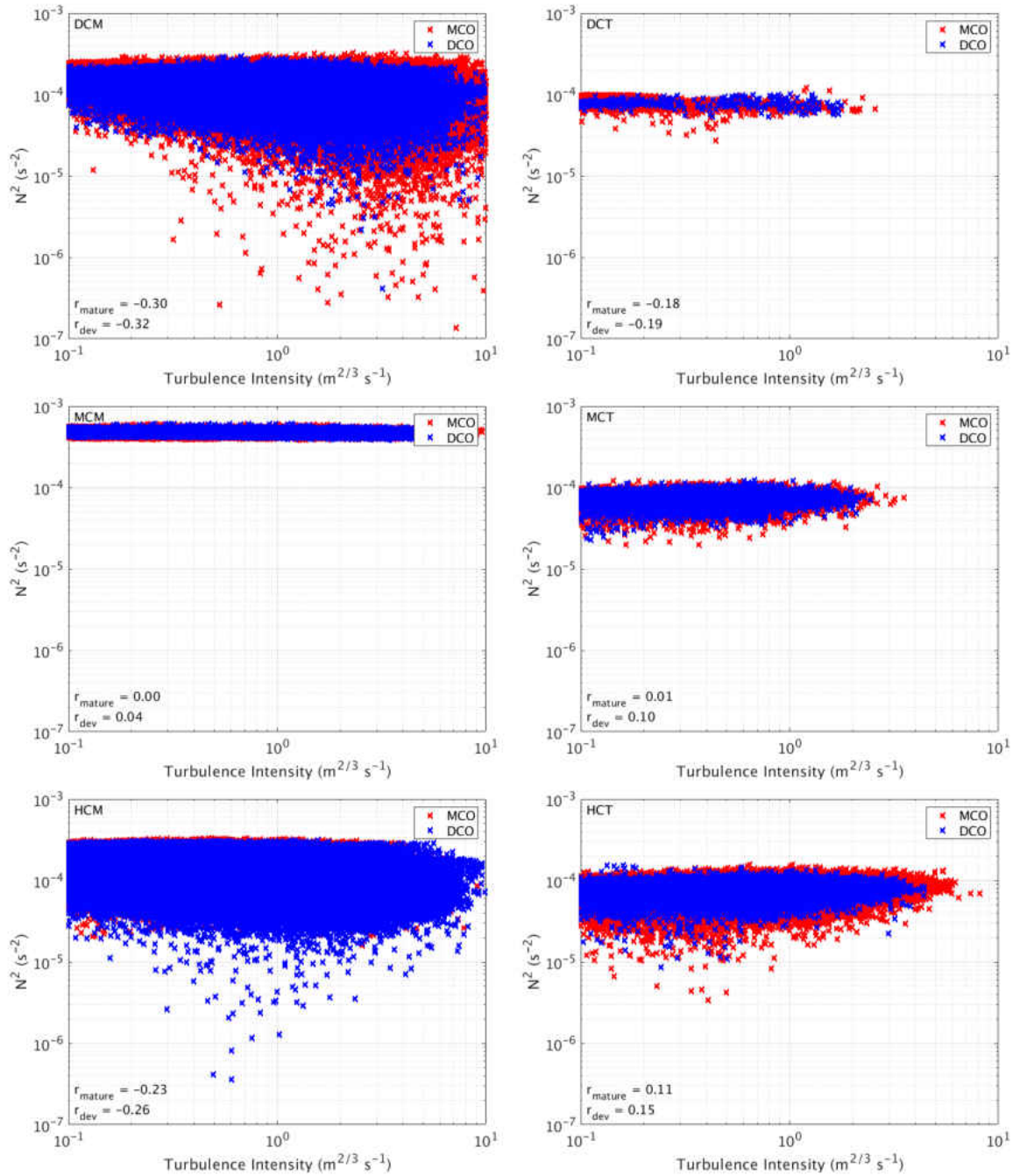


Figure 62: Correlation of mean out-of-cloud static stability and turbulence intensity (uncalibrated second-order structure functions) between 8 km and 12 km nearest to mature convection (MCO) and developing convection (DCO) for the six simulations. The correlation coefficients for the data subset by convective object type (r_{mature} and r_{dev}).

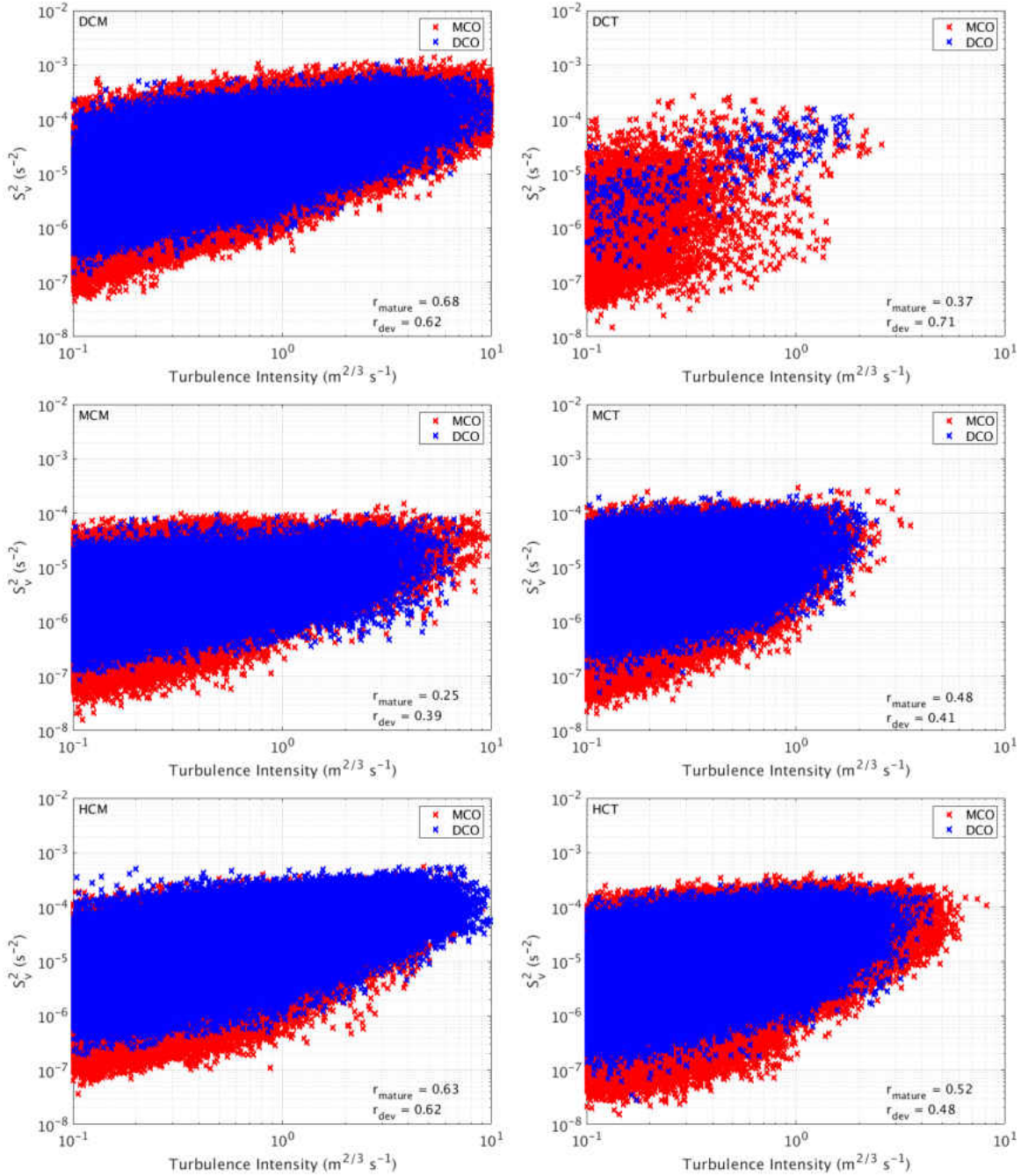


Figure 63: Correlation of mean out-of-cloud vertical wind shear and turbulence intensity (uncalibrated second-order structure functions) between 8 km and 12 km nearest to mature convection (MCO) and developing convection (DCO) for the six simulations. The correlation coefficients for the data subset by convective object type (r_{mature} and r_{dev}).

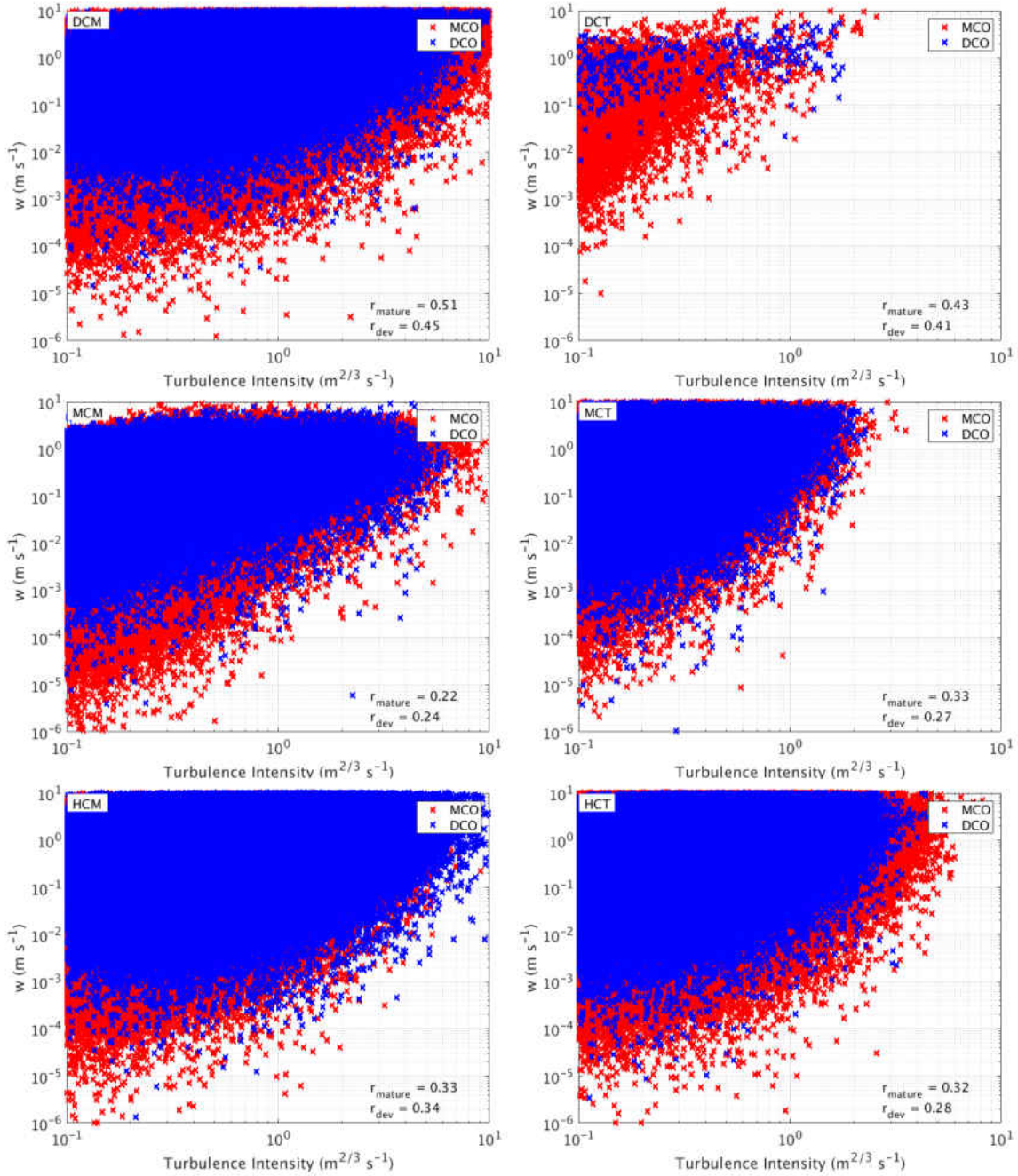


Figure 64: Correlation of mean out-of-cloud vertical velocities and turbulence intensity (uncalibrated second-order structure functions) between 8 km and 12 km nearest to mature convection (MCO) and developing convection (DCO) for the six simulations. The correlation coefficients for the data subset by convective object type (r_{mature} and r_{dev}).

6.4 Discussion and Conclusions

Several cases of convectively induced turbulence (CIT) were simulated at high vertical and horizontal resolution to investigate the accuracy of current turbulence diagnostics and to determine if the environment near convection varies for storm type and region, and how the variation influences turbulence intensity. Simulated convection compared well to observations in morphology and strength for the majority of the cases, while timing for the tropical simulations generally had a lag of up to four hours. A developing convective case in the midlatitudes (DCM) had much stronger convection than observed likely due to the microphysics of the simulation.

The turbulence diagnostics varied in success based on the particular case, but generally Richardson number indicated regions of turbulence out of cloud and within convective cloud. Eddy dissipation rate (EDR) underestimated the likelihood of out-of-cloud turbulence for the tropical cases, likely a result of weaker vertical velocities which are used in the turbulent kinetic energy formulation of the boundary layer scheme. EDR in the midlatitudes had mixed results but for the majority of the cases agreed with Richardson number. The inconsistency of EDR highlights the need for more research on the influence of the PBL scheme and upper level turbulence prediction for model-derived diagnostics. Second-order structure functions (SF) indicated the greatest potential for turbulence in all of the cases but likely suffers from resolution sensitivity for the strongest convective cases. In regards to global turbulence prediction, this study finds that the diagnostics do perform differently in various regions and more investigation as to the statistical bias of these diagnostics are needed to increase confidence in turbulence prediction.

Storm type and region does influence the probability of in-cloud and out-of-cloud turbulence between cruising altitudes. Tropical convection has a lower proba-

bility of turbulence when compared to midlatitude convection of similar convective type. The probability of turbulence near both tropical and midlatitude developing convection is greater than the probability of turbulence near mature convection in the tropics and midlatitudes. The increased probability of turbulence near developing convection in the tropics and midlatitudes is important for aviation operations because generally pilots avoid flying near mature convection and will fly closer to developing convection.

The environmental conditions out of cloud near convection in the midlatitudes and tropics vary significantly. Static stability is lower for the tropical environment on average than in the midlatitudes, and is greater around mature convection than developing convection. The variation in storm type does not influence the stability around the convection significantly. Vertical shear is lower for the tropical environment than in the midlatitudes, and increases around developing convection in both regions. The type of storm does influence the vertical wind shear as does the stage of development. Vertical velocities on average were larger for the midlatitude cases than the tropical cases, but both increased significantly near developing convection. When turbulence was subset by intensity, stability was not significantly different between light or moderate or greater (MOG) turbulent locations. However, average vertical wind shear and vertical velocities increased by more than an order of magnitude for turbulent locations with MOG intensity in both the tropics and midlatitudes. In terms of turbulence prediction, increased vertical wind shear and vertical velocities are indicative of increased turbulence intensity. Static stability is less indicative of turbulence intensity in either region.

Aviation operations currently do not abide by region specific thunderstorm guidelines even though convective properties are different in the tropics and midlatitudes. This study found that turbulence probability varies by region and storm type

and that the avoidance guidelines need to address these differences in order to be more efficient. Developing convection was also found to have a higher probability of turbulence when compared to mature convection. For turbulence associated with developing convection, the probability was similar between all six cases and may indicate that storm and regions specific guidelines are not necessary. This study found stark differences in turbulence potential in the six cases and motivates the need for more simulations of CIT at high resolution to reduce turbulence encounters by increasing the understanding of CIT and with time, adapting the avoidance guidelines.

Table 19: Correlation coefficients for out-of-cloud static stability, vertical wind shear, vertical velocity, and eddy dissipation rate between 8 km and 12 near mature and developing (italicized) convection.

Case day	N^2 and TI	S_v^2 and TI	$ w $ and TI
DCT	-0.18		
<i>-0.19</i>	0.37		
<i>0.71</i>	0.43		
<i>0.41</i>			
DCM	-0.30		
<i>-0.32</i>	0.68		
<i>0.62</i>	0.51		
<i>0.45</i>			
MCT	0.01		
<i>0.10</i>	0.48		
<i>0.41</i>	0.33		
<i>0.27</i>			
MCM	0.00		
<i>0.04</i>	0.24		
<i>0.39</i>	0.22		
<i>0.24</i>			
HCT	0.11		
<i>0.15</i>	0.52		
<i>0.48</i>	0.32		
<i>0.28</i>			
HCM	-0.23		
<i>-0.26</i>	0.63		
<i>0.62</i>	0.33		
<i>0.34</i>			

CHAPTER 7

CONCLUSIONS

Out-of-cloud convectively induced turbulence (CIT) is an atmospheric phenomenon that continues to be a challenge to the aviation industry from flight planning to in-flight operations. Numerical modeling offers in-depth analysis of turbulence generation mechanisms and characteristics of out-of-cloud turbulence. Unfortunately, the model resolution required to properly resolve turbulence is not currently implemented in operational forecasting systems due to computational cost limitations. The coarser grid spacing used in operational models leads to turbulence being diagnosed with metrics that are related to large scale features such as convergence, vorticity, and gradients of velocity components, without verification for convective cases. An additional challenge in CIT prediction is the accuracy of simulated convective properties, including timing, location, type, and intensity. While convective forecasting and nowcasting are improving significantly due to the increased volume of observations and improved model physics, CIT avoidance still has large uncertainty. Furthermore, tropical oceanic CIT prediction is nearly limited to nowcasting only as continuous observations from ground and space-borne platforms are sparse. As the number of flights per day and with more flight paths over remote tropical areas, CIT prediction must be improved for numerous regions and convective types. Due to the challenges of forecasting CIT, in-flight systems that aid pilots in convective hazards detection are becoming common for many airlines. While these systems are proving to be a beneficial tool for pilots, the efficiency of flight planning, air traffic control and flight

management interactions, and flight routes around convection require improvement. The Federal Aviation Administration (FAA) avoidance guidelines, specifically the lateral avoidance of 20 miles from severe convection also hinders flight efficiency, as turbulence is not isotropic. Lastly, the FAA avoidance guidelines are not specific to convective type or region further limiting efficiency. This study addressed the numerous limitations of out-of-cloud CIT prediction using numerical modeling, from uncertainty of impacts of model resolution, to the influence of convective type and stage of development on turbulence characteristics. This study offers steps towards implementing region dependent and convective type CIT avoidance guidelines.

Model resolution is of particular concern to convective forecasting and turbulence prediction because turbulence diagnostics need to perform accurately across numerous scales. Three common model resolution setups (NAM-12 km, HRRR-3 km, and research-500 m) were used to simulate convection over eight days in the northern Great Plains. The Ellrod Index, a diagnostic that evaluates convergence, vertical wind shear, and deformation to indicate turbulence, and eddy dissipation rate (EDR) were evaluated across various resolutions. Ellrod was found to perform very poorly and would need significant calibrate; in constrast, EDR performed well. Simulated convective depth and intensity for the coarsest model resolution were found to be under predicted, and therefore turbulence probability was underestimated. A distinctive limitation in the convective simulations with 3 km horizontal grid spacing was the storm depth was often too low, which likely influenced the turbulence probability between 8 km and 12 km.

Model resolution was found to influence the distribution and areal coverage of out-of-cloud turbulence. Coarser model resolutions distribute turbulence to lower intensities and to lower altitudes. This suggests that model resolution influences the generation sources of turbulence. The finest model resolution simulation identified

moderate turbulence at cruising altitudes within 50 km of convection. The distribution of turbulence varied for convective type, and between the three model setups, indicating that resolution influences the generation of turbulence from various convective types. Turbulence intensity and areal coverage are sensitive to model resolution, promoting the need of scale-aware thresholds.

In addition to analyzing the distribution of turbulence for various modeling setups, the location of turbulence was examined. CIT is not isotropic and generally has a directional preference. The influence of resolution on the direction preference directly relates to turbulence avoidance for aviation operations. Turbulence location varied amongst the model setups within 20 miles of convection. Convective type also influenced the preferred direction of turbulence and little agreement between the models based on convective type was found. Generally, the coarser model resolutions agreed in the preferred direction of turbulence. The directional preference of turbulence is nearly evenly distributed amongst the directions for more intense and organized convection, supporting the FAA guidelines of an avoidance distance of 20 miles in all directions from convection.

Out-of-cloud environmental parameters related to turbulence production were analyzed between 8 km and 12 km to determine if resolution influences the environmental conditions, and therefore turbulence likelihood. Model resolution was found to influence the distribution of static stability towards lower values for the finest resolution setups. However, the distribution of static stability did not vary significantly by direction. The distribution of vertical wind shear varied amongst the model setups but the finest model setup did not have the greatest likelihood of larger vertical wind shear values. The distribution of vertical wind shear did vary by direction but the greatest wind shear values were not always associated with the preferred direction of turbulence. The distribution of vertical velocities between 8 km and 12

km were influenced by the horizontal resolution of the model setup. The finest resolution model setup had the greatest probability of larger vertical velocities which varied by direction. Model resolution influences turbulence generation by altering the stability of the environment more so than the vertical wind shear. Developing convection is of particular concern to aviation because it is difficult to forecast and is best treated with nowcasting systems. Over tropical oceans, where observational platforms are limited, aviation is vulnerable to encountering turbulence generated by developing convection. In addition, turbulence prediction systems that are in use over the tropics diagnose turbulence from metrics that were calibrated in the midlatitudes. A model simulation of a turbulence encounter over the Gulf of Mexico was completed to assess the accuracy of prominent midlatitude turbulence diagnostics in the tropics. Richardson number and second-order structure functions had limited success predicting turbulence near convection. Unlike in the midlatitude study, EDR underestimated the intensity and areal coverage of turbulence. Because EDR is calculated from turbulent kinetic energy output from the planetary boundary layer (PBL) parameterization, the variable performance of EDR shows the need to determine the uncertainty of upper level turbulence generation as a result of the utilized PBL scheme.

Turbulence was analyzed during a period of time where convection was rapidly growing and intensifying. Although developing convection was associated with a small portion of turbulence, it was more intense in severity than turbulence associated with mature convection. Pilots generally avoid regions with stronger radar echo returns (mature convection), but this research finds that developing convection is responsible for the most severe turbulence, highlighting the need for updated guidelines including developing convection. As previously discussed, the FAA guidelines are neither convective type nor region specific, which hinders aviation efficiency. Convec-

tive strength, duration, and depth are a few of the convective characteristics that are known to vary between tropical and midlatitude convection, all of which influence turbulence generation. Aviation encounters of severe CIT in both the midlatitudes and tropics were simulated at high horizontal and vertical resolution to examine various turbulence metrics and the variability in the environment near developing and mature convection. The success of the turbulence metrics was found to be varied and again EDR did not consistently diagnose out-of-cloud turbulence, prompting the additional examination of the PBL scheme. Second-order structure functions were found to diagnose turbulence for all convective types, but for convection that was too intense when compared to observations, calibration is necessary. Turbulence likelihood and areal coverage varied amongst the simulations both in cloud and out of cloud. Tropical turbulence was generally less likely when compared to midlatitude turbulence; however, near developing convection the probability increased more than midlatitude turbulence. In addition to differences in the convective properties of tropical and midlatitude convection, the environmental conditions also vary. The variation in static stability and vertical wind shear influences turbulence propagation. Midlatitude static stability and vertical wind shear were found to be greater than in the tropics. The stage of convection did not alter the static stability significantly in either region, but did alter the vertical wind shear significantly around developing convection. In regards to aviation applications, turbulence generated by developing convection is a greater hazard than turbulence generated by mature convection in the tropics and needs to be addressed by avoidance guidelines. While the success of the individual diagnostics are inconsistent, an increase in vertical wind shear and velocity may be a useful indicator of turbulence probability, especially in the tropics. Numerical simulations of convection give insight into the characteristics of CIT in the tropics and midlatitudes for various convective types which can be used to aid

aviation in improving flight operations. Developing convection is the largest threat to aviation in both the midlatitudes and tropics because it is poorly forecasted and alters the environment more so than mature convection, increasing the severity of turbulence. Turbulence diagnostics are not consistent in identifying out-of-cloud CIT and it is recommended that the properties of convection themselves are used as indicators of turbulence potential. An additional concern with turbulence diagnostics is the necessary recalibration of the metrics as the resolution of operational forecasting systems trends towards finer grid spacing. In order to make FAA policy changes, a significant number of additional simulations are needed to statistically identify the risks of developing convection in the tropics and midlatitudes.

CHAPTER 8

APPENDIX

The following section provides the calculations and details about the popular turbulence diagnostics currently utilized in numerous turbulence prediction systems.

8.1 Richardson number

Numerous past studies have found that Richardson number (Ri) can diagnose conditions favorable for turbulence production, including shear induced instability and gravity wave breaking (Lee and Chun 2018; Trier and Sharman 2018; Zovko-Rajak and Lane 2014; Trier et al. 2012; Kim and Chun 2011; Endlich 1964). The gradient Richardson number is expressed as,

$$Ri = \frac{N^2}{S_v^2}, \quad (8.1)$$

where S_v^2 is the vertical wind shear defined as,

$$S_v^2 = \left(\left| \frac{\partial u}{\partial z} \right|^2 + \left| \frac{\partial v}{\partial z} \right|^2 \right). \quad (8.2)$$

Ri is indicative of turbulence when it is less than 0.25. In convection, regions of low Ri include anvil outflow regions and overshooting tops. One limitation with Ri is the lack of conversion to turbulence intensity thresholds.

8.2 Brown index

The Brown index (Brown 1973; hereafter B1), is a commonly applied turbulence metric that diagnoses turbulence likelihood from absolute vorticity, shearing deformation, and stretching deformation. B1 was developed to improve the prediction of clear-air turbulence due to the inconsistent prediction of turbulence using Richardson number (Brown 1973). The index is beneficial for turbulence prediction because it incorporates large scale analysis fields (i.e. vorticity) with mesoscale analysis fields (i.e. deformation). B1 is expressed as

$$B1 = (0.3\zeta_a^2 + D_{SH}^2 + D_{ST}^2)^{1/2} \quad (8.3)$$

and is in units of s^{-1} . Absolute vorticity (ζ_a) is calculated by,

$$\zeta_a = \frac{\partial v}{\partial x} - \frac{\partial u}{\partial y} + f, \quad (8.4)$$

where f is

$$f = 2\Omega \sin \phi, \quad (8.5)$$

ϕ is latitude, and u and v are the horizontal components of wind. Shearing (D_{SH}) and stretching (D_{ST}) deformations are defined as

$$D_{SH} = \frac{\partial v}{\partial x} + \frac{\partial u}{\partial y} \quad (8.6)$$

and

$$D_{ST} = \frac{\partial u}{\partial x} - \frac{\partial v}{\partial y}. \quad (8.7)$$

A supplemental version of B1 that is used explicitly as an expression for energy dissipation, the Brown 2 index (Brown 1973; Roach 1970; hereafter B2) is calculated

Table 20: Turbulence intensity as determined for the Brown 1 index (Brown 1973).

Turbulence Intensity	Brown Index (s^{-1})
Light	2×10^{-5}
Moderate	5×10^{-5}
Severe	1×10^{-4}
Extreme	2×10^{-4}

as

$$B2 = \frac{1}{24}(B1)S_v^2. \quad (8.8)$$

The empirical thresholds that relate to turbulence intensity were calibrated by Brown (1973) by comparing 12 days of turbulence reports to the calculated values from Eq. 8.3. However, during the 12 days, no turbulence was related to convection. Yet, this index is still implemented on a daily basis for regional turbulence prediction. The thresholds for turbulence intensity using B1 are provided in Table 20. B2 was developed by Roach (1970) with the assumption that turbulence would counteract the deformation processes and reduce the Richardson number within a layer. Brown (1973) examined the performance of B2 again using the same non-convective turbulence cases from the previous 12 days. The thresholds for turbulence intensity using B2 are the same as eddy dissipation rate (Table 21). B1 and B2 are computed daily in numerous turbulence prediction algorithms including GTG-2 (Sharman and Pearson 2017), but these indices were not developed for identification of convectively induced turbulence in either the midlatitudes or the tropics. According to Galvin (2016), B1 has been shown to accurately predict turbulence along the sub-tropical jet. However, no other studies have examined B1 or B2 in the tropics.

8.3 Dutton index

The Dutton index (DI; Dutton 1980) is an empirical index that was calibrated from linear regressions of turbulence reports and synoptic-scale turbulence indices in the North Atlantic and northwest Europe. The Dutton index is calculated by,

$$DI = 1.25S_H + 0.25S_v^2 + 10.5, \quad (8.9)$$

where S_H is defined as the horizontal wind shear calculated by,

$$S_H = \frac{u}{s} \frac{\partial s}{\partial y} - \frac{v}{s} \frac{\partial s}{\partial x}, \quad (8.10)$$

and s is

$$s = (u^2 + v^2)^{1/2}. \quad (8.11)$$

8.4 Ellrod index

The Ellrod index is a turbulence intensity (TI) metric used for aviation turbulence avoidance. There are two different methods of calculating the Ellrod index, TI1 and TI2.

$$TI1 = VSHxDEF(s^{-2}), \quad (8.12)$$

where VSH is the vertical wind shear and DEF is the deformation of the horizontal components.

$$TI2 = VSHx(DEF + CON)(s^{-2}), \quad (8.13)$$

where CON is the convergence of the horizontal components (Ellrod and Knapp 1992). The U.S. Air Force Weather Agency (AFWA) includes TI2 as part of their

turbulence forecast output at seven altitude ranges, from 1.5 km extending to 12.7 km (Creighton et al. 2014). TI2 values of 4–8 represent clear-air turbulence intensities of light to moderate, values of 8–12 represent turbulence intensities of moderate, and values greater than 12 represent severe turbulence. TI2 generated from the NAM simulations are also provided by the Aviation Weather Center as turbulence guidance and uses these same thresholds. There are two limitations with the thresholds used for TI2, the first being the verification of the empirical values. Empirical values were correlated to only clear-air turbulence PIREPs and convectively induced turbulence PIREPs were neglected (Ellrod and Knapp 1992). Second, the empirical values were derived from models designed with grid spaces greater than 50 km (Ellrod and Knapp 1992). This research will calculate the Ellrod index and examine the distribution of numerical values out of cloud for each simulation using the original thresholds.

8.5 Subgrid-scale eddy dissipation rate

Turbulence intensity is estimated by computing EDR from turbulent kinetic energy (TKE) of each simulation. TKE is obtained from the subgrid-scale planetary boundary layer (PBL) parameterization, which is the Mellor–Yamada–Janjić (MYJ) scheme for the entirety of this study. The calculation of TKE is derived from the vertical component of velocity only (Janjić 1994). At 500 m horizontal grid spacing, it is possible that a portion of the TKE is resolved. However, for consistency in approach across all simulations, this “resolved” component of TKE is ignored in these simulations. EDR is a popular aviation turbulence metric that is not dependent on physical aircraft variables such as type, weight, and speed (Emanuel et al. 2013; Poellot and Grainger 1991). EDR can be calculated using various inflight data such as vertical acceleration, true airspeed, and three-dimensional winds (Emanuel et al. 2013; Ahmad

and Proctor 2012; Cornman et al. 1995; Poellot and Grainger 1991). The calculation for EDR used in this study is

$$EDR^{1/3} = \left(\frac{TKE^{3/2}}{L} \right)^{1/3} \quad (8.14)$$

where TKE is the turbulent kinetic energy ($\text{m}^2 \text{s}^{-2}$) and L is a length scale (Ahmad and Proctor 2012). Ahmad and Proctor (2012) investigated the accuracy of boundary layer turbulence intensity when using a length scale L that is dependent on the model PBL scheme. Their study concluded that EDR at 40 m above ground level (AGL) when calculated using a model-predicted L was less accurate than a constant L of 336 m. Other constant length scales were evaluated but also found to be less accurate. Many have continued to improve the validity of the length scale from model output, but most progress has been made for boundary layer turbulence estimations (Muñoz-Esparza et al. 2016; Sauer et al. 2016). There is much uncertainty in how length scales estimated by a PBL scheme relates to a length scale in the upper atmosphere. In this study,

$$L = \left(\Delta x \Delta y \Delta z \right)^{1/3} \quad (8.15)$$

where Δx is the horizontal resolution in the x direction, Δy is the horizontal resolution in the y direction, and Δz is the vertical resolution in the z direction (Schumann 1991; Sharman et al. 2012). Atmospheric turbulence is commonly defined as light, moderate, and severe based on the cubed root of EDR ($\text{m}^{2/3} \text{s}^{-1}$; Table 21; Lane et al. 2012). This study will use thresholds corresponding to Lane et al. (2012) and the more current thresholds (Sharman and Pearson 2017; Pearson and Sharman 2017; Sharman et al. 2014) which are based on climatological PIREPs and various sources including the Global Turbulence Guidance (GTG-2) product.

Table 21: Turbulence intensity thresholds as determined from the cubed root of eddy dissipation rate (ε ; Lane et al. 2012, Sharman and Pearson 2017).

Turbulence Intensity	$\varepsilon^{1/3}$ ($\text{m}^{2/3} \text{s}^{-1}$)
Light	0.1-0.3, 0.15-0.22
Moderate	0.3-0.5, 0.22-0.34
Severe	≥ 0.5 , ≥ 0.34

8.6 Second-order structure functions

Second-order structure functions D_s are used in this study as an estimation method for EDR in the inertial range (Sharman et al. 2006; Frehlich and Sharman 2004a, b; Kolmogorov 1941). To compute the second order structure function (hereafter, SF), the following equations are implemented:

$$D_{s(u)} = (u(i + \Delta s) - u(i))^2, \quad (8.16)$$

$$D_{s(v)} = (v(i + \Delta s) - v(i))^2, \quad (8.17)$$

in both the transverse (x) and longitudinal (y) directions, i is the grid index, and s is a separation distance expressed in units of spatial grid steps (dx).

$$\langle D_s^2 \rangle = C_k \varepsilon^{2/3} \Delta s, \quad (8.18)$$

$$\varepsilon^{1/3} = \left(\frac{\langle D_s^2 \rangle}{\Delta s C_k} \right)^{1/2}. \quad (8.19)$$

To calculate $\varepsilon^{1/3}$, the average of the four D_s components (u-longitudinal, u-transverse (latitudinal), v-longitudinal, and v-transverse (latitudinal), represented by brackets) of $\varepsilon^{2/3}$ is taken, where C_k equals 2 for the longitudinal direction calculation and $4/3C_k$

for the transverse direction (Frehlich and Sharman 2010), and s is chosen as 10 (the maximum spatial lag is 10 grid points) for chapter 5 and 7 for chapter 6. Research has shown that the separation distance should mirror the spectral resolution of the model advection scheme which is between $7-10\Delta x$ (Muñoz-Esparza et al. 2018; Skamarock 2004). The EDR intensity thresholds apply without additional calibration to the structure function values because the structure functions are within the Kolmogorov inertial range (Fig. 65). Turbulence intensity can be determined from the second-order structure functions following the same thresholds as EDR provided in Table 16. Second-order structure functions are included in the diagnostics because they have been shown in past studies to be successful for turbulence prediction (Muñoz-Esparza et al. 2018; Sharman and Pearson 2017; Pearson and Sharman 2017; Sharman et al. 2006; Frehlich and Sharman 2004a, b), are currently represented in GTG-2, and can be used to diagnose motions across various scales. Second-order structures functions adequately capture turbulence generated by convective and clear-air mechanisms by diagnosing localized high gradient regions.

8.7 Colson-Panofsky turbulent kinetic energy

The Colson-Panofsky TKE (CP; Colson and Panofsky 1965) index is used to estimate turbulence intensity in clear air environments. Turbulence intensity is calculated by,

$$CP = \lambda^2 S_v^2 \left(1 - \frac{Ri}{Ri_{crit}} \right) \quad (8.20)$$

In the CP equation λ is defined as a length scale equal to the local value of the Δz grid increment, and Ri_{crit} is a constant ≈ 0.5 . The thresholds for CP are provided in Table 22.

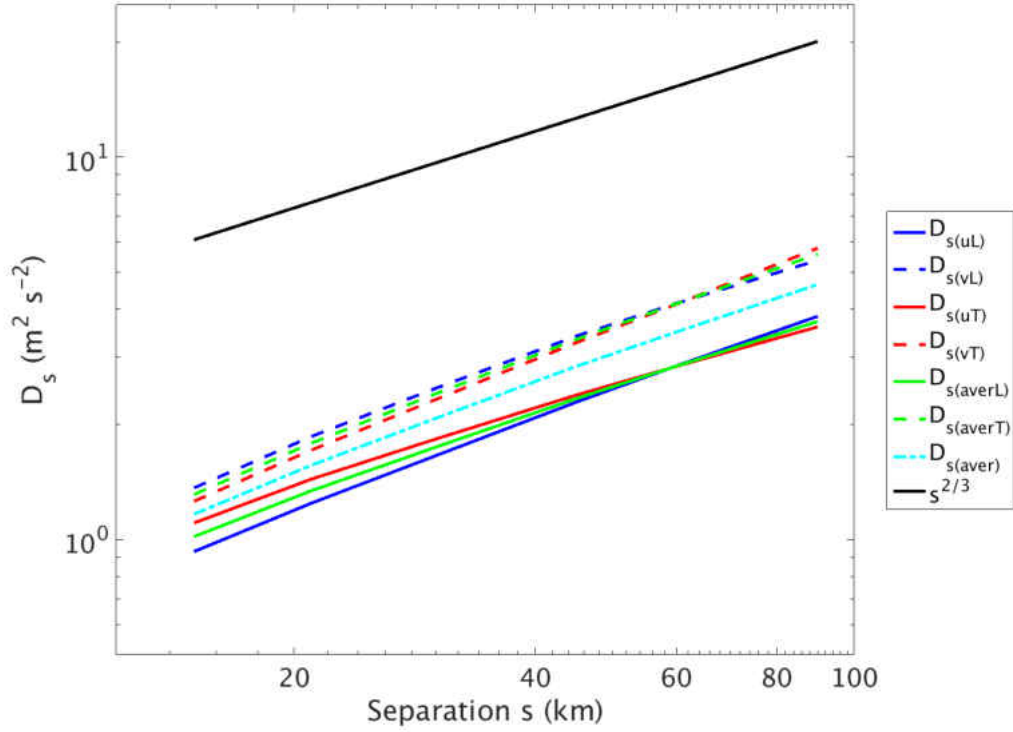


Figure 65: Structure functions (longitudinal direction- solid lines, transverse direction- dashed lines) as a function of separation distance, and the maximum of the Kolmogorov 2/3 inertial range (black line) for all heights from 1510-1800 UTC.

8.8 Marroquin DTF3

The Marroquin DTF3 diagnostic is used to derive turbulent kinetic energy and eddy dissipation rate (Marroquin 1998). DTF3 is expressed as,

$$DTF3 = K_M \left(\frac{c_1}{c_3} S_v^2 - \frac{c_2}{c_3} \frac{N^2}{Pr} \right), \quad (8.21)$$

where c_1 , c_2 , c_3 are constants equal to 1.44, 1.0, and 1.92, and K_M and Pr are adjustable constants but set to 75 and 1 in GTG-2. The thresholds for DTF3 are provided in Table 23.

Table 22: Turbulence intensity thresholds for CP (Sharman et al. 2006).

Turbulence Intensity	CP (kt^2)
Light	$\geq 1 \times 10^3$
Moderate	$\geq 5 \times 10^3$
Severe	$\geq 12 \times 10^3$

Table 23: Turbulence intensity thresholds for DTF3 (Sharman et al. 2006).

Turbulence Intensity	DTF3 ($\text{m}^2 \text{s}^{-2}$)
Light	≥ 1.0
Moderate	≥ 2.0
Severe	≥ 5.0

REFERENCES

- [1] , Adler, R. F., and R. A. Mack, 1986: Thunderstorm cloud-top dynamics as inferred from satellite observations and a cloud-top parcel model. *J. Atmos. Sci.*, **43**, 1945–1960.
- [2] Ahmad, N. N., and F. H. Proctor, 2011: Large eddy simulations of severe convection induced turbulence. NASA Tech Report AIAA Paper-2011-3201, 42 pp.
- [3] Ahmad, N. N., and F. H. Proctor, 2012: Estimation of eddy dissipation rates from mesoscale model simulations. NASA Tech. Report AIAA 0429, 24 pp.
- [4] AIRBUS, 2007: Optimum use of the weather radar. [Available online at <https://skybrary.aero/bookshelf/books/163.pdf>].
- [5] Alappattu, D., and P. K. Kunhikrishnan, 2010: First observations of turbulence parameters in the troposphere over the Bay of Bengal and the Arabian Sea using radiosonde. *J. Geophys. Res.*, **115:D6**.
- [6] Alcala, C. M., and A. E. Dessler, 2002: Observations of deep convection in the tropics using the Tropical Rainfall Measuring Mission (TRMM) precipitation radar. *J. Geophys. Res.*, **107**, 4792.
- [7] Alexander, M. J., J. R. Holton, and D. R. Durran, 1995: The gravity wave response above deep convection in a squall line simulation. *J. Atmos. Sci.*, **52**, 2212–2226.

- [8] Alexander, M. J., and J. R. Holton, 1997: A model study of zonal forcing in the equatorial stratosphere by convectively induced gravity waves. *J. Atmos. Sci.*, **54**, 408–419.
- [9] Alexander, M. J., J. H. Richter, and B. R. Sutherland, 2006: Generation and trapping of gravity waves from convection with comparison to parameterization. *J. Atmos. Sci.*, **63**, 2963–2977.
- [10] Allen, B., E. R. Mansell, D. C. Dowell, and W. Deierling, 2016: Assimilation of pseudo geostationary lightning mapper data using the Ensemble Kalman Filter. *Mon. Wea. Rev.*, **144**, 3465–3496.
- [11] American Meteorological Society, cited 2015: Turbulence. Glossary of Meteorology.[Available online at <http://glossary.ametsoc.org/wiki/Turbulence>].
- [12] Ball, M., C. Barnhart, M. Dresner, M. Hansen, K. Neels, A. Odoni, E. Peterson, L. Sherry, A. Trani, and B. Zou, 2010: Total delay impact study: A comprehensive assessment of the costs and impacts of flight delay in the United States. NEXTOR report prepared for the Federal Aviation Administration, 1–99.
- [13] Barber, K. A., 2015: Simulations of convectively-induced turbulence based on radar-based climatology of tropical storm types. M.S. thesis, Dept. Atmospheric Sciences, University of North Dakota, 169 pp.
- [14] Barber, K. A., G. L. Mullendore, and M. J. Alexander, 2018: Out-of-cloud convective turbulence: Estimation method and impacts of model resolution. *J. Appl. Meteor. Climatol.*, **57**, 121–136.
- [15] Barber, K. A., W. Deierling, G. L. Mullendore, C. Kessinger, R. Sharman, and D. Muñoz-Esparza, 2019: Properties of convectively induced turbulence over developing oceanic convection. *Mon. Wea. Rev.*, accepted in revisions.

- [16] Barthe, C., W. Deierling, and M. C. Barthe, 2010: The estimation of total lightning from various storm parameters: A cloud-resolving model study. *J. Geophys. Res.*, **115**, D24202.
- [17] Behne, D., 2008: NAM-WRF verification of subtropical jet turbulence. *Electronic J. Oper. Meteor.*, **EJ-3**, 1–11.
- [18] Beres, J. H., M. J. Alexander, and J. R. Holton, 2002: Effects of tropospheric wind shear on the spectrum of convectively generated gravity waves. *J. Atmos. Sci.*, **59**, 1805–1824.
- [19] Bernardet, L. R., L. D. Grasso, J. E. Nachamkin, C. A. Finley, and W. R. Cotton, 2000: Simulating convective events using a high resolution mesoscale model. *J. Geophys. Res.*, **105(D11)**, 14963–14982.
- [20] Black, M. L., R. W. Burpee, and F. D. Marks, 1996: Vertical motion characteristics of tropical cyclones determined with airborne Doppler radial velocities, *J. Atmos. Sci.*, **53**, 1887–1909.
- [21] Bluestein, H. B., E. W. McCaul Jr., G. P. Byrd, and G. R. Woodall, 1988: Mobile sounding observations of a tornadic storm near the dryline: The Canadian, Texas, storm of 7 May 1986. *Mon. Wea. Rev.*, **116**, 1790–1804.
- [22] Bowles, R. L., and B. Buck, 2009: A methodology for determining statistical performance compliance for airborne Doppler radar with forward-looking turbulence detection capability. NASA CR 2009-215769.
- [23] Brown, R., 1973: New indices to locate clear air turbulence. *Meteor. Mag.*, **102**, 347–361.

- [24] Bryan, G. H., J. C. Wyngaard, and J. M. Fritsch, 2003: Resolution requirements for the simulation of deep moist convection, *Mon. Wea. Rev.*, **131**, 2394–2416.
- [25] Buldovskii, G. S., S. A. Bortnikov, and M. V. Rubinshtejn, 1976: Forecasting zones of intense turbulence in the upper troposphere. *Meteor. Gidrol*, **2**, 9–18.
- [26] Bunkers, M. J., M. R. Hjelmefelt, and P. L. Smith, 2006: An observational examination of long-lived supercells. Part I: Characteristics, evolution, and demise. *Wea. Forecasting*, **21**, 673–688.
- [27] Byers, H. R., and R. R. Braham, 1949: The thunderstorm: Report of the Thunderstorm Project. Tech. rep., U.S. Government Printing Office, Washington, D.C, 297 pp.
- [28] Carey, L. D., and S. A. Rutledge, 2000: The relationship between precipitation and lightning in tropical island convection: A C-Band polarimetric radar study, *Mon. Wea. Rev.*, **128**, 2687–2710.
- [29] Carlberg, B. R., W. A. Gallus, and K. J. Franz, 2018: A preliminary examination of WRF ensemble prediction of convective mode evolution. *Wea. Forecasting*, **33**, 783–798.
- [30] Cecil, D.J., and Coauthors, 2014: Weather avoidance guidelines for NASA global hawk high-altitude unmanned aircraft systems (UAS). Poster, *93rd Annual American Meteorological Society Meeting*, Atlanta, GA.
- [31] Cetrone, J. and R. A. Houze, 2006: Characteristics of tropical convection over the ocean near Kwajalein. *Mon. Wea. Rev.*, **134**, 834–853.

- [32] Chen S. S., and R. A. Houze, 1997: Diurnal variation and life-cycle of deep convective systems over the tropical pacific warm pool. *Quart. J. Roy. Meteor. Soc.*, **123**, 357–388.
- [33] Chin, H. S., M. M. Bradley, Q. Fu, and C. R. Molenkamp, 1995: Modeling of a tropical squall line in two dimensions: Sensitivity to radiation and comparison with a midlatitude case, *J. Atmos. Sci.*, **52**, 3172–3193.
- [34] Cho, J. Y., R. E. Newell, B. E. Anderson, J. D. Barrick, and K. L. Thornhill, 2003: Characterizations of tropospheric turbulence and stability layers from aircraft observations. *J. Geophys. Res.*, **108**, 8784.
- [35] Chun, H.-Y., H.-J. Choi, and I.-S. Song, 2008: Effects of nonlinearity on convectively forced internal gravity waves: Application to a gravity wave drag parameterization. *J. Atmos. Sci.*, **65**, 557–575.
- [36] Clark, T. L., T. Hauf, J. P. Kuettner, 1986: Convectively forced internal gravity waves: results from two-dimensional numerical experiments. *Q. J. R. Meteorol. Soc.*, **112**, 899–925.
- [37] Colson, D., and H. A. Panofsky, 1965: An index of clear-air turbulence. *Quart. J. Roy. Meteor. Soc.*, **91**, 507–513.
- [38] Cornman, L. B., C. Morse, and G. Cuning, 1995: Real-time estimation of atmospheric turbulence severity from in-situ aircraft measurements. *J. Aircraft*, **32**, 171–177.
- [39] Cornman, L. B., G. Meymaris and M. Limber, 2004: An update on the FAA Aviation weather Research Programs in situ turbulence measurement and reporting system. *11th Conf. of Aviation, Range and Aerospace Meteorology*, Hyannis, MA.

- [40] Creighton, G., E. Kuchera, R. Adams-Selin, J. McCormick, S. Rentschler, B. Wickard, NCAR, AFWA, AER, UCAR, and NGC, 2014: AFWA diagnostics in WRF. AFWA Rep., 17 pp.
- [41] Dai, A., F. Giorgi, and K. Trenberth, 1999: Observed and model-simulated diurnal cycles of precipitation over the contiguous United States. *J. Geophys. Res.*, **104**, 6377–6402.
- [42] Dai, A., 2001: Global precipitation and thunderstorm frequencies. Part II: Diurnal variations. *J. Climate*, **14**, 1112–1128.
- [43] Deierling, W., 2018: Forecasting Convectively Induced Turbulence. *Preprints, 15th Annual Meeting*, Honolulu, HI, Asia Oceanic Geosciences Society.
- [44] Doyle, J. D., and Coauthors, 2011: An intercomparison of T-REX mountain-wave simulations and implications for mesoscale predictability. *Mon. Wea. Rev.*, **139**, 2811–2831.
- [45] Dutton, M. J. O., 1980: Probability forecasts of clear-air turbulence based on numerical output. *Meteor. Mag.*, **109**, 293–310.
- [46] Eastin, M. D., W. M. Gray, and P. G. Black, 2005: Buoyancy of convective vertical motions in the inner core of intense hurricanes. Part I: General statistics. *Mon. Wea. Rev.*, **133**, 188–208.
- [47] Eastin, M. D., W. M. Gray, and P. G. Black, 2005: Buoyancy of convective vertical motions in the inner core of intense hurricanes. Part II: Case studies. *Mon. Wea. Rev.*, **133**, 209–227.
- [48] Ellrod, G. P., and D. I. Knapp, 1992: An objective clear-air turbulence forecasting technique: Verification and operational use. *Wea. Forecasting*, **25**, 150–165.

- [49] Ellrod, G. P., and J. A. Knox, 2010: Improvements to an operational clear-air turbulence diagnostic index by addition of a divergence trend term. *Wea. Forecasting*, **7**, 789–798.
- [50] Emanuel, M., J. Sherry, S. Catapano, L. Cornman, and P. Robinson, 2013: In situ performance standard for eddy dissipation rate. *16th Conf. of Aviation, Range, and Aerospace Meteorology*, Austin, TX, Amer. Meteor. Soc., 11.3.
- [51] Endlich, R. M., 1964: The mesoscale structure of some regions of clear-air turbulence. *J. Appl. Meteor.*, **3**, 261–276.
- [52] Evans, C. D., D. F. Van Dyke, and T. Lericos, 2014: How do forecasters utilize output from a convection-permitting ensemble forecast system? Case study of a high impact precipitation event. *Wea. Forecasting*, **29**, 466–486.
- [53] Federal Aviation Administration, 1977: Aviation weather services, Department of Transportation, 112-113.
- [54] FAA, 2012: Aeronautical information manual. *Official guide to basic flight information and ATC procedures*, Ch. **7**.
- [55] FAA, 2014: Aeronautical information manual. *Official guide to basic flight information and ATC procedures*, Ch. **7**, 435–539.
- [56] FAA, 2017: Aeronautical information manual. *Official guide to basic flight information and ATC procedures*, Ch. **7**, 435–539.
- [57] FAA, 2017: FAQ: Weather Delay. Accessed 2 February 2018. [Available at <https://www.faa.gov/nextgen/programs/weather/faq/>].
- [58] Fovell, R., D. Durran, and J. R. Holton, 1992: Numerical simulations of convectively generated stratospheric gravity waves. *J. Atmos. Sci.*, **49**, 1427–1442.

- [59] Frehlich, R., and R. Sharman, 2004a: Estimates of turbulence from numerical weather prediction model output with applications to turbulence diagnosis and data assimilation. *Mon. Wea. Rev.*, **132**, 2308–2324.
- [60] Frehlich, R., and R. Sharman, 2004b: Estimates of upper level turbulence based on second order structure functions derived from numerical weather prediction model output. *Preprints, 11th Conf. on Aviation, Range, and Aerospace Meteorology*, Hyannis, MA, Amer. Meteor. Soc., P4.13.
- [61] Frehlich, R., and R. Sharman, 2010: Climatology of velocity and temperature turbulence statistics determined from rawinsonde and ACARS/AMDAR data. *J. Appl. Meteor. Climatol.*, **49**, 1149–1169.
- [62] Frierson, D. M. W., 2006: Robust increases in midlatitude static stability in simulations of global warming. *Geophys. Res. Lett.*, **33**, 1–4.
- [63] Frierson, D. M. W., and N. A. Davis, 2011: The seasonal cycle of midlatitude static stability over land and ocean in global reanalyses. *Geophys. Res. Lett.*, **38**, 1–6.
- [64] Fujiwara, M., M. K. Yamamoto, H. Hashiguchi, T. Horinouchi, and S. Fukao, 2003: Turbulence at the tropopause due to breaking Kelvin waves observed by the Equatorial Atmosphere Radar. *J. Geophys. Res. Letts.*, **30:D4**.
- [65] Futyan, J., and A. Del Genio, 2007: Deep convective system evolution over Africa and the tropical Atlantic. *J. Climate*, **20**, 5041–5060.
- [66] Galvin, J. F. P., 2016: *The Subtropical jet streams*. Wiley-Blackwell, 29–37.
- [67] Garstang, M., and D. R. Fitzjarrald 1999: *Observations of surface to atmosphere interactions in the tropics: Introduction*. Oxford University Press, 3–48.

- [68] Golding, W. L., 2000: Turbulence and its impact of commercial aviation. *J. Aviation/Aerospace Edu. and Res.*, **11**, 19–29.
- [69] Gray, W. M. and R. W. Jacobson, 1977: Diurnal variation of deep cumulus convection. *Mon. Wea. Rev.*, **105**, 1171–1188.
- [70] Güsten, H., G. Heinrich, E. Mönnich, M. Nolle, and J. Weppner, 2003: Two automated Ozone analyzers for use on civil aircraft operating in the tropopause region. *J. Atmos. Oceanic Technol.*, **20**, 292–300.
- [71] Haertel, P. T., G. N. Kiladis, A. Denno, and T. M. Rickenbach, 2008: Vertical-mode decompositions of 2-day waves and the Madden–Julian Oscillation. *J. Atmos. Sci.*, **65**, 813–833.
- [72] Heymsfield, G. M., R. Fulton, and J. Spinhirne, 1991: Aircraft overflight measurements of Midwest severe thunderstorms: Implications of geosynchronous satellite interpretations. *Mon. Wea. Rev.*, **119**, 436–456.
- [73] Herzegh, P., 2002: Development of automated aviation weather products for oceanic/remote regions: Scientific and practical challenges, research strategies, and first steps. *Preprints, 10th Conf. on Aviation, Range, and Aerospace Meteorology*, Portland, OR, Amer.Meteor. Soc., P3.1.
- [74] Hoinka, K. P., 1999: Temperature, h, and wind at the global tropopause. *Mon. Wea. Rev.*, **127**, 2248–2265.
- [75] Hong, G., G. Heygster, J. Notholt, and S. A. Buehler, 2008: Interannual to diurnal variations in tropical and subtropical deep convective clouds and convective overshooting from seven years of AMSU-B measurements. *J. Climate*, **21**, 4168–4189.

- [76] Houze, R. A., Jr., K. L. Rasmussen, M. D. Zuluaga, and S. R. Brodzik, 2015: The variable nature of convection in the tropics and subtropics: A legacy of 16 years of the Tropical Rainfall Measuring Mission satellite. *Rev. Geophys.*, **53**, 994–1021.
- [77] Iyer, E. R., A. J. Clark, M. Xue, and F. Kong, 2016: A comparison of 36–60-h precipitation forecasts from convection-allowing and convection-parameterizing ensembles. *Wea. Forecasting*, **31**, 647–661.
- [78] Janjić, Z., 1994: The step-mountain Eta coordinate model: Further developments of the convection, viscous sublayer, and turbulence closure schemes. *Mon. Wea. Rev.*, **122**, 927–945.
- [79] Jorgensen, D. P., and M. A. LeMone, 1989: Vertical velocity characteristics of oceanic convection. *J. Atmos. Sci.*, **46**, 621–640.
- [80] Kaplan, M. L., Y- L. Lin, A. J. Riordan, K. T. Waight, K. M. Lux, and A. W. Huffinan, 1999: Flight safety characterization studies. Part I: Turbulence categorization analyses. Interim Subcontractor Report to Research Triangle Institute, NASA contract NAS 1-99074.
- [81] Kauffmann, P., and A. Sousa-Poza, 2001: Market assessment of forward-looking turbulence sensing systems. NASA Rep. CR-2001-210905, 78 pp. [Available online at <http://gltrs.grc.nasa.gov/reports/2001/CR-2001-210905.pdf>].
- [82] Kessinger, C. J., and Coauthors, 2008: Convection diagnosis and nowcasting for oceanic aviation applications. *Remote Sensing Applications for Aviation Weather Hazard Detection and Decision Support*, San Diego, CA, Optical Engineering and Applications, 12.

- [83] Kessinger, C. J., 2017: An update on the convective diagnosis oceanic algorithm. *18th Conf. of Aviation, Range, and Aerospace Meteorology*, Seattle, WA, Amer. Meteor. Soc., 211.
- [84] Kim, J. H., and H. Chun, 2011: Statistics and possible sources of aviation turbulence over South Korea. *J. Appl. Meteor. Climatol.*, **50**, 311–324.
- [85] Kim, J. H., and H. Y. Chun, 2012: A numerical simulation of convectively induced turbulence above deep convection. *J. Appl. Meteor. Climatol.*, **51**, 1180–1200.
- [86] Kim, J. H., H. Y. Chun, R. D. Sharman, and S. B. Trier, 2014: The role of vertical wind shear on aviation turbulence within cirrus bands of simulated Western Pacific cyclone, *Mon. Wea. Rev.*, **142:8**, 2794–2813.
- [87] KNKT, 2015: Aircraft Accident Investigation Report. KNKT.14.12.29.04 Final Report, 206 pp.
- [88] Koch, S. E., B. D. Jamison, C. Lu, T. L. Smith, E. I. Tollerud, C. Girz, N. Wang, T. P. Lane, M. A. Shapiro, D. D. Parrish, and O. R. Cooper, 2005: Turbulence and gravity waves within an upper-level front. *J. Atmos. Sci.*, **62**, 3885–3908.
- [89] Kolmogorov, A. N., 1941: The local structure of turbulence in incompressible viscous fluid at high Reynolds number. *Dokl. Akad. Nauk SSSR*, **30**, 299–303.
- [90] Kuester, M. A., Alexander, M. J., and Ray, E. A., 2008: A model study of gravity waves over Hurricane Humberto (2001). *J. Atmos. Sci.*, **65**, 3231–3246.
- [92] Lane, T. P., M. J. Reeder, and T. L. Clark, 2001: Numerical modeling of gravity wave generation by deep tropical convection. *J. Atmos. Sci.*, **58**, 1249–1274.

- [92] Lane, T. P., and M. J. Reeder, 2001: Modelling the generation of gravity waves by a maritime continent thunderstorm. *Quart. J. Roy. Meteor. Soc.*, **127**, 3408–3419.
- [93] Lane, T. P., R. D. Sharman, T. L. Clark, and H. M. Hsu, 2003: An investigation of turbulence generation mechanisms above deep convection. *J. Atmos. Sci.*, **60**, 1297–1321.
- [94] Lane, T. P., and J. C. Knievel, 2005: Some effects of model resolution on simulated gravity waves generated by deep, mesoscale convection. *J. Atmos. Sci.*, **62**, 3408–3419.
- [95] Lane, T. P., and R. D. Sharman, 2008: Some influences of background flow conditions on the generation of turbulence due to gravity wave breaking above deep convection. *J. Appl. Meteor. Climatol.*, **47**, 2777–2796.
- [96] Lane, T. P., J. D. Doyle, R. D. Sharman, M. A. Shapiro, and C. D. Watson, 2009: Statistics and dynamics of aircraft encounters of turbulence over Greenland. *Mon. Wea. Rev.*, **137**, 2687–2702.
- [97] Lane, T. P., R. D. Sharman, S. B. Trier, R. G. Fovell, and J. K. Williams, 2012: Recent advances in the understanding of near-cloud turbulence. *Bull. Amer. Meteor. Soc.*, **93**, 499–515.
- [98] Lane, T. P., and R. D. Sharman, 2014: Intensity of thunderstorm-generated turbulence revealed by large-eddy simulation. *Geophys. Res. Lett.*, **41**, 2221–2227.
- [99] Lee, D., and H. Chun, 2018: A numerical study of aviation turbulence encountered on 13 February 2013 over the Yellow Sea between China and the Korean Peninsula. *J. Appl. Meteor. Climatol.*, **57**, 1043–1060.

- [100] Lehmiller, G. S., H. B. Bluestein, P. J. Neiman, F. M. Ralph, and W. F. Feltz, 2001: Wind structure in a supercell thunderstorm as measured by a UHF wind profiler. *Mon. Wea. Rev.*, **129**, 1968–1986.
- [101] LeMone, M. A., and E. J. Zipser, 1980: Cumulonimbus vertical velocity events in GATE. Part I: Diameter, intensity and mass flux. *J. Atmos. Sci.*, **37**, 2444–2457.
- [102] Lester, P. F., 1994: *Turbulence: A New Perspective for Pilots*. Jeppesen Sanderson, 212 pp.
- [103] Lin, Y.-L., and R.B. Smith, 1986: Transient dynamics of airflow near a local heat source. *J. Atmos. Sci.*, **43**, 40–49.
- [104] Lin, Y.-L., 2007: *Dynamics. Mesoscale Dynamics*, Cambridge University Press, 22–54.
- [105] Lin, Y-Lang, 2010: *Isolated convective storms*. Cambridge University, 272–321.
- [106] Liu, C., and M. W. Moncrieff, 1998: A numerical study of the diurnal cycle of tropical oceanic convection. *J. Atmos. Sci.*, **55**, 2329–2344.
- [107] Liu, C., and E. J. Zipser, 2005: Global distribution of convection penetrating the tropical tropopause. *J. Geophys. Res.*, **110**, D23104.
- [108] Liu, N., and C. Liu, 2016: Global distribution of deep convection reaching tropopause in 1 year GPM observations. *J. Geophys. Res. Atmos.*, **121**, 3824–3842.
- [110] Lucas, C., E. J. Zipser, and M. A. LeMone, 1994a: Vertical velocity off tropical Australia. *J. Atmos. Sci.*, **51**, 3183–3193.
- [110] Lucas, C., E. J. Zipser, and M. A. LeMone, 1994b: Convective available potential energy in the environment of oceanic and continental clouds: Correction and comments. *J. Atmos. Sci.*, **51**, 3829–3830.

- [111] Marconnet, D., C. Norden, and L. Vidal, 2016: Optimal use of weather radar. [Available online at [<http://www.smartcockpit.com/docs/optimum-use-of-weather-radar-airbus-safety-first-nr22.pdf>]]
- [112] Markowski, P., and Y. Richardson, 2010: *Organization of isolated convection*. Wiley-Blackwell, 201–244.
- [113] Marroquin, A., 1998: An advanced algorithm to diagnose atmospheric turbulence using numerical model output. *16th Conf. on Weather Analysis and Forecasting*, Phoenix, AZ, Amer. Meteor. Soc., 79–81.
- [114] McNulty, R. P., 1995: Severe and convective weather: A Central Region forecasting challenge, *Wea. Forecasting*, **10**,187–202.
- [115] Mecikalski J. R., T. A. Berendes, W. F. Feltz, K. M. Bedka, S. T. Bedka, J. J. Murray, A. J. Wimmers, P. Minnis, D. B. Johnson, J. Haggerty, B. Bernstein, M. Pavolonis, and E. Williams, 2007: Aviation Applications for Satellite-Based Observations of Cloud Properties, Convection Initiation, In-Flight Icing, Turbulence, and Volcanic Ash. *Bull. Amer. Meteor. Soc.*, **88**, 1589–1607.
- [116] Meischner, P., R. Baumann, H. Hller, and T. Jank, 2001: Eddy dissipation rates in thunderstorms estimated by Doppler radar in relation to aircraft in Situ measurements. *J. Atmos. Oceanic Technol.*, **18**, 1609–1627.
- [117] Monette, S. A. and J. M. Sieglaff, 2014: Probability of convectively induced turbulence associated with geostationary satellite-inferred cloud-top cooling. *J. Appl. Meteor. Climatol.*, **53**, 429–436.
- [118] Mullendore, G. L., A. J. Homann, S. T. Jorgenson, T. J. Lang, and S. A. Tessendorf, 2013: Relationship between level of neutral buoyancy and dual-doppler

- observed mass detrainment levels in deep convection, *Atmos. Chem. Phys.*, **13**, 181–190
- [120] Muñoz-Esparza, D., R. Sharman, J. Sauer, and B. Kosović, 2018: Toward low-level turbulence forecasting at eddy-resolving scales: *Geophys. Res. Lett.*, **45**, 1–10.
- [120] Muñoz-Esparza, D., and R. Sharman, 2018: An improved algorithm for low-level turbulence forecasting, *J. Appl. Meteor. Climatol.*, **57**, 1249–1263.
- [121] Musil, D. J., A. J. Heymsfield, and P. L. Smith, 1986: Microphysical characteristics of a well-developed weak echo region in a High Plains supercell thunderstorm. *J. Climate Appl. Meteor.*, **25**, 1037–1051.
- [122] Nastrom, G. D. and K. S. Gage, 1985: A climatology of atmospheric wavenumber spectra of wind and temperature observed by commercial aircraft. *J. Atmos. Sci.*, **42**, 950–960.
- [123] Nesbitt, S., and E. J. Zipser, 2003: The diurnal cycle of rainfall and convective intensity according to three years of TRMM measurements. *J. Climate*, **16**, 1456–1475.
- [124] Nesbitt, S. W., R. Cifelli, and S. A. Rutledge, 2006: Storm morphology and rainfall characteristics of TRMM precipitation features. *Mon. Wea. Rev.*, **134**, 2702–2721, <https://doi.org/10.1175/MWR3200.1>.
- [125] NTSB, 1997: Accident Rep. FTW97IA261. The National Transportation Safety Board, 4 pp. [Available from NTSB, Public Inquiries Branch, 490 L’Enfant Plaza, SW, Washington, DC 20594.].

- [126] NTSB, 2011: Accident Rep. DCA09IA071. The National Transportation Safety Board, 7 pp. [Available from NTSB, Public Inquiries Branch, 490 L'Enfant Plaza, SW, Washington, DC 20594.].
- [127] Orlandi, I., and K. Bryan, 1969: Formation of the thermocline step structure by large-amplitude internal gravity waves. *Journal of Geophysical Research*, **74**(28), 6975-6983.
- [128] Pantley, K. C., 1989: Turbulence near thunderstorm tops. M.S. thesis, Dept. of Meteorology, San Jose State University, 132 pp.
- [129] Pantley, K. C., and P. F. Lester, 1990: Observations of severe turbulence near thunderstorm tops. *J. Appl. Meteor.*, **29**, 1171-1179.
- [130] Pearson, J. M., and R. D. Sharman, 2017: Prediction of energy dissipation rates for aviation turbulence. Part II: Nowcasting convective and nonconvective turbulence. *J. Appl. Meteor. Climatol.*, **56**(2), 339-351.
- [131] Pearson, J. M., R. D. Sharman, W. Deierling, and G. Meymaris, 2019: Using in-cloud turbulence observations to improve nowcasting and forecasting of convectively induced turbulence. *Preprints, 19th Conf. on Aviation, Range, and Aerospace Meteorology*, Phoenix, AZ, Amer. Meteor. Soc., 4.3.
- [132] Pfister, L., S. Scott, M. Loewenstein, S. Bowen, and M. Legg, 1993: Mesoscale disturbances in the tropical stratosphere excited by convection: Observations and effects on the stratospheric momentum budget. *J. Atmos. Sci.*, **50**(8), 1058-1075.
- [133] Piani, C., D. Durran, M. J. Alexander, and J. R. Holton, 2000: A numerical study of three-dimensional gravity waves triggered by deep tropical convection and their role in the dynamics of the QBO. *J. Atmos. Sci.*, **57**, 3689-3702.

- [134] Poellot, M. R., and C. A. Grainger, 1991: A comparison of several airborne measures of turbulence. *Preprint, 4th International Conference of the Aviation Weather Systems*, Paris, France, Amer. Meteor. Soc.
- [135] Politovich, M. K., R. K. Goodrich, C. S. Morse, A. Yates, R. Barron, and S. A. Cohn, 2011: The Juneau terrain-induced turbulence alert system. *Bull. Amer. Meteor. Soc.*, **92**, 299-313.
- [136] Reiter, E. R., and P. F. Lester, 1968: Richardson's number in the free atmosphere. *Meteorol. Atmos. Phys.*, **17**, 1-7.
- [137] Roach, W. T., 1970: On the influence of synoptic development on the production of high level turbulence. *Quart. J. Roy. Meteorol. Soc.*, **96**, 413-429.
- [138] Romps, D. M., and Z. Kuang, 2009: Overshooting convection in tropical cyclones. *Geophys. Res. Lett.*, **36**, L09804.
- [139] Saha, K. R., and S. S. Singh, 1972: On the distribution of mean static stability and mean Richardson number in the tropical atmosphere. *J. Meteor. Soc. Japan*, **109**, 313-323.
- [140] Satheesan, K., and B. V. Krishna Murphy, 2002: Turbulence parameters in the tropical troposphere and lower stratosphere. *J. Geophys. Res.*, **107:D1**.
- [141] Sauer, J. A., Sauer, D. Muñoz-Esparza, J. M. Canfield, K. R. Costigan, R. R. Linn, and Y. Kim, 2016: A large-eddy simulation study of atmospheric boundary layer influence on stratified flows over terrain. *J. Atmos. Sci.*, **73**, 2615-2632.
- [142] Schumann, U., 1991: Subgrid length-scales for large-eddy simulation of stratified turbulence. *Theor. Comput. Fluid Dyn.*, **2**, 279-290.

- [143] Sharman, R. D., C. Tebaldi, G. Wiener, and J. Wolff, 2006: An integrated approach to mid- and upper-level turbulence forecasting, *Wea. Forecasting*, **21**, 268–287.
- [144] Sharman, R. D., J. D. Doyle, and M. A. Shapiro, 2012: An investigation of a commercial aircraft encounter with severe clear-air turbulence over western Greenland. *J. Appl. Meteor. Climatol.*, **51**, 42–53.
- [145] Sharman, R. D., L. B. Cornman, G. Meymaris, J. Pearson, T. Farrar, 2014: Description and derived climatologies of automated in situ eddy dissipation rate reports of atmospheric turbulence, *J. Appl. Climatol.*, **53**, 1416–1432
- [146] Sharman, R. D., and J. M. Pearson, 2017: Prediction of energy dissipation rates for aviation turbulence. Part I: Forecasting nonconvective turbulence. *J. Appl. Meteor. Climatol.*, **56**, 317–337.
- [147] Sharman, R. D., and S. B. Trier, 2018: Influences of gravity waves on convectively induced turbulence (CIT): A Review. *Pure and Applied Geophysics*, **52**.
- [148] Skamarock, W. C., 2004: Evaluating mesoscale NWP models using kinetic energy spectra. *Mon. Wea. Rev.*, **132**, 3019–3032.
- [149] Skamarock, W. C., and J. B. Klemp, 2008: A time-split nonhydrostatic atmospheric model for weather and forecasting applications. *J. Comp. Phys.*, **227**, 3465–3485.
- [150] Smit, H. G., A. Volz-Thomas, M. Helten, W. Paetz, and D. Kley, 2008: An in-flight calibration method for near-real-time humidity measurements with the airborne MOZAIC sensor. *J. Atmos. Oceanic Technol.*, **25**, 656–666.

- [151] Soden, B. J., 2000: The diurnal cycle of convection, clouds and water vapor in the tropical upper troposphere. *Geophys. Res. Lett.*, **27**, 2173–2176.
- [152] Song, I-S., H-Y. Chun, and T. P. Lane, 2003: Generation mechanisms of convectively forced internal gravity waves and their propagation to the stratosphere. *J. Atmos. Sci.*, **60**, 1960–1980.
- [153] Statista, 2018: Estimated annual growth rates for passenger air traffic from 2017 to 2036, by region. Accessed 20 January 2018. [Available at <https://www.statista.com/statistics/269919/growth-rates-for-passenger-and-cargo-air-traffic/>].
- [154] Stephan, C., and M. J. Alexander, 2014: Summer season squall line simulations: Sensitivity of gravity waves to physics parameterization and implications for their parameterization in global climate models. *J. Atmos. Sci.*, **71**, 3376–3391.
- [155] Stephan, C., and M. J. Alexander, 2015: Realistic simulations of atmospheric gravity waves over the continental US using precipitation radar data. *J. Adv. Model. Earth Syst.*, **7(2)**, 823–835.
- [156] Storer, L. N., P. G. Gill, and P. D. Williams, 2018: Multi-model ensemble predictions of aviation turbulence. *Meteorological Applications*, **1**, 1002–1041.
- [157] Tapia, A., J. A. Smith, and M. Dixon, 1998: Estimation of convective rainfall from lightning observations. *J. Appl. Meteor.*, **37**, 1497–1509.
- [158] Tanaka, H., and N. Yoshizawa, 1987: A Slowly varying model of the Quasi-biennial Oscillation involving effects of transience, self-acceleration and saturation of equatorial waves. *J. Atmos. Sci.*, **44**, 1427–1436.

- [159] Towns, J., and Coauthors, 2014: XSEDE: Accelerating scientific discovery. *Comput. Sci. Eng.*, **16**, 62–74, <http://doi.ieeecomputersociety.org/10.1109/MCSE.2014.80>.
- [160] Trier, S. B., and R. D. Sharman, 2009: Convection-permitting simulations of the environment supporting widespread turbulence within the upper-level outflow of a mesoscale convective system. *Mon. Wea. Rev.*, **137**, 1972–1990.
- [161] Trier, S. B., R. D. Sharman, R. G. Fovell, and R. G. Frehlich, 2010: Numerical simulation of radial cloud bands within the upper-level outflow of an observed mesoscale convective system. *J. Atmos. Sci.*, **67**, 2990–2999.
- [162] Trier, S. B., R. D. Sharman, and T. P. Lane, 2012: Influences of moist convection on a cold-season outbreak of clear-air turbulence (CAT). *Mon. Wea. Rev.*, **140**, 2477–2496.
- [163] Trier, S. B., and R. D. Sharman, 2016: Mechanisms influencing cirrus banding and aviation turbulence near a convectively enhanced upper-level jet stream. *Mon. Wea. Rev.*, **144**, 3003–3027.
- [164] Trier, S. B., and R. D. Sharman, 2018: Trapped gravity waves and their association with turbulence in a large thunderstorm anvil during PECAN. *Mon. Wea. Rev.*, **146**, 3031–3052.
- [165] U.S. Department of the Air Force, 1982: *Weather for aircrews*. Air Force Manual 51-12, Vol. 1, Dept. of the Air Force, 187 pp.
- [166] U.S. Department of Transportation Federal Aviation Administration, 2013: Subject: Thunderstorms. *Advisory Circular*, **00-24c**, 1-13.

- [167] Vant-Hull, B., W. Rossow, and C. Pearl, 2016: Global comparisons of regional life cycle properties and motion of multiday convective systems: Tropical and mid-latitude land and ocean. *J. Climate*, **29**, 5837–5858.
- [168] Vasquez, T., 2009: Investigative Meteorology Report Continental Flight 128 Turbulence near Dominican Republic. 9 pp.
- [169] Vinnichenko, N. K., N. Z. Pinus, S. M. Shmeter, and G. N. Shur, 1980: *Turbulence in the Free Atmosphere*. 2nd ed. Consultants Bureau, 310 pp.
- [170] Wakimoto, R. M., and H. V. Murphey, 2009: Analysis of a dryline during IHOP: Implications for convection initiation. *Mon. Wea. Rev.*, **137**, 912–936.
- [171] Walterscheid, R. L., and G. Schubert, 1990: Nonlinear evolution of an upward propagating gravity wave: Overturning, convection, transience and turbulence. *J. Atmos. Sci.*, **47**, 101–125.
- [172] Weisman, M. L., C. Davis, W. Wang, K. W. Manning, and J. B. Klemp, 2008: Experiences with 0–36-h explicit convective forecasts with the WRF-ARW model. *Wea. Forecasting*, **23**, 407–437.
- [173] Williams, J. K., 2004: NCAR turbulence detection algorithm. *NEXRAD Technical Advisory Committee Meeting*, Indianapolis, IN.
- [174] Williams, J. K., G. Craig, G. Blackburn, and W. Deierling, 2011: Measuring in-cloud turbulence: the NEXRAD Turbulence Detection Algorithm. *15th Conf. on Aviation, Range and Aerospace Meteorology*, Los Angeles, CA, Amer. Meteor. Soc., 2.1.

- [175] Williams, J. K., and G. Meymaris, 2016: Remote turbulence detection using ground-based Doppler radar. *Aviation Turbulence: Processes, Detection, Prediction*, R. D. Sharman, and T. P. Lane, Eds., Springer, 149–177.
- [176] Wimmers, A., S. Griffin, J. Gerth, S. Bachmeier, and S. Lindstrom, 2018: Observations of gravity waves with high-pass filtering in the new generation of geostationary imagers and their relation to aircraft turbulence. *Wea. Forecasting*, **33**, 139–144.
- [177] Wissmeier, U. and R. Goler, 2009: A comparison of tropical and midlatitude thunderstorm evolution in response to wind shear. *J. Atmos. Sci.*, **66**, 2385–2401.
- [178] Wolff J. K., and R. D. Sharman, 2008: Climatology of upper-level turbulence over the continental United States, *J. Appl. Meteor. Climatol.*, **47**, 2198–2214.
- [179] Xu, K. and D.A. Randall, 2001: Updraft and downdraft statistics of simulated tropical and midlatitude cumulus convection. *J. Atmos. Sci.*, **58**, 1630–1649.
- [180] Yamamoto, M. K., M. Fujiwara, T. Horinouchi, H. Hashiguchi, and S. Fukao, 2003: Kelvin-Helmholtz instability around the tropical tropopause observed with Equatorial Atmosphere Radar. *Geophys. Res. Lett.*, **30(9)**, 1476.
- [181] Yang, G-Y., and J. M. Slingo, 2001: The diurnal cycle in the tropics. *Mon. Wea. Rev.*, **129**, 784–801.
- [182] Yang, G., and B. Hoskins, 2013: ENSO Impact on kelvin waves and associated tropical convection. *J. Atmos. Sci.*, **70**, 3513–3532, <https://doi.org/10.1175/JAS-D-13-081.1>.

- [183] Yuter, S. E., R. A. Houze, A. Smith, T. T. Wilheit, and E. Zipser, 2005: Physical characterization of tropical oceanic convection observed in KWAJEX. *J. Appl. Meteor.*, **44**, 385–415.
- [184] Zhang, Y., and S. A. Klein, 2010: Mechanisms affecting the transition from shallow to deep convection over land: Inferences from observations of the diurnal cycle collected at the ARM Southern Great Plains site. *J. Atmos. Sci.*, **67**, 2943–2959.
- [185] Zipser, E. J., and M. A. LeMone, 1980: Cumulonimbus vertical velocity events in GATE. Part II: Synthesis and model core structure. *J. Atmos. Sci.*, **37**, 2458–2469.
- [186] Zipser, E. J., 2003: Some views on “Hot Towers” after 50 years of tropical field programs and two years of TRMM Data. *Meteorological Monographs*, **51**, 49–58.
- [187] Zovko-Rajak, D., and T. P. Lane, 2014: The generation of near-cloud turbulence in idealized simulations. *J. Atmos. Sci.*, **71**, 2430–2451.

Boom, thee end.